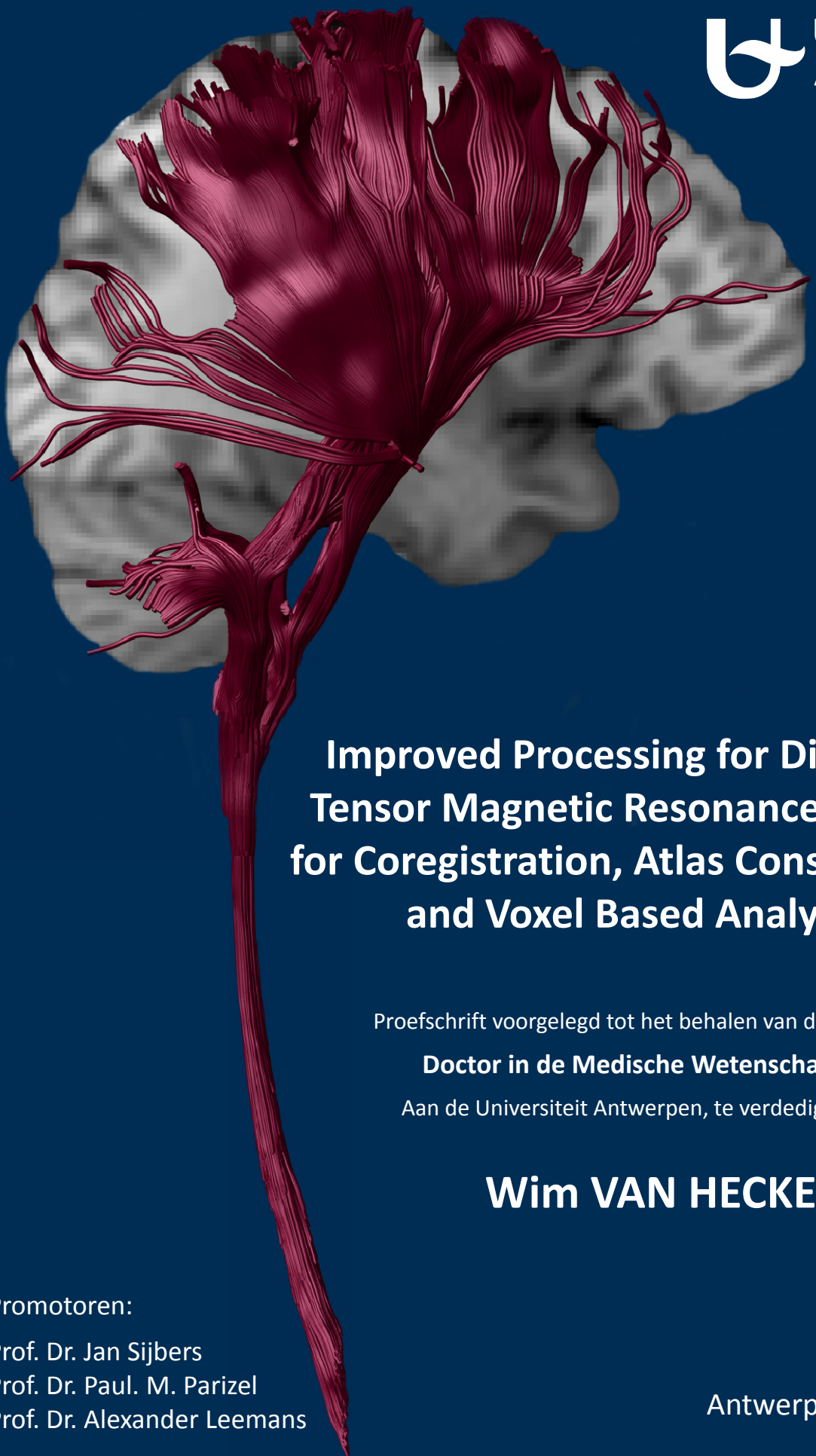

Universiteit Antwerpen

Improved Processing for Diffusion Tensor Magnetic Resonance Images for Coregistration, Atlas Construction, and Voxel Based Analysis

Proefschrift voorgelegd tot het behalen van de graad van

Doctor in de Medische Wetenschappen

Aan de Universiteit Antwerpen, te verdedigen door

Wim VAN HECKE

Promotoren:

Prof. Dr. Jan Sijbers
Prof. Dr. Paul. M. Parizel
Prof. Dr. Alexander Leemans

Antwerpen, 2009

Improved Processing for Diffusion Tensor Magnetic Resonance Images for Coregistration, Atlas Construction, and Voxel Based Analysis.

Verbeterde Diffusie Tensor Magnetische Resonantie Beeldverwerking voor Coregistratie, Atlas Constructie en Voxel Gebaseerde Analyses

Proefschrift voorgelegd tot het behalen van de graad van

Doctor in de Medische Wetenschappen

aan de Universiteit Antwerpen, te verdedigen door

Wim VAN HECKE

Promotors
Prof. Dr. Jan Sijbers
Prof. Dr. Paul M. Parizel
Prof. Dr. Alexander Leemans

Antwerpen, 2009

If the brain would be so simple that we could understand it, we would be so simple that we could not understand it.

– Emerson Pugh

Doctoral committee

Chairman
Prof. Dr. W. Cras

Supervisors
Prof. Dr. J. Sijbers
Prof. Dr. P.M. Parizel

External members
Prof. Dr. A. Vanderlinden
Prof. Dr. J. Van Goethem

Contact information

✉ Wim Van Hecke
Vision Lab, Dept. of Physics
University of Antwerp (CDE)
Universiteitsplein 1, Building N1.18
B-2610 Wilrijk – Antwerpen, Belgium

☎ +32 (0)3 820 24 77

🖷 +32 (0)3 820 22 45

🖂 wim.vanhecke@ua.ac.be

🌍 http://webhost.ua.ac.be/visielab/vanhecke

ISBN ??

Cover illustration
Virtual reconstruction of the human pyramidal white matter fiber tracts in the left hemisphere.

The research presented in this thesis was performed at the Vision Lab (Dept. of Physics) and the Antwerp University Hospital (Dept. of Radiology)

Contents

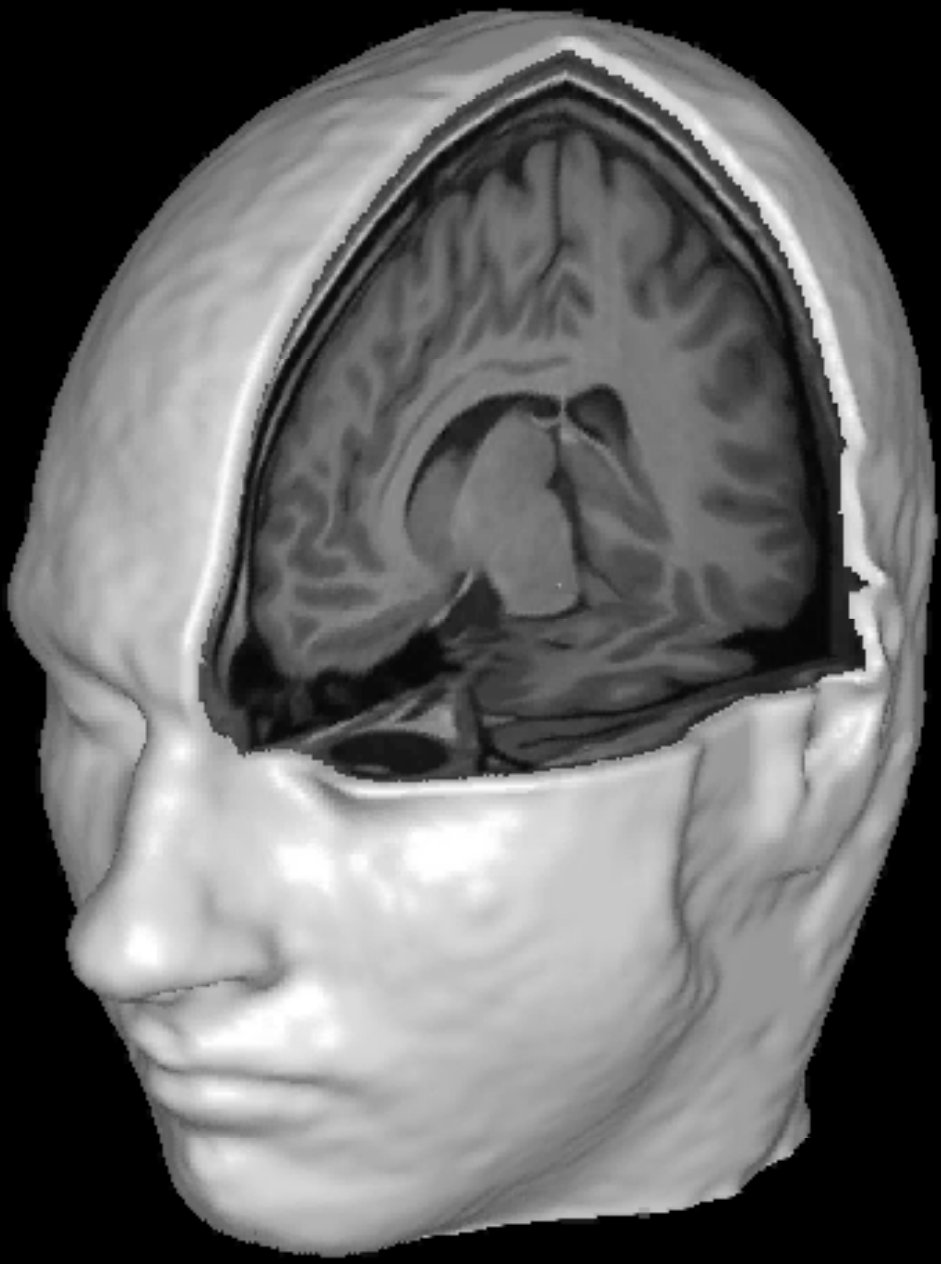

I

INTRODUCTION

If a man will begin with certainties he shall end in doubts, but if he will be content to begin with doubts, he shall end in certainties

– Sir Francis Bacon (1561 – 1626)

1 Introduction to this thesis

Contents

1.1 Context

Science is organized knowledge. Wisdom is organized life.
– Immanuel Kant

The human brain contains a very complex network of fiber bundles that connect different brain regions, allowing them to communicate. A little more than a decade ago, dissection and histology studies on postmortem human brains or invasive studies on primates were the only way to acquire information on the neural architecture [1–5]. However, recent advancements in magnetic resonance imaging (MRI) allow virtual in-vivo dissection of major white matter (WM) bundles in the brain. Information about the WM fibers is obtained by measuring the diffusion of water molecules, using a technique called diffusion tensor magnetic resonance imaging (DT-MRI) or diffusion tensor imaging (DTI) [6]. A virtual reconstruction of the fiber network in three dimensions can then be derived from this diffusion information using diffusion tensor tractography (DTT) [7, 8].
Since DTI is capable of accurately describing the underlying architecture of the WM microstructure in a non-invasive way, i.e. by placing a subject for a few minutes in an MRI scanner, it has a lot of potential for unraveling the human brain connectivity in healthy subjects and in patients with neurological and psychiatric disorders. Nowadays, a lot of research is done to reveal the relationship between DTI measures and the underlying microstuctural alterations that are induced by a pathology. DTI is already used in the daily clinical routine of many hospitals for the presurgical planning of patients with a brain tumor. In addition, DTI has the potential of being applied in the hospitals as a diagnostic tool for patients with neurological symptoms. To this end, large scale group studies that compare patient and healthy subject DTI data sets need to be performed.
The goal of this thesis is to optimize the post-processing of DTI data sets of the human brain for a reliable detection of WM altering pathologies. In addition, the post-processing of spinal cord DTI data sets is examined for the detection of neurological spinal cord affecting disorders.

1.2 Manuscript organization

Oh, how much is today hidden by science! Oh, how much it is expected to hide!
– Friedrich Nietzsche (1844-1900)

This thesis is subdivided in three parts:

Background: In the first part, an introduction to the central nervous system (Chapter 2) and to the diffusion tensor imaging technique (Chapter 3) is

provided. The anatomy of the central nervous system is thereby briefly described on a cellular as well as a functional level. Thereafter, an overview of brain imaging techniques is given. In Chapter 3, the fundamentals of the DTI technique, from the Brownian motion of water molecules to the virtual reconstruction of three-dimensional (3D) fiber tracts and clinical applications, are elucidated. Subsequently, different approaches for the post-processing of DTI data sets are introduced.

Diffusion Tensor Image Processing of the human brain: In the second part of this thesis, some new techniques for the post-processing of DTI data sets are explained.

In Chapter 4, a non-rigid coregistration method based on a viscous fluid model and mutual information is presented. This image alignment algorithm is specifically designed for the coregistration of the multi-valued DT images. The goal of coregistration is to transform one image to another so that the corresponding anatomical structures are aligned and that the image information can be compared objectively in the same spatial framework. Although the different anatomical structures of the brain are present in all persons, they can significantly differ in size and/or shape. Therefore, in order to map images from different subjects to each other, non-rigid transformations, in which the deformation fields can be adapted locally, are necessary. In contrast to other medical images, such as computed tomography (CT), ultrasound (US), or anatomical magnetic resonance (MR) data sets, which contain a scalar value in each voxel, DTI data sets contain a multi-valued tensor in each voxel. Coregistration algorithms therefore need to be adapted in order to include this multi-valued image information.

The construction of an atlas allows the mapping of individual brain images to a common reference frame. Subsequently, image properties can be compared on a voxel-by-voxel level between healthy subjects and patients with a certain pathology. In Chapter 5, a population specific DTI atlas is constructed and compared with a subject based atlas method using simulations and real data sets.

After all DTI data sets of a subject group are transformed to the atlas space, the diffusion properties of these images can be analyzed on a voxel level. To this end, statistical tests are performed in each voxel in order to detect differences between healthy subject and patient data sets. This post processing approach is referred to as a voxel based analysis (VBA). In VBA, the whole brain is tested for control-patient differences without any a priori hypothesis of the expected spatial location of the abnormalities. This VBA method has many advantages compared to other post-processing approaches, such as the region of interest (ROI) method. However, correspondence between the

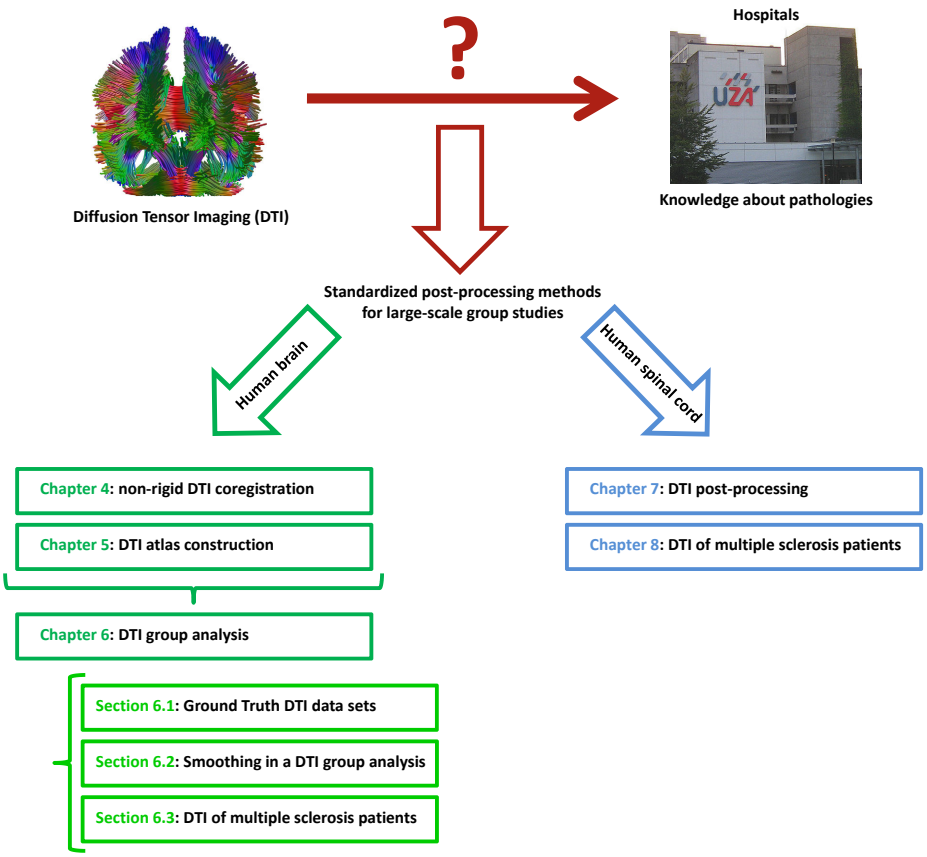

Figure 1.1. *A schematic overview of this thesis.*

findings is not always observed, such as for example in the study of patients with schizofrenia [9–22]. The subject group and disease heterogeneity across the different studies, including confounding factors such as age, sex, handedness, disease state, etc., can partially explain these observed discrepancies. However, methodological differences in implementation of VBA are possibly even more decisive for explaining the variances in the VBA results of different studies [17, 23, 24].

In Chapter 6 simulated DTI data sets are constructed, which allows for modeling of anomalies in the diffusion properties in a predefined location. These simulated DTI data sets can be used to investigate the sensitivity and specificity of a VBA or ROI analysis to detect pathologies. In addition, the effect of the different parameters and post processing steps that are involved in the

pipeline of a VBA analysis can be examined, which will lead to a more reliable, standardized, and consistent post-processing of DT images for studying different pathologies. As a first application of these simulated DTI data sets, the effect of different smoothing approaches, i.e. isotropic vs. anisotropic, and different smoothing kernel widths on the sensitivity and specificity of the pathology detection is examined in Chapter 6.

Finally, the new post-processing techniques (i.e. coregistration, atlas construction, and anisotropic smoothing) were applied in the analysis of cognitive decline in patients with multiple sclerosis (MS).

Diffusion Tensor Image Processing of the human spinal cord: The third part of this thesis is focussed on the post-processing of spinal cord DTI data sets. Several factors, such as physiologic and respiratory movement of the subject and the relative motion of the spinal cord itself due to the pulsation of the surrounding cerebro spinal fluid (CSF), hamper a robust DTI study of the spinal cord. In addition, the relatively small diameter of the spinal cord (12 mm on average) and the restricted resolution of the diffusion tensor images further impede a quantitative study. In Chapter 7, a standardized and robust segmentation technique for the analysis and interpretation of DTI spinal cord data based on diffusion tensor tractography is introduced. This new post-processing is then applied to analyze the DTI data of MS patients with and without spinal cord lesions (Chapter 8).

Bibliography

[1] H. Gray, Grays Anatomy of the Human Body., Lea and Febriger, 1918.

[2] W. J. S. Krieg, Functional neuroanatomy., Brain Books, Evanston, Ill, 1966.

[3] M. G. Yasargil, Anatomy. In: Microneurosurgery IVA CNS Tumors: Surgical Anatomy, Neuropathology, Neuroradiology, Neurophysiology, Clinical Considerations, Operability, Treatment Options., Thieme Medical Publishers, Inc, New York, 1994.

[4] L. Heimer, The human brain and spinal cord: functional neuroanatomy and dissection guide., Springer-Verlag, New York, 1995.

[5] A. K. Afifi, R. A. Bergman, Functional Neuroanatomy: Text and Atlas., McGraw-Hill Professional Publishing, 1997.

[6] P. Basser, J. Mattiello, D. Le Bihan, MR diffusion tensor spectroscopy and imaging, Biophysics Journal 66 (1) (1994) 259–267.

[7] P. Basser, S. Pajevic, C. Pierpaoli, J. Duda, A. Aldroubi, In vivo fiber tractography using DT-MRI data, Magn Reson Med 44 (4) (2000) 625–632.

[8] S. Mori, B. Crain, V. Chacko, P. van Zijl, Three-dimensional tracking of axonal projections in the brain by magnetic resonance imaging, Ann Neurol 45 (2) (1999) 265–269.

[9] I. Agartz, J. Andersson, S. Skare, Abnormal brain white matter in schizophrenia: a diffusion tensor imaging study, NeuroReport 12 (10) (2001) 2251–2254.

[10] J. Foong, M. R. Symms, G. J. Barker, M. Maier, D. H. Miller, M. A. Ron, Investigating regional white matter in schizophrenia using diffusion tensor imaging., NeuroReport 13 (3) (2002) 333–6.

[11] B. A. Ardekani, J. Nierenberg, M. J. Hotman, D. C. Javitt, K. O. Lim, MRI Study of White Matter Diffusion Anisotropy in Schizophrenia., NeuroReport 14 (16) (2003) 2025–2029.

[12] J. Burns, D. Job, M. Bastin, H. Whalley, T. Macgillivray, E. Johnstone, S. Lawrie, Structural disconnectivity in schizophrenia: a diffusion tensor magnetic resonance imaging study, British Journal of Psychiatry 182 (2003) 439–443.

[13] P. R. Szeszko, B. A. Ardekani, M. Ashtari, S. Kumra, D. G. Robinson, S. Sevy, H. Gunduz-Bruce, A. K. Malhotra, J. M. Kane, R. M. Bilder, K. O. Lim, White matter abnormalities in first-episode schizophrenia or schizoaffective disorder: a diffusion tensor imaging study., Am J Psychiatry 162 (3) (2005) 602–605.

[14] M. Kubicki, H. Park, C.-F. Westin, P. Nestor, R. Mulkern, S. Maier, M. Niznikiewicz, E. Connor, J. Levitt, M. Frumin, R. Kikinis, F. Jolesz, R. McCarley, M. Shentona, DTI and MTR abnormalities in schizophrenia: analysis of white matter integrity, NeuroImage 26 (4) (2005) 1109–1118.

[15] B. A. Ardekani, A. Bappal, D. D'Angelo, M. Ashtari, T. Lencz, P. R. Szeszko, P. D. Butler, D. C. Javitt, K. O. Lim, J. Hrabe, J. Nierenberg, C. A. Branch, M. J. Hoptman, Brain morphometry using diffusion weighted MRI: Application to schizophrenia., NeuroReport 16 (13) (2005) 1455–1459.

[16] M. S. Buchsbaum, J. Friedman, B. R. Buchsbaum, K. Chu, E. A. Hazlett, R. Newmark, J. S. Schneiderman, Y. Torosjan, C. Tang, P. R. Hof, D. Stewart, K. L. Davis, J. Gorman, Diffusion tensor imaging in schizophrenia., Biol Psych 60 (11) (2006) 1181–1187.

[17] D. K. Jones, X. A. Chitnis, D. Job, P. L. Khong, L. T. Leung, S. Marenco, S. M. Smith, M. R. Symms, What happens when nine different groups analyze the same DT-MRI data set using voxel-based methods?, Proc. ISMRM 15th Annual Meeting, Berlin (2007) 74.

[18] G. Douaud, S. Smith, M. Jenkinson, T. Behrens, H. Johansen-Berg, J. Vickers, S. James, N. Voets, K. Watkins, P. M. Matthews, A. James, Anatomically related grey and white matter abnormalities in adolescent-onset schizophrenia., Brain 130 (2007) 2375–2386.

[19] J. H. Seok, H. J. Park, J. W. Chun, S. K. Lee, H. S. Cho, J. S. Kwon, J. J. Kim, White

matter abnormalities associated with auditory hallucinations in schizophrenia: A combined study of voxel-based analyses of diffusion tensor imaging and structural magnetic resonance imaging., Psychiatry Res. 156 (2) (2007) 93–104.

[20] K. H. Karlsgodt, T. G. M. van Erp, R. A. Poldrack, C. E. Bearden, K. H. Nuechterlein, T. D. Cannon, Diffusion tensor imaging of the superior longitudinal fasciculus and working memory in recent-onset schizophrenia., Biol Psych 63 (5) (2007) 512–518.

[21] M. Kyriakopoulos, N. S. Vyas, G. J. Barker, X. A. Chitnis, S. Frangou, A diffusion tensor imaging study of white matter in early-onset schizophrenia., Biol Psychiatry 63 (5) (2007) 519–523.

[22] T. White, A. T. K. Kendi, S. Lehricy, M. Kendi, C. Karatekin, A. Guimaraes, N. Davenport, S. C. Schulz, K. O. Lim, Disruption of hippocampal connectivity in children and adolescents with schizophrenia - a voxel-based diffusion tensor imaging study., Schizophr Res 90 (1–3) (2007) 302–307.

[23] D. Jones, M. Symms, M. Cercignani, R. Howarde, The effect of filter size on VBM analyses of DT-MRI data, NeuroImage 26 (2) (2005) 546–554.

[24] H. Zhang, B. B. Avants, P. A. Yushkevich, J. H. Woo, S. Wang, L. F. McCluskey, L. B. Elman, E. R. Melhem, J. C. Gee, High-dimensional spatial normalization of diffusion tensor images improves the detection of white matter differences: An example study using amyotrophic lateral sclerosis, IEEE Trans. Med. Imaging 26 (11) (2007) 1585–1597.

II

BACKGROUND

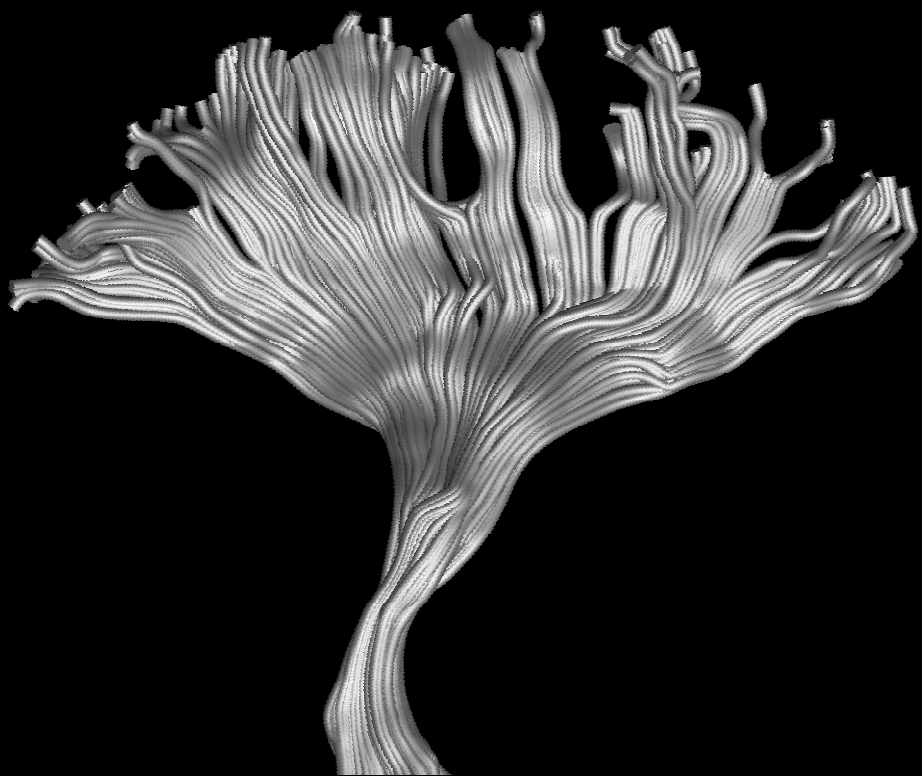

Mind is ever the ruler of the universe.
– Philebus Plato (429 – 347 BC)

2

A brief introduction to the central nervous system

Contents

Overview

Although the human brain only weights about 1.4 kg and consists of very small and simple entities, it endows a person with an immense number of abilities. The brain operates in the background of every action, sensation, and thought and makes it possible to laugh, cry, communicate, etc. All of this is achieved by one hundred billion nerve cells, which communicate by a hundred trillion interconnecting axons. For more than 2000 years, scientists are fascinated by the complexity of the brain. Despite the interest in the working of the human brain and the accelerating pace of discovery in neuroscience, scientists often face the limitations of our intellect to understand our intellect. We are a long way from a complete physical and functional understanding of the healthy and impaired human brain. However, new functional imaging techniques can provide an additional insight into the complexity of the brain.
In this chapter, a short overview is provided of more than 2000 years of brain research. Additionally, the human brain anatomy is discussed and different methods of macroscopic brain imaging are introduced.

2.1 A brief history of the human brain

> *The seat of the soul and the control of voluntary movement - in fact, of nervous functions in general - are to be sought in the heart. The brain is an organ of minor importance.*
> – Aristotle ($384-322$ BC)

Hippocrates ($460-370$ bc) is usually referred to as being the first to argue that the brain is the most important organ for sensation, thought, emotion, and cognition. However, Aristotle ($384-322$ bc), who lived a hundred years later, stated that the heart was the ruler of the body. He considered the brain to be a secondary organ that served as a cooling agent for the heart. For centuries, this was the generally accepted view.
Since Claudius Galenus of Pergamum ($131-201$ ad), better known as Galen, was a physician at a school for gladiators in Rome, he had access to a lot of 'patients' with open skulls and different brain lesions. Based on his observations, he agreed with Hippocrates that the brain is the most important organ of the body for sensation, thought, emotion, and cognition [1]. Galen also stated that fluid from the ventricles in the brain was distributed to the muscles and organs. In the centuries after the death of Galen, the study of the human brain was ceased, because of a church ban on the study of the human anatomy using dissections.
In 1543, the anatomist Andreas Vesalius publishes 'De humani corporis fabrica' (On the workings of the human body), one of the first known neuroscience textbooks

[2]. According to Vesalius, the brain functions are not regulated by the fluid in the ventricles, as Gales stated. The 17^{th} century French philosopher, René Descartes ($1596-1650$), reformulated the brains functioning and compared the brain with the working of a complex machine, controlled by hydraulic systems [3]. According to the Englishman Thomas Willis ($1621-1675$), the solid cerebral tissue has important functions that are responsible for the working of the brain. He stated that the brain functioning depends on the flow of blood to this cerebral tissue. This idea forms the basis of the functional magnetic resonance imaging (fMRI) technique, in which local increases in blood flow are associated with the activation of nerve cells.
In the 18^{th} century, Luigi Galvani ($1737-1798$) and Alessandro Volta ($1745-1827$) discovered the importance of electrical signals to the brain functioning. The German physiologist Du Bois-Reymond ($1818-1896$) demonstrated in the middle of the 19^{th} century that nerves can indeed generate electrical signals. The relation between the discrete cells at the microscopic level and the working of the brain, was first recognized by the Spanish neuroanatomist Santiago Ramon y Cajal ($1852-1934$). Cajal furthermore proposed that information flows between different neuron cell bodies along the axons. The ideas of Cajal were confirmed towards the end of the 19^{th} century by the Italian anatomist Camillo Golgi ($1843-1926$), who developed a technique to highlight few neurons in any particular region of the brain. By the end of the 20^{th} century, a more or less complete understanding of how neurons generate electrical and chemical signals was achieved.

2.2 Anatomy of the central nervous system

> *I don't think there's anything unique about human intelligence. All the neurons in the brain that make up perceptions and emotions operate in a binary fashion. We can someday replicate that on a machine. Earthly life is carbon based and computers are.*
> – Bill Gates

The central nervous system (CNS) consists of the brain and the spinal cord. The nerves that emanate from them, and connect the nerve fibers with the rest of our body, constitute the peripheral nervous system.

2.2.1 The cellular level

Neural information processing is conducted by neurons, cells that process and transmit information using electrochemical signals. The cell body of the neuron integrates information from other neurons, while the function of the axons is to transmit this information to other neurons (see Fig. 2.1). When a neuron receives input from other neurons, an electrical action potential is produced, which travels down

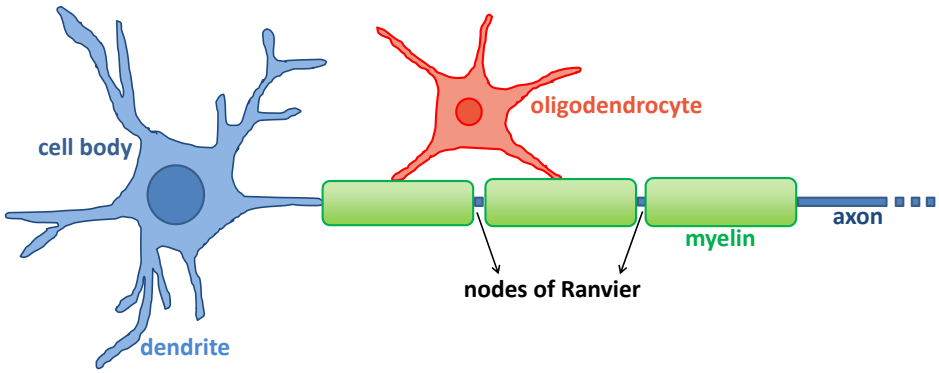

Figure 2.1. *The neuron consists of a cell body and dendrites. The axon is the long fiber extending from the neuron cell body. It contains myelin sheaths that are interrupted by nodes of Ranvier. The oligodendrocyte is a glial cell that plays a supportive role.*

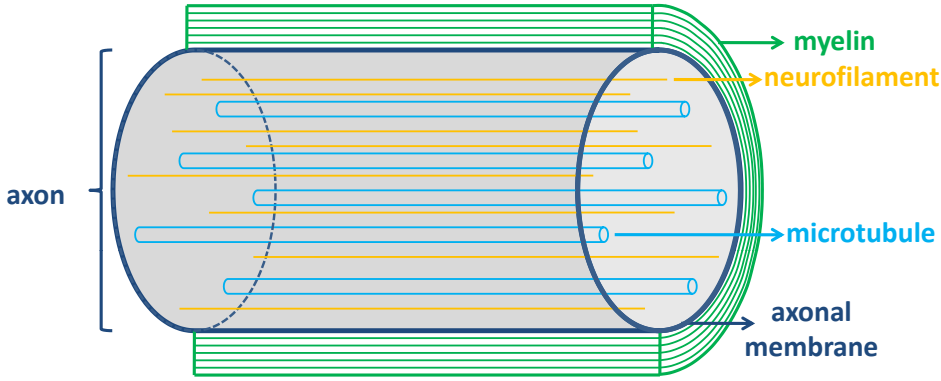

Figure 2.2. *The axon is surrounded by myelin and contains several structures, such as neurofilaments, microtubuli, and the axonal membrane.*

the axon to the synapses with other neurons. Neurotransmitter is then released at the synapses, and the postsynaptic neuron may depolarize. The velocity of the action potential is increased by an insulating process called myelination. Supporting glial cells wrap layers of myelin around the axon, periodically leaving open small regions called nodes of Ranvier (see Fig. 2.2).

When observing a post-mortem brain, as shown on as a coronal slice in Fig. 2.3, a natural division based on the color can be made: the white matter (WM) and the gray matter (GM). The GM primarily contains the cell bodies of neurons, dendrites, glial cells, and capillaries. The WM contains myelinated axons that travel together

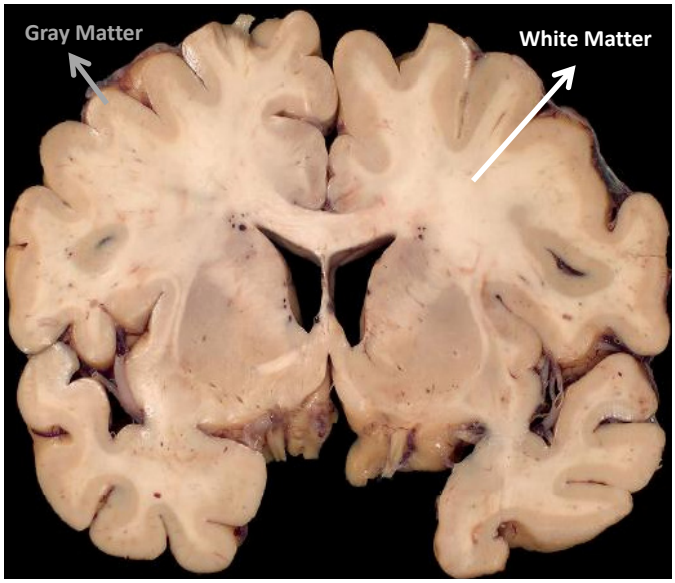

Figure 2.3. *On this coronal post-mortem brain slice, a color difference can be observed between the gray matter, which is mainly situated on the outside of the brain, and the white matter [4].*

and are called WM bundles or fiber tracts. WM is colored white because of the presence of lipids in the myelin. As can be seen on the coronal post-mortem brain slice of Fig. 2.3, the GM is located around the outside of the human brain and in internal brain structures such as the basal ganglia and the thalamus. In addition to the WM and GM regions, there are two important fluid systems in the brain: CSF, which fills the ventricles and spaces around the brain, and a vasculature system.
In summary, these are the important cellular components of the central nervous system:

Neurons or nerve cells are the basic functional units of the nervous system. They vary in size from 4 microns (0.004 mm) to 100 microns (0.1 mm) in diameter. In the brain, neurons are responsible for information processing. A neuron consists of a compact cell body, many long branched extensions (dendrites) and a long fiber (the axon) with branching extensions at its end. A single neuron can receive signals from thousands of other neurons, and its axon can branch repeatedly, sending signals to thousands more.

Dendrites form the branched extensions of a neuron that receive nerve impulses from other nerve cells and carry them toward the cell body.

Glial cells support and feed neurons, outnumbering them 10 to one. They play

an important supportive role in maintaining efficiency along the brain nerve network.

Axons are long, unbranched fibers extending from a neuron that carry nerve impulses to other cells. Axons are cylinders with a diameter from $1\mu m$ to $30\mu m$. It consists of microtubule, neurofilaments, and the axonal membrane. Most axons are surrounded by myelin sheets (see Fig. 2.2).

Myelin is a material composed of lipids and proteins that forms a protective sheath around axons and helps facilitate the transmission of electrical signals. The abnormal breakdown of myelin, such as in MS, is called demyelination, and seriously disrupts normal communication between neurons.

2.2.2 Functional anatomy of the brain

The brain consists of two hemispheres, which are connected by a fiber bundle called the corpus callosum. Each side of the brain consists of three main areas:

The brain stem is the extension of the spinal cord within the brain and consists of the midbrain, medulla, and pons. Neurological functions of the brain stem are associated with survival, such as the control of breathing, digestion, heart rate, blood pressure, etc.

The cerebellum is located at the lower back of the brain. It is regarded as a structure that can help motor as well as non-motor regions to do their work effectively.

The cerebrum is the largest area of the brain, containing four lobes. The frontal lobe is associated with a persons personality and thought. Within the parietal lobe are areas that control pain and sensations. The temporal lobes are involved in speech, memory, and hearing. The occipital lobe is responsible for interpreting visual information.

The different functional regions of the brain are interconnected by WM fiber bundles. The WM contains three types of fiber bundles: commissural, association, and projection bundles. In the next paragraphs, the different fiber bundles are visualized using diffusion tensor tractography.

2.2.2.1 Commissural fiber bundles

A commissure is a crossing site for fibers which connect similar areas of the two cerebral hemispheres.

Corpus Callosum: The corpus callosum is the largest fiber bundle in the nervous system and connects left and right cerebral hemispheres, allowing them to communicate with each other (see Fig. 2.4 (a)). It can be divided into an anterior (i.e. genu, see Fig. 2.4 (b)), a central (i.e. body, see Fig. 2.4 (c)), and a posterior portion (i.e. splenium, see Fig. 2.4 (d)). The corpus callosum allocates each kind of processing to the area of the brain which is programmed for the job. It plays an important role in motor, perceptual and cognitive functioning [5–7].

2.2.2.2 Association fiber bundles

Association fibers connect regions in the same hemisphere, primarily have anterior-posterior trajectories.

Cingulum: The cingulum is a tract of association fibers that encircles the corpus callosum and lies within the cingulate gyrus and connecting the callosal and hippocampal convolutions of the brain (see Fig. 2.5) [8]. The cingulum is part of the limbic system and is involved in attention, memory and emotions [9, 10].

Inferior longitudinal fasciculus: The inferior longitudinal fasciculus connects the occipital lobe with the temporal lobe (see Fig. 2.6). The exact function of the inferior longitudinal fasciculus has not been clearly demonstrated, but it is involved in face recognition, visual perception, reading, visual memory [11–18].

Arcuate fasciculus: The arcuate fasciculus is an association bundle that links Brocca's and Wernicke's area. It is composed of long and short fibers connecting the frontal, parietal, and temporal lobes (see Fig. 2.7). The arcuate fasciculus links key language areas in the human brain. [18–20].

Uncinate fasciculus: The uncinate fasciculus connects the frontal and temporal lobes of the cerebrum (see Fig. 2.8) [24]. This fasciculus is probably involved in language, memory, and emotional recognition functions [17, 18, 25].

Inferior fronto-occipital fasciculus: The inferior fronto-occipital fasciculus is a fiber bundle that connects the occipital lobe and the frontal cortex (see Fig. 2.9). The functions of the inferior fronto-occipital fasciculus are poorly understood, although it is possible that it participates to reading, attention and visual processing [9, 13, 16, 18, 21].

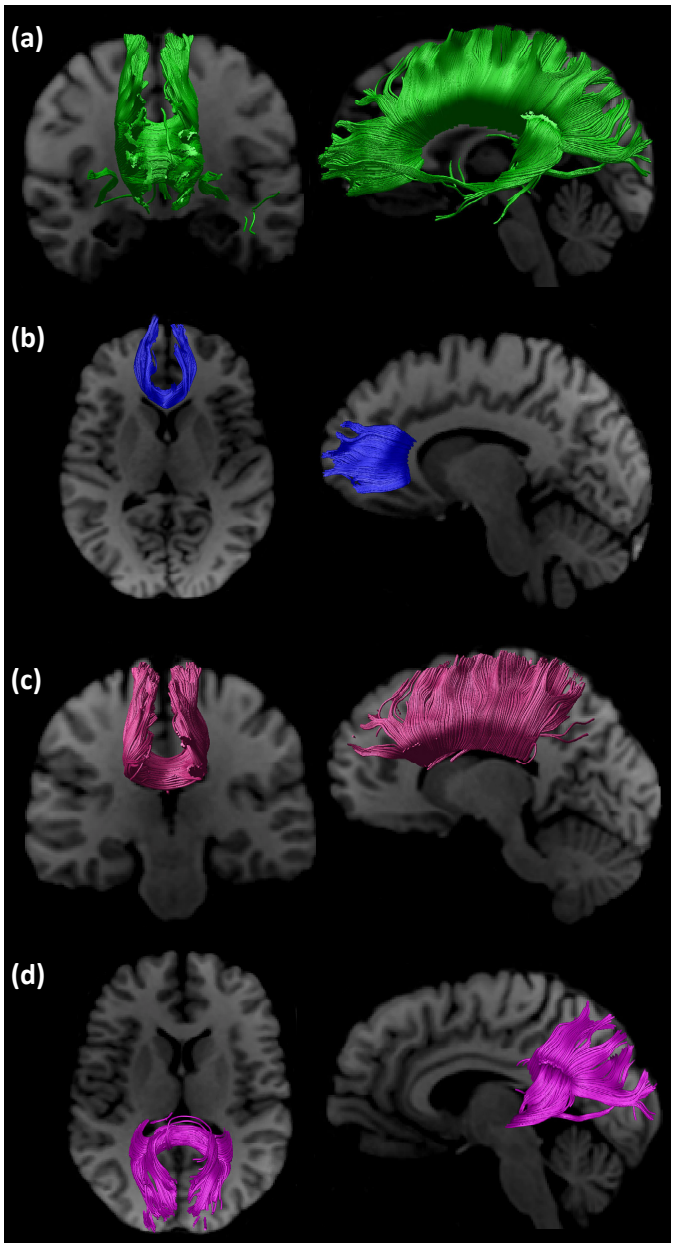

Figure 2.4. *The corpus callosum (a) and the genu (b), body (c), and splenium (d) of the corpus callosum*

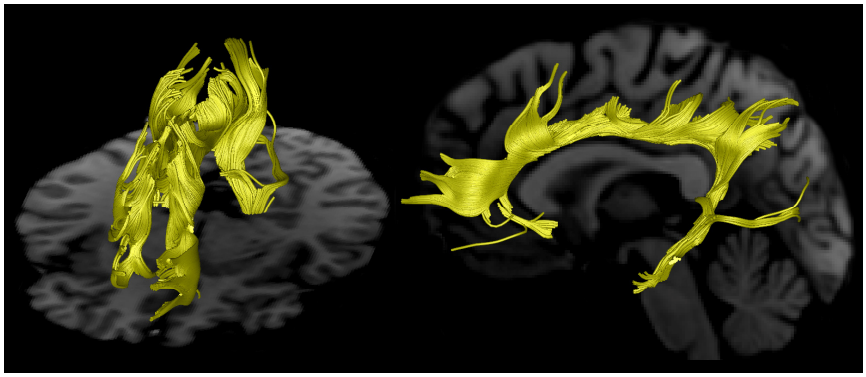

Figure 2.5. *The cingulum*

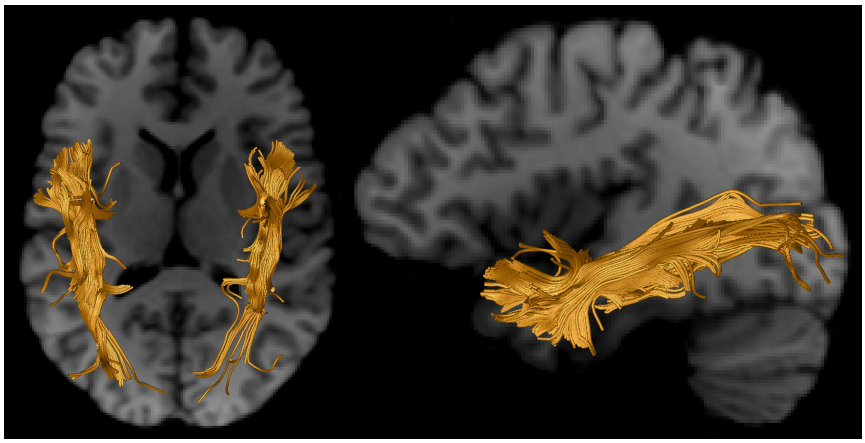

Figure 2.6. *The inferior longitudinal fasciculus*

2.2.2.3 Projection fiber bundles

Projection fibers connect the cortex and subcortical structures such as the thalamus, basal ganglia, and spinal cord. The connections to and from the cerebellum are also called projection tracts.

Sensory and motor cortico spinal tracts: The corticospinal or pyramidal tract contains fibers that originate in the sensorimotor areas of the cerebral cortex and descend through the brain stem to the spinal cord and fibers that ascend from the spinal cord to the cerebral cortex. The corticospinal tract is responsible for transmitting motor and sensory impulses [26].

Fornix: The fornix is a projection bundle that connects hippocampus to the mam-

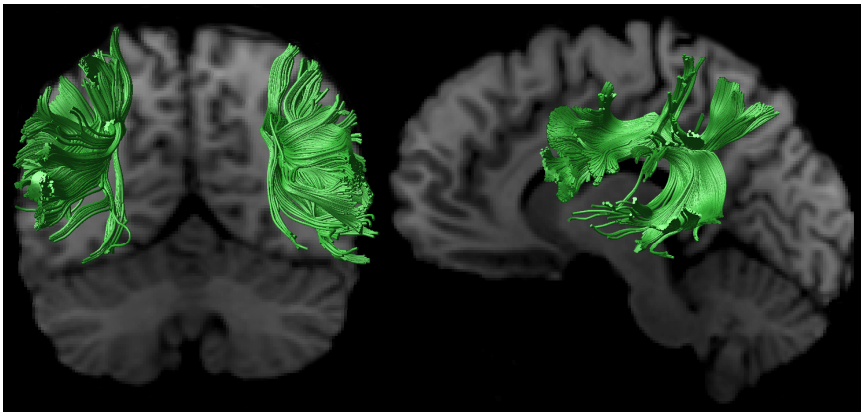

Figure 2.7. *The arcuate fasciculus*

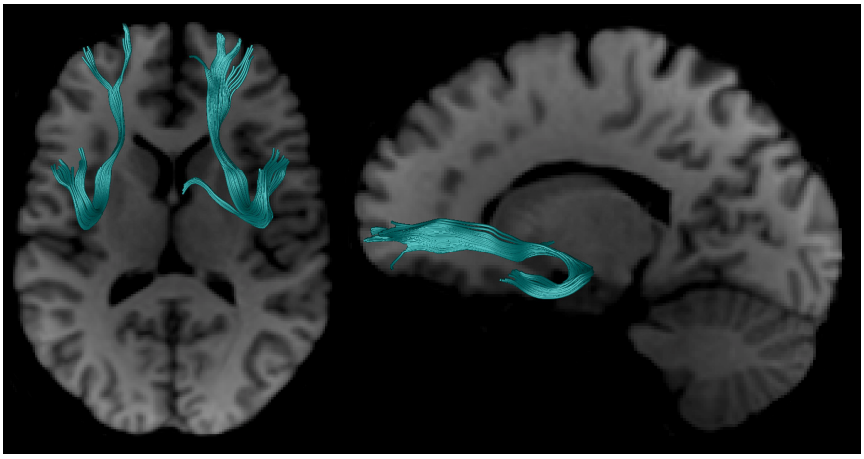

Figure 2.8. *The uncinate fasciculus*

millary bodies (see Fig. 2.12). The fornix belongs to the limbic system and is involved in emotion and memory functions [17, 25].

Cerebellar peduncles: The cerebellar peduncle carries many types of input and output fibers that are mainly concerned with integrating sensory input with motor functions such as balance (see Fig. 2.13).

2.2.3 Spinal Cord

The spinal cord is a long bundle of nerves located inside the vertebral canal, extending from the base of the brain running along the inside of the spine (backbone).

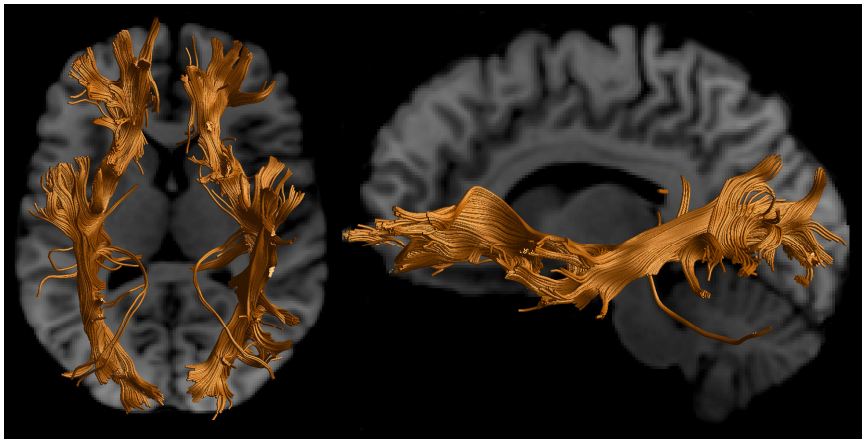

Figure 2.9. *The inferior fronto occipital fasciculus*

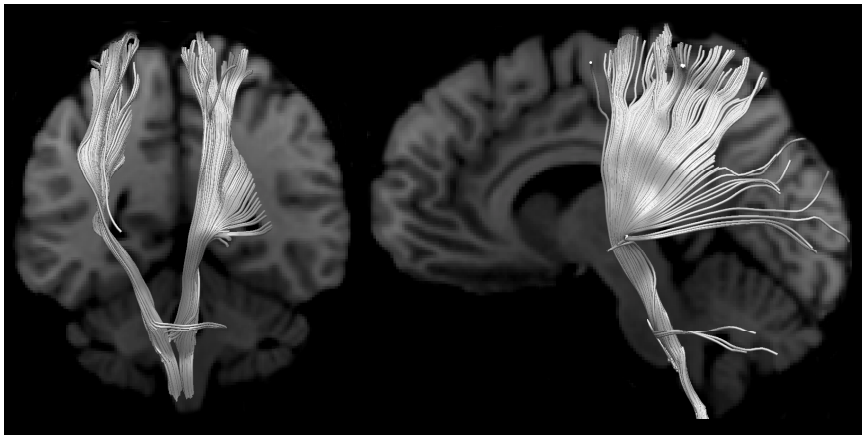

Figure 2.10. *The sensory cortico spinal tracts*

The spinal cord is composed of 31 segments: 8 cervical, 12 thoracic, 5 lumbar, 5 sacral, and 1 coccygeal. Like the brain, the spinal cord contains both GM and WM. The GM lies in the center of the spinal cord and consists of cell bodies of the motor neurons that pass signals to body muscles. A thick layer of WM surrounds the GM as can be seen in Fig. 2.14. WM is made up primarily of axons and contains the nerve fibers that pass signals to and from the brain. The spinal nerves comprise the sensory nerve roots, which enter the spinal cord at each level, and the motor roots, which emerge from the cord at each level.

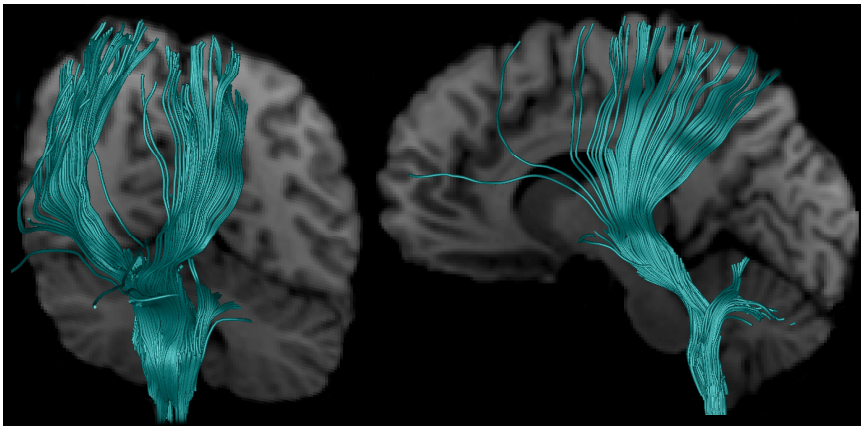

Figure 2.11. *The motor cortico spinal tracts*

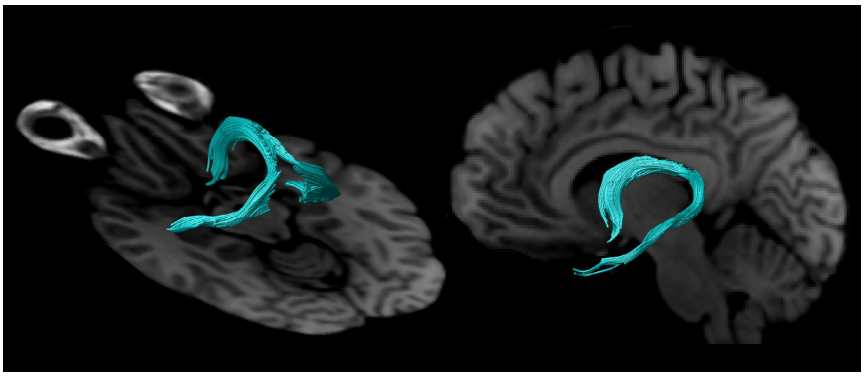

Figure 2.12. *The fornix*

2.3 Brain imaging

> *Strange coincidence, that every man whose skull has been opened had a brain!*
> – Ludwig Wittgenstein

Traditional methods for examining the brain, including post-mortem visual inspection and chemical tracer methods are invasive and time-consuming, and therefore limited in application. To address these problems, imaging methods for studying neuroanatomy were pioneered at the end of the 19th century.

X-ray imaging: The foundations of the medical specialty of radiology were laid when German physics professor Wilhelm Roentgen (1845 – 1923) presented

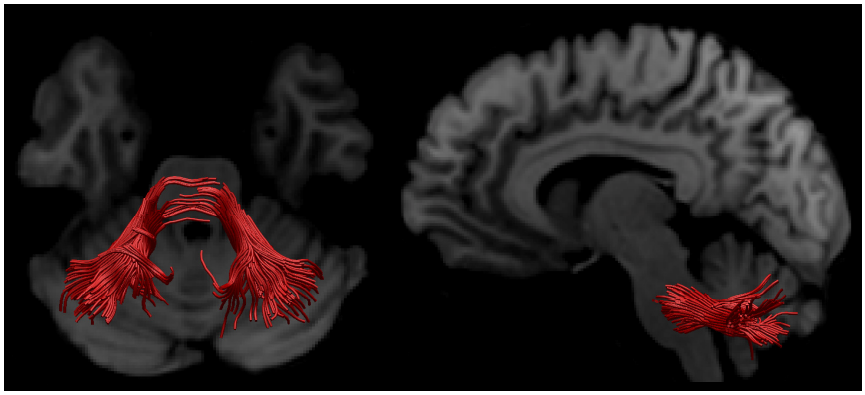

Figure 2.13. *The cerebellar peduncles*

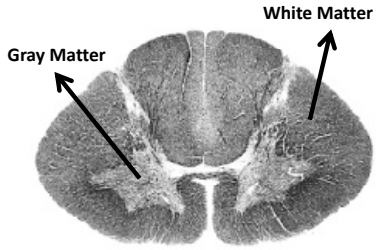

Figure 2.14. *A cross-sectional view of the spinal cord [27]*

his preliminary report, 'On a New Kind of Rays', on December 28, 1895, announcing the discovery of X-rays, for which he would later receive the first Nobel Prize in physics. Roentgen discovered accidently that shimmers of light were produced on a nearby fluorescent screen while experimenting with cathode ray tubes. This mysterious phenomenon was called X radiation or X-rays. Further experiments revealed that X-rays produces an image on photographic plates and penetrates many materials such as paper, wood, certain metals, and living tissue.

Nuclear imaging: Nuclear imaging studies were first done in the 1950's using special gamma cameras. These studies require the introduction of very low-level radioactive chemicals into the body. These radionuclides are taken up by the organs in the body and subsequently emit faint radiation signals which are measured or detected by the gamma camera.

Ultrasound imaging: In the 1960's, the principals of sonar were applied to diagnostic imaging, resulting in the ultrasound imaging technique. In this

method, a part of the body is exposed to high-frequency sound waves. Ultrasound exams do not use ionizing radiation (such as X-rays). Because ultrasound images are captured in real-time, they can show the structure and movement of the body's internal organs, as well as blood flowing through blood vessels.

Computed tomography imaging: Digital imaging techniques were implemented in the 1970's with the first clinical use and acceptance of the Computed Tomography or CT scanner, invented by Godfrey Hounsfield. Hounsfield used gamma rays (and later X-rays) and a detector that was placed on a rotating frame. The resulting data was reconstructed with a computer to create detailed cross sectional images of objects. The CT scanners for clinical use were first installed in 1975. During its 25-year history, CT has made great improvements in speed, patient comfort, and resolution. The new scanners provide excellent images of diagnostic quality at low doses of radiation.

Magnetic resonance imaging: MR principals were initially investigated in the 1950's showing that different materials resonated at different magnetic field strengths. MR imaging was cleared for commercial and clinical availability by the Food and Drug Administration (FDA) in 1984. Over the next few years, MRI became a supplementary modality to CT specially for investigating the brain and spinal cord. Today MRI is the imaging modality of choice for many parts of the body.

Bibliography

[1] Galen, Galen on the Usefulness of the Parts of the Body., Cornell University Press, transl. Margaret Tallmadge May, Ithaca, 1968.

[2] E. Clarke, C. D. OMalley, The Human Brain and Spinal Cord, University of California Press, Berkeley, California, 1968.

[3] R. Descartes, Treatise on Man., Cambridge University Press, Cambridge, U. K., 1985.

[4] http://www.neuroanatomy.ca .

[5] M. Glickstein, G. Berlucchi, Classical disconnection studies of the corpus callosum, Cortex 44 (8) (2008) 914–927.

[6] K. W. Doron, M. S. Gazzaniga, Neuroimaging techniques offer new perspectives on callosal transfer and interhemispheric communication, Cortex 44 (8) (2008) 1023–1029.

[7] M. Balsamo, L. Trojano, A. Giamundo, D. Grossi, Left hand tactile agnosia after posterior callosal lesion, Cortex 44 (8) (2008) 1030–1036.

[8] B. A. Vogt, D. L. Rosene, D. N. Pandya, Thalamic and cortical afferents differentiate anterior from posterior cingulate cortex in the monkey, Science 204 (1979) 205–207.

[9] D. Rudrauf, S. Mehta, T. Grabowski, Disconnections renaissance takes shape: Formal incorporation in group-level lesion studies, Cortex 44 (8) (2008) 1084–1096.

[10] M. Catani, Diffusion tensor Magn Reson Imaging tractography in cognitive disorders., Curr Opin Neurol 19 (6) (2006) 599–606.

[11] R. J. Tusa, L. G. Ungerleider, The inferior longitudinal fasciculus: a reexamination in humans and monkeys, Ann Neurol 18 (1985) 583–591.

[12] M. Catani, D. Jones, R. Donato, D. Ffytche, Occipito-temporal connections in the human brain, Brain 126 (9) (2003) 2093–2107.

[13] C. J. Fox, G. Iaria, J. J. S. Barton, Disconnection in prosopagnosia and face processing, Cortex 44 (8) (2008) 996–1009.

[14] D. H. ffytche, The hodology of hallucinations, Cortex 44 (8) (2008) 1067–1083.

[15] D. H. ffytche, M. Catani, Beyond localization: from hodology to function, Philosophical Transactions of the Royal Society of London B Biological Sciences 360 (2005) 767–779.

[16] S. Epelbaum, P. Pinel, R. Gaillard, C. Delmaire, M. Perrin, S. Dupont, Pure alexia as a disconnection syndrome: New diffusion imaging evidence for an old concept, Cortex 44 (8) (2008) 962–974.

[17] E. D. Ross, Sensory-specific amnesia and hypoemotionality in humans and monkeys: Gateway for developing a hodology of memory, Cortex 44 (8) (2008) 1010–1022.

[18] M. Catani, M. Mesulam, The arcuate fasciculus and the disconnection theme in language and aphasia: history and current state, Cortex 44 (8) (2008) 953–961.

[19] M. Catani, D. K. Jones, D. H. ffytche, Perisylvian language networks of the human brain, Annals of Neurology 57 (2005) 8–16.

[20] K. M. Heilmann, R. T. Watson, Disconnectional apraxia, Cortex 44 (8) (2008) 975–982.

[21] F. Doricchi, M. Thiebaut de Schotten, F. Tomaiuolo, P. Bartolomeo, White matter (dis)connections and gray matter (dys)functions in visual neglect: Gaining insights into the brain networks of spatial awareness, Cortex 44 (8) (2008) 983–995.

[22] M. Thiebaut de Schotten, S. Kinkingnehun, C. Delmaire, S. Lehericy, H. Duffau, L. Thivard, E. Volle, R. Levy, B. Dubois, P. Bartolomeo, Visualization of disconnection syndromes in humans, Cortex 44 (8) (2008) 1097–1103.

[23] M. Catani, M. Allin, M. Husain, L. Pugliese, M. Mesulam, R. Murray, D. K. Jones, Symmetries in human brain language pathways predict verbal recall, Proc. Natl. Acad. Sci. U. S. A. 104 (2007) 17163–17168.

[24] M. Catani, R. Howard, S. Pajevic, D. Jones, Virtual in vivo interactive dissection of white

matter fasciculi in the human brain, NeuroImage 17 (1) (2002) 77–94.

[25] D. Gaffan, C. R. E. Wilson, Medial temporal and prefrontal function: Recent behavioural disconnection studies in the macaque monkey, Cortex 44 (8) (2008) 928–935.

[26] J. Schmahmann, D. N. Pandya, Disconnection syndromes of basal ganglia, thalamus, and cerebrocerebellar systems, Cortex 44 (8) (2008) 1037–1066.

[27] http://www.britannica.com .

Water is the driving force of all nature.

– Leonardo Da Vinci

3

Diffusion tensor imaging and analysis

Contents

Overview

In this chapter, the diffusion tensor magnetic resonance imaging technique is introduced. In the brain WM, the diffusion of water molecules is hindered by various tissue components, such as for example the cell membrane, the axon sheath and myelin. Based on the measurement of the diffusion of water molecules in the central nervous system, information regarding the WM connectivity is derived. In this chapter, the theoretical underpinnings of DTI are introduced, including the acquisition of the images and the visualization of the tensors. In addition, some possible applications of DTI are discussed. Finally, a short overview of the different methods for a DTI group analysis is provided.

3.1 Introduction

> *Take your dead hydrogen-atoms, your dead nitrogenatoms, your dead phosphorus-atoms, and all the other atoms, dead as grains of shot, of which the brain is formed. Imagine them separate and sensationless, observe them running together and forming all imaginable combinations. This, as a purely mechanical process, is seeable by the mind. But can you see, or dream, or in any way imagine, how out of that mechanical act, and from these individually dead atoms, sensation, thought, and emotion are to arise?*
> – John Tyndall (1820 – 1893)

In 1946, Felix Bloch and Edward M. Purcell independently published their findings that an atomic nucleus with unpaired protons, when placed in a strong magnetic field, rotates with a frequency that depends on the strength of the magnetic field [1, 2]. After applying a radio frequency (RF) field of this particular frequency, which is called the resonance frequency, the atomic nucleus absorbs energy. Subsequently, when the RF field is stopped, this energy is emitted through an electromagnetic wave of the resonance frequency. This discovery laid the foundation for MRI. In 1952, Bloch and Purcell were awarded the Nobel Prize for this research. In 1950, Hahn discovered that the amplitude of the observed signal is reduced in the presence of a magnetic field inhomogeneity when the spins undergo a random thermal motion [3]. This discovery was fundamental in the development of DTI.
In 1972, Paul Lauterbur developed the idea of using magnetic field gradients to examine the human body. He published the first MR image in *Nature* in 1973 [4]. Peter Mansfield proposed a new ultrafast acquisition method, known as the echo-planar imaging (EPI) technique, by studying the mathematical properties of the MRI signal [5, 6]. In 2003, Paul C. Lauterbur and Sir Peter Mansfield were awarded the Nobel price for their work within this field.

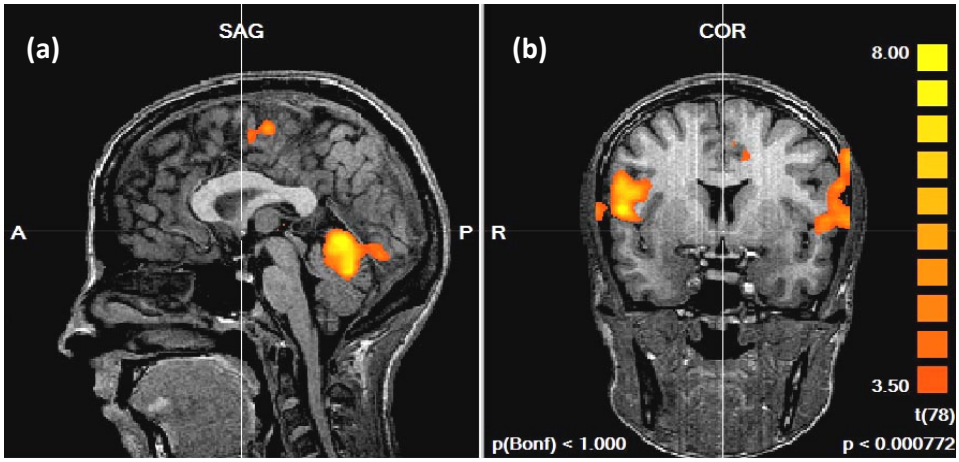

Figure 3.1. *The statistical activation map, obtained by fMRI, is superimposed on a sagittal (a) and coronal (b) slice of the anatomical MRI scan.*

In the early 1980s, there were 12 MR machines worldwide, and since then the use of MR scanners has rapidly increased. At this moment, there are 98 MR scanners in Belgium, and more than 25000 worldwide (http://www.emrf.org/). Compared with other imaging modalities, MRI has many advantages. First of all, since magnetic fields are used instead of ionizing radiation for the image acquisition, MRI is a non-invasive technique. In addition, it provides an amazingly strong imaging contrast between different soft tissues which is not feasible with other imaging modalities. Finally, the MR image acquisition can be adapted to display other physical phenomenons, such as for example the blood flow (a method called MR angiography), brain activation (functional MRI) or brain connectivity (diffusion tensor MRI).

Today, the most frequently used MRI method in medicine is the anatomical MRI scan, which is designed to differentiate various tissues, and can be applied to examine any part of the body. Another, more recent imaging method is functional MRI (fMRI). Since this technique maps activation patterns in the brain, it is an important modality for better understanding the function of different regions in the brain of healthy subjects and subjects with various pathologies. The fMRI method is based on the idea that, when a brain region is activated, new energy must be transported to this region, which leads to an increased blood flow in this part of the brain. This can be imaged by repetitive MR scans and detected by appropriate signal processing methods. In Fig. 3.1, fMRI results are superimposed on an anatomical MRI scan. Since fMRI indirectly maps activation signals from neurons, it is a technique that is focused on the brain GM.

In this thesis, we will focus on another MRI modality, i.e. diffusion tensor imaging. This imaging method, introduced in 1994, maps the movement of water molecules in the brain. Since this motion of water molecules is related to the WM architecture, DTI provides a useful insight into the neural connectivity.

3.2 From Brownian motion to diffusion tensor images

> *White matter may provide liars with the tools necessary to master the complex art of deceit.*
> – Adrian Raine

3.2.1 Diffusion

3.2.1.1 Brownian Motion and Diffusion

Molecules in an environment with a temperature above absolute zero (i.e., $> -273.15°C$) contain a certain thermal energy and are therefore in constant motion. This phenomenon was first described in 1828 by the English botanist Robert Brown. He observed the random motion of grains of pollen, which were suspended in water. In 1905, Einstein predicted the random motion of molecules in a liquid. The molecular self-diffusion can be described as a random walk process of molecules with a very complex distribution of step sizes and directions on a molecular scale. The concept of diffusion can be considered as the transport of molecules due to the Brownian motion.
The probability of finding a particle at position **r'** after a time τ, given its initial position **r**, can be described by the probability density function of the self-diffusion $P_s(\mathbf{r'}|\mathbf{r},\tau)$. The probability of finding a particle at position **r'** at time τ is then given by:

$$P(\mathbf{r}',\tau) = \int \rho(\mathbf{r}) P_s(\mathbf{r'}|\mathbf{r},\tau) d\mathbf{r}, \tag{3.1}$$

where $\rho(\mathbf{r})$ is the particle density at position **r**.
The classical phenomenological description of diffusion is based on the assumption of concentration gradients of molecules. This is expressed in Ficks first law [7, 8]. When considering self-diffusion, there is no net concentration gradient, so instead of using the concentration, the probability of self-diffusion, P_s can be used:

$$J = -\mathbf{D}\nabla P_s, \tag{3.2}$$

where J is the molecular flux density, $\mathbf{D}$ the diffusion coefficient (usually expressed in mm^2/s), and C is the concentration of molecules. The principle of the conservation of mass can be expressed as:

$$\frac{\delta}{\delta\tau}P_s = -\nabla J. \tag{3.3}$$

Fick's second law is obtained by combining Eq. (3.2) and (3.2):

$$\frac{\delta}{\delta\tau}P_s = \nabla.(\mathbf{D}\nabla P_s). \tag{3.4}$$

According to Einstein, the diffusion coefficient $\mathbf{D}$ can be found by [9]:

$$\mathbf{D} = \frac{1}{6\tau}\langle \boldsymbol{R}^T \cdot \boldsymbol{R}\rangle \ , \tag{3.5}$$

where $\mathbf{R} = \mathbf{r} - \mathbf{r'}$. The displacement of the water molecules in time is thereby considered over the ensemble of the water molecules, as reflected by $\langle\rangle$ in Eq. (3.5). Because the diffusion is random and it was assumed that the molecules could move freely, $\mathbf{D}$ is isotropic (i.e., directionally independent) and can be described by a scalar value, i.e. D. The magnitude of D depends on the viscosity and temperature of the medium, and the size of the molecules.
Ficks second law can be solved for the case of unrestricted diffusion, obtaining the following relation for the probability density function of the self-diffusion:

$$P_s(\boldsymbol{r'}|\boldsymbol{r},\tau) = \frac{1}{\sqrt{\left(4\pi t D(\boldsymbol{r})\right)}}\, e^{-\frac{\|\boldsymbol{r'}-\boldsymbol{r}\|^2}{4\tau D(\boldsymbol{r})}} \ , \tag{3.6}$$

3.2.1.2 The diffusion tensor

As aforementioned, the diffusion of water can be considered as a random walk process. In biological tissues, however, the diffusion is additionally modulated by the interactions with the cellular structures. The total diffusion is therefore a mixture of intra- and extra-cellular diffusion, and the exchange between the two sides of the cell membranes. Consequently, the diffusion coefficient is 2 to 10 times lower in brain tissue than in pure water [10]. In contrast to the diffusion in an isotropic environment, where the diffusion coefficient is the same for all directions and can be described by a scalar value D, molecules undergoing Brownian motion in biological tissues are displaced with greater magnitudes in directions parallel to boundaries, and smaller magnitudes in directions perpendicular to boundaries [11].

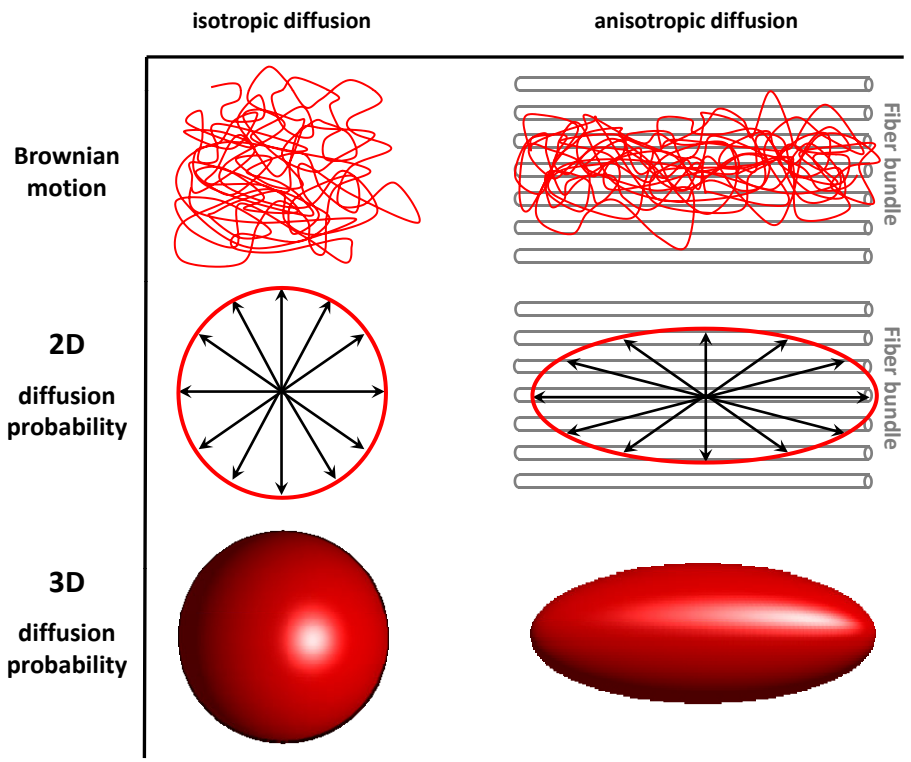

Figure 3.2. *The Brownian motion process, the 2D diffusion probability, and the 3D diffusion probability are presented for the case of isotropic and anisotropic diffusion.*

Since the WM fiber bundles containing many axons are very organized, the diffusion probability is much larger along the fiber bundles than perpendicular to them (see Fig. 3.2). Consequently, information about the diffusion of water molecules can provide an insight into the WM fiber architecture.
Diffusion is called 'anisotropic' when the displacement is directionally dependent. An example of Brownian motion, 2D diffusion and 3D diffusion is presented in Fig. 3.2 for the isotropic and anisotropic situation. In order to describe anisotropic diffusion, Einstein's relation of Eq. (3.5) must be adapted to include the directional dependency of the diffusion. It has been demonstrated that anisotropic, Gaussian diffusion can be characterized by a second-order, symmetric, and positive definite tensor, called the diffusion tensor [11–13]:

$$\mathbf{D} = \begin{bmatrix} D_{xx} & D_{xy} & D_{xz} \\ D_{yx} & D_{yy} & D_{yz} \\ D_{zx} & D_{zy} & D_{zz} \end{bmatrix} . \ , \tag{3.7}$$

Since **D** is a symmetric and positive definite second-rank tensor, it can be decomposed in real eigenvalues and eigenvectors:

$$\boldsymbol{D} = \boldsymbol{E} \cdot \boldsymbol{\Lambda} \cdot \boldsymbol{E^{-1}} \ , \tag{3.8}$$

with

$$\boldsymbol{E} = \begin{bmatrix} \boldsymbol{e}_1 & \boldsymbol{e}_2 & \boldsymbol{e}_3 \end{bmatrix} \qquad \text{and} \qquad \boldsymbol{\Lambda} = \begin{bmatrix} \lambda_1 & 0 & 0 \\ 0 & \lambda_2 & 0 \\ 0 & 0 & \lambda_3 \end{bmatrix} \tag{3.9}$$

defining the matrix of orthonormal eigenvectors $\boldsymbol{e}_i$ and the diagonal matrix of eigenvalues λ_i (with $i = 1, 2, 3$), respectively [14]. It has been demonstrated that in CSF and GM, the diffusion properties are relatively independent of orientation or isotropic [11]. Conversely, in fibrous tissues such as brain WM, the diffusion properties vary with orientation.
In DTI, it is assumed that the average diffusion of water molecules follows a Gaussian distribution. While the Gaussian assumption is adequate for voxels in which only a single fiber orientation is present it is no longer valid for voxels that contain fibers with more than one fiber orientation. This is an important limitation, since resolution of DTI acquisition is between $1mm^3$ and $3mm^3$ while the physical diameter of fibers can be between $1\mu m$ and $30\mu m$ [15, 16]. Hence, higher order models that are able to describe non-Gaussian distributions are needed.

3.2.1.3 Quantitative measures of diffusion

In contrast to anatomical MR images, where a scalar gray value represents the local tissue properties, a 3×3 matrix is derived in each voxel of a DTI data set (see Eq. (3.7)). The interpretation of 3D image data that contain a 3×3 DT at each voxel is not straightforward, especially, since the value of the different DT elements depend on the spatial orientation of the laboratory frame. Therefore, rotationally invariant diffusion measures were introduced, which have the same intensity for the same anatomical location regardless of the orientation of the patient in the scanner. Although these measures represent simplifications of the diffusion tensor **D**, they are very useful for the visualization of the DT images and for the quantitative assessment of tissue damage in patients. Many rotationally invariant scalar measures have been defined in the literature [11, 17–27, 27–31]. Here, only those that are used in this thesis are introduced: the eigenvalues, the mean diffusivity, and the fractional anisotropy metric.
As aforementioned, in each voxel, the diffusion tensor can be decomposed in three eigenvalues λ_1, λ_2, and λ_3, which represent the magnitude of the diffusion along the

corresponding three eigenvectors. Different rotationally invariant scalar measures can be calculated from these eigenvalues.

(i) the longitudinal diffusivity $\lambda_{\parallel} = \lambda_1$ [32–37];

(ii) the transverse diffusivity $\lambda_{\perp} = \frac{\lambda_2+\lambda_3}{2}$ [32–37];

(iii) the mean diffusivity (MD) is a measure of the average diffusion in a voxel, and is calculated as:

$$MD = \frac{\lambda_1 + \lambda_2 + \lambda_3}{3} \ , \tag{3.10}$$

(iv) The degree of diffusion anisotropy is commonly represented by the Fractional Anisotropy (FA) measure [11]. Fibers that are strongly aligned (for example, in compact WM structures) result in a high FA, whereas fibers that are more weakly aligned (for example, in regions of the GM) have a relatively lower FA.

$$FA = \frac{\sqrt{3\left[(\lambda_1 - \lambda_2)^2 + (\lambda_2 - \lambda_3)^2 + (\lambda_3 - \lambda_1)^2\right]}}{\sqrt{2(\lambda_1^2 + \lambda_2^2 + \lambda_3^2)}} \tag{3.11}$$

3.2.2 Image acquisition

3.2.2.1 Diffusion weighted images

In 1950, Hahn observed that the random thermal motion of spins in the presence of a magnetic field inhomogeneity result in attenuations of the acquired MR signal [3]. The first MRI experiment that was designed to measure the diffusion was performed in 1965 by Stejskal and Tanner and is known as the Pulse Gradient Spin Echo (PGSE) [39]. The Stejskal-Tanner imaging sequence is used to measure the diffusion of water molecules in a given direction g [39]. First, a 90° degrees RF is applied to flip the magnetization in the transverse plane (see Fig. 3.3). Thereafter, two gradient pulses $g(t)$ in z-direction g_z with magnitude $\|\boldsymbol{g}\|$ and duration time δ are applied. They are symmetrically placed before and after a 180° degrees refocusing pulse, with a time Δ between both pulses. The first gradient pulse induces a phase shift ϕ_1 of the spin transverse magnetization:

$$\phi_1 = \gamma \int_0^{\delta} g_z(t) z(t) \mathrm{d}t = \gamma \delta g_z z_1 \ . \tag{3.12}$$

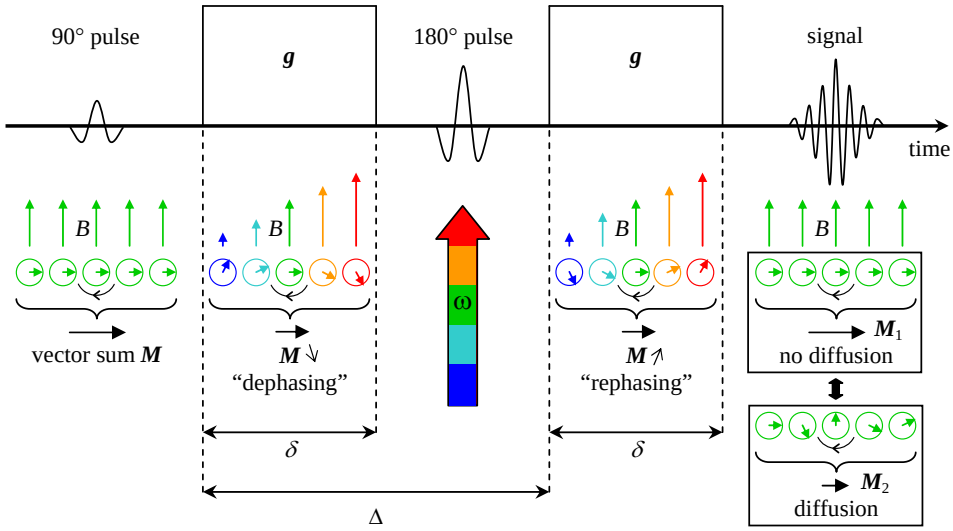

Figure 3.3. *A schematic illustration of the diffusion-weighted imaging sequence [38]. The length of the colored vertical arrows indicates the strength of the magnetic field B, which is non-uniform during the application of the gradients g. After the first gradient application following the 90. RF pulse, signals lose their uniform phase (called dephasing, i.e. the vector sum of the magnetic spin moments M decreases) because each proton starts to precess at different rates ω depending on its position in space (the color-encoding represents the amount of this precession rate). After the second gradient application following the* 180° *RF pulse, the system restores the uniform phase (called rephasing, i.e. M increases). This rephasing is complete only when spins do not undergo a Brownian motion (i.e., do not diffuse) during the time Δ in between the two applications of the gradients (|| M1 ||>|| M2 ||)*

The spin position $z(t) = z_1$ is thereby assumed to be constant during the short pulse duration δ [40]. In this equation, γ represents the gyromagnetic ratio for hydrogen nuclei (i.e. $42MHz/T$). The 180° pulse combined with the second gradient pulse induces a second phase shift:

$$\phi_2 = -\gamma \int_{\Delta}^{\Delta+\delta} g_z z(t) \mathrm{d}t = -\gamma \delta g_z z_2 \ . \tag{3.13}$$

For static spins (i.e. $z_1 = z_2$), this second pulse cancels the first phase shift, resulting in a total phase-shift $\phi = \phi_1 + \phi_2$ of zero. Spins that are displaced during the time period Δ separating the two pulses undergo different phase shifts by the two gradient pulses, resulting in a net total phase-shift ϕ, which can then be written as [41]:

$$\phi = \phi_1 + \phi_2 = \gamma \delta g (z_1 - z_2) \ . \tag{3.14}$$

The measured phase-shift is proportional to the spin displacement and maps the mean diffusion within a voxel in the direction g. When the spins are not completely refocused due to a shift of the spins between the dephasing and rephasing magnetic field gradients, the MR signal is attenuated. The signal loss at position $\mathbf{r}$ can be written as:

$$S(\mathbf{r}) = S_0(\mathbf{r}) \langle e^{i\phi} \rangle \ , \tag{3.15}$$

with $S(\mathbf{r})$ the measured spin-echo signal and $S_0(\mathbf{r})$ the MR signal without any diffusion sensitizing gradients. $\langle e^{i\phi} \rangle$ represents the ensemble average of the different phase shifts within a voxel, whereby the mean displacement within a voxel is considered as the expectation value. Stejskal and Tanner (1965) demonstrated that the signal attenuation $S(\mathbf{r})$ can be expressed as the 3D Fourier transform $\mathcal{F}$ of the diffusion probability density function $P_s(\boldsymbol{r'}|\boldsymbol{r}, \tau)$ [39]:

$$\frac{S(\boldsymbol{r})}{S_0(\boldsymbol{r})} = \int P_s(\boldsymbol{r}|\boldsymbol{r'}, t) e^{i\phi(\boldsymbol{r'}-\boldsymbol{r})} \mathrm{d}\boldsymbol{r} = \mathcal{F}[P_s(\boldsymbol{r'}|\boldsymbol{r}, \tau)] \ . \tag{3.16}$$

Finally, the Stejskal-Tanner relation can be obtained by combining Eq. (3.16) and (3.6) [39]:

$$S(\boldsymbol{r}) = S_0(\boldsymbol{r}) \, e^{-bD(\boldsymbol{r})} \ , \tag{3.17}$$

where the diffusion weighting factor b in Eq. (3.17), introduced by Le Bihan et al. (1986), is defined as [42]:

$$b = \gamma^2 \delta^2 \Delta \|\boldsymbol{g}\|^2 \ . \tag{3.18}$$

However, the effective diffusion time is $\tau = (\Delta - \delta/3)$ instead of $\tau = \Delta$, where $\delta/3$ is a correction due to the diffusion that occurs while the gradient is applied.
Since b can be derived from the acquisition parameters and since the non-diffusion weighted image $S_0(\boldsymbol{r})$ and the diffusion weighted (DW) image $S(\boldsymbol{r})$ are acquired by measuring the signal with $b = 0$ and $b \neq 0$, respectively, the diffusion coefficient $D(\boldsymbol{r})$ can be calculated in each voxel using Eq. (3.17). This diffusion coefficient model is based on the hypothesis that the diffusion is unrestricted and can therefore

be modeled by a Gaussian distribution. Since, in biological tissues this assumption is not correct, the diffusion coefficient is referred to as the apparent diffusion coefficient (ADC). Note that the resulting diffusion coefficient $D(\boldsymbol{r})$ is dependent on the direction of $\boldsymbol{g}$, the gradient strength $\|\boldsymbol{g}\|$ and the time sequence parameters δ and Δ and that the diffusion of water molecules is measured in a predefined direction g, without detecting water diffusion in other directions.
At low diffusion weighting (low b values), the sensitivity to diffusion is minimal and the image contrast will be determined predominantly by the anatomical MR scan. At high b values, the image contrast is largely produced by the diffusion properties of water molecules. Lesions with diffusion restriction appear bright on DW images and dark on ADC maps. Structures with increased diffusion, such as CSF, will appear dark on DW images and bright on ADC maps.

3.2.2.2 Acquisition of diffusion tensor images

In 1994, Basser et al. described the 3D diffusion process based on a series of diffusion weighted images (DWIs) [17, 18]. In this approach, a second order symmetric tensor is fitted to the diffusion data in every voxel. Since the DT is symmetric, only six elements have to be estimated to characterize the full DT. Consequently, DW images have to be acquired in at least six independent directions $\boldsymbol{g}_k$ $(k = 1, \ldots, 6)$ [11, 43]. In addition, a reference image $S_0(\boldsymbol{r})$ should be obtained without diffusion weighting. In practice, more than six directions $\boldsymbol{g}_k$ $(k = 1, \ldots, N)$ are often used for a more reliable measurement of the diffusion tensor, with N the total number of unique gradient directions [44].
The symmetric second-rank tensor $\boldsymbol{D}(\boldsymbol{r})$ is calculated for each voxel at position $\boldsymbol{r}$ by solving the equation system

$$S_k(\boldsymbol{r}) = S_0(\boldsymbol{r})\, e^{-b\hat{\boldsymbol{g}}_k^T \cdot \boldsymbol{D}(\boldsymbol{r}) \cdot \hat{\boldsymbol{g}}_k} \quad \text{with} \quad \hat{\boldsymbol{g}}_k = \frac{\boldsymbol{g}_k}{\|\boldsymbol{g}_k\|} \quad \text{and} \quad k = 1, \ldots, N \ , \qquad (3.19)$$

which can be considered as the generalized anisotropic form of the Stejskal-Tanner relationship of Eq. (3.17). The distribution $P_s(\boldsymbol{r}|\boldsymbol{r'}, \tau)$ for isotropic media in Eq. (3.6) can be extended for the general anisotropic case [39]:

$$P_s(\boldsymbol{r}|\boldsymbol{r'}, \tau) = \frac{1}{\sqrt{(4\pi\tau)^3 |\boldsymbol{D}|}}\, e^{-\frac{(\boldsymbol{r}-\boldsymbol{r'})^T \cdot \boldsymbol{D}^{-1} \cdot (\boldsymbol{r}-\boldsymbol{r'})}{4\tau}} \ , \qquad (3.20)$$

where $|\mathbf{D}|$ represents the determinant of the diffusion tensor $\mathbf{D}$.

3.2.3 Visualization

Unlike conventional scalar MR images, DTI is fundamentally 3D, since 3D diffusion information is measured in each voxel. This poses some visualization challenges.

3.2.3.1 Scalar maps

Generally, the diffusion information in each voxel is represented by a scalar measure, such as the FA, or the MD. Since the FA metric provides better contrast between WM structures, it is used more often compared to the MD for visualizing DTI data sets. In the FA image, the WM structures appear bright, whereas the GM and especially the CSF have a darker color.

3.2.3.2 Color-encoded scalar maps

By using scalar measures to visualize the DT, a lot of diffusion information is discarded. Therefore, an additional color encoding is sometimes introduced based on the direction of the first eigenvector to include directional diffusion information. The most commonly applied color scheme to represent the orientation of the major eigenvector is as follows: blue is superior-inferior, red is left-right, and green is anterior-posterior [45–52]. This directional diffusion information is then added to the FA maps. In the resulting images, the color is encoded for the diffusion direction and the image intensity is determined by the FA. In Fig. 3.4 (a), an axial slice containing anatomical MR information is visualized. The non-diffusion weighted, MD, FA, and color-encoded FA image of the same axial slice are depicted in Fig. 3.4 (b).

3.2.3.3 Glyphs

3D objects, called glyphs, are also used to display the diffusion tensor information. These glyphs can be lines that represent the orientation of the first eigenvector, ellipsoids that are related to the diffusion iso-probability surfaces [11, 27], and other objects such as super-quadric tensor glyphs [53–55]. In Fig. 3.4 (c) the diffusion ellipsoids of an axial slice are depicted. The ellipsoids of the splenium are visualized in more detail in Fig. 3.4 (d). To include directional diffusion information and facilitate the visual interpretation, the glyphs can be color-encoded, whereby a blue, red, and green color represent superior-inferior, left-right, and anterior-posterior diffusion, respectively. A detailed overview of visualization methods for DTs fields can be found in the work of Masutani et al. (2003) and Vilanova et al. (2006) [56, 57].

As can be seen in Fig. 3.5, the diffusion information, as visualized by color-encoded ellipsoids, corresponds well to the anatomical fiber bundle information. Although these glyphs contain much more information compared to the scalar maps, they are often hard to interpret, due to the staggering amount of information that is included in the visualization.

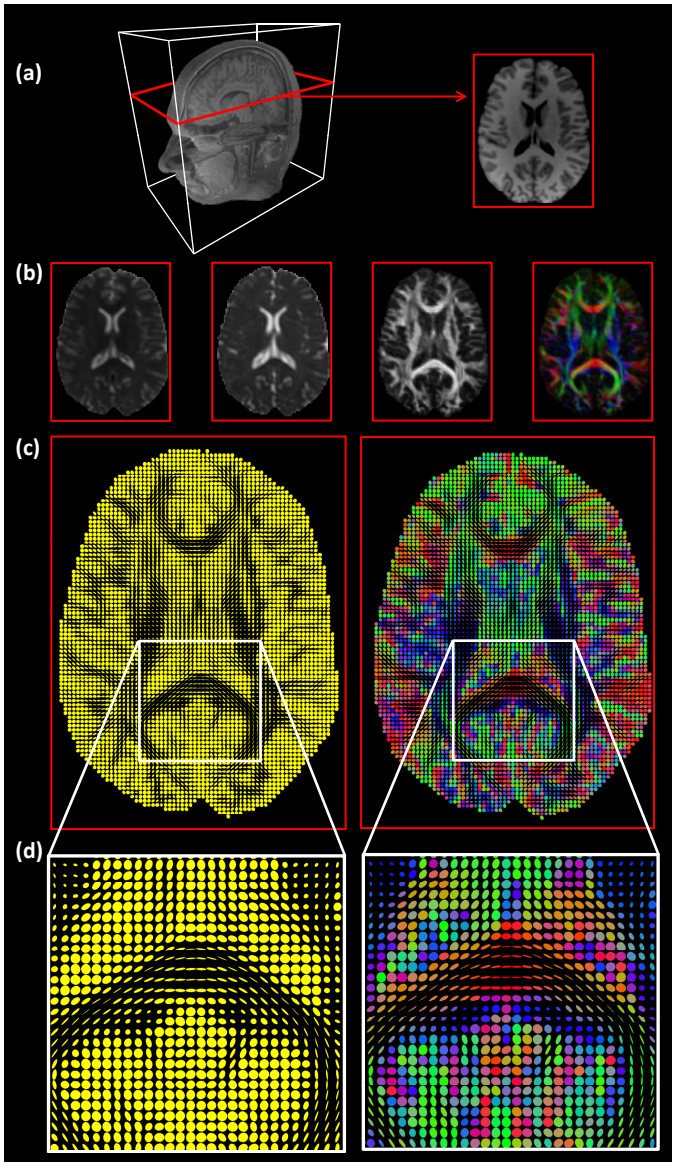

Figure 3.4. *In (a), an axial slice of a T_2 weighted MR image is shown. The same axial slice of the non-diffusion weighted image, MD map, FA map, and color encoded FA image is displayed in (b). In (c), the diffusion information of this axial slice color is visualized using ellipsoids in (c). On the left, they are colored in yellow, on the right, they are color encoded according to the diffusion direction. In (d), the diffusion ellipsoids of the splenium of the corpus callosum are depicted in more detail in (d).*

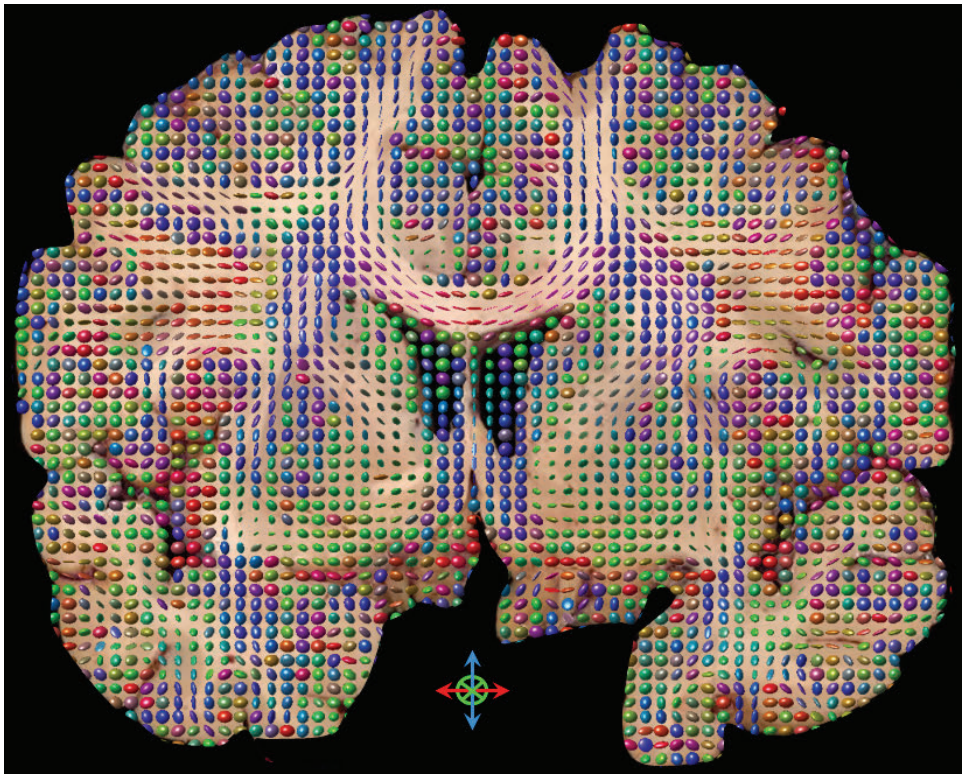

Figure 3.5. *The diffusion ellipsoids, color encoded for the diffusion direction, are superimposed on a coronal slice of a post-mortem brain.*

3.2.3.4 Diffusion tensor tractography

In order to obtain more global information about the WM architecture, the local diffusion information needs to be integrated. This is done by fiber tractography or fiber tracking, which is based on the assumption that the main direction of diffusion in a voxel - as derived from the tensor model - corresponds to the longitudinal axis of the fiber bundle [50, 58–68]. In Fig. 3.6 (a), a fiber tract that follows the main direction of the diffusion tensors in the splenium is reconstructed. The fiber tracts of the whole brain are visualized in Fig. 3.6 (b). Generally, the fiber tracts are color encoded for the diffusion direction for a better visual interpretation of the fiber bundles, as can be seen in Fig. 3.6 (c).

Currently, diffusion tensor tractography is the only non-invasive tool to obtain information about the neural architecture of the human brain. Many methods have been proposed in the literature for addressing this problem, and most produce output which corresponds well to the known anatomy [15, 29, 30, 60, 63, 64, 66, 68–

119].
A first category of algorithms, proposed by Basser et al. (2000,2002), uses a streamline propagation approach where fiber trajectories are generated in a stepwise fashion [58–61]. Streamline tractography uses the first eigenvector of the diffusion tensor as an estimate of local tract orientation. In other tractography methods, a probability of the fiber orientation is estimated at each voxel based on the diffusion information [95–98, 101, 104, 105, 110, 111, 120–130]. Instead of producing one path from each seed point, a distribution of paths is produced by sampling this probability model of the fiber orientation.

3.3 Clinical applications of DTI

> *It's really critical that we find ways to prevent, or at least delay the onset of, cognitive decline. Once the pathology is established in the brain, it's very difficult to treat. We need better ways to prevent the disease in the first place, which could make a huge difference for the future.*
> – Neil Buckholtz

In DTI, information about WM fibers that pass within a voxel is obtained. This WM consists of thousands of axons in each voxel, as well as myelin sheaths, microtubuli, neurofilaments, and glial cells. The diffusion signal that is measured in DTI originates from contributions from all these structures. It is therefore not straightforward to correlate diffusion signal alterations with changes of the underlying microstructure. However, since DTI measures the diffusion in the organized WM, many researchers agree that DTI can provide an additional insight into a wide range of pathologies. In this section, some clinical applications of DTI are discussed.

Stroke: Moseley et al. (1990) were the first to observe hyperintensity on DW images in the ischemic region [131–133]. By evaluating quantitative diffusion measures, the severity of strokes can be assessed. Furthermore, acute ischemic changes can be distinguished from chronic ischemic changes, a difference that may affect treatment [134–138].

Development of the brain and aging: DTI has already proven to be useful in the study of aging, [139–149], lateralization [48, 150–154], cognitive performance and reading ability [155–158], and brain development in premature infants, 'normal' infants, children, adolescents, and adults [160–170].

In general, DTI studies report age-related declines in WM FA and increases of the WM MD in normal healthy adults [140, 142, 143, 146, 171]. The decline is equivalent in men and women and appears to be linear from about age 20 years onwards [171–173].

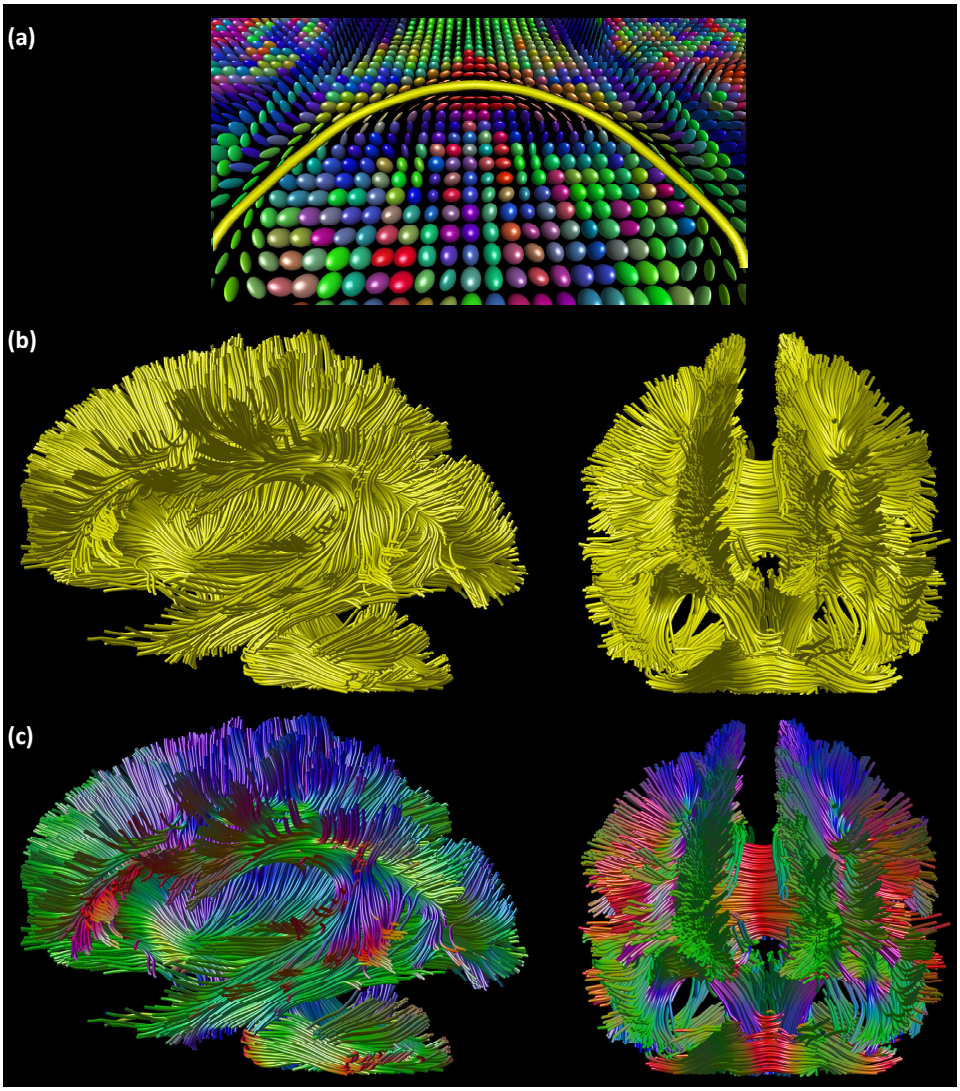

Figure 3.6. *In (a) mathematical reconstruction of a fiber bundle is superimposed on the diffusion information, as visualized by color-encoded ellipsoids. The whole brain diffusion tensor tractography result, colored in yellow, is shown in (b). In (c), the same tracts, color encoded for the diffusion direction, are displayed.*

Psychiatric disorders: A lot of DTI studies have demonstrated WM differences in patients with psychiatric disorders, such as schizophrenia, alcoholism, depression, etc. compared to healthy control subjects. For example, many DTI studies reported an FA decrease in patients with schizofrenia compared to healthy controls in a wide range of WM structures [174–188]. Exposure to addictive drugs, such as alcohol, cocaine, methamphetamine, marijuana, heroin, and nicotine has also been shown to alter the FA [189–192].

Multiple Sclerosis: Although it has been demonstrated that conventional MR images are sensitive for detecting MS lesions, the T_2 lesions reflect the clinical manifestations only to a limited extent [193, 194]. Recently, more advanced imaging techniques, such as diffusion tensor imaging (DTI), have been employed to examine MS [195]. Pathologically, MS is characterized by the presence of areas of demyelination and axonal loss. Since myelin restricts diffusion of water transverse to the axons, it is regarded as an important factor that contributes to the anisotropic nature of the diffusion. However, Beaulieu and Allen (1994) demonstrated that anisotropy in myelinated nerves and non-myelinated nerves are similar and that myelination is therefore not a prerequisite for diffusion anisotropy [196]. Other studies showed that anisotropy measures are altered significantly when myelin is damaged or absent, either in a demyelinating disease such as MS or in a pre-myelination condition at different stages of neuronal development [159, 197–199]. Recently, Song et al. (2003) examined the longitudinal and transverse diffusivities of white matter in a mouse model of demyelination [33]. They observed that the absence of myelin appeared to increase the longitudinal diffusivity, but did not significantly affect the transverse diffusivity.

Obviously, axonal loss will also have modulatory effects on the diffusion measures. Recent studies have suggested that the axial diffusivity may be a more specific marker of axonal damage [34, 37].

Brain tumors: Diffusion tensor tractography is used to localize WM fiber tracts that are important for critical brain functions and are located near a tumor [82, 200–202]. This information can then be used by a neurosurgeon to plan the surgical procedures that will minimize injury to these WM fiber bundles. DTI has also been applied to characterize tumor tissues. In general, it is assumed that increased cellular densities will decrease the MD and that the MD will be significantly elevated in areas of tissue necrosis. A study of pediatric tumor patients revealed relationships between MD and both tumor grade and cellularity [203]. Another study demonstrated that the MD was slightly or not elevated relative to normal-appearing tissue measured in the contralateral hemisphere in lymphomas (with high cellularities) and that the MD was significantly higher in high-grade astrocytomas [204]. Beppu

et al. (2003, 2005) reported correlations between FA and cell density and proliferation in both astrocytomas and glioblastomas, with higher FA values corresponding to higher cell densities [205, 206].

3.4 DTI Group Analysis Methods

It all starts with an analysis of data.
– Ruth O'Dell

Since DTI is the only technique that can measure the WM integrity non-invasively, it has a lot of potential to be of great diagnostic value in a wide range of WM altering neurologic disorders. However, the relation between diffusion properties alterations and changes of the underlying microstructure need to be well understood. Additionally, large-scale, standardized group studies, comparing healthy subject and patient DTI data sets, are necessary to evaluate the effect of specific pathophysiologic damage of a certain neurologic disorder on the measured diffusion properties. In the past years, different methods to compare diffusion properties of control subjects and patients were introduced. The most frequently applied methods are discussed below: region of interest, tractography, and voxel based analysis approaches.

3.4.1 Region of interest based approaches

In the ROI analysis, a 2D shape is manually drawn around a WM structure. Alternatively, a geometrical shape, such as a box or a circle, can be placed within the structure of interest. The diffusion values are then derived from the voxels that are included in the segmented region. In most ROI studies, the WM structures of interest are delineated for each subject independently, which makes this approach very labor intensive. In addition, a relatively low reproducibility of the results is sometimes observed, since the obtained diffusion properties depend on the manual delineation or ROI placement that is done by an observer. Alternatively, the data sets of all subjects can be initially transformed to a certain atlas space. Thereafter, a single ROI can be used to delineate the same WM structure in all subjects, since it is assumed that the data sets are aligned after coregistration.

3.4.2 Tractography based approaches

In this method, diffusion tensor tractography is applied to reconstruct and segment a certain WM structure of interest. Thereafter, all the voxels contributing to the tract are treated as a 3D ROI. This approach has the advantage of utilizing the semi-automated nature of tractography, where the tract-selection regions can be

defined more loosely compared to the ROI approach. The observer does not have to precisely outline a structure of interest, but provide regions through which a tract must pass. Obviously, this reduces the user dependence of the post processing. Another advantage is that 3D structures can be defined easily, whereas the delineation of 3D structures with 2D ROIs is far more complex. As with the ROI approach, the investigator must choose the structures of interest in advance, and therefore must have an a priori hypothesis regarding the location of the diffusion changes.

3.4.3 Voxel based Analysis

3.4.3.1 Standard Voxel based Analysis

The analysis of each structure on each subject can be very laborious, especially for large group studies. Alternatively, in a voxel based analysis, DTI data sets from different subjects are transformed/coregistered/warped to a template or atlas. Thereafter, statistical tests are applied in each voxel in order to detect differences in the diffusion measures between a control group and a patient group. In this way, the whole brain is tested for control-patient differences without any a priori hypothesis of the expected spatial location of the abnormalities. Although the VBA approach is computationally more intensive, it is far less laborious compared to the ROI method or even the tractography based post processing approach. In addition, the user-dependency of the ROI approach is replaced by a parameter-dependency in VBA, making the subsequent quantitative analysis more reproducible and standardized. However, for example in the published DTI studies of patients with schizofrenia, no general correspondence between the findings is observed [174–177, 179–188]. The subject group and disease heterogeneity across the different studies, including confounding factors such as age, sex, handedness, disease state, etc., can partially explain these observed discrepancies. However, methodological differences in implementation of VBA are possibly even more decisive for explaining the variances in the VBA results of different studies.

3.4.3.2 Tract Based Spatial Statistics

In tract based spatial statistics (TBSS), the FA maps are aligned to a template. A mean FA image is subsequently created and thinned to generate a mean FA skeleton which represents the centers of all tracts common to the group. Then, a skeleton map is created for each subject by projecting his/her FA maps onto the skeleton in the standard space. Thereafter, voxel-wise statistics across subjects can be performed on the skeleton. Similarly to VBA, significant differences are highlighted. The disadvantage of this method is that it only analyzes a relatively small proportion of all the available white matter, i.e. only those voxels with the

highest local FA. Valuable information from a large number of voxels in several WM structures is therefore lost in a TBSS analysis.

Bibliography

[1] F. Bloch, W. Hansen, M. Packard, Nuclear Induction., Physical Review 7–8 (70) (1946) 460–474.

[2] E. Purcell, H. Torrey, R. Pound, Resonance Absorption by Nuclear Magnetic Moments in a Solid., Physical Review 1–2 (69) (1946) 37–38.

[3] E. Hahn, Spin Echoes., Physical Review 80 (1950) 580–594.

[4] P. Lauterbur, Image Formation by Induced Local Interactions: Examples Employing Nuclear Magnetic Resonance., Nature (242) (1973) 190–191.

[5] M. P., Multi-Planar Image Formation Using NMR Spin Echoes., Journal Of Physics C-Solid State Physics 3 (10) (1977) 55–58.

[6] M. P., A. Maudsley, Medical imaging by NMR., British Journal of Radiology 591 (50) (1977) 188–194.

[7] A. Fick, On liquid diffusion., Philos Mag 10 (1855) 30–39.

[8] J. Crank, The Mathematics of Diffusion., Oxford University Press, London, 1975.

[9] A. Einstein, Über die von der molekularkinetischen Theorie der Wärme geforderte Bewegung von in ruhenden Flüssigkeiten suspendierten Teilchen, Annal Phys 4 (1905) 549–560.

[10] D. Le Bihan, R. Turner, C. T. Moonen, J. Pekar, Imaging of diffusion and microcirculation with gradient sensitization: design, strategy, and significance. .

[11] P. Basser, C. Pierpaoli, Microstructural and physiological features of tissues elucidated by quantitative-diffusion-tensor MRI, J Magn Reson B 111 (3) (1996) 209–219.

[12] L. Onsager, Electric moments of molecules in liquids, J Am Chem Soc 58 (1936) 1486–1493.

[13] L. Landau, E. Lifschitz, Statistical physics, Butterworth-Heinemann, 1999.

[14] K. Hasan, P. Basser, D. Parker, A. Alexander, Analytical computation of the eigenvalues and eigenvectors in DT-MRI, J Magn Reson 152 (1) (2001) 41–47.

[15] C. Poupon, C. Clark, V. Frouin, I. Bloch, D. Bihan, M. J.-F., Tracking white matter fascicles with diffusion tensor imaging, in: ISMRM, 1999, p. 325.

[16] C. Beaulieu, The basis of anisotropic water diffusion in the nervous system - a technical review, NMR in Biomedicine 15 (7–8) (2002) 435–455.

[17] P. Basser, J. Mattiello, D. Le Bihan, MR diffusion tensor spectroscopy and imaging, Biophysics Journal 66 (1) (1994) 259–267.

[18] P. Basser, J. Mattiello, D. L. Bihan, Estimation of the effective self-diffusion tensor from the NMR spin echo, J Magn Reson B 103 (3) (1994) 247–254.

[19] P. Basser, D. Jones, Diffusion-tensor MRI: theory, experimentel design and data analysis - a technical review, NMR biomed 15 (2002) 456–467.

[20] D. Le Bihan, J.-F. Mangin, C. Poupon, C. Clark, S. Pappata, N. Molko, H. Chabriat, Diffusion tensor imaging: concepts and applications, J Magn Reson Imaging 13 (4) (2001) 534–546.

[21] D. Le Bihan, P. van Zijl, From the diffusion coefficient to the diffusion tensor, NMR Biomed 15 (7–8) (2002) 431–434.

[22] R. Watts, C. Liston, S. Niogi, A. Uluğ, Fiber tracking using magnetic resonance diffusion tensor imaging and its applications to human brain development, Ment Retard Dev Disabil Res Rev 9 (3) (2003) 168–177.

[23] W. Taylor, E. Hsu, K. Krishnan, J. MacFall, Diffusion tensor imaging: Background, potential, and utility in psychiatric research, Biol Psychiatry 55 (2004) 201–207.

[24] M. Bahn, Invariant and orthonormal scalar measures derived from magnetic resonance diffusion tensor imaging, J Magn Reson 141 (1) (1999) 68–77.

[25] M. Bahn, Comparison of scalar measures used in magnetic resonance diffusion tensor imag-

ing, J Magn Reson 139 (1) (1999) 1–7.

[26] P. Basser, Inferring microstructural features and the physiological state of tissues from diffusion-weighted images, NMR Biomed 8 (7–8) (1995) 333–344.

[27] C. Pierpaoli, P. Basser, Toward a quantitative assessment of diffusion anisotropy, Magn Reson Med 36 (6) (1996) 893–906.

[28] T. Conturo, R. McKinstry, E. Akbudak, B. Robinson, Encoding of anisotropic diffusion with tetrahedral gradients: a general mathematical diffusion formalism and experimental results, Magn Reson Med 35 (3) (1996) 399–412.

[29] C.-F. Westin, S. Maier, B. Khidhir, P. Everett, F. Jolesz, R. Kikinis, Image processing for diffusion tensor magnetic resonance imaging, in: MICCAI, 1999, pp. 441–452.

[30] C.-F. Westin, S. Maier, H. Mamata, A. Nabavi, F. Jolesz, R. Kikinis, Processing and visualization for diffusion tensor MRI, Med Image Anal 6 (2) (2002) 93–108.

[31] A. Alexander, K. Hasan, G. Kindlmann, D. Parker, J. Tsuruda, A geometric analysis of diffusion tensor measurements of the human brain, Magn Reson Med 44 (2) (2000) 283–291.

[32] S. Song, S. Sun, M. Ramsbottom, C. Chang, J. Russell, A. Cross, Dysmyelination revealed through MRI as increased radial (but unchanged axial) diffusion of water, NeuroImage 17 (3) (2002) 1429–1436.

[33] S.-K. Song, S.-W. Sun, W.-K. Ju, S.-J. Lin, A. Cross, A. Neufeld, Diffusion tensor imaging detects and differentiates axon and myelin degeneration in mouse optic nerve after retinal ischemia, NeuroImage 20 (3) (2003) 1714–1722.

[34] S. Song, J. Yoshino, T. Le, S. Lin, S. Sun, A. Cross, R. Armstrong, Demyelination increases radial diffusivity in corpus callosum of mouse brain, Neuroimage 21 (2005) 132–140.

[35] M. D. Budde, J. H. Kim, H.-F. Liang, R. E. Schmidt, J. H. Russell, A. H. Cross, S. S-K., Toward accurate diagnosis of white matter pathology using diffusion tensor imaging., Magn Reson Med 57 (4) (2007) 688–695.

[36] E. D. Schwartz, E. T. Cooper, Y. Fan, A. F. Jawad, C. L. Chin, J. Nissanov, D. B. Hackney, MRI diffusion coefficients in spinal cord correlate with axon morphometry., NeuroReport 16 (1) (2005) 73–76.

[37] L. A. Harsan, P. Poulet, B. Guignard, J. Steibel, N. Parizel, P. L. de Sousa, N. Boehm, D. Grucker, M. S. Ghandour, Brain dysmyelination and recovery assessment by noninvasive in vivo diffusion tensor Magn Reson Imaging., J Neurosci Res 83 (3) (2006) 392–402.

[38] A. Leemans, Modeling and Processing of Diffusion Tensor Magnetic Resonance Images for Improved Analysis of Brain Connectivity., 2006.

[39] E. Stejkal, J. Tanner, Spin diffusion measurements: spin echoes in the presence of a time dependent field gradient, J Chem Phys 42 (1965) 288–292.

[40] R. Hashemi, W. Bradley, C. Lisanti, MRI: the basics, Lippincott Williams and Wilkins, Philadelphia, 2nd edition, 2004.

[41] M. Cercignani, M. Horsfield, The physical basis of diffusion-weighted MRI, J Neurol 186 (1) (2001) S11–S14.

[42] D. Le Bihan, E. Breton, D. Lallemand, P. Grenier, E. Cabanis, M. Laval-Jeantet, MR imaging of intravoxel incoherent motions: application to diffusion and perfusion in neurologic disorders, Radiology 161 (2) (1986) 401–407.

[43] D. Jones, M. Horsfield, A. Simmons, Optimal strategies for measuring diffusion in anisotropic systems by magnetic resonance imaging, Magn Reson Med 42 (3) (1999) 515–525.

[44] D. Jones, The effect of gradient sampling schemes on measures derived from diffusion tensor MRI: a Monte Carlo study, Magnetic Resonance in Medicine 51 (2004) 807–815.

[45] P. Douek, R. Turner, J. Pekar, N. Patronas, D. Le Bihan, MR color mapping of myelin fiber orientation, J Comput Assist Tomogr 15 (6) (1991) 923–929.

[46] J. Coremans, R. Luypaert, F. Verhelle, T. Stadnik, M. Osteaux, A method for myelin

fiber orientation mapping using diffusion-weighted MR images, Magn Reson Imaging 12 (3) (1994) 443–454.

[47] B. Inglis, L. Yang, E. Wirth, D. Plant, T. Mareci, Diffusion anisotropy in excised normal rat spinal cord measured by NMR microscopy, Magn Reson Imaging 15 (4) (1997) 441–450.

[48] S. Peled, H. Gudbjartsson, C.-F. Westin, R. Kikinis, F. Jolesz, Magnetic resonance imaging shows orientation and asymmetry of white matter fiber tracts, Brain Res 780 (1) (1998) 27–33.

[49] S. Pajevic, C. Pierpaoli, Color schemes to represent the orientation of anisotropic tissues from diffusion tensor data: application to white matter fiber tract mapping in the human brain, Magn Reson Med 42 (3) (1999) 526–540.

[50] D. Jones, S. Williams, M. Horsfield, Full representation of white-matter fibre direction on one map via diffusion tensor analysis, in: ISMRM, 1997, p. 1743.

[51] C. Pierpaoli, Oh no! one more method for color mapping of fiber tract direction using diffusion MR imaging data, in: ISMRM, 1997, p. 1741.

[52] M. Lazar, J. Lee, A. Alexander, Axial asymmetry of water diffusion in brain white matter, Magn Reson Med 54 (4) (2005) 860–867.

[53] G. Kindlmann, D. Weinstein, D. Hart, Strategies for direct volume rendering of diffusion tensor fields, IEEE T Vis Comput Gr 6 (2) (2000) 124–138.

[54] A. Barr, Superquadrics and angle-preserving transformations, IEEE CG&A 18 (1981) 11–23.

[55] D. Ennis, G. Kindlman, I. Rodriguez, P. Helm, E. McVeigh, Visualization of tensor fields using superquadric glyphs, Magn Reson Med 53 (1) (2005) 169–176.

[56] Y. Masutani, S. Aoki, O. Abe, N. Hayashi, K. Otomo, MR diffusion tensor imaging: recent advance and new techniques for diffusion tensor visualization, Eur J Radiol 46 (1) (2003) 53–66.

[57] A. Vilanova, S. Zhang, G. Kindlmann, D. Laidlaw, Visualization and image processing of tensor fields, Springer Verlag series Mathematics and Visualization, 2006, Ch. An introduction to visualization of diffusion tensor imaging and its applications, pp. 121–153.

[58] P. Basser, Fiber-tractography via diffusion tensor MRI (DT-MRI), in: ISMRM, 1998, p. 1226.

[59] P. Basser, S. Pajevic, C. Pierpaoli, A. Aldroubi, J. Duda, Fiber-tractography in human brain using diffusion tensor MRI (DT-MRI), in: ISMRM, 2000, p. 784.

[60] P. Basser, S. Pajevic, C. Pierpaoli, J. Duda, A. Aldroubi, In vivo fiber tractography using DT-MRI data, Magn Reson Med 44 (4) (2000) 625–632.

[61] P. Basser, S. Pajevic, C. Pierpaoli, A. Aldroubi, Fiber tract following in the human brain using DT-MRI data, IEICE T Inf Syst E85–D (2002) 15–21.

[62] S. Mori, B. Crain, P. van Zijl, 3D brain fiber reconstruction from diffusion MRI, in: Intl Conf on Func Mapping (HBM), 1998.

[63] S. Mori, B. Crain, V. Chacko, P. van Zijl, Three-dimensional tracking of axonal projections in the brain by magnetic resonance imaging, Ann Neurol 45 (2) (1999) 265–269.

[64] S. Mori, P. Barker, Diffusion magnetic resonance imaging: its principles and applications, Anat Rec B New Anat 257 (3) (1999) 102–109.

[65] S. Mori, R. Xue, B. Crain, M. Solaiyappan, V. Chacko, P. van Zijl, 3D reconstruction of axonal fibers from diffusion tensor imaging using Fiber Assignment by Continuous Tracking (FACT), in: ISMRM, 1999, p. 320.

[66] S. Mori, W. Kaufmann, G. Pearlson, B. Crain, B. Stieltjes, M. Solaiyappan, P. Van Zijl, In vivo visualization of human neural pathways by magnetic resonance imaging, Ann Neurol 47 (3) (2000) 412–414.

[67] D. Jones, A. Simmons, W. S.C.R., M. Horsfield, Noninvasive assessment of structural con-

nectivity in white matter by diffusion tensor MRI, in: ISMRM, 1998.

[68] D. Jones, A. Simmons, S. Williams, M. Horsfield, Non-invasive assessment of axonal fiber connectivity in the human brain via diffusion tensor MRI, Magn Reson Med 42 (1) (1999) 37–41.

[69] R. Xue, P. van Zijl, B. Crain, M. Solaiyappan, S. Mori, In vivo three-dimensional reconstruction of rat brain axonal projections by diffusion tensor imaging, Magn Reson Med 42 (6) (1999) 1123–1127.

[70] M. Catani, R. Howard, S. Pajevic, D. Jones, Virtual in vivo interactive dissection of white matter fasciculi in the human brain, NeuroImage 17 (1) (2002) 77–94.

[71] D.-S. Kim, I. Kim, M. Ronen, E. Formisano, K.-H. Kim, K. Ugurbil, S. Mori, R. Goebel, In vivo mapping of functional domains and axonal connectivity in cat visual cortex using magnetic resonance imaging, Magn Reson Imaging 21 (10) (2003) 1131–1140.

[72] C. Poupon, J.-F. Mangin, C. Clark, V. Frouin, J. Rgis, D. Le Bihan, I. Bloch, Towards inference of human brain connectivity from MR diffusion tensor data, Med Image Anal 5 (1) (2001) 1–15.

[73] B. Stieltjes, W. Kaufmann, P. van Zijl, G. Fredericksen, K. ans Pearlson, M. Solaiyappan, S. Mori, Diffusion tensor imaging and axonal tracking in the human brainstem, NeuroImage 14 (3) (2001) 723–735.

[74] S. Wakana, H. Jiang, L. Nagae-Poetscher, P. van Zijl, S. Mori, Fiber tract-based atlas of human white matter anatomy, Radiology 230 (1) (2004) 77–87.

[75] T. Conturo, N. Lori, T. Cull, E. Akbudak, A. Snyder, J. Shimony, R. McKinstry, H. Burton, M. Raichle, Tracking neuronal fiber pathways in the living human brain, in: Proc Natl Acad Sci USA, Vol. 96, 1999, pp. 10422–10427.

[76] D. Weinstein, G. Kindlmann, E. Lundberg, Tensorlines: advection-diffusion based propagation through diffusion tensor fields, in: IEEE Vis, 1999, pp. 249–254.

[77] M. Lazar, D. Weinstein, J. Tsuruda, K. Hasan, K. Arafakinis, M. Meyerand, B. Badie, H. Rowley, V. Haughton, A. Field, A. Alexander, White matter tractography using diffusion tensor deflection, Hum Brain Mapp 18 (4) (2003) 306–321.

[78] D. Xu, S. Mori, M. Solaiyappan, P. van Zijl, C. Davatzikos, A framework for callosal fiber distribution analysis, NeuroImage 17 (3) (2002) 1131–1143.

[79] C. Tench, P. Morgan, M. Wilson, L. Blumhardt, White matter mapping using diffusion tensor MRI, Magn Reson Med 47 (5) (2002) 967–972.

[80] L. Zhukov, A. Barr, Oriented tensor reconstruction: tracing neural pathways from diffusion tensor MRI, in: IEEE Vis, 2002, pp. 387–394.

[81] L. Zhukov, A. Barr, Heart-muscle fiber reconstruction from diffusion tensor MRI, in: IEEE Vis, 2003.

[82] C. Gössl, L. Fahrmeir, B. Pütz, L. Auer, D. Auer, Fiber tracking from DTI using linear state space models: detectability of the pyramidal tract, NeuroImage 16 (2) (2002) 378–388.

[83] K. Terajima, T. Nakada, EZ-tracing: a new ready-to-use algorithm for magnetic resonance tractography, J Nucl Med 116 (2) (2002) 147–155.

[84] G. Parker, K. Stephan, G. Barker, J. Rowe, D. MacManus, C. Wheeler-Kingshott, O. Ciccarelli, R. Passingham, R. Spinks, R. Lemon, R. Turner, Initial demonstration of in vivo tracing of axonal projections in the macaque brain and comparison with the human brain using diffusion tensor imaging and fast marching tractography, NeuroImage 15 (4) (2002) 779–809.

[85] G. Parker, C. Wheeler-Kingshott, G. Barker, Estimating distributed anatomical connectivity using fast marching methods and diffusion tensor imaging, IEEE Trans Med Imaging 21 (5) (2002) 505–512.

[86] O. Ciccarelli, A. Toosy, G. Parker, C. Wheeler-Kingshott, G. Barker, D. Miller, A. Thomp-

son, Diffusion tractography based group mapping of major white-matter pathways in the human brain, NeuroImage 19 (4) (2003) 1545–1555.

[87] O. Ciccarelli, G. Parker, A. Toosy, C. Wheeler-Kingshott, G. Barker, P. Boulby, D. Miller, A. Thompson, From diffusion tractography to quantitative white matter tract measures: a reproducibility study, NeuroImage 18 (2) (2003) 348–359.

[88] H. Powell, M. Guye, G. Parker, M. Symms, P. Boulby, M. Koepp, G. Barker, J. Duncan, Noninvasive in vivo demonstration of the connections of the human parahippocampal gyrus, NeuroImage 22 (2) (2004) 740–747.

[89] J. Duncan, X. Papademetris, J. Yang, M. Jackowski, X. Zeng, L. Staiba, Geometric strategies for neuroanatomic analysis from MRI, NeuroImage 23 (1) (2004) S34–S45.

[90] L. Jonasson, X. Bresson, P. Hagmann, O. Cuisenaire, R. Meuli, J.-P. Thiran, White matter fiber tract segmentation in DT-MRI using geometric flows, Med Image Anal 9 (3) (2005) 223–236.

[91] J.-D. Tournier, F. Calamente, D. Gadian, A. Connelly, Diffusion-weighted magnetic resonance imaging fibre tracking using a front evolution algorithm, NeuroImage 20 (1) (2003) 276–288.

[92] B. Vemuri, Y. Chen, M. Rao, T. McGraw, Z. Wang, T. Mareci, Fiber tract mapping from diffusion tensor MRI, in: IEEE VLSM, 2001.

[93] Y. Cointepas, J.-F. Mangin, C. Poupon, A spin glass based framework to reconstruct brain fiber bundles from images of te water diffusion process, Information Processes 2 (1) (2002) 30–36.

[94] J.-F. Mangin, C. Poupon, Y. Cointepas, D. Rivière, D. Papadopoulos-Orfanos, C. Clark, J. Régis, D. Le Bihan, A framework based on spin glass models for the inference of anatomical connectivity from diffusion-weighted MR data - a technical review, NMR Biomed 15 (7–8) (2002) 481–492.

[95] T. Behrens, M. Woolrich, M. Jenkinson, H. Johansen-Berg, R. Nunes, S. Clare, P. Matthews, J. Brady, S. Smith, Characterization and propagation of uncertainty in diffusion-weighted MR imaging, Magn Reson Med 50 (5) (2003) 1077–1088.

[96] G. Parker, D. Alexander, Probabilistic Monte Carlo based mapping of cerebral connections utilising whole-brain crossing fibre information, in: Inf Process Med Imaging, Vol. 2737, 2003, pp. 684–695.

[97] G. Parker, C. Haroon, H.A. Wheeler-Kingshott, A framework for a streamline-based Probabilistic Index of Connectivity (pico) using a structural interpretation of MRI diffusion measurements, J Magn Reson Imaging 18 (2) (2003) 242–254.

[98] A. Toosy, O. Ciccarelli, G. Parker, C. Wheeler-Kingshott, D. Miller, A. Thompson, Characterizing functionstructure relationships in the human visual system with functional MRI and diffusion tensor imaging, NeuroImage 21 (4) (2004) 1452–1463.

[99] P. Batchelor, D. Hill, F. Calamante, D. Atkinson, Study of connectivity in the brain using the full diffusion tensor from MRI, in: Inf Process Med Imaging, 2001, pp. 121–133.

[100] P. Hagmann, J.-P. Thiran, L. Jonasson, P. Vandergheynst, S. Clarke, P. Maeder, R. Meuli, DTI mapping of human brain connectivity: statistical fibre tracking and virtual dissection, NeuroImage 19 (3) (2003) 545–554.

[101] M. Lazar, A. Alexander, Bootstrap white matter tractography (BOOT-TRAC), NeuroImage 24 (2) (2005) 524–532.

[102] S. Zhang, M. Bastin, D. Laidlaw, S. Sinha, P. Armitage, T. Deisboeck, Visualization and analysis of white matter structural asymmetry in diffusion tensor MRI data, Magn Reson Med 51 (1) (2004) 140–147.

[103] P. Staempfli, T. Jaermann, G. Crelier, S. Kollias, A. Valavanis, P. Boesiger, Resolving fiber crossing using advanced fast marching tractography based on diffusion tensor imaging, NeuroImage 30 (1) (2006) 110–120.

[104] D. Jones, C. Pierpaoli, Confidence mapping in diffusion tensor magnetic resonance imaging tractography using a bootstrap approach, Magn Reson Med 53 (5) (2005) 1143–1149.

[105] D. Jones, A. Travis, G. Eden, C. Pierpaoli, P. Basser, PASTA: pointwise assessment of streamline tractography attributes, Magn Reson Med 53 (6) (2005) 1462–1467.

[106] M. Jackowski, C. Kao, M. Qiu, R. Constable, L. Staib, White matter tractography by anisotropic wavefront evolution and diffusion tensor imaging, Med Image Anal 9 (5) (2005) 427–440.

[107] N. Kang, J. Zhang, E. Carlson, D. Gembris, White matter fiber tractography via anisotropic diffusion simulation in the human brain, IEEE Trans Med Imaging 24 (9) (2005) 1127–1137.

[108] S. Sun, S. Song, C. Hong, W. Chu, C. Chang, Directional correlation characterization and classification of white matter tracts, Magn Reson Med 49 (2) (2003) 271–275.

[109] M. Koch, D. Norris, M. Hund-Georgiadis, An investigation of functional and anatomical connectivity using magnetic resonance imaging, NeuroImage 16 (1) (2002) 241–250.

[110] D. Jones, Determining and visualizing uncertainty in estimates of fiber orientation from diffusion tensor MRI, Magn Reson Med 49 (1) (2003) 7–12.

[111] M. Lazar, K. Hasan, A. Alexander, Bootstrap analysis of DT-MRI tractography techniques: streamlines and tensorlines, in: ISMRM, 2001, p. 1527.

[112] C. Poupon, J.-F. Mangin, V. Frouin, J. Régis, F. Poupon, M. Pachot-Clouard, D. Le Bihan, I. Bloch, Regularization of MR diffusion tensor maps for tracking brain white matter bundles, Lect Notes Comp Sci 1496 (1998) 489–498.

[113] C. Poupon, C. Clark, V. Frouin, J. Régis, I. Bloch, D. Le Bihan, J.-F. Mangin, Regularization of diffusion-based direction maps for the tracking of brain white matter fascicles, NeuroImage 12 (2) (2000) 184–195.

[114] C. Tench, P. Morgan, L. Blumhardt, C. Constantinescu, Improved white matter fiber tracking using stochastic labeling, Magn Reson Med 48 (4) (2002) 677–683.

[115] G. Parker, C. Wheeler-Kingshott, G. Barker, Distributed anatomical brain connectivity derived from diffusion tensor imaging, in: Inf Process Med Imaging, 2001, pp. 106–120.

[116] J. Campbell, K. Siddiqi, B. Vemuri, G. Pike, A geometric flow for white matter fibre tract reconstruction, in: ISBI, 2002, pp. 505–508.

[117] J. Campbell, K. Siddiqi, G. Pike, White matter fibre tract likelihood evaluated using normalized RMS diffusion distance, in: ISMRM, 2002, p. 1130.

[118] M. Jackowski, C. Kao, M. Qiu, R. Constable, L. Staib, Estimation of anatomical connectivity by anisotropic front propagation and diffusion tensor imaging, Lect Notes Comp Sci 3217 (2004) 663–671.

[119] S. Sun, S. Song, C. Hong, W. Chu, C. Chang, Improving relative anisotropy measurement using directional correlation of diffusion tensors, Magn Reson Med 46 (6) (2001) 1088–1092.

[120] G. Sela, N. Lobaugh, G. Stanisz, Brain white matter tractography from DT images using global coverings and maximal likelihood connectivity, in: ISMRM, 2004, p. 1284.

[121] D. Tuch, Mapping cortical connectivity with diffusion MRI, in: ISBI, 2002, pp. 392–394.

[122] T. Behrens, H. Johansen-Berg, I. Drobnjak, J. Brady, P. Matthews, S. Smith, D. Higham, Deliniation of functional subunits in the human cortex from diffusion based connectivity matrices, in: ISMRM, 2004, p. 621.

[123] M. Lazar, A. Alexander, White matter tractography using random vector (RAVE) perturbation, in: ISMRM, 2002, p. 539.

[124] D. Jones, C. Pierpaoli, Towards a marriage of deterministic and probabilistic tractography methods: bootstrap analysis of fiber trajectories in the human brain, in: ISMRM, 2004, p. 1276.

[125] D. Jones, A. Travis, G. Eden, C. Pierpaoli, P. Basser, Artifact or architecture? An integrated approach to visualizing uncertainty and partial volume effects in DT-MRI tractog-

raphy, in: ISMRM, 2004, p. 618.

[126] Y. Lu, Z. Ding, J. Gore, A. Anderson, Adaptive Bayesian tracking of neuronal fiber pathways from diffusion tensor images, in: ISMRM, 2004, p. 1275.

[127] G. Parker, G. Barker, N. Thacker, A. Jackson, A framework for a streamline-based Probabilistic Index of Connectivity (PICo) using a structural interpretation of anisotropic diffusion, in: ISMRM, 2002, p. 1165.

[128] T. Behrens, M. Jenkinson, J. Brady, S. Smith, A probabilistic framework for estimating neural connectivity from diffusion weighted MRI, in: ISMRM, 2002, p. 1142.

[129] T. Behrens, M. Woolrich, M. Jenkinson, J. Brady, S. Smith, Bayesian parameter estimation in diffusion weighted MRI, in: ISMRM, 2002, p. 1160.

[130] D. Tuch, J. Belliveau, V. Wedeen, A path integral approach to white matter tractography, in: ISMRM, 2000, p. 791.

[131] M. Moseley, J. Kucharczyk, J. Mintorovitch, Y. Cohen, J. Kurhanewicz, N. Derugin, H. Asgari, D. Norman, Diffusion-weighted MR imaging of acute stroke: correlation with T2-weighted and magnetic susceptibility-enhanced MR imaging in cats, AJNR Am J Neuroradiol 11 (3) (1990) 423–429.

[132] M. Moseley, Y. Cohen, J. Kucharczyk, H. Asgari, M. Wendland, J. Tsuruda, D. Norman, Diffusion-weighted MR imaging of anisotropic water diffusion in cat central nervous system, Radiology 176 (2) (1990) 439–445.

[133] M. Moseley, Y. Cohen, J. Mintorovitch, Early detection of regional cerebral ischemia in cats: comparison of diffusion- and T2-weighted MRI and spectroscopy, Magn Reson Med 14 (2) (1990) 330–346.

[134] R. A. Knight, M. O. Dereski, J. A. Helpern, R. J. Ordidge, M. Chopp, Magnetic resonance imaging assessment of evolving focal cerebral ischemia – comparison with histopathology in rats, Stroke 25 (1994) 1252–1262.

[135] Q. Jiang, M. Chopp, Z. G. Zhang, R. Knight, M. Jacobs, J. P. Windham, D. Peck, J. R. Ewing, K. M. A. Welch, The temporal evolution of MRI tissue signatures after transient middle cerebral artery occlusion in rat, J Neurol Sci 145 (1) (1997) 15–23.

[136] A. G. Sorensen, O. Wu, W. A. Copen, T. L. Davis, R. G. Gonzalez, W. J. Koroshetz, T. G. Reese, B. R. Rosen, V. J. Wedeen, R. M. Weisskoff, Human acute cerebral ischemia: detection of changes in water diffusion anisotropy by using MR imaging, Radiology 212 (3) (1999) 785–92.

[137] Q. Yang, B. M. Tress, P. A. Barber, P. M. Desmond, D. G. Darby, R. P. Gerraty, T. Li, S. M. Davis, Serial study of apparent diffusion coefficient and anisotropy in patients with acute stroke, Stroke 30 (1999) 2382–2390.

[138] P. van Gelderen, M. de Vleeschouwer, D. DesPres, J. Pekar, P. van Zijl, C. Moonen, Water diffusion and acute stroke, Magn Reson Med 31 (2) (1994) 154–163.

[139] J. Krejza, E. Melhem, Quantitative diffusion tensor imaging of the brain in young adults shows age-related structural changes in gray and white matter, Acad Radiol 12 (3) (2005) 265–267.

[140] D. Madden, W. Whiting, S. Huettel, L. White, J. MacFall, J.R. andProvenzale, Diffusion tensor imaging of adult age differences in cerebral white matter: relation to response time, NeuroImage 21 (3) (2004) 1174–1181.

[141] M. Moseley, Diffusion tensor imaging and aging - a review, NMR Biomed 15 (7–8) (2002) 553–560.

[142] A. Nusbaum, C. Tang, M. Buchsbaum, T. Wei, S. Atlas, Regional and global changes in cerebral diffusion with normal aging, AJNR Am J Neuroradiol 22 (1) (2001) 136–142.

[143] A. Pfefferbaum, E. Sullivan, M. Hedehus, K. Lim, E. Adalsteinsson, M. Moseley, Age-related decline in brain white matter anisotropy measured with spatially corrected echo-planar diffusion tensor imaging, Magn Reson Med 44 (2) (2000) 259–268.

[144] A. Pfefferbaum, E. Adalsteinsson, E. Sullivan, Frontal circuitry degradation marks healthy adult aging: evidence from diffusion tensor imaging, NeuroImage 26 (3) (2005) 891–899.

[145] A. Pfefferbaum, E. Adalsteinsson, E. Sullivan, Dysmorphology and microstructural degradation of the corpus callosum: Interaction of age and alcoholism, Neurobiol Aging .

[146] D. Salat, D. Tuch, D. Greve, A. van der Kouwe, N. Hevelone, A. Zaleta, B. Rosen, B. Fischl, S. Corkin, H. Rosas, A. Dale, Age-related alterations in white matter microstructure measured by diffusion tensor imaging, Neurobiol Aging 26 (2005) 1215–1227.

[147] V. Schmithorst, M. Wilke, B. Dardzinski, S. Holland, Correlation of white matter diffusivity and anisotropy with age during childhood and adolescence: a cross-sectional diffusion-tensor MR imaging study, Radiology 222 (1) (2002) 212–218.

[148] E. Sullivan, A. Pfefferbaum, Diffusion tensor imaging in normal aging and neuropsychiatric disorders, Eur J Radiol 45 (3) (2003) 244–255.

[149] T. Yoshiura, F. Mihara, A. Tanaka, O. Togao, T. Taniwaki, A. Nakagawa, T. Nakao, T. Noguchi, Y. Kuwabara, H. Honda, Age-related structural changes in the young adult brain shown by magnetic resonance diffusion tensor imaging, Academic Radiology 12 (3) (2005) 268–275.

[150] C. Büchel, T. Raedler, M. Sommer, M. Sach, C. Weiller, M. Koch, White matter asymmetry in the human brain: a diffusion tensor MRI study, Cereb Cortex 14 (9) (2004) 945–951.

[151] R. Westerhausen, C. Walter, F. Kreuder, R. Wittling, E. Schweiger, W. Wittling, The influence of handedness and gender on the microstructure of the human corpus callosum: a diffusion-tensor magnetic resonance imaging study, Neurosci Lett 351 (2) (2003) 99–102.

[152] R. Westerhausen, F. Kreuder, S. Dos Santos Sequeira, C. Walter, W. Woerner, R. Wittling, E. Schweiger, W. Wittling, Effects of handedness and gender on macro- and microstructure of the corpus callosum and its subregions: a combined high-resolution and diffusion-tensor MRI study, Brain Res Cogn Brain Res 21 (3) (2004) 418–426.

[153] G. Parker, S. Luzzi, D. Alexander, C. Wheeler-Kingshott, O. Ciccarelli, M. Lambon Ralph, Lateralization of ventral and dorsal auditory-language pathways in the human brain, NeuroImage 24 (3) (2005) 656–666.

[154] H.-J. Park, C.-F. Westin, M. Kubicki, S. Maier, M. Niznikiewicz, A. Baer, M. Frumin, R. Kikinis, F. Jolesz, R. McCarley, M. Shenton, White matter hemisphere asymmetries in healthy subjects and in schizophrenia: a diffusion tensor MRI study, NeuroImage 23 (1) (2004) 213–223.

[155] M. Moseley, R. Bammer, J. Illesa, Diffusion-tensor imaging of cognitive performance, Brain Cogn 50 (3) (2002) 396–413.

[156] S. Shenkin, M. Bastin, T. MacGillivray, I. Deary, J. Starr, J. Wardlaw, Childhood and current cognitive function in healthy 80 - year- olds: a DT-MRI study, NeuroReport 14 (3) (2003) 1–5.

[157] C. Beaulieu, C. Plewes, L. Paulson, D. Roy, L. Snook, L. Concha, L. Phillips, Imaging brain connectivity in children with diverse reading ability, NeuroImage 25 (4) (2005) 1266–1271.

[158] T. Klingberg, M. Hedehus, E. Temple, T. Salz, J. Gabrieli, M. Moseley, R. Poldrack, Microstructure of temporo-parietal white matter as a basis for reading ability: evidence from diffusion tensor magnetic resonance imaging, Neuron 25 (2) (2000) 493–500.

[159] D. Werring, C. Clark, G. Parker, D. Miller, A. Thompson, G. Barker, A direct demonstration of both structure and function in the visual system: combining diffusion tensor imaging with functional magnetic resonance imaging, NeuroImage 9 (3) (1999) 352–361.

[160] J. Berman, P. Mukherjee, S. Partridge, S. Miller, D. Ferriero, A. Barkovich, D. Vigneron, R. Henry, Quantitative diffusion tensor MRI fiber tractography of sensorimotor white matter development in premature infants, NeuroImage 27 (4) (2005) 862–871.

[161] L. Maas, P. Mukherjee, J. Carballido-Gamio, S. Veeraraghavan, S. Miller, S. Partridge, R. Henry, A. Barkovich, D. Vigneron, Early laminar organization of the human cerebrum

demonstrated with diffusion tensor imaging in extremely premature infants, NeuroImage 22 (3) (2004) 1134–1140.

[162] B. Murphy, G. Zientara, P. Huppi, S. Maier, P. Barnes, F. Jolesz, J. Volpe, Line scan diffusion tensor MRI of the cervical spinal cord in preterm infants, J Magn Reson Imaging 13 (6) (2001) 949–953.

[163] S. Partridge, P. Mukherjee, R. Henry, S. Miller, J. Berman, H. Jin, Lu, O. Glenn, D. Ferriero, A. Barkovich, D. Vigneron, Diffusion tensor imaging: serial quantitation of white matter tract maturity in premature newborns, NeuroImage 22 (3) (2004) 1302–1314.

[164] S. Boujrafa, R. Luypaert, W. Shabana, L. De Meirleirb, S. Sourbron, M. Osteaux, Study of pediatric brain development using magnetic resonance imaging of anisotropic diffusion, Magn Reson Imaging 20 (4) (2002) 327–336.

[165] J. Dubois, L. Hertz-Pannier, G. Dehaene-Lambertz, Y. Cointepas, D. Le Bihan, Assessment of the early organization and maturation of infants' cerebral white matter fiber bundles: a feasibility study using quantitative diffusion tensor imaging and tractography, NeuroImage .

[166] L. Hermoye, C. Saint-Martin, G. Cosnard, S.-K. Lee, J. Kim, M.-C. Nassogne, R. Menten, P. Clapuyt, P. Donohue, K. Hua, S. Wakana, H. Jiang, P. van Zijl, S. Mori, Pediatric diffusion tensor imaging: normal database and observation of the white matter maturation in early childhood, NeuroImage 29 (2) (2006) 493–504.

[167] T.-Q. Li, M. Noseworthy, Mapping the development of white matter tracts with diffusion tensor imaging, Dev Sci 5 (3) (2002) 293–300.

[168] J. Neil, J. Miller, P. Mukherjee, P. Hüppi, Diffusion tensor imaging of normal and injured developing human brain - a technical review, NMR Biomed 15 (7-8) (2002) 543–552.

[169] L. Snook, L.-A. Paulson, D. Roy, L. Phillips, C. Beaulieu, Diffusion tensor imaging of neurodevelopment in children and young adults, NeuroImage 26 (4) (2005) 1164–1173.

[170] A. Uluğ, Monitoring brain development with quantitative diffusion tensor imaging, Dev Sci 5 (3) (2002) 286–292.

[171] A. Pfefferbaum, E. Sullivan, Increased brain white matter diffusivity in normal adult aging: relationship to anisotropy and partial voluming, Magn Reson Med 49 (5) (2003) 953–961.

[172] E. V. Sullivan, E. Adalsteinsson, M. Hedehus, C. Ju, M. Moseley, K. O. Lim, A. Pfefferbaum, Equivalent disruption of regional white matter microstructure in aging healthy men and women 12 (2001) 99–104.

[173] M. Ota, T. Obata, Y. Akine, H. Ito, H. Ikehira, T. Asada, T. Suhara, Age-related degeneration of corpus callosum measured with diffusion tensor imaging, Neuroimage 31 (2006) 1445–1452.

[174] I. Agartz, J. Andersson, S. Skare, Abnormal brain white matter in schizophrenia: a diffusion tensor imaging study, NeuroReport 12 (10) (2001) 2251–2254.

[175] J. Foong, M. R. Symms, G. J. Barker, M. Maier, D. H. Miller, M. A. Ron, Investigating regional white matter in schizophrenia using diffusion tensor imaging., NeuroReport 13 (3) (2002) 333–6.

[176] B. A. Ardekani, J. Nierenberg, M. J. Hotman, D. C. Javitt, K. O. Lim, MRI Study of White Matter Diffusion Anisotropy in Schizophrenia., NeuroReport 14 (16) (2003) 2025–2029.

[177] J. Burns, D. Job, M. Bastin, H. Whalley, T. Macgillivray, E. Johnstone, S. Lawrie, Structural disconnectivity in schizophrenia: a diffusion tensor magnetic resonance imaging study, British Journal of Psychiatry 182 (2003) 439–443.

[178] R. Kanaan, J.-S. Kim, W. Kaufmann, G. Pearlson, G. Barker, P. McGuire, Diffusion tensor imaging in schizophrenia, Biol Psychiatry 58 (12) (2005) 921–929.

[179] P. R. Szeszko, B. A. Ardekani, M. Ashtari, S. Kumra, D. G. Robinson, S. Sevy, H. Gunduz-Bruce, A. K. Malhotra, J. M. Kane, R. M. Bilder, K. O. Lim, White matter abnormalities in first-episode schizophrenia or schizoaffective disorder: a diffusion tensor imaging study.,

Am J Psychiatry 162 (3) (2005) 602–605.

[180] M. Kubicki, H. Park, C.-F. Westin, P. Nestor, R. Mulkern, S. Maier, M. Niznikiewicz, E. Connor, J. Levitt, M. Frumin, R. Kikinis, F. Jolesz, R. McCarley, M. Shentona, DTI and MTR abnormalities in schizophrenia: analysis of white matter integrity, NeuroImage 26 (4) (2005) 1109–1118.

[181] B. A. Ardekani, A. Bappal, D. D'Angelo, M. Ashtari, T. Lencz, P. R. Szeszko, P. D. Butler, D. C. Javitt, K. O. Lim, J. Hrabe, J. Nierenberg, C. A. Branch, M. J. Hoptman, Brain morphometry using diffusion weighted MRI: Application to schizophrenia., NeuroReport 16 (13) (2005) 1455–1459.

[182] M. S. Buchsbaum, J. Friedman, B. R. Buchsbaum, K. Chu, E. A. Hazlett, R. Newmark, J. S. Schneiderman, Y. Torosjan, C. Tang, P. R. Hof, D. Stewart, K. L. Davis, J. Gorman, Diffusion tensor imaging in schizophrenia., Biol Psych 60 (11) (2006) 1181–1187.

[183] D. K. Jones, X. A. Chitnis, D. Job, P. L. Khong, L. T. Leung, S. Marenco, S. M. Smith, M. R. Symms, What happens when nine different groups analyze the same DT-MRI data set using voxel-based methods?, Proc. ISMRM 15th Annual Meeting, Berlin (2007) 74.

[184] G. Douaud, S. Smith, M. Jenkinson, T. Behrens, H. Johansen-Berg, J. Vickers, S. James, N. Voets, K. Watkins, P. M. Matthews, A. James, Anatomically related grey and white matter abnormalities in adolescent-onset schizophrenia., Brain 130 (2007) 2375–2386.

[185] J. H. Seok, H. J. Park, J. W. Chun, S. K. Lee, H. S. Cho, J. S. Kwon, J. J. Kim, White matter abnormalities associated with auditory hallucinations in schizophrenia: A combined study of voxel-based analyses of diffusion tensor imaging and structural magnetic resonance imaging., Psychiatry Res. 156 (2) (2007) 93–104.

[186] K. H. Karlsgodt, T. G. M. van Erp, R. A. Poldrack, C. E. Bearden, K. H. Nuechterlein, T. D. Cannon, Diffusion tensor imaging of the superior longitudinal fasciculus and working memory in recent-onset schizophrenia., Biol Psych 63 (5) (2007) 512–518.

[187] M. Kyriakopoulos, N. S. Vyas, G. J. Barker, X. A. Chitnis, S. Frangou, A diffusion tensor imaging study of white matter in early-onset schizophrenia., Biol Psychiatry 63 (5) (2007) 519–523.

[188] T. White, A. T. K. Kendi, S. Lehricy, M. Kendi, C. Karatekin, A. Guimaraes, N. Davenport, S. C. Schulz, K. O. Lim, Disruption of hippocampal connectivity in children and adolescents with schizophrenia - a voxel-based diffusion tensor imaging study., Schizophr Res 90 (1–3) (2007) 302–307.

[189] A. Pfefferbaum, E. V. Sullivan, M. Hedehus, E. Adalsteinsson, K. O. Lim, M. Moseley, In vivo detection and functional correlates of white matter microstructural disruption in chronic alcoholism., Alcohol Clin Exp Res 24 (2000) 1214–1221.

[190] M. D. De Bellis, E. Van Voorhees, S. R. Hooper, N. Gibler, L. Nelson, S. G. Hege, M. E. Payne, J. MacFall, Diffusion tensor measures of the corpus callosum in adolescents with adolescent onset alcohol use disorders, Alcohol Clin Exp Res 32 (3) (2008) 395–404.

[191] K. O. Lim, J. R. Wozniak, B. A. Mueller, D. T. Franc, S. M. Specker, C. P. Rodriguez, A. B. Silverman, J. P. Rotrosen, Brain macrostructural and microstructural abnormalities in cocaine dependence, Drug Alcohol Depend 92 (1–3) (2008) 164–172.

[192] H. Liu, L. Li, Y. Hao, D. Cao, L. Xu, R. Rohrbaugh, Z. Xue, W. Hao, B. Shan, Z. Liu, Disrupted White Matter Integrity in Heroin Dependence: A Controlled Study Utilizing Diffusion Tensor Imaging, Am J Drug Alcohol Abuse In Press (–) (2008) –.

[193] M. Filippi, M. A. Horsfield, H. J. Adr, F. Barkhof, P. Bruzzi, A. Evans, J. A. Frank, R. I. Grossman, H. F. McFarland, P. Molyneux, D. W. Paty, J. Simon, P. S. Tofts, J. S. Wolinsky, D. H. Miller, Guidelines for using quantitative measures of brain magnetic resonance imaging abnormalities in monitoring the treatment of multiple sclerosis., Annals of Neurology 43 (4) (1998) 499–506.

[194] D. H. Miller, R. I. Grossman, S. C. Reingold, H. F. Mcfarland, The role of magnetic

resonance techniques in understanding and managing multiple sclerosis., Brain 121 (1) (1998) 3–24.

[195] M. Filippi, M. A. Rocca, G. Comi, The use of quantitative magnetic-resonance-based techniques to monitor the evolution of multiple sclerosis., Lancet Neurol 2 (6) (2003) 337–346.

[196] C. Beaulieu, P. S. Allen, Determinants of anisotropic water diffusion in nerves., Magn Reson Med 31 (4) (1994) 394–400.

[197] P. S. Huppi, S. E. Maier, S. Peled, G. P. Zientara, P. D. Barnes, F. A. Jolesz, J. J. Volpe, Microstructural development of human newborn cerebral white matter assessed in vivo by diffusion tensor magnetic resonance imaging, Pediatric Research 44 (1998) 584–590.

[198] M. A. Horsfield, H. B. Larsson, D. K. Jones, A. Gass, Diffusion magnetic resonance imaging in multiple sclerosis, Journal of Neurology, Neurosurgery and Psychiatry 64 (S1) (1998) S80–S84.

[199] P. Mukherjee, J. H. Miller, J. S. Shimony, T. E. Conturo, B. C. Lee, C. R. Almli, R. C. McKinstry, Normal brain maturation during childhood: developmental trends characterized with diffusiontensor MR imaging, Radiology 221 (2001) 349–358.

[200] U. Wieshmann, M. Symms, G. Parker, C. Clark, L. Lemieux, G. Barker, S. Shorvon, Diffusion tensor imaging demonstrates deviation of fibres in normal appearing white matter adjacent to a brain tumour, J Neurol Neurosurg Psychiatry 68 (4) (2000) 501–503.

[201] S. Mori, K. Frederiksen, P. Van Zijl, B. Stieltjes, M. Kraut, M. Solaiyappan, M. Pomper, Brain white matter anatomy of tumor patients evaluated with diffusion tensor imaging, Ann Neurol 51 (3) (2002) 377–380.

[202] B. Witwer, R. Moftakhar, K. Hasan, P. Deshmukh, V. Haughton, A. Field, K. Arfanakis, J. Noyes, C. Moritz, M. Meyerand, H. Rowley, A. Alexander, B. Badie, Diffusion-tensor imaging of white matter tracts in patients with cerebral neoplasm, J Neurosurg 97 (3) (2002) 568–575.

[203] K. M. Gauvain, R. C. McKinstry, P. Mukherjee, A. Perry, J. J. Neil, B. A. Kaufman, R. J. Hayashi, Evaluating pediatric brain tumor cellularity with diffusion-tensor imaging, AJR Am J Roentgenol 177 (2001) 449–454.

[204] A. C. Guo, T. J. Cummings, R. C. Dash, J. M. Provenzale, Lymphomas and high-grade astrocytomas: comparison of water diffusibility and histologic characteristics, Radiology 224 (2002) 177–183.

[205] T. Beppu, T. Inoue, Y. Shibata, A. Kurose, H. Arai, K. Ogasawara, A. Ogawa, S. Nakamura, H. Kabasawa, Measurement of fractional anisotropy using diffusion tensor mri in supratentorial astrocytic tumors .

[206] T. Beppu, T. Inoue, Y. Shibata, N. Yamada, A. Kurose, K. Ogasawara, A. Ogawa, H. Kabasawa, Fractional anisotropy value by diffusion tensor magnetic resonance imaging as a predictor of cell density and proliferation activity of glioblastomas, Surg Neurol 63 (1) (2005) 56–61.

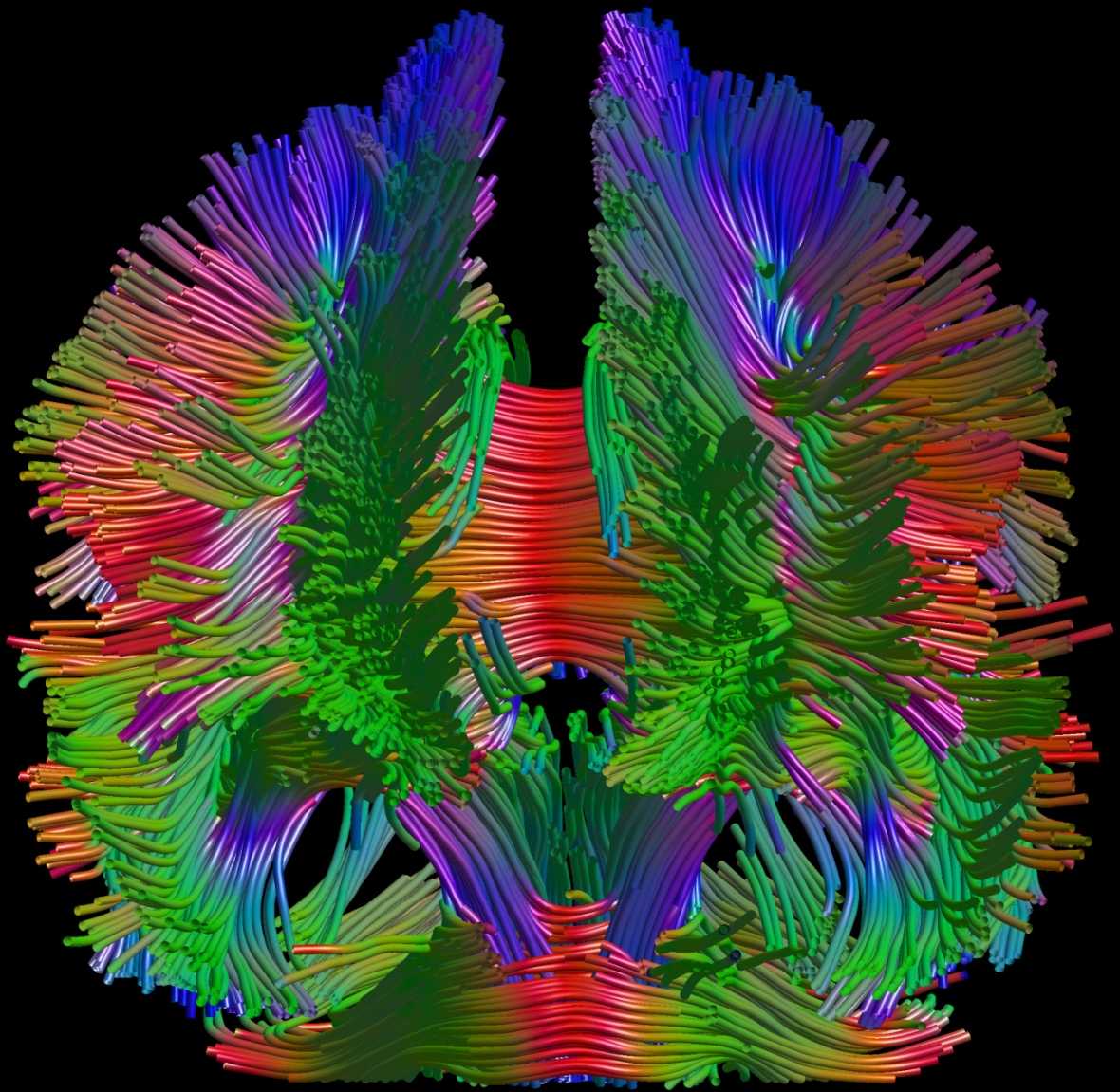

III

DIFFUSION TENSOR IMAGE PROCESSING OF THE HUMAN BRAIN

Most of us have spent some time wondering how our brain works. Brain scientists spend their entire lives pondering it, looking for a way to begin asking the question, How does the brain generate mind? The brain, after all, is so complex an organ and can be approached from so many different directions using so many different techniques and experimental animals that studying it is a little like entering a blizzard, the Casbah, a dense forest. It's easy enough to find a way in - an interesting phenomenon to study - but also very easy to get lost.

– Susan Allport

4

Coregistration of diffusion tensor images

Contents

Overview

A very important step in a voxel based analysis of DTI data sets is the coregistration of all data sets to a template or atlas. In this way, the diffusion properties of the corresponding voxels can be compared between the different data sets in the atlas space. The goal of coregistration is thus to find a set of 3D deformation fields that map the different data sets to the atlas space. The image alignment of DTI data sets is particularly challenging compared to aligning scalar images, such as anatomical MR images, CT images, etc., since each DTI voxel is represented by a symmetric second rank tensor, i.e. the six components describing the 3D diffusion process. This tensor information should be included in the coregistration algorithm in order to align the DTI data sets more accurately. In this chapter, the concept of image coregistration is briefly introduced. Thereafter, the image alignment method, based on a viscous fluid model and mutual information, that is used in our work to map DTI data sets to each other is elucidated.

The work in this chapter has been published in:
W. Van Hecke, A. Leemans, E. D'Agostino, S. De Backer, E. Vandervliet, P. M. Parizel and J. Sijbers, *Nonrigid Coregistration of Diffusion Tensor Images Using a Viscous Fluid Model and Mutual Information*, IEEE Transactions on Medical Imaging, Vol. 26, Nr. 11, p. 1598-1612, (**2007**)

4.1 Image coregistration

The objective of coregistration or spatial normalization is to search for the spatial transformations that map different images to a common reference space, in which direct comparison of various image properties is possible [1, 2]. However, in practice, it is not feasible to coregister data sets from different subjects perfectly, due to the lack of information in the images (given the restricted resolution), the limited degrees of freedom of the deformable model that is used to align the data sets, the inherent variability of brain structures of different subjects, etc. An optimization procedure is therefore used to approximate the actual transformation of the different images. The goal of image alignment is thus to find the deformation field T that describes the transformation between a reference (also referred to as target or template) image I_1 and a source or floating image I_2 in a way that the similarity between both images I_1 and I_2 is maximized. To this end, there is a need for a:

Deformation model: defines the number of degrees of freedom and the possible transformations of a coregistration algorithm;

Similarity measure: determines the correspondence between different images;

Optimization strategy: selects the optimal transformation between the images.

These different coregistration features are discussed in more detail in the following paragraphs. Reviews of different image coregistration techniques can be found in [1–5].

4.1.1 Deformation Models

4.1.1.1 Rigid transformations

Rigid transformations only allow images to rotate and translate globally. As a result, a rigid transformation in 3D is defined by six degrees of freedom: translations in x, y and z directions, and rotations about the same three axes. The rigid body transformation can be described by a rotation R followed by a translation t, and maps voxel $\mathbf{r} = (x, y, z)$ to voxel $\mathbf{r}' = (x', y', z')$:

$$\boldsymbol{r'} = \boldsymbol{R}\boldsymbol{r} + \boldsymbol{t} \ . \tag{4.1}$$

This transformation of voxel $\mathbf{r}$ to $\mathbf{r}'$ can also be written as:

$$\underbrace{\begin{bmatrix} x' \\ y' \\ z' \end{bmatrix}}_{\boldsymbol{r'}} = \underbrace{\begin{bmatrix} r_{11} & r_{12} & r_{13} & t_x \\ r_{21} & r_{22} & r_{23} & t_y \\ r_{31} & r_{32} & r_{33} & t_z \\ 0 & 0 & 0 & 1 \end{bmatrix}}_{T} \underbrace{\begin{bmatrix} x \\ y \\ z \end{bmatrix}}_{\boldsymbol{r}} \ , \tag{4.2}$$

with

$$\mathbf{R} = \begin{bmatrix} r_{11} & r_{12} & r_{13} \\ r_{21} & r_{22} & r_{23} \\ r_{31} & r_{32} & r_{33} \end{bmatrix} \qquad \text{and} \qquad \mathbf{t} = \begin{bmatrix} t_x \\ t_y \\ t_z \end{bmatrix} \ . \tag{4.3}$$

4.1.1.2 Affine transformations

In addition to rotations and translations, affine transformations include scaling and shearing components in the deformation model. Equations 4.4 and 4.2 can then be rewritten more generally as:

$$\boldsymbol{r'} = \boldsymbol{A}\boldsymbol{r'} + \boldsymbol{t} \ . \tag{4.4}$$

and

$$\underbrace{\begin{bmatrix} x' \\ y' \\ z' \end{bmatrix}}_{\boldsymbol{r'}} = \underbrace{\begin{bmatrix} a_{11} & a_{12} & a_{13} & t_x \\ a_{21} & a_{22} & a_{23} & t_y \\ a_{31} & a_{32} & a_{33} & t_z \\ 0 & 0 & 0 & 1 \end{bmatrix}}_{T} \underbrace{\begin{bmatrix} x \\ y \\ z \end{bmatrix}}_{\boldsymbol{r}} , \tag{4.5}$$

In this case, matrix A contains rotation, scaling and shearing components and can be described with 12 degrees of freedom. Although affine transformations are able to align two images better compared to he rigid transformation, they are restricted to global deformations. A typical example of an image transformation whereby only a global deformation field can be used, is the coregistration of data sets from the same subject, acquired on different time points or on different scan modalities. Only a global transformation is needed in this case, since the internal brain structures from the same subject usually have the same size and shape, except when a pathology such as a tumor is present in the second image. However, since brain images of different subjects do vary locally, non-affine transformations are required.

4.1.1.3 Non-affine or non-rigid transformations

As aforementioned, it is generally assumed that global affine transformations are inadequate for an inter-subject coregistration, since local morphological differences between different subjects can then not be taken into account [6]. The transformations that are needed for an accurate inter-subject coregistration require to accommodate both complex, large, and locally-adaptive deformations. Non-affine, also called non-rigid, coregistration techniques utilize local adaptive deformation fields for the image alignment, and are thus, in theory, more adequate to correct for inter-subject variations of different brain structures.
However, not all transformations are physically feasible or realistic. Additionally, the intensity information that is present in the images may be insufficient to unambiguously define such a local transformation field. It is, for example in homogeneous image regions, very hard to define the accurate deformation field that maps corresponding voxels. A solution to this problem is to regularize the transformation field in order to impose local consistency or smoothness on the transformation. Two important regularization approaches are discussed here: splines based transformations and transformations based on a physical model.

4.1.1.3.1 Spline based transformations Spline-based registration techniques typically require a set of corresponding control points or landmarks that have to be identified in both source and target images.

Thin plate splines: Thin plate splines are based on radial-basis functions and refers to a physical analogy involving the bending of a thin sheet of metal. The aim of thin plate spline based image coregistration is to minimize the bending energy of the spline.

B-splines: When radial basis functions are used, every control point contributes to the whole transformation. This hampers the modeling of local deformations, and furthermore, prohibits the use of very large numbers of control points due to the increased computational complexity. An alternative is provided by free-form deformations based on B-splines, which are piecewise continuous polynomials. B-splines are a generalization of the Bézier curve and were introduced for medical image coregistration by Rueckert et al. (1999) [7, 8]. They are easy to construct and can approximate complex shapes through curve fitting and interactive curve design [8].

4.1.1.3.2 Transformations based on a physical model

Elastic coregistration The idea of the elastic models is to treat the image as an elastic material, such as rubber. This allow the transformations in different regions of the image to be more independent of the transformation in the surrounding regions. The external force of the elastic model is commonly provided by the image similarity.

Viscous fluid coregistration The amount of deformation obtained using elastic registration is proportional to the force. For this reason elastic deformations cannot easily model highly localized deformations. This has led to interest in fluid registration techniques which enable large as well as local deformations (including corners) to be smoothly recovered. The basic idea is to treat the image as a fluid, and then apply a viscous fluid model to drive and control the deformation.

4.1.2 Similarity Metrics

The similarity measure calculates the spatial correspondence between both data sets that are transformed to each other. In the iterative optimization approach, this similarity measure is optimized to achieve a maximal image correspondence. Different intensity based similarity measures can be calculated. Here, the correlation coefficient, sum of squared differences, and mutual information are discussed:

4.1.2.1 Correlation Coefficient

In the correlation coefficient (CC), the product of the difference from the image mean of corresponding intensity values is calculated. The correlation coefficient

assumes a linear relationship between corresponding intensities in the images. To reduce this dependency, the normalized cross-correlation can be used. If image $I_1(\mathbf{r})$ is the reference image and $I_2(T(\mathbf{r}))$ the source image that is transformed to $I_1(\mathbf{r})$, the normalized correlation coefficient of images $I_1(\mathbf{r})$ and $I_2(T(\mathbf{r}))$ can then be written as:

$$CC = \frac{\sum[(I_1(\mathbf{r}) - \overline{I}_1(\mathbf{r}))(I_2(T(\mathbf{r})) - \overline{I}_2(T(\mathbf{r}))]}{\sqrt{\sum(I_1(\mathbf{r})) - \overline{I}_1(\mathbf{r}))^2 \sum(I_2(T(\mathbf{r}) - \overline{I}_2(T(\mathbf{r}))^2}} \ , \tag{4.6}$$

whereby the sum is taken over all corresponding voxels of $I_1(\mathbf{r})$ and $I_2(T(\mathbf{r})$. Thereby, $\overline{I}_1(\mathbf{r})$ and $\overline{I}_2(T(\mathbf{r})$ represent the mean of images $I_1(\mathbf{r})$ and $I_2(T(\mathbf{r})$ over all corresponding voxels, respectively. The maximum correlation coefficient corresponds to the strongest linear relationship between corresponding pairs of intensity values [9].

4.1.2.2 Sum of Squared Differences

The sum of squared distance (SSD) between the target and the source image is given by:

$$SSD = \sum[(I_1(\mathbf{r}) - I_2(T(\mathbf{r}))]^2 \ . \tag{4.7}$$

When both data sets are perfectly aligned and the corresponding voxels in both images have exactly the same intensities, the SSD is zero. This similarity metric assumes that corresponding voxels contain the same intensity after image alignment, except for Gaussian noise. Therefore, as with the CC metric, the SSD can be strongly affected by a small number of voxels having large intensity differences.

4.1.2.3 Mutual Information

Information theory was developed out of Shannons pioneering work in the 1940s at Bell Laboratories [10]. His work focused on characterizing information for communication systems by finding ways of measuring data based on the uncertainty or randomness present in the given system. Shannon proved that for probabilities p_i,

$$-\sum_i p_i log(p_i), \tag{4.8}$$

is the only functional form that satisfies all the conditions that a measure of uncertainty should satisfy. For a discussion on this topic, I would like to refer to Hajnal et al. (2001). Shannon named this quantity of Eq. (4.8) entropy because it shares the same mathematical form as the entropy of statistical mechanics.
Mutual information (MI) was proposed as a similarity measure independently by Collignon et al. (1995), Wells et al. (1996), and Maes et al. (1997) [11–13]. MI

quantifies how much information one image provides about another image, instead of comparing intensities directly. Maximizing mutual information involves maximizing the information contained in each image while minimizing the information contained in the overlayed images. The marginal entropies of images I_1 and I_2 with intensities $i_1(\mathbf{r})$ and $i_2(\mathbf{r})$ are defined as follows:

$$H(I_1) = -\sum_{i_1 \in I_1} p(i_1) log(p(i_1)) \ , \tag{4.9}$$

$$H(I_2) = -\sum_{i_2 \in I_2} p(i_2) log(p(i_2)) \ , \tag{4.10}$$

where $p(i_1)$ and $p(i_2)$ are the probabilities of voxels with intensities i_1 and i_2 occurring in the corresponding image. The joint entropy of images I_1 and I_2 is given by:

$$H(I_1, I_2) = -\sum_{\substack{i_1 \in I_1 \\ i_2 \in I_2}} p(i_1, i_2) log(p(i_1, i_2)) \ , \tag{4.11}$$

where $p(i_1, i_2)$ represents the joint probability density function of the images I_1 and I_2. The mutual information is then given by:

$$MI(I_1, I_2) = H(I_1) + H(I_2) - H(I_1, I_2) = -\sum_{\substack{i_1 \in I_1 \\ i_2 \in I_2}} p(i_1, i_2) log(p(i_1, i_2)) \ , \tag{4.12}$$

Similarity measures borrowed from information theory are applicable in coregistrations of images from the same modality as well as images from different modalities, since MI makes no assumptions about the relationship between image intensity maps. An overview of entropy based coregistration methods can be found in Pluim et al. (2003).

4.1.3 Optimization Strategies

Transformation parameters are adjusted to improve the image similarity using an optimization method. Optimization is a broad discipline in mathematics and a lot of methods have been proposed for function optimization (finding the minimum or maximum value of a function) [14–16]. Most methods are iterative, whereby the correspondence between the images is improved at each iteration, until a maximum is found. In order to reach the global optimum rather than a local optimum, the gradient of the function is generally computed during the optimization. In other methods, such as the conjugate gradient or quasi Newton approaches, the second order derivative are computed. The functions should therefore be smooth and differentiable. For noisy functions, statistical or randomized methods like simulated annealing [56] or genetic algorithms [57] are adopted.

4.2 Coregistration of diffusion tensor images using a viscous fluid model and mutual information

All great deeds and all great thoughts have a ridiculous beginning.
– Albert Camus

4.2.1 Introduction

In the previous paragraphs, some general concepts about the coregistration of scalar images were introduced. The coregistration of DT images is particularly challenging compared to aligning scalar images, since each DTI voxel is represented by a symmetric second rank tensor, i.e. the six components describing the 3D diffusion process. Consequently, scalar coregistration algorithms have to be adapted so that they can deal with these multi-component data sets. In addition, the alignment of the DT field with the underlying microstructure has to be preserved after the coregistration process. For the latter, a tensor reorientation (TR) strategy has to be performed [17]. Since Alexander et al. (2001) raised the TR problem, their proposed TR strategies have been applied widely [17, 18]. The finite strain (FS) method decomposes the transformation matrix in a deformation and a rotation component, whereafter only the latter is used to reorient the tensors. However, shearing, non-uniform scaling and stretching factors affect the orientation as well. Together with the rotational component, they are taken into account in the preservation of principal direction (PPD) strategy. In this study, the PPD algorithm is implemented as described by the direct DT reconstruction approach of Leemans et al. (2005) [19].
The most trivial approach to coregister DTI data is by registering scalar images associated with the DTI data sets, such as T_2-weighted MR images, FA maps, or the non-diffusion weighted images [20, 21]. Alexander and Gee proposed a multiresolution elastic matching algorithm and introduced similarity measures based on the DT data [22]. Ruiz-Alzola et al. (2000,2002) optimized affine transformations in certain restricted windows of the image domain, measuring image correspondence based on DT data [23, 24]. Note that in [22] and [24], no TR was applied during the optimization.
Park et al. (2003) and Guimond et al. (2002) extended the demons algorithm to DTI data and applied an iterative TR strategy [25–27]. This iterative tensor adaptation increases the algorithmic complexity and computation time drastically. Furthermore, although the DT information is more exploited compared to [22] and [24], errors caused by an imperfect TR can affect the alignment at each iteration. In addition, no initial correction is performed for the presence of voxel intensity differences in corresponding structures of different data sets or subjects, caused by

a different brain morphology. This potentially results in a non-optimal starting point of the SSD similarity measurement. Finally, Zhang et al. (2006) proposed a local affine coregistration algorithm using DT data in the similarity measure in order to optimize the tensor reorientation explicitly [28].

4.2.2 Multi-component viscous fluid coregistration

4.2.2.1 The viscous fluid model

The general goal of coregistration is to map a particular floating image $\phi(\vec{x})$ to a reference image $\tau(\vec{x})$ in order to align both. In the following framework, the images are modeled as a viscous fluid. Such a viscous fluid model, which imposes constraints on the local deformation field during coregistration, can be described by the free-form nonrigid coregistration algorithm of [29], in which a regularization function from elasticity theory has been applied [29, 30]. D'Agostino et al. (2003) replaced this elastic model with a viscous fluid regularization model of Christensen et al. (1996) which allows the viscous fluid model to be described by the following simplified Navier-Stokes equation [30–32]:

$$\mu\nabla^2\vec{v} + (\mu+\lambda)\vec{\nabla}(\vec{\nabla}\cdot\vec{v}) + \vec{F}(\vec{x},\vec{u}) = \vec{0}, \tag{4.13}$$

with $\vec{v}$ the deformation velocity and $\vec{F}$ the force field, which depends on the local deformation $\vec{u}$ and the deformation position $\vec{x}$. The material parameters μ and λ are set to 1 and 0, respectively [31]. At each iteration k of the gradient descent optimizer of the coregistration algorithm, the new displacement $\vec{u}^{(k+1)}$ is calculated from the previous displacement $\vec{u}^{(k)}$, taking into account the perturbation $\vec{R}^{(k)}$ of the deformation field and the time step parameter $\Delta t^{(k)}$:

$$\vec{u}^{(k+1)} = \vec{u}^{(k)} + \vec{R}^{(k)}\Delta t^{(k)}. \tag{4.14}$$

In (4.14), $\vec{R}^{(k)}$ is defined as,

$$\vec{R}^{(k)} = \vec{v}^{(k)} - \sum_{i=1}^{3} v_i^{(k)}\Big(\frac{\delta\vec{u}^{(k)}}{\delta x_i}\Big), \tag{4.15}$$

with $\vec{v}^{(k)}$ defined as the convolution of the force field $\vec{F}^{(k)}$ and a Gaussian spatial smoothing kernel Ψ_s with a width s [27, 30]:

$$\vec{v}^{(k)} = \Psi_s \otimes \vec{F}^{(k)}. \tag{4.16}$$

The force field $\vec{F}$ is defined in such a way that the viscous fluid deformation strives at maximizing the MI between the deformed floating image $\phi(\vec{x}-\vec{u})$ and the target image $\tau(\vec{x})$. To this end, the gradient of the MI with respect to an infinitesimally changed deformation field $\vec{u}$ is required [29]. The joint intensity distribution $p_{\vec{u}}^{\phi,\tau}(i_1,i_2)$ of the deformed floating image and the target image is therefore modeled as a continuous function using Parzen windowing, making it differentiable with respect to the deformation field. Hereby, i_1 and i_2 represent the intensities of images ϕ and τ. The MI between $\phi(\vec{x}-\vec{u})$ and $\tau(\vec{x})$ can be defined as [11]:

$$MI(\vec{u}) = \sum_{i_1}\sum_{i_2} p_{\vec{u}}^{\phi,\tau}(i_1,i_2)\log\frac{p_{\vec{u}}^{\phi,\tau}(i_1,i_2)}{p^{\tau}(i_2)p_{\vec{u}}^{\phi}(i_1)}. \tag{4.17}$$

Hereby, p^{τ} and p^{ϕ} represent the marginal intensity distributions of τ and ϕ, respectively. The gradient of the MI with respect to a deformation field $\vec{u}$ that is perturbed into $\vec{u}+\epsilon\vec{h}$ can be calculated and simplified to [29]:

$$\left.\frac{\partial MI(\vec{u}+\epsilon\vec{h})}{\partial\epsilon}\right|_{\epsilon=0} = \sum_{i_1}\sum_{i_2}\left(\left(1+\log\frac{p_{\vec{u}+\epsilon\vec{h}}^{\phi,\tau}(i_1,i_2)}{p^{\tau}(i_2)p_{\vec{u}+\epsilon\vec{h}}^{\phi}(i_1)}\right)\cdot\left.\frac{\partial p_{\vec{u}+\epsilon\vec{h}}^{\phi,\tau}(i_1,i_2)}{\partial\epsilon}\right|_{\epsilon=0}\right). \tag{4.18}$$

Thereby, the joint intensity distribution $p_{\vec{u}}^{\phi,\tau}(i_1,i_2)$ of the reference and deformed floating image is estimated from the region of overlap v' (with volume V) using a Parzen window kernel $\psi_h(i_1,i_2)$ with width h:

$$p_{\vec{u}}^{\phi,\tau}(i_1,i_2) = \frac{1}{V}\int_{v'}\psi_h(i_1-\phi(\vec{x}-\vec{u}),i_2-\tau(\vec{x}))d\vec{x}. \tag{4.19}$$

The force field can now be written as [29, 30]:

$$\vec{F}(\vec{x},\vec{u}) = \vec{\nabla}_{\vec{u}}MI = \frac{1}{V}\left[\frac{\delta\psi_h}{\delta i_1}\otimes L_{\vec{u}}\right]\big(\phi(\vec{x}-\vec{u}),\tau(\vec{x})\big)\vec{\nabla}\phi(\vec{x}-\vec{u}), \tag{4.20}$$

with

$$L_{\vec{u}}(i_1,i_2) = 1+\log\frac{p_{\vec{u}}^{\phi,\tau}(i_1,i_2)}{p^{\tau}(i_2)p_{\vec{u}}^{\phi}(i_1)}. \tag{4.21}$$

The force field, driving the deformation to maximize MI, is defined as the gradient of MI with respect to $\vec{u}(\vec{x})$, and can be calculated using the intensity gradient of the deformed floating image $\phi(\vec{x}-\vec{u})$, weighted by the impact on the MI of a voxel

in ϕ at $\vec{x} - \vec{u}$ being displaced in this direction [29, 30]. This force field is calculated at each iteration of the gradient-descent optimization procedure, until the MI no longer increases or the Jacobian determinant of the total deformation becomes negative. In this way, it is ensured that the transformation is homeomorphic. At each time step during the deformation, the force field is constant such that the modified Navier-Stokes equation can be solved iteratively as a temporal concatenation of linear equations [30]. A velocity field is obtained by solving the modified Navier-Stokes equation (4.13). This velocity field is computed with (4.16), as in Thirion et al. (1998) approximating the approach of Bro-Nielsen and Gramkow [27, 33]. Thereafter, the perturbation to the deformation field is computed (4.15) and used to obtain the displacement field at a given iteration (4.14).
At each iteration, the determinant of the Jacobian is constrained to reduce the chance that the underlying anatomical microstructure is forced in a physical or anatomical non-acceptable way [34]. When the determinant of the local Jacobian becomes smaller than 0.5, a regridding of the deformed floating image is applied to generate a new floating image, setting the incremental displacement field to zero [32]. A width of $h = 4$ and $s = 3$ were used for the Gaussian Parzen windowing kernel ψ_h and for the spatial smoothing kernel Ψ_s, as described in [30]. The time step parameter Δt in (4.14) is adapted each iteration and set to:

$$\Delta t^{(k)} = \max(||\vec{R}^k||)\Delta u, \tag{4.22}$$

with Δu (in voxels) the maximal allowed voxel displacement in each iteration. D'Agostino et al. (2003) demonstrated that an optimal balance between speed of convergence and need for regridding is obtained for $\Delta u = 0.6$.

4.2.2.2 Multi-component coregistration

In its simplest form, coregistration of DTI data sets is based on the alignment of two scalar T_2-weighted images. Thereafter, the resulting transformation is applied to the DT images. Although T_2-weighted images have a higher spatial resolution compared to DTI, the coregistration result will be strongly affected by the severe lack of white matter contrast in these images. Indeed, conventional MR protocols, such as T_1- or T_2-weighted pulse sequences, represent the white matter as a rather homogeneous region. Since nonrigid coregistration algorithms are mainly driven by the contrast of different brain structures, low contrast regions, such as the white matter on conventional MR images, will be poorly aligned. As a result, the structural and particularly the orientation correspondence will be very low in the white matter after coregistration [25].
In order to provide more structural information to guide the coregistration in white matter regions, DTI features are used. For this purpose, the scalar FA map, con-

taining a high white matter contrast, has demonstrated to be an appropriate feature [20]. In this context, Guimond et al. (2002) introduced a multi-component normalization method based on the DT eigenvalue images (λ_1, λ_2, λ_3) [26]. As argued by Alexander et al. (2001) to preserve the intrinsic information of the tensor, only rigid transformations should reorient the tensors, independent of the nature of the local transformation that is applied [17]. The scalar measures, such as the FA and the eigenvalues, are invariant to rigid transformations, and therefore, TR is not required during coregistration. Park et al. (2003) demonstrated that the use of DT elements improved the coregistration quality significantly [25]. They implemented the demons algorithm and used the SSD as a similarity criterion [27].

When the DTI alignment is based on images that contain orientation information, such as the DT components or the DW images, the coregistration problem becomes more complex. In contrast to the voxel intensities of the images that are invariant to rigid transformations, the voxel intensities of the DT components or the DW images are dependent on the position of the subject in the scanner and on the local morphology of the brain. For example, when a particular white matter tract follows a different path in two subjects, its DT or DW intensity values can vary significantly in corresponding voxels, whereas the FA can be similar. Since the intensity variation in corresponding voxels has a local, spatial-dependent nature, image intensity transformations, which are often used to deal with multi-modal images, are not applicable under these circumstances. DTI coregistration, that incorporates orientation information to align the images, is therefore one of the few applications that has to accommodate both the alignment of inter-subject images and the presence of non-linear inter-voxel intensity differences.

In a study of Park et al. (2003) a TR was applied iteratively during coregistration using the FS approach [25]. By iteratively adjusting the tensor orientation, the accuracy of the image alignment may be increased. However, the necessity for an iterative tensor adaptation increases the algorithmic complexity and computation time drastically. Furthermore, errors caused by an imperfect TR can affect the alignment at each iteration. Note that, by implementing an iterative TR, no initial correction is performed for the presence of voxel intensity differences in corresponding structures, potentially resulting in a non-optimal starting point of the SSD similarity measurement. Moreover, FA or eigenvalue image data are known to be non-Gaussian distributed, due to the non-linearity in the calculation of the eigenvalue system [35]. Since, the widely used SSD similarity measure presupposes similar voxel intensity values in various images that only differ from each other by a Gaussian noise term, it can therefore not be used optimally for this purpose.

In an attempt to mitigate the aforementioned DTI coregistration issues, we propose to use MI as a criterion for DT image similarity. By applying MI, the non-linear inter-voxel intensity differences are taken into account without the need for an explicit tensor reorientation during the optimization procedure. Consequently, the

tensors are only reoriented after the application of the final deformation field. In this study, three different coregistration approaches are evaluated using a different number of components (L): FA map ($L = 1$), the DT elements ($L = 6$), and the DW images ($L = 60$).

4.2.2.3 Mutual information and force field calculation for multiple components

Generally, in the context of coregistration, MI is defined and studied between two scalar images, measuring their statistical dependency. The concept of multivariate MI was introduced as an extension of the bivariate case to multiple scalar images, thereby constructing a multi-dimensional histogram [36]. Since the 6 DT element images or the 60 DW images form multi-component data, the alignment of two DTI data sets becomes a multivariate coregistration problem. In contrast to the general multivariate problem, the data sets in the multi-component DTI coregistration process can be subdivided in two groups ϕ_l and τ_k that represent multi-component (DT or DWI) images of two different data sets ($l = 1, \ldots, L$ and $k = 1, \ldots, K$). Applying the general multivariate idea of evaluating statistical dependencies for each image combination to this specific problem, would increase the computation time dramatically. Therefore, some adjustments are introduced to adapt the general multivariate space to the specific multi-component DTI problem.
First, only images that have the same number of components are coregistered (L=K). Indeed, DT elements of data set ϕ_l are compared with DT elements of data set τ_k (L=K=6), and the DW images of ϕ_l are compared with the DW images of τ_k (L=K=60). Secondly, only cross-subject statistical dependencies are computed. The different components of data set ϕ_l are not compared with each other (and analogous for data set τ_k), thereby assuming that all image components of a single subject are aligned. Thirdly, the corresponding components are evaluated in parallel (l=k). For example, the first DT element image of data set ϕ_l (i.e., ϕ_1) is compared with the first DT element image of data set τ_k (i.e., τ_1), and never with another DT element image of data set τ_k. In this way, the general multivariate space is simplified with respect to the specific multi-component coregistration problem of DT images. Rohde et al. (2003) proposed a multivariate correlation approach for the coregistration of multi-component images [37]. However, by using correlation coefficients, the assumption is made that a linear relationship is present between the intensity values of the different components of different subjects.
We propose two similarity metrics based on the statistical dependencies of the multi-component DT images. Both represent a summary metric on the original multivariate space, based on MI.

'MI method 1'

In a first approach for the calculation of the multi-component MI, the bivari-

ate MI is computed for all L corresponding components separately, assuming them to be independent. A similar approach was adopted in Park et al. (2003) using the sum of squared distances as a similarity metric [25]. A global measurement of image similarity is proposed by averaging the MI_l of the different corresponding components: MI=$\frac{1}{L}\sum_{l=1}^{L} MI_l$. This MI metric is optimized in the iterative coregistration process. At each iteration, the force field of (4.20) is calculated for all corresponding components separately:

$$\vec{F}_l(\vec{x},\vec{u}) = \frac{1}{V_l}\Big[\frac{\delta\psi_h}{\delta i_1} \otimes L_{l,\vec{u}}\Big]\big(\phi_l(\vec{x}-\vec{u}),\tau_l(\vec{x})\big)\cdot\vec{\nabla}\phi_l(\vec{x}-\vec{u}), \qquad (4.23)$$

with $L_{l,\vec{u}}$ based on the joint intensity histogram of corresponding image component l. In this way, L force fields are calculated independently, based on the gradient of its corresponding floating image component and weighted by the effect on the MI between the corresponding floating and reference image component. A final force field is calculated as an average force field of all corresponding components: $\vec{F}=\frac{1}{L}\sum_{l=1}^{L}\vec{F}_l$. This force field $\vec{F}$ is then used to calculate the velocity field (4.16), whereafter the perturbation to the deformation field (4.15) and the displacement field (4.14) are computed at each iteration. This deformation field is applied to all L components of the floating image, ϕ_l, which is then used as the floating image in the next iteration.

'MI method 2'

In a second approach, the global MI is calculated from a histogram that already contains all information of the different components simultaneously. All components of a data set are concatenated to a single image. Thereafter, the global joint intensity histogram can be calculated on both concatenated images $\vec{\phi}$ and $\vec{\tau}$, containing all information of the L components. The MI is based on this global joint intensity histogram and can now be written as:

$$MI(\vec{\phi},\vec{\tau}) = \sum_{i_1}\sum_{i_2}\left(p^{\vec{\phi}\vec{\tau}}(i_1,i_2)\cdot\log\left(\frac{p^{\vec{\phi}\vec{\tau}}(i_1,i_2)}{p^{\vec{\phi}}(i_1)p^{\vec{\tau}}(i_2)}\right)\right), \qquad (4.24)$$

with i_1 and i_2 representing the voxel intensities and

$$\vec{\tau}\equiv[\tau_1,\ldots,\tau_L] \qquad \vec{\phi}\equiv[\phi_1,\ldots,\phi_L], \qquad (4.25)$$

denoting the collection of selected components of the floating image and the reference image, respectively. In practice, the multi-component image information is pooled into a single histogram, by adding the joint histograms of all image components. This histogram is then less sparse and contains all information of the histograms of the corresponding components. The MI of (4.24), containing information of all image components, is optimized during the iterative coregistration process. In (4.24), $p^{\vec{\phi},\vec{\tau}}$ is the joint intensity distribution of the images $\vec{\phi}$ and $\vec{\tau}$, and $p^{\vec{\phi}}$ and $p^{\vec{\tau}}$ represent the marginal intensity distributions of $\vec{\phi}$ and $\vec{\tau}$, respectively. In this approach, they are calculated as a sum of the histograms of the corresponding components:

$$\begin{aligned} p^{\vec{\phi}\vec{\tau}}(r,f) &= \frac{1}{L}\sum_{i=1}^{L} p^{\phi_i\tau_i}(r,f), \\ p^{\vec{\tau}}(r) &= \frac{1}{L}\sum_{i=1}^{L} p^{\tau_i}(r), \\ p^{\vec{\phi}}(f) &= \frac{1}{L}\sum_{i=1}^{L} p^{\phi_i}(f). \end{aligned} \tag{4.26}$$

Analogous as in 'MI method 1', the force field of (4.20) is calculated for all corresponding segments:

$$\vec{F}_l(\vec{x},\vec{u}) = \tfrac{1}{V}\left[\tfrac{\delta\psi_h}{\delta i_1}\otimes L_{\vec{u}}\right]\big(\phi_l(\vec{x}-\vec{u}),\tau_l(\vec{x})\big)\cdot\vec{\nabla}\phi_l(\vec{x}-\vec{u}). \tag{4.27}$$

In contrast with 'MI method 1', the $L_{\vec{u}}$ is based on the total joint intensity histogram of images $\vec{\phi}$ and $\vec{\tau}$. Again, L force fields are calculated based on the image gradient of each component. However, the force field weighting factors are now driven by the global MI of (4.24). The global force field is computed as an average of all L component force fields: $\vec{F}=\frac{1}{L}\sum_{l=1}^{L}\vec{F}_l$. This force field is then used to calculate the velocity field (4.16), whereafter the new deformation field $\vec{u}$ can be derived with (4.14) and (4.15). Finally, all floating image components are iteratively updated by the application of the deformation field.

4.2.3 Acquisition and evaluation methodology

In this section, the DTI acquisition parameters and the evaluation setup are first described (paragraph 4.2.3.1 and 4.2.3.2). Then, the measures that are used to

evaluate the coregistration method are presented in paragraph 4.2.3.3. Finally, the statistical tests are introduced for the interpretation of the results (paragraph 4.2.3.4).

4.2.3.1 Acquisition

DTI measurements of the human brain were performed with a 1.5 T MR scanner on 40 healthy subjects (16 males and 24 females), with a mean age of 28 years ($19-55$ years). An informed consent was signed by all participants. Axial DT images were obtained using a SE-EPI sequence with the following acquisition parameters: TR = 10.4 s; TE = 100 ms; diffusion gradient = 40 $mT.m^{-1}$; FOV = 256×256 mm^2; number of slices = 60; image resolution = $2 \times 2 \times 2$ mm^3; $b = 700$ $s.mm^{-2}$; acquisition time = 12 min 18 s. Diffusion measurements were performed along 60 directions for a robust estimation of FA, tensor orientation, and MD [38]. All DTI post processing, such as calculation of the eigenvalue system and the visualization, was performed with the diffusion toolbox 'ExploreDTI' (*http://www.dti.ua.ac.be*) [39].

4.2.3.2 General setup

All images are first coregistered to a randomly chosen single subject image with an affine coregistration algorithm that is designed for DTI, thereby using the MIRIT (Multimodality Image Registration using Information Theory) method [11, 40]. In order to evaluate our proposed viscous fluid coregistration method, two approaches are followed:

- The first evaluation approach, using 15 different nonrigid, predefined deformation fields, can be summarized as follows (see Fig. 4.1):
  - A predefined deformation field is applied to the DW images of an original DTI data set. This original DTI data set is referred to as the reference image (see Fig. 4.1(a), (b)).
  - The DT field is calculated from the deformed DW images (see Fig. 4.1 (c), (d)).
  - The DT are reoriented to preserve the alignment with the underlying, deformed microstructure (Fig. 4.1 (e)).
  - The DW images are recalculated from the reoriented DT field, resulting in the deformed data set, also referred to as the deformed data or floating image (Fig. 4.1 (f)).
  - The deformed data set (Fig. 4.1 (f)) is coregistered spatially to the reference data set (Fig. 4.1(a)), followed by a TR of the DT field and

a recalculation of the DW images. Since the difference between the deformed and the reference image is predefined, it can be regarded as ground-truth to evaluate the subsequent coregistration.

- To examine the applicability of our coregistration technique for VBA studies or the formation of a connectivity atlas, DT images of 40 different persons are normalized, and an arbitrary chosen data set is used as a reference image.

Multiple DTI components and MI calculation methods are used in both coregistration evaluation approaches, and are numbered as follows:

I Affine coregistration;

Viscous fluid coregistration using the:

II FA maps;

III DT elements and 'MI method 1';

IV DT elements and 'MI method 2';

V DW images and 'MI method 1';

VI DW images and 'MI method 2';

4.2.3.3 Evaluation measures

Only voxels with an FA value larger than 0.4 are considered in the quantitative analysis. Although these selected voxels do not strictly form a WM segmentation, they are referred to as the WM mask in the remainder of this paper. Both the spatial coregistration result and the orientation correspondence are evaluated as follows:

- When the theoretical deformation field is known, a quantitative value can be assigned, comparing the final transformation after coregistration with the ground-truth deformation for each voxel B:

$$C_B = \frac{||\vec{s}_B - \vec{s'}_B||}{||\vec{s}_B|| + ||\vec{s'}_B||}. \tag{4.28}$$

  Here, $\vec{s}_B$ and $\vec{s'}_B$ represent the theoretical and final deformation field, respectively. The median of C_B of all selected voxels, referred to as C, can then be interpreted as an overall measure of the transformation field correspondence. When C is 0, the final deformation field exactly equals the theoretical deformation field, representing a perfect spatial alignment. On the other hand, when C is 1, the final deformation field is the opposite of the theoretical deformation field, resulting in the worst alignment.

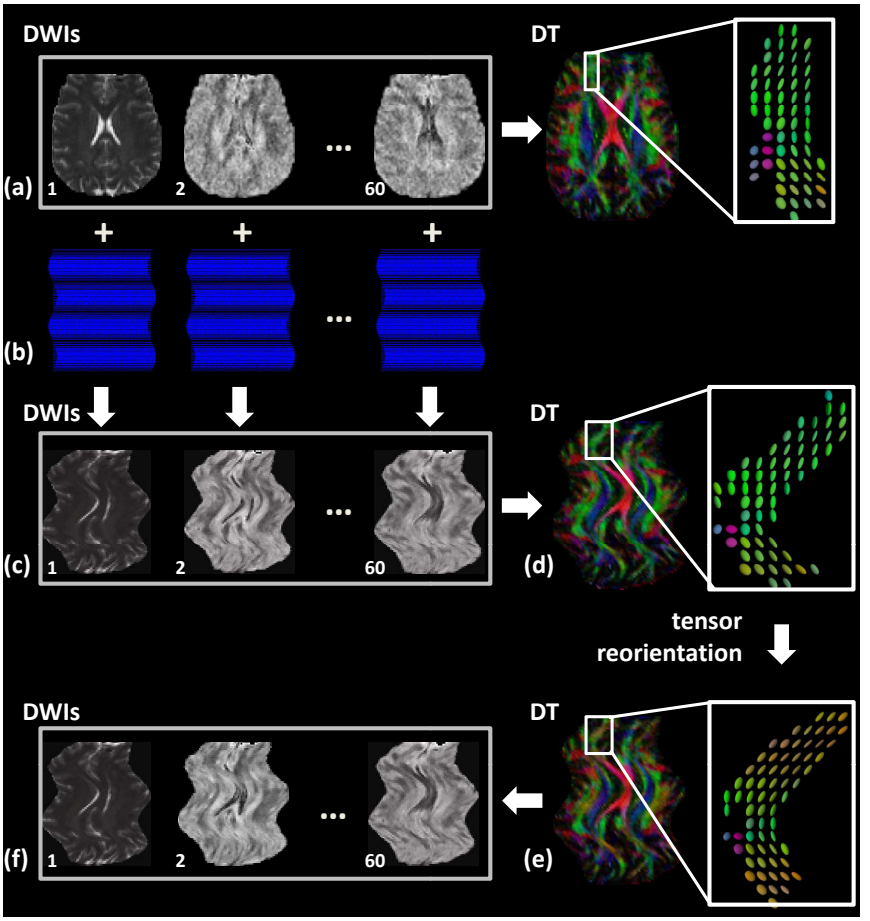

Figure 4.1. *The DW images of a DTI data set (a) are deformed with a known deformation field (b), resulting in a set of deformed DW images (c). The DT elements are calculated from these deformed DW images (d). Thereafter a tensor reorientation is performed to realign the deformed tensors with their underlying microstructure (e). Finally, the DW images are recalculated from the realigned DT elements (f) to construct the deformed DT data set that is used as a floating image in the coregistration algorithm. The DT maps are color encoded according to the diffusion direction.*

- In order to evaluate the coregistration technique with respect to the orientation information, the angle a_B between the first eigenvector of the reference image $\vec{n}_B$ and the transformed floating image $\vec{n'}_B$ can be calculated for each WM voxel B:

$$a_B = \cos^{-1}\left(\frac{|\vec{n'}_B \cdot \vec{n}_B^T|}{||\vec{n'}_B|| \cdot ||\vec{n}_B||}\right). \tag{4.29}$$

  The median a of all selected voxels B is a measurement of the preservation of orientation information after coregistration, since it represents a general value of the first eigenvector alignment. The smaller this first eigenvector angle difference, the better the orientation alignment between the images involved. Another measure which we will apply in our evaluation method is the overlap of eigenvalue-eigenvector pairs (OVL) between tensors [41]:

$$OVL = \frac{1}{N_B}\sum_B \frac{\sum_{i=1}^3 \lambda_i \lambda'_i (\vec{\epsilon'}_i \cdot \vec{\epsilon}_i^T)^2}{\sum_{i=1}^3 \lambda'_i \lambda_i}, \tag{4.30}$$

  with N_B the total number of selected WM voxels, and λ'_i, λ_i, and $\vec{\epsilon'}_i$, $\vec{\epsilon}_i$ eigenvalues and eigenvectors of the deformed floating image and the reference image, respectively. The minimum value 0 indicates no overlap and the maximum value 1 represents complete overlap of the principal axes of the DT field.

4.2.3.4 Statistics

The non-parametric Wilcoxon matched-pairs signed-rank test is applied to find the potential statistical significant difference between the coregistration results. On the other hand, a paired t-test is used to interpret the inter-subject alignment results.

4.2.4 Results

In paragraph 4.2.4.1, the orientation of the DT field after deformation of the DTI data set is evaluated on synthetic DTI phantoms [42]. Next, paragraph 4.2.4.1.1 presents the viscous fluid coregistration results with respect to accuracy and as a function of the amount of image noise. Additionally, a qualitative example is provided. In order to investigate the effect of nonrigid deformation fields on the subsequent TR, different TR methodologies, applied after the viscous fluid coregistration, are evaluated (paragraph 4.2.4.1.2). In paragraph 4.2.4.1.3, the methodology without an iterative TR is compared with a method that performs an iterative TR. Finally, the effect of different thresholds for defining the white matter masks for quantitative evaluation will be examined in paragraph 4.2.4.1.4.

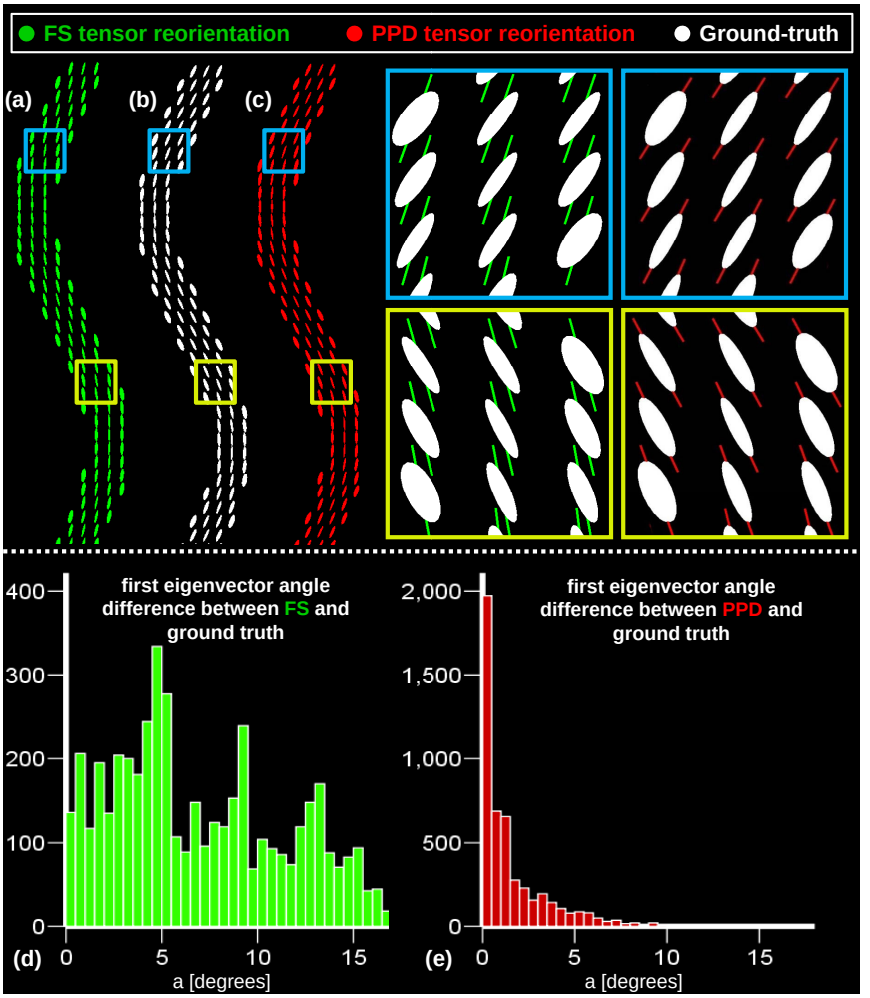

Figure 4.2. *First, a straight, synthetic fiber bundle is deformed with a nonrigid, sinusoidally shaped deformation field. A tensor reorientation (TR) is subsequently performed, using the FS (a) and the PPD (c) approach. Second, a sinusoidally shaped, synthetic fiber bundle with exactly the same frequency and amplitude as the aforementioned deformation field is defined (b). The orientation of these diffusion tensors can be regarded as ground-truth. The white ellipsoids represent the ground-truth tensors and the first eigenvectors after FS and PPD tensor reorientation are superimposed in green and red, respectively. The first eigenvector angle difference between the ground-truth and the TR result is displayed in (d) for the FS TR, and in (e) for the PPD TR.*

4.2.4.1 TR evaluation using synthetic DTI data sets

In this section, the TR approaches are evaluated for the nonrigid coregistration using a synthetic DTI phantom [42]. An estimation of the error caused by the TR itself is important for the interpretation of the tensor correspondence after coregistration.
The synthetic DTI data experiments for the evaluation of the TR techniques can be summarized as follows:

- The DW images of a straight, synthetic fiber bundle d_1 were deformed with different nonrigid, sinusoidally shaped deformation fields, resulting in a deformed bundle d_2 (analogous as in Fig. 4.1(a), (b), and (c)).
- The DT field was calculated from the deformed DW images of d_2 (analogous as in Fig. 4.1(d)).
- In order to realign the DT field with the deformed microstructure, a TR was performed with the FS and the PPD method (see Fig. 4.2(a) and (c), respectively).
- The DW images were recalculated from the reoriented DT field (analogous as in Fig. 4.1(f)).
- In order to evaluate the TR approaches, a ground-truth is necessary. Therefore, a new synthetic fiber bundle d_3 was simulated (see Fig. 4.2(b)). This bundle exhibits a sine function trajectory with exactly the same frequency and amplitude as the aforementioned deformation fields that were used to deform the first straight bundle. The DT field of d_3 was regarded as ground-truth, since it exactly follows the spatial pattern of the defined white matter fiber bundle.
- The DT field of d_2 after TR was then compared with the ground-truth DT field of d_3, as displayed in Fig. 4.2.

In order to quantify the tensor difference, the angle between the first eigenvectors of the deformed and the ground-truth tensors was calculated in each selected WM voxel. For the FS tensor reorientation method, the median angle was $7^\circ \pm 4^\circ$. Since the PPD TR technique clearly outperforms the FS method, with a median angle of $1.6^\circ \pm 1.5^\circ$, it was implemented to reorient the tensors a priori with a predefined deformation field resulting in the ground truth data sets.
These deformed data sets are used in the following sections as the floating images that are coregistered to the reference DTI data set. In order to align the DT field with the underlying microstructure after coregistration to the reference image, both FS and PPD strategies were applied. In this way, the effect of local coregistration inaccuracies on the TR result is studied.

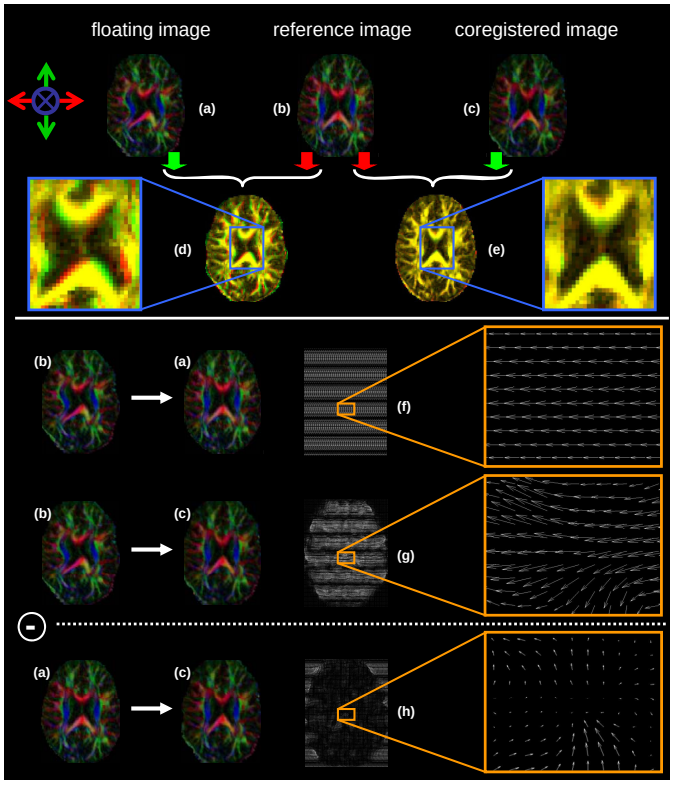

Figure 4.3. *Qualitative coregistration result of a synthetic DTI data set. The reference DT image, given in (b), is deformed with a predefined deformation field (see (f)), resulting in the image as displayed in (a). For the following coregistration analysis, this deformed data set is used as the floating image, whereas the data set in (b) is used as the reference image. The coregistered image is shown in (c). In order to evaluate the image correspondence visually, the FA intensity map of the reference image is given a red color, whereas the FA intensities of the floating and coregistered images are given a green color. Consequently, when the reference and floating image are overlapping, a yellow color is indicated (d). Therefore, this can be used to visually detect the correspondence quality of the coregistration. An analogous image is composed for the reference and the coregistered images (e), demonstrating a better image alignment after coregistration. In order to get a more detailed view of the alignment, the different vector fields are displayed in (f), (g), and (h). In (f), the predefined, ground-truth deformation field used to deform the reference image (b) to the floating image (a) is shown. The final deformation field after coregistration of the floating image (a) to the reference image is displayed in (g). After subtraction of these vector fields, the spatial coregistration error can be visualized in (h).*

4.2.4.1.1 Multi-component viscous fluid coregistration

(i) Qualitative coregistration results

An example of the alignment of a DTI data set, deformed with a predefined deformation field, to the reference image is shown in Fig. 4.3. In Fig. 4.3(a), 4.3(b), and 4.3(c), the deformed data set, the ground-truth DT image, and the coregistered image are displayed, respectively. In order to evaluate the image correspondence before coregistration, the FA map of the reference image is given a red color, and the FA map of the (deformed) floating image is given a green color. Therefore, when both images are overlayed (see Fig. 4.3(d)), corresponding voxels that contain similar intensity values in the reference and floating image will appear yellow after overlaying both images. Similar maps are shown after viscous fluid coregistration (see Fig. 4.3(e)). The theoretical deformation field (between 4.3(a) and 4.3(b)) and the obtained deformation field after coregistration (between 4.3(a) and 4.3(c)) are displayed in 4.3(f) and 4.3(g), respectively. The difference between these deformation fields is presented in Fig. 4.3(h), demonstrating a high vector field correspondence and a sub-voxel mean vector field error.

An axial, coronal, and sagittal representation of the inter-subject coregistration result is given in Fig. 4.4. Again, the FA map of the reference image was given a red color, whereas the FA map of the affine and nonrigid coregistration result were both given a green color. Consequently, the overlay of the reference image (red) with the affine and nonrigid coregistration maps (green) will display a yellow color when correspondence is high, and a red or green color when the correspondence is low.

(ii) Evaluation measures of the coregistration

Quantitative coregistration results of DTI data sets deformed with predefined deformations are shown in Fig. 4.5(a), (b), and (c). The FS approach was applied to reorient the DT field after coregistration. In Fig. 4.5 (e) and (f), the first eigenvector angle difference a and OVL are displayed for inter-subject data. The quantitative results, displayed in Fig. 4.5, demonstrate that the nonrigid coregistration method clearly outperforms the affine alignment results. In addition, the use of multiple components (methods III-VI) always resulted in an improved alignment, compared to the FA coregistration. This amelioration is furthermore statistically significant in the case of deformed data with a predefined deformation field and in the case for inter-subject data (see Fig. 4.5(d): II vs III). In Fig. 4.5(d) (III vs. V), it is demonstrated that the coregistration based on the DT elements outperformed the DWI coregistration outcome. It is furthermore shown that the calculation of the global

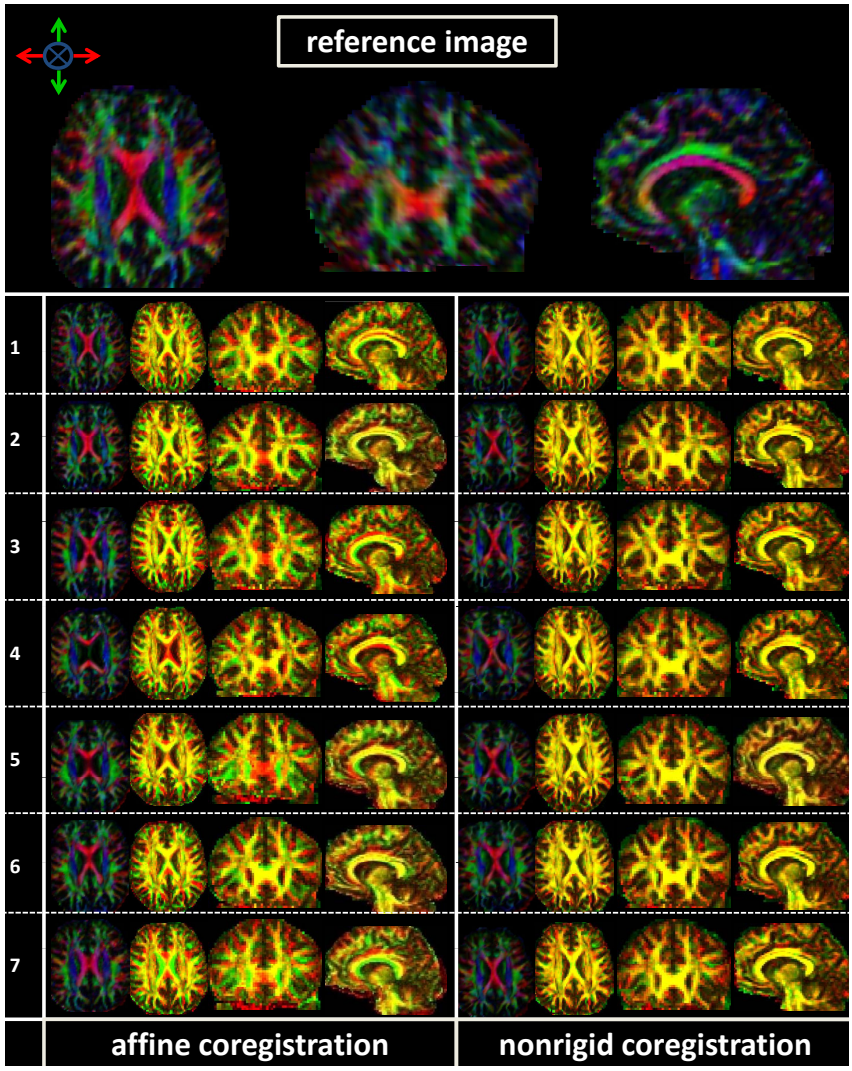

Figure 4.4. *At the top of this figure, an axial, coronal, and sagittal slice of the reference data set are shown. The color is encoded according to the diffusion direction. In the bottom part of this figure,* 7 *arbitrarily chosen images of different subjects are shown after affine (left column) and a subsequent viscous fluid model based (right column) coregistration with the reference image. In each column, the diffusion direction encoded axial slices of the coregistered data set are shown on the left. The other images are composed of the red colored FA intensity values of the reference image on the one hand, and the green colored FA intensity values of the coregistered image on the other hand. The yellow color indicates that similar FA intensities are present in corresponding voxels.*

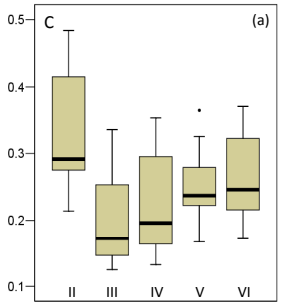

(d)

p-values		C	a	OVL
II vs III	def	0.043	0.001	0.001
II vs III	in-sub		< 0.001	< 0.001
III vs V	def	0.045	0.001	0.001
III vs V	in-sub		< 0.001	< 0.001
III vs IV	def	0.5	0.02	0.01
III vs IV	in-sub		< 0.001	< 0.001

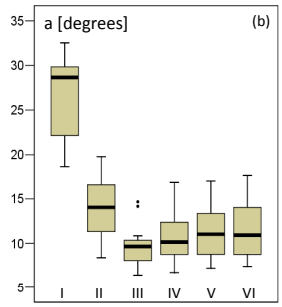

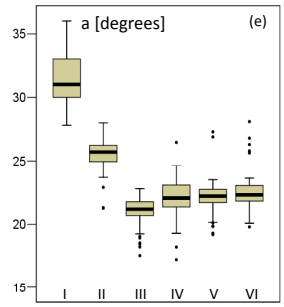

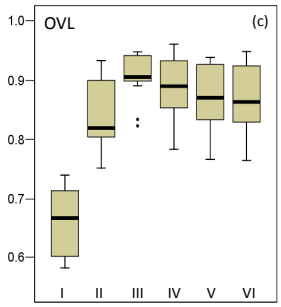

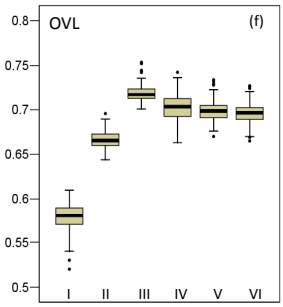

Figure 4.5. *Quantitative coregistration results of deformed data sets with known deformation fields and inter-subject data are shown on the left and right, respectively. The different coregistration methods are grouped on the horizontal axis. (I) represents the affine result, (II) is the FA based coregistration, (III) uses DT components and iteratively averages the mutual information during coregistration, and (IV) uses DT components and calculates the global histogram from all DT elements. Method (V) and (VI) are analogous to (III) and (IV), respectively, but use the DW images as information components. Parameter C calculates the correspondence of the final deformation field after coregistration with the predefined deformation field (a). The angle difference a between the first eigenvectors of corresponding voxels of different data-sets is displayed in the middle row for the deformed (b), and inter-subject (e) DTI data. In (c), and (f) the OVL, measuring the eigenvalue-eigenvector overlap of tensors in corresponding voxels, is given for the deformed, and inter-subject data, respectively. Finally, in (d), the p-values between the coregistration methods are shown for the quantitative parameters.*

MI on one histogram, containing all components, does not result in a better alignment, compared to the iterative averaging of all component MIs. Especially in the case of inter-subject data, the latter difference is statistically significant, whereas this is not always the case for the deformed data (see Fig. 4.5(d): II vs IV).

(iii) Effect of noise

In order to study the effect of noise on the coregistration outcome, the reference and the DW images, deformed with a known deformation field, were corrupted with different levels of Rician distributed noise (represented by σ). Next, all DTI features were calculated from the noisy DW images. After coregistration, a transformation is found for each voxel from the floating image to the reference image. Instead of applying this deformation field to the noisy floating image, it is used to transform the floating image without noise. In this way, quantitative values described in paragraph 4.2.3.3, give insight into the effect of noise on the alignment error itself.

In Fig. 4.6(a), (b), and (c), the alignment results are displayed in the presence of different levels of noise. Notice that, even when very high noise levels are added, the image alignment, and especially the orientation correspondence, is still preserved. The upper part of Fig. 4.6 displays an axial DTI slice, corrupted with different levels of noise. The signal to noise ratio (SNR) measure is defined as the average intensity value of all diffusion weighted images divided by the level σ of the Rician distributed noise that is added.

4.2.4.1.2 Tensor Reorientation after nonrigid coregistration

Comparison of FS and PPD tensor reorientation methods

In paragraph 4.2.4.1, we demonstrated that the PPD method outperformed the FS approach when applied after the deformation with a smooth, known deformation field. In contrast to what was expected, the FS technique outperformed the PPD approach when applied after coregistration, as can be seen in Fig. 4.7. Furthermore, this difference is statistically significant ($p < 0.001$). These results are obtained from the FA image coregistration of 10 data sets that were first deformed with a predefined deformation field. Equivalently, these findings were analogous to the other methods, in which other components were used for the coregistration. In Fig. 4.7(a) and (b), a part of the corpus callosum is displayed on an axial slice. Here, the white ellipsoids represent the ground-truth tensors of the reference image. The first eigenvector, as obtained after FS and PPD reorientation are superimposed in Fig.

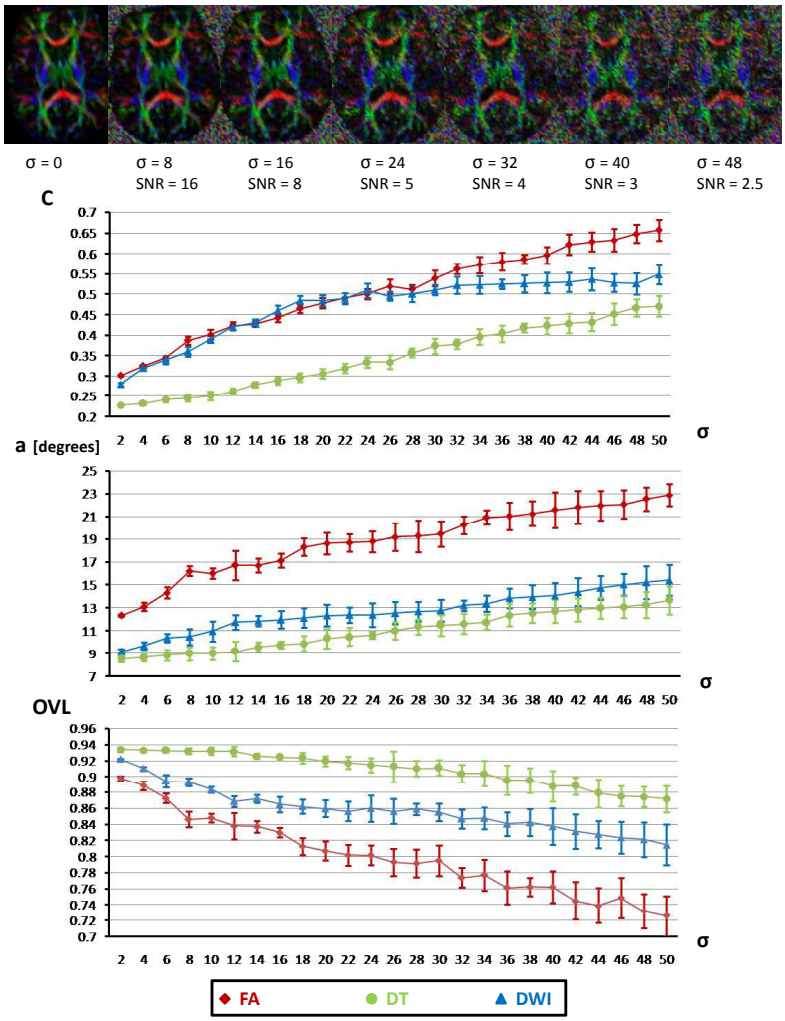

Figure 4.6. *Different levels of Rician noise, represented by σ are added to the DW images. A visual presentation of the noise DTI data is given at the top. The color is hereby encoded according to the predominant diffusion direction. At the bottom of the figure, the spatial and orientation correspondence are given using the FA map (method (II) of Fig. 4.5), the DT elements (method (III) of Fig. 4.5), and the DW images (method (V) of Fig. 4.5) as coregistration components. C, a, and OVL represent the deformation field correspondence, the first eigenvector angle difference, and the eigenvalue-eigenvector overlap, respectively.*

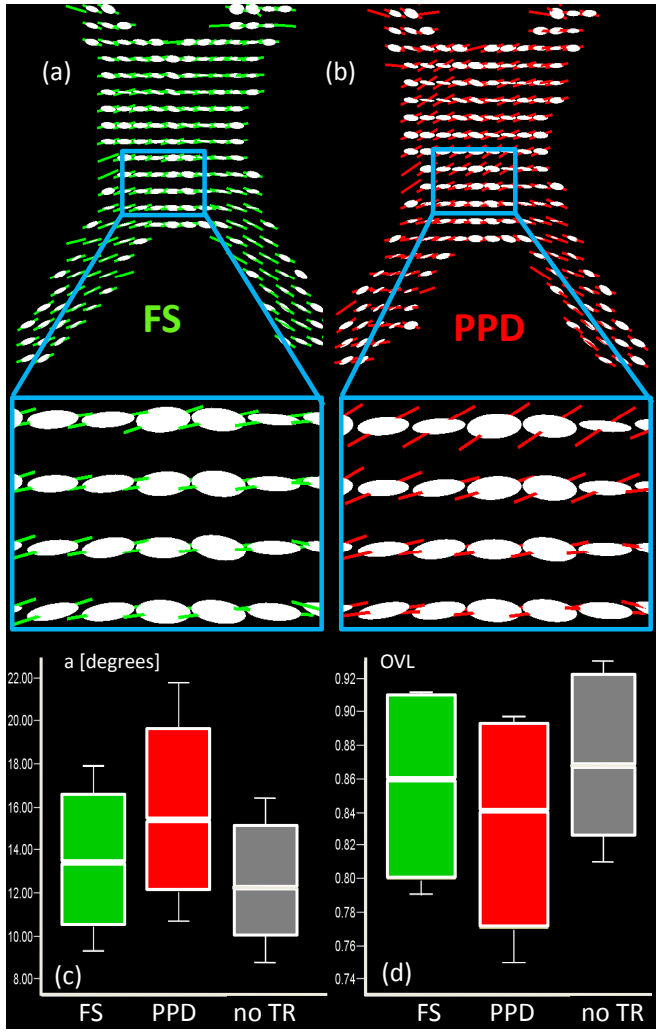

Figure 4.7. *In (a) and (b), a part of the corpus callosum as seen on an axial slice is shown. The white ellipsoids represent the ground-truth tensors of the reference image. The FS (in green) and PPD (in red) TR result after nonrigid coregistration are superimposed by means of the first eigenvector in (a) and (b), respectively. The first eigenvector correspondence with the ground-truth a and OVL of the the tensor reorientation approaches are presented in (c), and (d), respectively. These results originate from the coregistration of deformed data with a predefined deformation field, based on the FA maps, but are similar when other components are used. Note the higher tensor correspondence, when no tensor reorientation (in grey) is performed ((c) and (d)).*

4.7(a), and (b), respectively. In Fig. 4.7(c), and (d), the first eigenvector angle difference a and OVL are compared between both TR techniques.

Another remarkable result was observed when no TR was performed after coregistration. This method outperformed the FS and PPD tensor reorientation methodologies with respect to the tensor alignment, as described by a and OVL (see Fig. 4.7(c) and (d)). For the inter-subject coregistration, the following results were derived for the FS approach, PPD method, and without TR, respectively (for a random group of 15 persons, using the FA maps): $a = 26.3° \pm 1.2°$, $29.4° \pm 1.3°$, and $23.6° \pm 1.2°$; $OVL = 0.66 \pm 0.01$, 0.63 ± 0.02, and 0.68 ± 0.01. Similar results were found when other DTI information components were used for the coregistration.

Effect of the coregistration inaccuracies on the tensor reorientation

Although, in theory, the PPD method outperforms the FS approach (see paragraph 4.2.4.1), results turn out to be worse than the results of the FS approach when applied after the nonrigid viscous fluid deformation field (see Fig. 4.7). In addition, tensors are better aligned when no TR is applied. These unexpected results can be explained by the fact that, because there are less constraints on the local level of coregistration, small coregistration inaccuracies, which hardly affect the spatial alignment result, can occur, having a severe impact on the subsequent tensor reorientation. We hypothesize that these alignment errors contain more skewness and scaling than rotational components, thereby having a larger effect on the PPD than on the FS TR approach. The latter is verified by decomposing the Jacobian of the coregistration inaccuracies into a rotation component on the one hand, and a deformation component – containing scaling- and skewness factors – on the other hand.

The error Jacobian is constructed from the vector field difference between the theoretical and the obtained deformation field after coregistration. The rotation and the deformation component are calculated from the error Jacobian as follows:

$$R_e = (U_e U_e^T)^{-1/2} U_e \qquad S_e = U_e R_e^{-1}, \tag{4.31}$$

with R_e the rotation and S_e the deformation component, and $U_e = I + J_e$, where I is the identity matrix and J_e is the Jacobian, calculated on the error field [17, 43]. Note that U_e, R_e, and S_e are 3×3 matrices that are attributed to each voxel, describing the local transformation, rotation, and deformation, respectively. In order to study the presence of rotation and deformation components in the error Jacobian, the magnitude of U_e, R_e, and

S_e is calculated. This is done by taking the following Frobenius matrix norms $N_J \equiv \|U_e - I\|^2$, $N_R \equiv \|R_e - I\|^2$, and $N_S \equiv \|S_e - I\|^2$ for each WM voxel.

For the deformed data with known deformation fields, the aforementioned matrix norms averaged over all voxels within the WM mask, are $N_J = 0.55 \pm 0.05$, $N_R = 0.22 \pm 0.03$, and $N_S = 0.42 \pm 0.05$, for the transformation, rotation, and deformation respectively. These results indicate that the contribution of rotations is much smaller compared to the contribution of the skewness and scaling factors in the Jacobian of the alignment inaccuracies. Furthermore, they confirm the hypothesis that the PPD is more affected by local, small coregistration errors compared to the FS approach, resulting in a worse first eigenvector correspondence.

Deformation field regularization

In order to improve the TR, an isotropic Gaussian smoothing of the obtained deformation field is performed. This regularization is performed after the coregistration process and is only used to improve the accuracy of the Jacobian matrices of the global deformation. It will therefore not affect the spatial alignment of the images. The results after deformation field regularization are presented in Fig. 4.8 both for the deformed data with a known deformation field, and inter-subject data. It is clear that especially the PPD results are improved by this regularization. In Fig. 4.8(a), and (b), the quantitative results for the regularization procedure of the data deformed with a predefined deformation field are presented for both TR methods and different deformation field smoothing kernel widths, represented by s. In Fig. 4.8(d), and (e), the final vector field and the error field before smoothing are displayed. The same vector fields are presented in Fig. 4.8(h), and (i), after a Gaussian smoothing of the final deformation field with a kernel width of 3 voxels. In Fig. 4.8(f), and (g), a small part of the corpus callosum, similar to that in Fig. 4.7, is displayed. Here, the white ellipsoids represent the ground truth of the reference image and the first eigenvectors of the FS and PPD method after coregistration are superimposed in green and red, respectively. The large first eigenvector difference of the PPD approach with the ground-truth in Fig. 4.8(g) is decreased when the final deformation field is regularized, as can be seen in Fig. 4.8(k). In contrast to this, the FS result does not show a visual improvement in this restricted part of the corpus callosum after deformation field regularization (see Fig. 4.8(j)). A similar analysis is performed with 15 randomly chosen inter-subject data (Fig. 4.8(l), and (m)). These quantitative and visual results confirm the hypothesis that especially the skewness, and scaling factors will be regularized, thus particularly improving the PPD results. Above a specific kernel smoothing width,

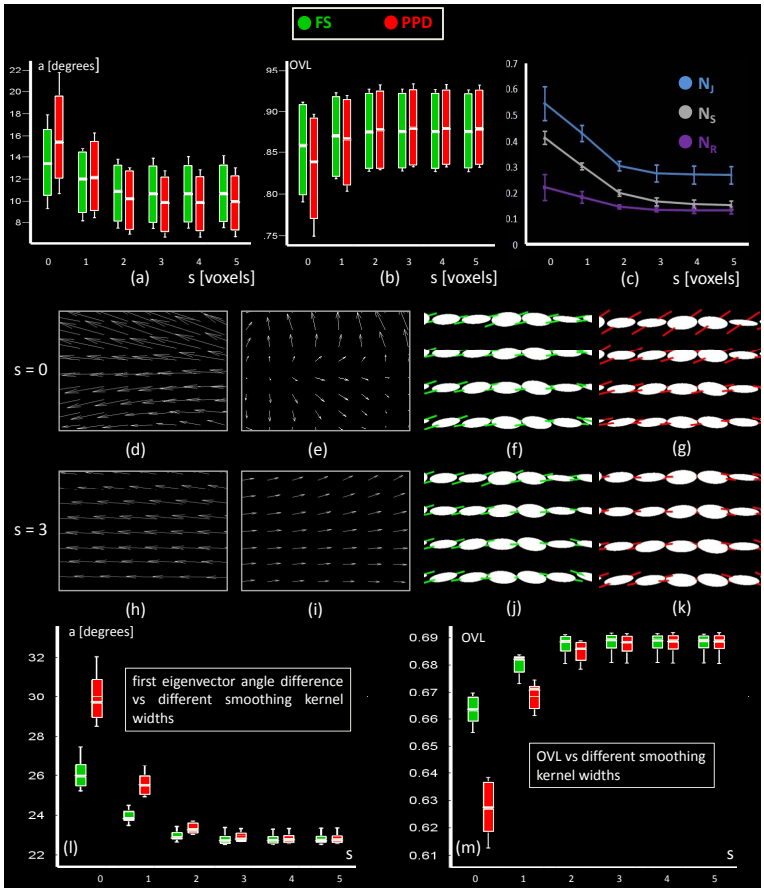

Figure 4.8. *The first eigenvector angle difference and OVL are given in (a) and (b), respectively, for both the FS and PPD method, using different Gaussian smoothing kernels for the deformation field regularization. In (c), the transformation N_J, rotation N_R, and deformation N_S of the error field are displayed for different smoothing kernel widths. The obtained deformation field before and after smoothing is given in (d) and (h), respectively. The error field before and after filtering is displayed in (e) and (i), respectively. The first eigenvector alignment for a part of the corpus callosum after FS and PPD TR are shown in (f) and (g) before smoothing, and in (j) and (k) after smoothing. The white ellipsoids represent the ground-truth orientations of the reference image. These results are obtained from data deformed with predefined deformation fields. The first eigenvector correspondence a and the tensor overlap with the ground-truth are given in (l) and (m), respectively, for the inter-subject results.*

the PPD method outperforms the FS approach. The Frobenius norms of the Jacobian, rotation, and deformation matrices of the error field further validate this hypothesis. As can be seen in Fig. 4.8(c), N_S is reduced up to the level of N_R during deformation field regularization with different kernel widths.

While initially the results without TR were better compared to the results after TR, the tensor reorientation methods outperform the approach without the TR when a deformation field regularization is applied (see Fig. 4.7(c) and (d), and Fig. 4.8(a) and (b) for the simulated data results). For the inter-subject coregistration without TR, a and OVL were 23.4° ± 1.1° and 0.680 ± 0.014, respectively. Results after final deformation field smoothing are better compared with these results (see Fig. 4.8(l) and (m)). Furthermore, the Wilcoxon matched-pairs signed-rank test demonstrates that the difference between results with TR and without TR are statistically significant for both the simulated and the inter-subject data ($p < 0.05$).

A similar deformation field regularization is performed on data sets containing different levels of Rician noise. It is clear that the FS method outperforms the PPD when no smoothing of the final deformation field is performed (Fig. 4.9(a), and (b)). For an arbitrary noise level of $\sigma = 6$, the effect of the proposed regularization method is shown in Fig. 4.9(c), and (d). If the kernel width is larger than 2 voxels, the PPD method outperforms the FS approach. In Fig. 4.9(e), and (f), the coregistration results as a function of different levels of Rician distributed noise are displayed, in which deformation field smoothing has been performed with a kernel width of 3 voxels.

4.2.4.1.3 Iterative tensor reorientation When the DTI alignment is based on images that contain orientation information, like the DT components or the DWIs, voxel intensities of various data sets can have different values in corresponding structures. Therefore, MI was used as an image similarity metric to take into account the potential non-linear inter-voxel intensity relationship. In this context, no TR was applied during the iterative optimization process, which results in a reduced computational time. In order to evaluate the ability of MI to compare the non-reoriented tensor data, the results are compared with a similar method in which the TR is applied iteratively. In Fig. 4.10, the first eigenvector angle difference a, the OVL, and the computation time are shown for the method without an iterative TR ((a) and (b)), a method with an iterative FS based TR ((c) and (d)), and a method using an iterative PPD based TR ((e) and (f)). Figs 4.10 (a), (c), and (e) represent the coregistration results of 10 deformed images with a predefined deformation field, whereas Figs. 4.10 (b), (d), and (f) show the results of the 10 inter-subject coregistrations. All results of Fig 4.10 are derived after DT based

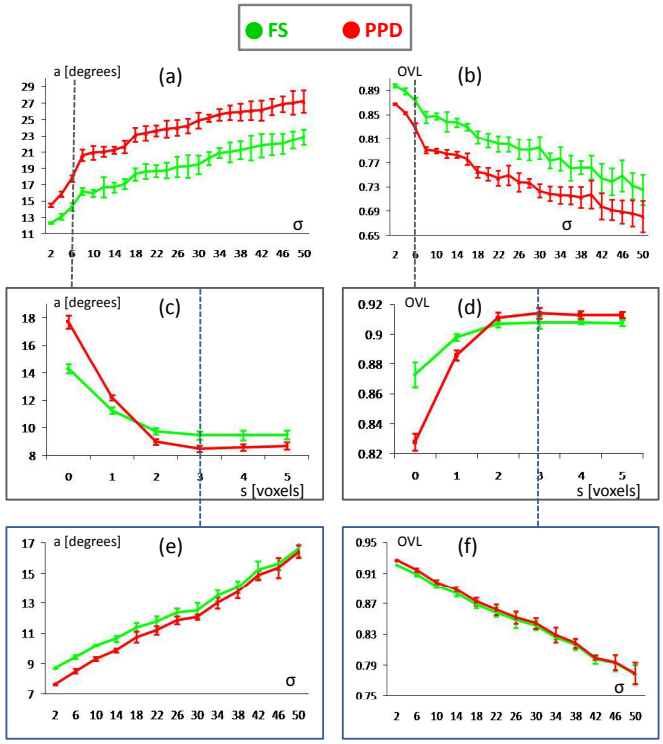

Figure 4.9. *Different levels of Rician noise, represented by σ are added to the DW images. The orientation correspondence after coregistration is calculated for both TR methods as a function of these different noise levels ((a) and (b)). At an arbitrary noise level of $\sigma = 6$, the effect of deformation field regularization is shown ((c) and (d)). In (e) and (f), the same noise study is performed, but now the deformation field, as obtained after coregistration, is smoothed with a kernel width of 3 voxels.*

coregistration, in which the MI and force field are calculated with 'MI method 1'. Furthermore, for all approaches, the FS method was used for the tensor reorientation on the final deformation field without applying a Gaussian smoothing on the final deformation field.

4.2.4.1.4 The use of different WM masks All previous results are obtained by only selecting FA mask voxels with an FA value above 0.4. In Fig. 4.11 (a), and (b), the first eigenvector angle difference a, and the OVL, respectively, are displayed as a function of the FA mask threshold. The blue line represents the results without a final deformation field regularization. The results derived after Gaussian smoothing of the final deformation field with a kernel width of 3 voxels are displayed in purple. In Fig. 4.11(c), a scatter plot of the FA value and the first eigenvector angle difference is shown. The scatter plot of the FA value and the

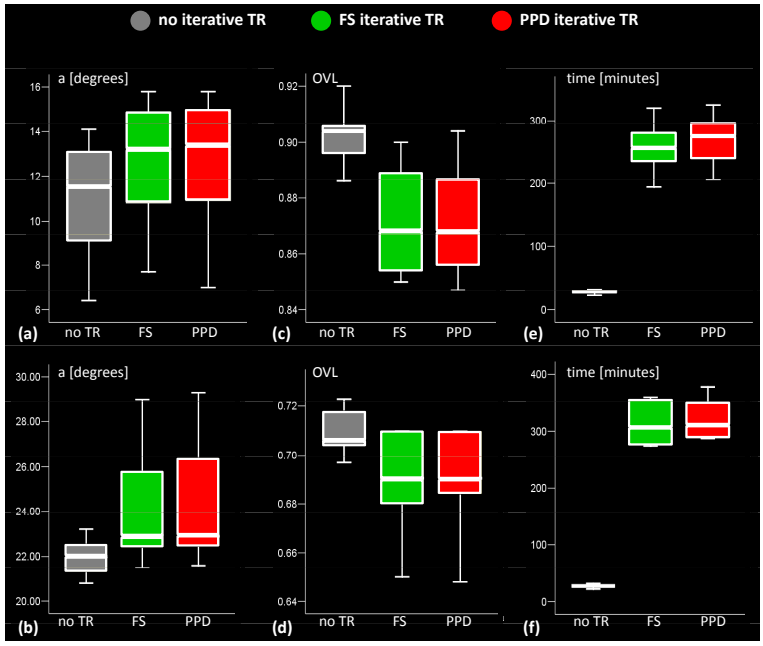

Figure 4.10. *The first eigenvector angle difference a ((a) and (b)), the OVL ((c) and (d)), and the computation time ((e) and (f)) are displayed for different iterative tensor reorientation approaches. Figures (a), (c), and (e) result from a coregistration of* 10 *deformed DTI data sets with a predefined deformation field, whereas figures (b), (d), and (f) result from an inter-subject coregistration of* 10 *DTI data sets.*

OVL is displayed in Fig. 4.11(d). The voxels used for this analysis were obtained from a specific region around the corpus callosum within the coregistered data set. Analogous scatter plots of the same data sets are displayed in Fig. 4.11 (e), and (f), in which a deformation field regularization is applied with a kernel width of 3 voxels.

4.2.5 Discussion

The aim of this chapter was to explore the feasibility of a nonrigid viscous fluid model for the alignment of inter-subject DTI data sets. First, we investigated the use of multiple DTI information components with respect to the coregistration accuracy. Second, different measures were introduced to calculate the MI and the viscous fluid force field. Finally, a thorough investigation of the diffusion tensor reorientation methods was performed.

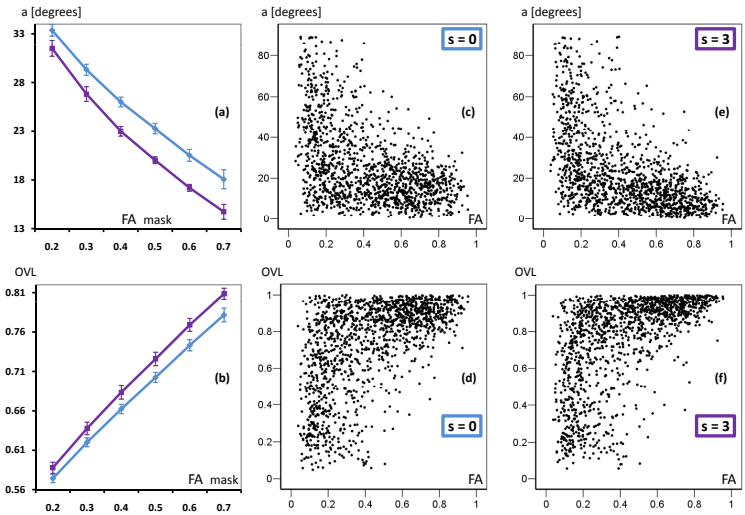

Figure 4.11. *In (a) and (b), the first eigenvector angle difference a, and OVL are displayed as a function of the threshold that defines the FA mask. To this end, a random subgroup of* 10 *data sets of different subjects are coregistered based on the FA maps. The FA mask refers to the minimum FA value in a voxel to be included in the quantitative analysis. In blue, the results without smoothing are shown, whereas the purple lines represent the results after a Gaussian smoothing of the deformation field with a kernel width of* 3 *voxels. In (c), (d), (e), and (f), scatter plots are displayed. They are obtained from an inter-subject coregistration of two DTI data sets. Scatter plots of the FA and a (c) and of the FA and OVL (d) are depicted, containing values of all voxels in a predefined region (a total of* 1400 *voxels). In (e) and (f), the same scatter plots are displayed, but now after the regularization of the deformation field with a kernel width of* 3 *voxels.*

4.2.5.1 TR evaluation using synthetic DTI data sets

The errors that are found between the reoriented and the ground-truth tensors in the synthetic DTI data analysis (see Fig. 4.2) are not affected by noise factors or coregistration inaccuracies, since the deformation fields are perfectly known and the sinusoidal fiber bundle matches the deformed straight bundle exactly. Alexander et al. (2001) demonstrated that PPD tensor reorientation after application of a known, affine deformation field to synthetic data, resulted in a mean angle difference of $0° \pm 0°$ when compared with the ground-truth data set [17]. In contrast with these results, we observed a small, but significant tensor difference. Therefore, even if two images are spatially aligned in a theoretically perfect way, tensor orientation errors will occur. These errors originate from the nonrigid nature of the deformation fields and the accompanying interpolation artifacts. Note that the use of Log-Euclidean metrics can further minimize these interpolation errors and potentially improve the image similarity [44].

4.2.5.2 Multi-component viscous fluid coregistration

Overall, the results of Fig. 4.3 and 4.4 indicate the potential of our proposed coregistration technique to coregister inter-subject DTI data. In these figures, it can clearly be observed that the alignment errors can be minimized using the viscous fluid coregistration method as compared to the affine DT image alignment. These coregistration results are confirmed by the quantitative analysis, as can be seen in Figs. 4.5 and 4.8. Both for the synthetic data and the multi-subject brain DTI data sets, the average angle between the first eigenvectors of the coregistered and the reference image is relatively small. In addition, the DT correspondence, as measured with the OVL, is relatively large, compared to the results of Park et al. (2003) [25]. It should be mentioned, however, since they used a WM mask derived from SPM on MR-images, in contrast to our FA value based WM mask, this comparison should be considered with great caution.

Although all available information is present in the DWIs, the DT elements demonstrated to provide the best result for inter-subject coregistration. In our opinion, this can be explained by the reduction in dimensionality through the fitting of a DT to the DW data. The DT data are more compact and still contain the orientational diffusion information. In addition, coregistration using the DT data is less sensitive to noise than using the DW data.

Two image similarity measures, based on MI, are proposed that represent a summary metric on the multivariate space. The general multivariate space is simplified to two multi-component data sets with the same length, whereby only corresponding components of different data sets are compared, assuming alignment of the components of each data set a priori. The first image similarity metric averages the MI of the different components, which is done in a similar way with the SSD measure as described in the work of Park et al. (2003) [25]. The second image similarity metric pools all data into a single histogram, whereafter the MI is calculated on this histogram. This methodology can be seen as the histogram and MI computation on two images that are composed of a concatenation of all components in each data set. Since MI is a statistical measure, it can be biased by a lack of data in the histogram. This bias of a sparse histogram is minimized by pooling all multi-component image information into this single histogram. Our results demonstrated that this methodology does not outperform the method of averaging the MI of all components. However, when only a small number of data is available for the histogram calculation, as in a window based coregistration of for example Ruiz-Alzola et al. (2002) the methodology using the pooled histogram would be favorable [24].

Since both proposed similarity metrics in the simplified multivariate space remain ad-hoc, more research is planned to improve the similarity metric based on MI for the multi-component DTI problem.

When noise was added to the DW images, image alignment worsened. Note that large noise levels were added, resulting in a small SNR. The DT based coregistration outperformed the DWI based alignment after the addition of Rician noise to the DWIs.

4.2.5.3 Tensor Reorientation after nonrigid coregistration

Alexander et al. (2001) studied the behavior of both TR methods under affine and nonrigid conditions [17, 18]. When three different DTI data sets of a same person were aligned affinely, both TR strategies showed almost identical results, since the transformation mainly contained rigid components [17]. The PPD method just outperformed the result without TR and the FS method, when two DTI data sets were aligned with a nonrigid elastic matching algorithm [18]. In contrast to this elastic model, the viscous fluid force field relaxes over time. Therefore, the viscous fluid model is a very appropriate regularization method that can correct for the large variations that occur during inter-subject coregistration.
Since there are less constraints on a local coregistration level, the Jacobian of the viscous fluid coregistration will be overestimated, resulting in relatively large deformation components. Several results in this paper indicate that small coregistration inaccuracies can result in relatively large tensor orientational differences. We hypothesized that the local coregistration errors will especially contain a deformation component, rather than a rotation factor, resulting in a worse PPD outcome compared to the FS tensor reorientation results. Note that, due to the high correspondence already existing after affine coregistration, the tensor correspondence was still very high when no tensor reorientation was performed after nonrigid alignment. These results appeared to be better than the FS and PPD tensor reorientation results.
In order to tackle this problem and to reduce the effect of local alignment errors on the TR result, a Gaussian regularization procedure was incorporated. As a result, the local alignment inaccuracies were diminished, and the tensor reorientation methods outperformed the approach without a reorientation. Furthermore, since especially the deformation component of the error field has been regularized, the PPD method outperformed the FS approach. In future work, anisotropic filtering methods will be applied to the final deformation field, to investigate the potential improvement of the TR results. Another approach, which will be subject of further research, is to make the TR approach dependent on the local Jacobian.

4.2.5.4 Iterative tensor reorientation

The results in Fig. 4.10 demonstrate that the use of MI without an iterative TR is an effective method. Indeed, similar coregistration methodologies, in which an iterative TR was applied, resulted in a worse tensor correspondence. These results

agree with the findings of Fig. 4.7, demonstrating that the tensor correspondence is higher when no TR is performed after coregistration. The tensor differences after FS or PPD reorientation are explained by the effect of small alignment errors on the local Jacobian. In this context, the application of an iterative TR increases the computation time drastically and decreases the tensor correspondence after coregistration.

4.2.6 Conclusion

In this chapter, we presented a multi-component viscous fluid model for the inter-subject coregistration of DT images. In the proposed coregistration technique, MI was implemented as an image similarity criterion. Our results demonstrated that the use of orientation information during the coregistration significantly improved the alignment results, compared to the FA based coregistration. A drawback of the local image alignment was that small coregistration inaccuracies can have a relatively large impact on the TR result. In an attempt to minimize these local reorientation errors, we provided a regularization method based on a Gaussian smoothing.

Bibliography

[1] B. Zitova, J. Flusser, Image registration methods: a survey, Image and Vision Computing 21 (2003) 977–1000.

[2] W. Crum, T. Hartkens, D. Hill, Non-rigid image registration: theory and practice, The British Journal of Radiology 77 (2004) S140–S153.

[3] L. G. Brown, A survey of image registration techniques, ACM Computing Surveys 24 (4) (1992) 325–376.

[4] J. Maintz, M. Viergever, A survey of medical image registration, Medical Image Analysis 2 (1998) 1–36.

[5] J. P. W. Pluim, J. Maintz, M. Viergever, Mutual-information-based registration of medical images: a survey, IEEE Transactions on Medical Imaging 22 (8) (2003) 986–1004.

[6] U. Bürgel, K. Amunts, L. Hoemke, H. Mohlberg, J. Gilsbach, K. Zilles, White matter fiber tracts of the human brain: three-dimensional mapping at microscopic resolution, topography and intersubject variability, NeuroImage 29 (4) (2006) 1092–1105.

[7] de Boor C., A practical guide to splines., Applied Mathematical Sciences Series,Springer-Verlag, 1978.

[8] D. Rueckert, L. I. Sonoda, C. Hayes, D. L. Hill, M. O. Leach, D. J. Hawkes, Nonrigid registration using free-form deformations: application to breast MR images., IEEE Trans Med Imaging 18 (8) (1999) 712–721.

[9] J. V. Hajnal, D. L. G. Hill, D. J. Hawkes, Medical image registration, Biomedical Engineering, CRC Press, Boca Raton, Florida, 2001.

[10] C. E. Shannon, A mathematical theory of communication, Bell System Technologies Journal 27 (1948) 379–423,623–656.

[11] F. Maes, A. Collignon, D. Vandermeulen, G. Marchal, P. Suetens, Multimodality image registration by maximization of mutual information, IEEE Transactions on Medical Imaging 16 (2) (1997) 187–198.

[12] A. Collingnon, F. Maes, D. Delaere, D. Vandermeulen, P. Suetens, G. Marchal, Automated multimodality medical image registration using information theory, Proc. 14th International Conference on Information Processing in Medical Imaging; Computational Imaging and Vision (1995) 263–274.

[13] W. Wells, P. Viola, H. Atsumi, S. Nakajima, R. Kikinis, Multi-modal volume registration by maximization of mutual information, Medical Image Analysis 1 (1) (1996) 35–51.

[14] D. Luenberger, Introduction to linear and nonlinear programming, Addison-Wesley, 1973.

[15] W. Press, B. Flannery, S. Teukolsky, W. Vetterling, Numerical recipes in C: the art of scientific computing, Cambridge University Press, New York, NY, USA, 1992.

[16] F. Maes, D. Vandermeulen, P. Suetens, Automatic construction of 3-D statistical deformation models of the brain using nonrigid registration., Medical Image Analysis 3 (4) (1999) 373–386.

[17] D. Alexander, C. Pierpaoli, P. Basser, J. Gee, Spatial Transformations of Diffusion Tensor Magnetic Resonance Images, IEEE Transactions on Medical Imaging 20 (11) (2001) 1131–1139.

[18] D. Alexander, J. Gee, R. Bajcsy, Strategies for data reorientation during non-rigid warps of diffusion tensor images, Medical Image Computing and Computer-Assisted Intervention (MICCAI) (1999) 463–472.

[19] A. Leemans, J. Sijbers, S. De Backer, E. Vandervliet, P. Parizel, Affine coregistration of diffusion tensor magnetic resonance images using mutual information, Lect Notes Comp Sci 3708 (2005) 523–530.

[20] D. Jones, L. Griffin, D. Alexander, M. Catani, M. Horsfield, R. Howard, S. Williams, Spatial

normalization and averaging of diffusion tensor MRI data sets, NeuroImage 17 (2) (2002) 592–617.

[21] D. Xu, S. Mori, D. Shen, P. van Zijl, C. Davatzikos, Spatial normalization of diffusion tensor fields, Magnetic Resonance in Medicine 50 (2003) 175–182.

[22] D. Alexander, J. Gee, R. Bajcsy, Elastic matching of diffusion tensor MRIs, in: Comp Vision and Patt Recog, 1999, pp. 1244–1249.

[23] J. Ruiz-Alzola, C. Westin, S. Warfield, A. Nabavi, R. Kikinis, Nonrigid registration of 3D scalar, vector and tensor medical data, Medical Image Computing and Computer-assisted Intervention 1935 (2000) 541–550.

[24] J. Ruiz-Alzola, C.-F. Westin, S. Warfield, C. Alberola, S. Maier, R. Kikinis, Nonrigid registration of 3D tensor medical data, Medical Image Analysis 6 (2002) 143–161.

[25] H.-J. Park, M. Kubicki, M. Shenton, A. Guimond, R. McCarley, S. Maier, R. Kikinis, F. Jolesz, C.-F. Westin, Spatial normalization of diffusion tensor MRI using multiple channels, NeuroImage 20 (4) (2003) 1995–2009.

[26] A. Guimond, C. Guttmann, S. Warfield, C.-F. Westin, Deformable registration of DT-MRI data based on transformation invariant tensor characteristics, Proceedings of the IEEE International Symposium on Biomedical Imaging (ISBI02), Washington, DC. USA. .

[27] J.-P. Thirion, Image matching as a diffusion process: an analogy with maxwell's demons, Medical Image Analysis 2 (3) (1998) 243–260.

[28] H. Zhang, P. Yushkevich, D. Alexander, J. Gee, Deformable registration of diffusion tensor MR images with explicit orientation optimization, Medical Image Analysis 10 (5) (2006) 764–785.

[29] G. Hermosillo, C. Chef d'Hotel, O. Faugeras, Variational methods for multimodal image matching, International Journal of Computer Vision 50 (3) (2002) 329–343.

[30] E. DAgostino, F. Maes, D. Vandermeulen, P. Suetens, A viscous fluid model for multimodal non-rigid image registration using mutual information, Medical image analysis 7 (4) (2003) 565–575.

[31] Y. Wang, L. Staib, Physical model-based non-rigid registration incorporating statistical shape information, Medical Image Analysis 4 (1) (2000) 7–20.

[32] G. Christensen, R. Rabbitt, M. Miller, Deformable templates using large deformation kinetics, IEEE Transactions on Image Processing 5 (10) (1996) 1435–1447.

[33] M. Bro-Nielsen, C. Gramkow, Fast fluid registration of medical images, in: R. Kikinis, K. Hoehne (Eds.), Visualization in Biomedical Computing (VBC'96), Vol. 1131 of Lecture Notes in Computer Science, Springer Verlag, Hamburg, Germany, 1996, pp. 267–276.

[34] V. Noblet, C. Heinrich, F. Heitz, J. Armspach, Retrospective evaluation of a topology preserving non-rigid registration method, Medical Image Analysis 10 (3) (2006) 366–384.

[35] A. Anderson, Theoretical analysis of the effects of noise on diffusion tensor imaging, Magn Reson Med 46 (6) (2001) 1174–1188.

[36] T. Han, Multiple Mutual Informations and Multiple Interactions in Frequency data, Information and Control 46 (1) (1980) 26–45.

[37] G. Rohde, S. Pajevic, C. Pierpaoli, P. Basser, A Comprehensive Approach for Multi-channel Image Registration, Lect Notes Comp Sci 2717 (2003) 214–223.

[38] D. Jones, The effect of gradient sampling schemes on measures derived from diffusion tensor MRI: a Monte Carlo study, Magnetic Resonance in Medicine 51 (2004) 807–815.

[39] A. Leemans, J. Sijbers, P. Parizel, A graphical toolbox for exploratory diffusion tensor imaging and fiber tractography, in: 14th Annual Meeting - Section for Magnetic Resonance Technologists, Miami, USA, 2005.

[40] A. Leemans, J. Sijbers, S. De Backer, E. Vandervliet, P. Parizel, Affine Coregistration of Diffusion Tensor Magnetic Resonance Images Using Mutual Information, Lecture Notes in

Computer Science (2005) 523–530.

[41] P. Basser, S. Pajevic, Statistical artifacts in diffusion tensor MRI (DT-MRI) caused by background noise, Magnetic Resonance in Medicine 44 (1) (2000) 41–50.

[42] A. Leemans, J. Sijbers, M. Verhoye, A. Van der Linden, D. Van Dyck, Mathematical framework for simulating diffusion tensor MR neural fiber bundles, Magn Reson Med 53 (4) (2005) 944–953.

[43] L. Malvern, Introduction to the Mechanics of a Continuous Medium, Prentice-Hall, Englewood Cliffs, NJ, 1969.

[44] V. Arsigny, P. Fillard, X. Pennec, N. Ayache, Log-Euclidean Metrics for Fast and Simple Calculus on Diffusion Tensors, Magnetic Resonance in Medicine 56 (2) (2006) 411–421.

Experience without theory is blind, but theory without experience is mere intellectual play.

– Immanuel Kant

5

On the construction of a population based diffusion tensor image atlas of the healthy human brain

Contents

Overview

As aforementioned, data sets of different subjects are aligned to an atlas or template, whereafter the image properties can be compared between the subjects in each voxel. The construction of an atlas thus allows the mapping of individual brain images to a common reference frame. In addition, the creation of atlases of different populations of subjects allows the comparison of typical anatomies for each group. In this chapter, a study specific DT atlas is constructed whereby the magnitude of the deformation fields that are needed to warp the different images to the atlas are minimized. This atlas is unbiased towards a single subject topology, since no single subject is selected as the initial reference data set. In addition, the directional diffusion information is reliably present in the DTI atlas model.Since it is very hard to objectively evaluate an atlas of a certain image group, a ground truth methodology is introduced to evaluate both the accuracy and precision of the spatial and orientational information in the atlas. In addition, inter-subject atlases are constructed based on the data sets of 20 healthy subjects to evaluate the different atlas frameworks in a realistic situation. Our results indicate that the atlas construction method affects the accuracy and the precision of the diffusion information in the final atlas.

The work in this chapter has been published in:
W. Van Hecke, J. Sijbers, E. Dagostino, F. Maes, S. De Backer, E. Vandervliet, P.M. Parizel and A. Leemans, *On the construction of an inter-subject diffusion tensor magnetic resonance atlas of the healthy human brain*, NeuroImage, (**2008**)

5.1 Introduction

Most VBA studies of diffusion tensor images utilize a standard reference image, such as the Montreal Neurological Institute (MNI) atlas, which was constructed from the affine transformation of 305 MR images of normal subjects to the stereotactic space defined by Talairach & Tournoux (1988). The advantage of a standard template such as the MNI atlas is that it contains coordinate, anatomic, and cytoarchitectonic labels and that the VBA results can be compared in a standard way across many studies that employed the this atlas. However, since this atlas is not study-specific, it might fail to provide a good representation of the given population, thereby potentially resulting in alignment errors after coregistration of the study group images to this reference space. Furthermore, since the MNI atlas is an MR atlas, many DTI based VBA studies utilize only the T_2 weighted image information of different subjects to drive the coregistration to the MNI space. This introduces WM alignment errors, because no DT information is considered during

the warping procedure [1]. In some studies, the deformation field which was acquired by the coregistration of anatomical MR images is subsequently applied to the FA maps to create an FA template, whereto all data sets are warped [2].

In other VBA studies, a single subject data set of the image group is selected as the reference or template image [3–5]. Although such an atlas is study-specific, it might fail to be a good representative of the whole subject group. Furthermore, the unique brain topology of this single subject can differ significantly from the brain topology of the other subjects in the image group, especially when patients with certain WM disorders are included in the analysis. Guimond et al. (2000) introduced an atlas construction methodology based on the coregistration of all subjects to a single subject data set which is selected as the initial reference image, followed by the averaging of all these coregistered images in the space of this initial reference image [6]. Finally, the resulting atlas is transformed with a deformation field that is equal to the average deformation of the initial reference image to all other images of the subject group. A previously reported disadvantage of this atlas construction method is that the resulting atlas can inherently contain unique features of the selected initial reference image, which results in a local topological bias [7].

During DTI atlas construction, Jones et al. (2002) incorporated FA maps for the affine coregistration of 10 subjects to a single subject image, which was previously transformed to the SPM T_2-weighted template [5]. Wakana et al. (2004) created a WM and tractography atlas based on a high-spatial-resolution DTI data set [8]. Dougherty et al. (2005) and Müller et al. (2007) used T_2-weighted and non-diffusion weighted images, respectively, for the image alignment during the atlas construction [9, 10]. Goodlett et al. (2006) applied the methodology of Joshi et al. (2004) to construct an atlas which was based on the alignment of scalar DT images [11, 12]. In their atlas method, the most representative template image is calculated as the data set that requires the minimum amount of transformation to each of the anatomical images. At each iteration, the updated template estimate is computed by the voxel-wise averaging of the deformed images. Ardekani et al. (2006) extended the atlas methodology that was developed by Guimond et al. (2000) to DT images, thereby using FA and MD images as information during the image alignment [6, 13]. Park et al. (2003) incorporated all DT information in their coregistration technique for the atlas construction, which was based on the methodology of Guimond et al. (2000) [1, 6]. Other coregistration methods incorporate tensor reorientation as part of the image alignment optimization [14–16]. Zhang et al. (2007) incorporated tensor information during the image alignment to construct an atlas based on the method of Joshi et al. (2004) [11, 17].

5.2 Methods

5.2.1 Data Acquisition

Diffusion tensor images of the brain were acquired with an 1.5 T MR scanner (Siemens, Erlangen, Germany) from 20 healthy subjects (8 males and 12 females), with a mean age of 25 $\pm$ 3 years (19 – 30 years). An informed consent was signed by all participants.
Axial diffusion tensor images were obtained using an SE-EPI sequence with the following acquisition parameters: TR: 10.4 s; TE: 100 ms; diffusion gradient: 40 $mT.m^{-1}$; FOV = 256×256 mm^2; number of slices = 60; voxel size = $2 \times 2 \times 2$ mm^3; b = 700 $s.mm^{-2}$; acquisition time: 12 min 18 s. Diffusion measurements were performed along 60 directions with 10 b_0-images for a robust estimation of FA, tensor orientation, and MD [18]. DTI post processing, tractography, and visualization were performed with the diffusion toolbox 'ExploreDTI' [19]. In this toolbox, the deterministic streamline fiber tracking approach is used for our purposes [20].

5.2.2 DTI coregistration

5.2.2.1 Global (affine) coregistration

In order to correct for global morphological differences, the DTI data sets were aligned to MNI space using an affine coregistration methodology. In this method, the FA images were used to estimate the affine transformation parameters, based on the maximization of mutual information [21]. For the remainder of the article, all images are considered to be aligned with an affine transformation to the MNI space, including a preservation of the PPD based tensor reorientation to realign the tensors with the underlying microstructure [22].

5.2.2.2 Local (non-rigid) coregistration

After affine coregistration, the different images of the subject group were aligned using a recently developed non-rigid DTI coregistration technique [23]. In this coregistration approach, the images are modeled as a viscous fluid, which imposes constraints on the local deformation field during normalization [24]. At each iteration, the determinant of the Jacobian is constrained to reduce the chance of forcing the underlying anatomical microstructure in an anatomically non-physical way. This viscous fluid model was optimized for the coregistration of multiple DTI information components [23].
As mentioned by several investigators, tensor reorientation inaccuracies might be introduced after a non-rigid, high-dimensional transformation [22, 23]. These orientational alignment inaccuracies are caused by local coregistration errors that

hardly affect the spatial alignment result, but on the other hand can have a severe impact on the accuracy of the subsequent tensor reorientation. In this context, it is important that the atlas construction framework minimizes this effect of the orientational alignment inaccuracies on the final atlas result.

5.2.3 DTI Atlas Construction

In the following sections, the multi-component DT images of the different subjects are denoted as I_i (with $i = 1, ..., N_S$, and N_S the number of subjects). The deformation field that warps image I_j to image I_i, is then defined as T_{ij}. The proposed atlas construction framework, referred to as the population based (PB) atlas method, will be compared to the atlas construction framework of Guimond et al. (2000) which is referred to as the subject based (SB) atlas method [6]. The latter method was utilized in the work of Ardekani et al. (2006) and Park et al. (2003) to construct a DTI atlas.

5.2.3.1 Subject based atlas method

The SB atlas methodology is based on the calculation of the non-rigid transformations T_{ij} of all data sets I_j to a specific data set I_i of the subject group, which was selected as the initial reference image. Thereafter, the mean deformation field of the initial reference image I_i to all other data sets I_j of the group (with $j = 1, ..., N_S$) is computed as:

$$T_i = \frac{1}{N_S - 1} \sum_j T_{ji}. \tag{5.1}$$

This is the transformation of the initial subject space to the average space of the population. Next, all images I_j of the subject group are transformed with one deformation field – constructed as the consecutive application of the deformation fields T_{ij} and T_i, noted as $T_i \circ T_{ij}$ – directly to the final atlas space. This concatenation of deformation fields includes an interpolation of the vector fields. However, by combining the two non-rigid transformations, only one image interpolation and tensor reorientation step is now included to construct the final atlas.

$$\tilde{I_j} = (T_i \circ T_{ij})(I_j) \qquad (j = 1, ..., N_S). \tag{5.2}$$

After transformation of the DWIs to the atlas space, a PPD based tensor reorientation is performed to realign the tensors with the underlying microstructure [22]. Subsequently, the DWIs are recalculated from these reoriented diffusion tensors, in order to obtain the correct diffusion signals in each voxel. Note that in this process the b-matrix is not rotated. Also note that log-Euclidean metrics are preferred when the interpolation is performed on the DTs [25]. Finally, the DWIs of the images $\tilde{I_j}$ are averaged to compose an SB atlas in the average space of population.

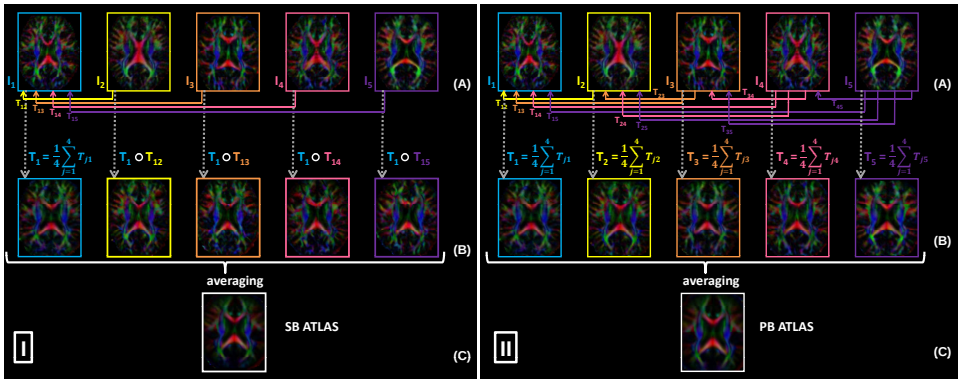

Figure 5.1. *A schematic overview of the subject and the population based atlas methodology is depicted for 5 DT images in I and II, respectively. In I(a) and II(a), the FA maps, color-encoded for the main diffusion direction, are shown after the affine deformation to the MNI space. In the subject based atlas framework, a single subject image is selected as the initial reference image (i.e., I_1 in this Figure). The deformation fields of all data sets to this reference image are calculated and denoted as T_{1j}, with $j = 2, ..., 5$. In addition, the mean inverse deformation field $T_1 = \frac{1}{4}\sum_{j\neq 1} T_{j1}$ of the reference image to all other images is computed, with N_S the number of subjects. Subsequently, as shown in (b), all images I_j are warped to the SB atlas space with a combined deformation field – containing the deformation field to the reference image, T_{1j}, and the mean deformation field of the reference image to the final atlas space, T_1. Finally the data sets in the SB atlas space are averaged to construct the SB atlas, as displayed in (c). In the population based atlas, non-rigid deformation fields are calculated between all images. Subsequently, for every image I_i, the mean deformation field T_i is calculated as the average transformation to all other images. This mean deformation field is applied to the corresponding data sets, including a tensor reorientation, resulting in the DT images of (b). The DW images of these data sets are averaged, resulting in the population based atlas, as represented in (c).*

Since the DWI intensities are corrected to represent the diffusion signal in the atlas space, and given the assumption that the coregistration performed well, averaging the DWIs within a single diffusion gradient direction across different subjects is allowed. Subsequently, the diffusion tensors of the atlas are estimated from these averaged DWIs. This atlas construction framework is elucidated in Fig. 5.1 (I).

5.2.3.2 Population based atlas method

In the PB atlas framework, non-rigid deformation fields T_{ij} need to be calculated between all images I_i and I_j (with $j = 1, ..., N_S$). Note that only $N_S(N_S - 1)/2$ non-rigid deformation fields are calculated, since the transformation of I_i to I_j can be computed as the inverse transformation of I_j to I_i. Subsequently, all N_S

images I_i are transformed to the average space of the population with a specific mean deformation field T_i that is calculated as the average deformation of this data set I_i to all other images (as in equation (1)). After trilinear interpolation of the DWIs, PPD based tensor reorientation, and recalculation of the DWIs, N_S images $\tilde{I}_i$ are constructed in a way that each of them require the least amount of deformation to all other images in the group. Finally, the DWIs of these data sets $\tilde{I}_i$ are averaged to compose the PB atlas [7, 26]. Notice that, in analogy of the SB atlas framework, only one tensor reorientation and one interpolation step are included in the PB atlas method, i.e. after the transformation of the N_S images I_i. The construction of the PB atlas is illustrated in Fig. 5.1 (II).

5.2.4 Atlas Evaluation Methodology

A general problem in the evaluation of an atlas is to find the optimal representation of a certain group of images. When SB and PB atlases are constructed from the same subject group, it is very difficult to interpret them visually and to compare them quantitatively. The synthetic data sets that are constructed in this work are based on a single subject DTI data set I, as elucidated in the following steps.

1. First, the DWIs of this single subject data set I are deformed with 10 predefined sinusoidal deformation fields T_i $(i = 1, ..., 10)$. All deformation fields differ from each other in amplitude, frequency, and direction. The maximal relative voxel displacement was 7 voxels.

2. The DTs are calculated from these deformed DWIs and reoriented using the PPD technique [22]. It has been demonstrated on a synthetic DTI data set that only a very small tensor reorientation error is made when these smooth, non-rigid deformation field are applied [23, 27]. Therefore, it can be assumed that the tensors of the deformed images are well aligned with their underlying microstructure.

3. The DWIs are recalculated from these reoriented DTs. In this way, 10 new DT images I_i are defined $(i = 1, ..., 10)$.

4. Next, 10 deformation fields are defined as the inverse of the first 10 transformations (T_j=T_{j-10}^{-1}, $j = 11, ..., 20$).

5. Analogously to step 2 and 3, 10 deformed DTI data sets I_j were constructed $(j = 11, ..., 20)$. As a result, the total vector sum over all deformation fields equals zero in each voxel: $\sum_{i=1}^{20} T_i$=0.

Consequently, an atlas that is constructed based on these 20 deformed data sets I_i $(i = 1, ..., 20)$, should closely resemble the original single subject image, since

the total vector sum of all deformation fields is zero in each voxel. In this way, the original single subject image is representative for the 20 deformed images. It will therefore be referred to as the ground truth or golden standard image. Notice that, in deforming the single subject DTI data set with sinusoidal deformation fields, the topology, or the architecture of WM connections, is not altered. The potential bias that exists in the SB atlas methodology by selecting a certain initial reference image with unique topological features will therefore not be present in this evaluation method. Furthermore, the quantitative diffusion properties – such as the FA – are the same in all simulated images. After this evaluation, atlases are constructed based on the DTI data sets of 20 different healthy subjects. The quantitative measures that are used for the evaluation of the atlases are expounded in the following section.

5.2.5 Quantitative Evaluation Measures

The atlas methodologies are compared using both a framework with simulated DTI data sets and actually measured human brain DTI data sets of different subjects. The quantitative measures which are calculated to evaluate the atlases are elucidated in the following paragraphs.

5.2.5.1 Deformation field difference C

When synthetic data sets are used to construct an atlas, the theoretical deformation fields S_i between the original data set I and the different data sets of the image group are known. Therefore, a value C is computed for each voxel to compare these predefined transformations S_i with the deformation fields that are obtained during coregistration to transform the simulated data sets to the final atlas space for the different atlas frameworks:

$$C = \frac{||S - T||}{||S|| + ||T||}. \tag{5.3}$$

Here, S represents the predefined deformation field and T the deformation field that is obtained to compute the DTI atlas. The latter equals the averaged deformation field T_j in the PB atlas framework and the combination of deformation fields T_{ij} and T_i in the SB atlas framework, when image I_i was the initial reference image. The median of values C across all voxels can then be interpreted as an overall measure of the transformation field correspondence. When this median is 0, the final deformation field exactly equals the theoretical deformation field, representing a perfect spatial alignment. On the other hand, when the median of all C's is 1, the final deformation field is the opposite of the theoretical deformation field, resulting in the worst alignment. This measure C is computed to compare all simulated deformation fields S_j with the corresponding deformation fields that are used during

the atlas construction, resulting in a quantitative measure of the deformation field correspondence for the different atlas frameworks.

5.2.5.2 Error in FA

The absolute value of the FA difference between an atlas and the golden standard data set is calculated and referred to as the FA accuracy of this atlas. In addition to measuring the FA accuracy of the atlases, the FA precision is calculated for each voxel as the standard deviation of the FA values across the images $\tilde{I}_i$ that are averaged to compose the atlases.
The FA accuracy and FA precision results of the SB and the PB atlas are compared statistically, using a Wilcoxon matched pairs signed rank test. In order to exclude voxels originating from deep GM and CSF in this statistical analysis, only voxels with an FA$>$ 0.25 are included in this analysis. Note that only the precision measures can be calculated to compare the atlases of the real subject group. The calculation of the FA accuracy and precision is elucidated in Fig. 5.2.

5.2.5.3 Error in overlap of eigenvalue-eigenvector pairs

In order to evaluate the orientational DT information of the atlases, the OVL between tensors D(λ, ϵ) and D'(λ', ϵ') is calculated [28]:

$$OVL = \frac{1}{N_V} \sum_V \frac{\sum_{i=1}^{3} \lambda_i \lambda_i' (\epsilon_i \cdot \epsilon_i')^2}{\sum_{i=1}^{3} \lambda_i \lambda_i'}, \tag{5.4}$$

with N_V the total number of selected WM voxels, and λ_i, λ_i', and ϵ_i, ϵ_i' eigenvalue-eigenvector pairs of a corresponding voxel. The minimum value 0 indicates no overlap and the maximum value 1 represents complete overlap of the DTs. In contrast to the FA accuracy and precision, orientational information is included in the OVL evaluation metric.
Analogously to the FA accuracy and precision, the OVL accuracy and OVL precision are defined. The OVL accuracy is calculated for each voxel as the OVL between an atlas and the ground truth image. In order to measure the precision of the orientational correspondence in each voxel, the OVL is calculated between the final atlas result on the one hand and all the deformed images $\tilde{I}_i$ that are averaged to compose this atlas on the other hand. Since they already represent a deviation from the atlas, these OVL measures are subsequently averaged for every voxel to compute the OVL precision for each atlas framework. The OVL accuracy and OVL precision results of the SB and the PB atlas are compared statistically, using a Wilcoxon matched pairs signed rank test. The computation of the OVL accuracy and the OVL precision is explained in Fig. 5.2.

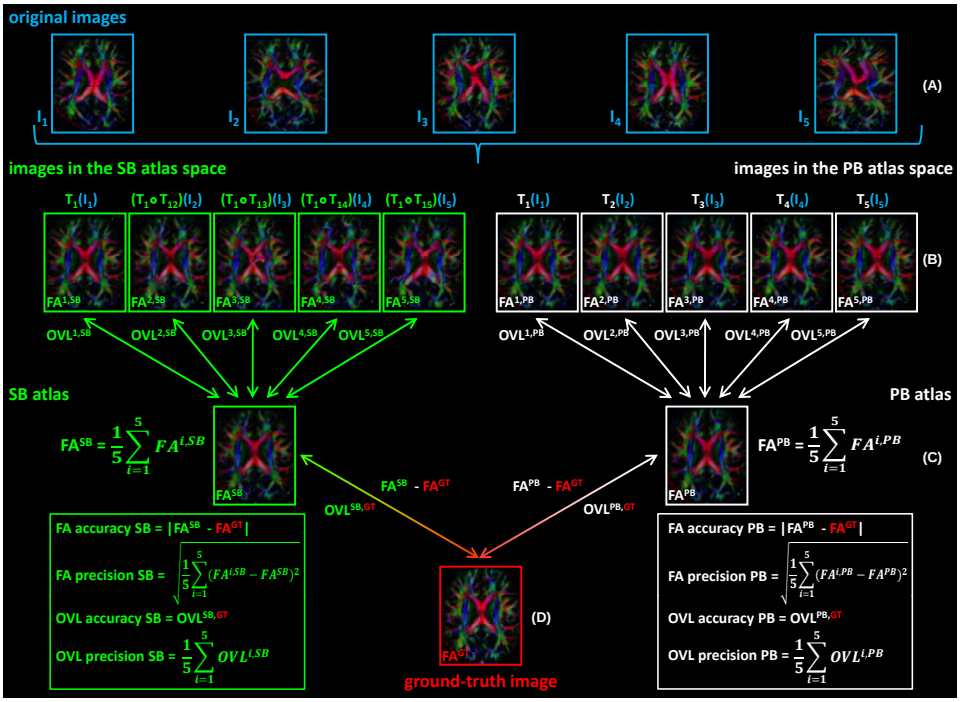

Figure 5.2. *In (a), the same axial slice of 5 different simulated data sets are displayed. These data sets are subsequently transformed to the SB and the PB atlas space with the appropriate deformation fields, as shown in (b), and averaged to construct the SB atlas and the PB atlas, as displayed in (c). The FA maps of the images in the SB and PB atlas space are denoted as $FA^{i,SB}$ and $FA^{i,PB}$, respectively ($i = 1, ..., 5$), and the FA maps of the SB and the PB atlas are denoted as FA^{SB} and FA^{PB}, respectively. An axial slice of the golden standard data set is displayed in (d), and its FA map is denoted as FA^{GT}. The FA accuracy is calculated for each voxel as the absolute value of the FA difference between an atlas and the ground truth image. The OVL accuracy is computed as the OVL between an atlas and the ground truth image for each voxel, and denoted as $OVL^{SB,GT}$ and $OVL^{PB,GT}$ for the respective atlases. The FA precision of the SB and PB atlases is calculated as the standard deviation of the FA maps of the images in their respective atlas space. Finally, the OVL is computed between all images in a specific atlas space and its resulting atlas. This is denoted as $OVL^{i,SB}$ and $OVL^{i,PB}$ for the SB and the PB atlas, respectively ($i = 1, ..., 5$). By averaging of $OVL^{i,SB}$ and $OVL^{i,PB}$ over the factor i, the OVL precision of the SB and the PB atlases is obtained.*

5.2.5.4 Fiber tract correspondence

Since DT inaccuracies – caused by small, local coregistration errors – are propagated along the fiber bundles, fiber tract correspondence can be used as a more sensitive marker to assess DT atlas correspondence. According to Ding et al. (2003), the similarity between a pair of fibers F_i and F_j can be defined as follows [29]:

$$S_{ij} = R_{cs} e^{-D_{ij}/C}. \tag{5.5}$$

D_{ij} is the mean Euclidean distance between corresponding segments of the two fiber tracts F_i and F_j [29]. R_{cs} represents the corresponding segment ratio, defined as the ratio of the length of the corresponding segment L_{cs} to the overall length of the pair of fibers [29]. Thereby, the corresponding segment L_{cs} is defined as the part of a fiber F_i (i.e. L_i) that has point-wise correspondence to the part of another fiber F_j (i.e. L_i).

$$R_{cs} = \frac{L_{cs}}{L_i + L_j - L_{cs}}. \tag{5.6}$$

When the corresponding segment ratio is 0, there is no tract overlap. In the case of a perfect overlap of the fiber tracts, the corresponding segment ratio is 1. The coefficient C in equation (5.5) regulates a trade-off between D and R_{cs}. In our work, C is chosen to be 1 voxel width, which is also the case in the article of Ding et al. (2003). Note that similar tract similarity measures have been proposed in other papers [30, 31]. In order to obtain a more objective interpretation of the results, an upper limit for the tract similarity measure is created. To this end, the simulated data sets are deformed with a deformation field that is exactly opposite to the theoretical deformation field that was used to compose these images. In this way, an atlas is constructed, using a perfect image alignment, but still including partial volume effects caused by interpolation.

5.3 Results

In Table 1, the deformation field difference C, the FA accuracy and precision, and the OVL accuracy and precision are presented for the SB and the PB atlas, which were constructed from the simulated data sets.

Table 1: The median and interquartile range (IQR) of different quantitative evaluation measures for different atlases as evaluated with the ground truth methodology.

	SB atlas		PB atlas	
	median	IQR	median	IQR
C	0.221	0.046	0.152	0.034
FA accuracy	0.094	0.089	0.067	0.061
FA precision	0.052	0.041	0.049	0.035
OVL accuracy	0.983	0.038	0.994	0.011
OVL precision	0.931	0.082	0.976	0.040

As can be observed, the deformation field difference is lower for the PB atlas construction framework compared to the SB method ($p < 10^{-6}$). The median and the interquartile range (IQR) of the FA accuracy, FA precision, OVL accuracy, and OVL precision are also displayed in Table 1. These results are also visualized in Figs. 5.3 and 5.4.

An axial, sagittal, and coronal FA slice of the ground truth image, the SB, and the PB atlas are depicted in Fig. 5.5 (a), (b), and (c), respectively. The image correspondence can be evaluated visually, by overlaying the red colored FA intensity map of the golden standard data set and the green colored FA intensity maps of the atlases. As can be observed in Fig. 5.5, the highest spatial correspondence with the ground truth image is obtained by the PB atlas.

In order to study the FA accuracy of the different atlases, the absolute value of the FA difference between the atlases and the golden standard data set is calculated for each voxel as explained in Fig. 5.2, and scaled between 0.1 and 0.2. The FA accuracy of the SB and the PB atlas are displayed in Fig. 5.3 (a) and (b), respectively. The highest FA accuracy or the lowest FA difference is detected for the PB atlas, as shown qualitatively by the histograms and boxplots in Fig. 5.3 (c) and (d), respectively. The Wilcoxon matched pairs signed rank test demonstrates that this FA accuracy difference is statistically significant ($p < 10^{-15}$). The FA precision results of the SB and the PB atlas are displayed in Fig. 5.3 (e) and (f), respectively. Analogously to the FA accuracy results, the PB atlas outperforms the SB atlas with respect to the FA precision. Histograms and boxplots confirm these findings (see Figs. 5.3 (g) and (h)), which are statistically significant ($p < 10^{-10}$).

In order to evaluate the preservation of the orientational information during the atlas construction, the OVL accuracy is measured at each voxel (see Fig.5.4). A higher OVL accuracy is observed for the PB atlas compared to the SB atlas (see Figs. 5.4 (a), (b), (c), and (d)). Analogously to the OVL accuracy results, the highest OVL precision is observed for the PB atlas, as illustrated in Figs. 5.4 (e), (f), (g), and (h). These differences in the OVL accuracy and precision are statistically significant ($p < 10^{-10}$).

In Fig. 5.6 (a), the cortico-spinal tracts of the golden standard image are visualized. The ROIs that are used to obtain these tracts are shown on an axial slice in Fig.

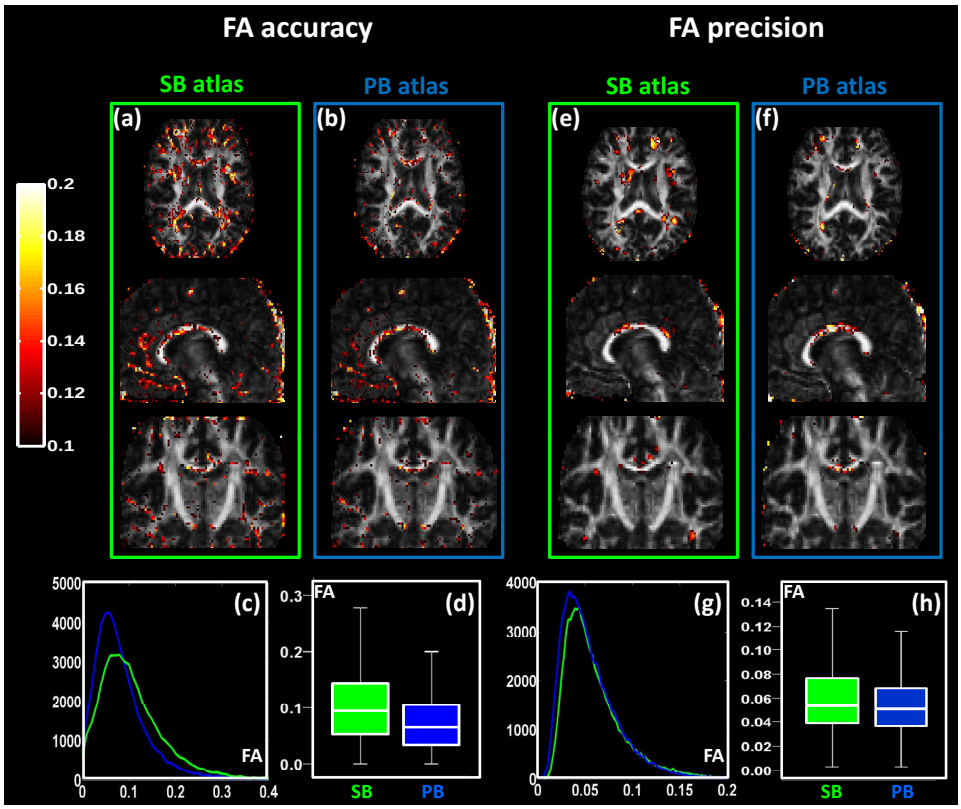

Figure 5.3. *The absolute value of the FA difference between the ground truth image and the atlases is given. This measure of FA accuracy (i.e., low values represent high accuracy) is visualized for the axial, sagittal, and coronal slice for the SB and the PB atlas in (a) and (b), respectively. In (c) and (d), the FA accuracy histograms and boxplots are displayed. The FA precision, calculated as the FA standard deviation of all images that compose the atlas (i.e., high precision is reflected by low values), is shown in (e) and (f) for the SB and the PB atlas, respectively. The histograms and boxplots of the FA precision are depicted in (g) and (h), whereby the SB and PB atlas results are colored in green and blue, respectively.*

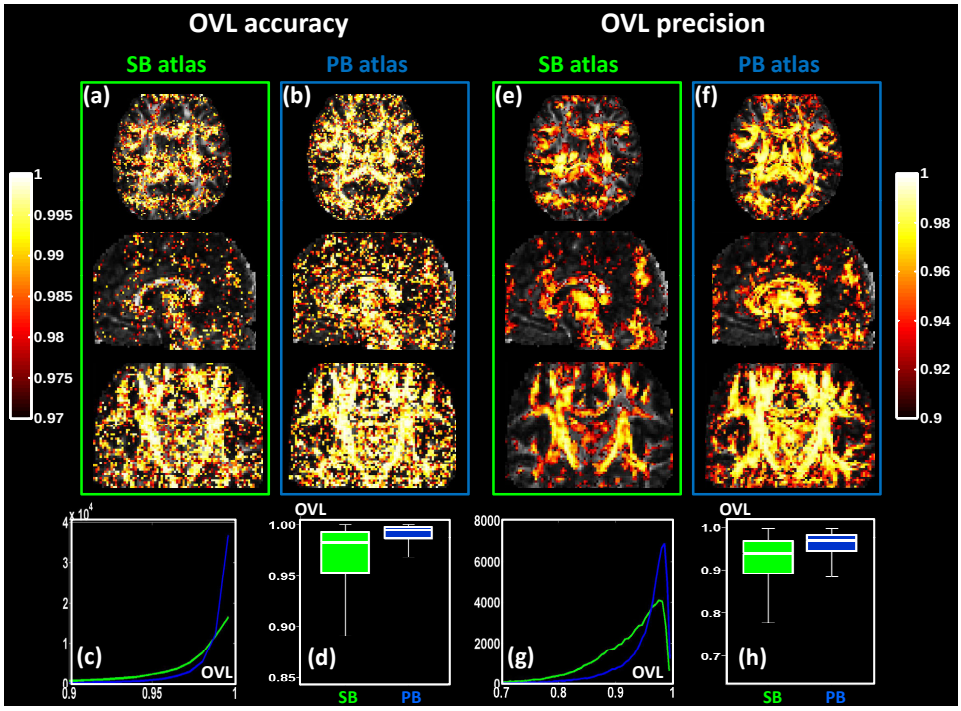

Figure 5.4. *The overlap of eigenvalue-eigenvector pairs between the DTs of the golden standard image and the DTs of the atlases (high values represent a high accuracy) is presented in each voxel for the SB and the PB atlas in (a) and (b), respectively. In (c) and (d), the OVL accuracy histograms and boxplots are visualized. The OVL precision is calculated as the mean OVL between all images that compose the atlas on the one hand and the atlas itself on the other hand (high values represent a high precision). In (e) and (f), the OVL precision of the SB and the PB atlas is depicted, respectively. The corresponding histograms and boxplots are shown in (g) and (h).*

5.6 (b). These ROIs are also utilized to define the fiber tractography seed points of the atlases (see Figs. 5.6 (b) and (c)). In Fig. 5.6 (b) and (c), the cortico-spinal tracts of the SB and the PB atlas are shown, respectively. An FA threshold of 0.25 and a maximal angle between consecutive points of 30° are used for fiber tracking [20]. In order to allow a better visual comparison of the fiber pathways, the green colored cortico-spinal tracts of the ground truth image and the red colored cortico-spinal tracts of the different atlases are overlaid. The tract similarity measure of Ding et al. (2003) is evaluated for several WM tracts to quantify the tract correspondence (Fig. 5.7). The corresponding segment ratio R and the mean Euclidean distance between corresponding segments D are presented in Fig. 5.7 (b) and (c), respectively. The quantitative tract correspondence measures confirm

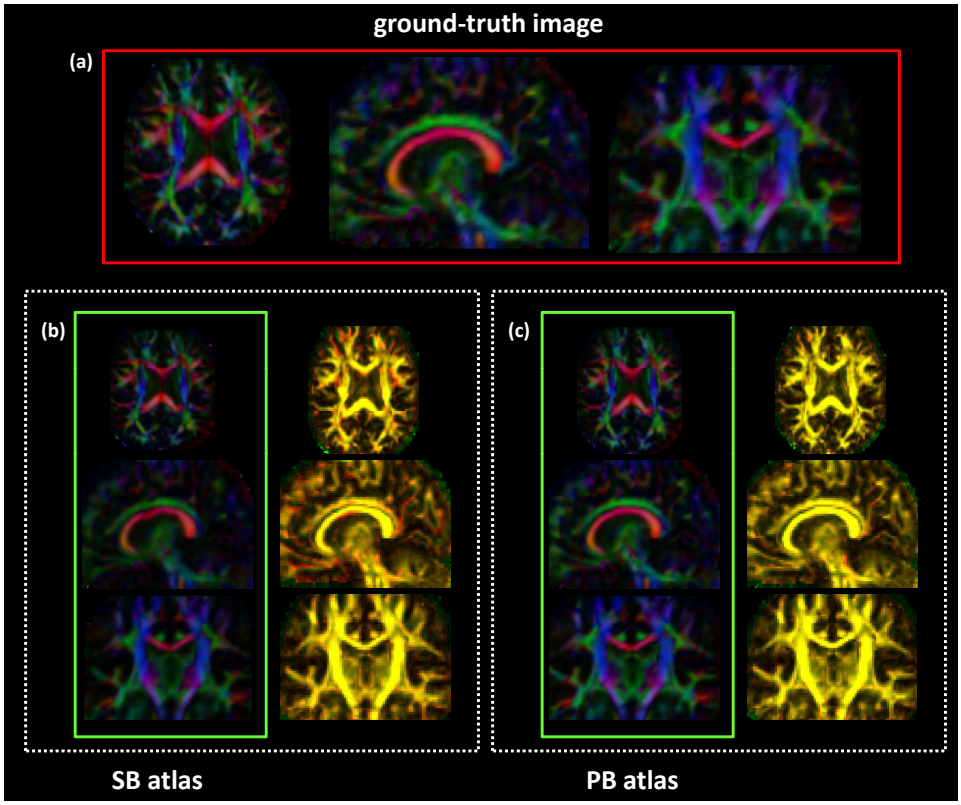

Figure 5.5. *In (a), an axial, sagittal, and coronal slice of the ground truth image are shown. The color is encoded for the diffusion direction and the image intensity is proportional to the diffusion anisotropy. The same axial, sagittal and coronal slice of the SB and the PB atlas, are visualized in (b) and (c), respectively. In order to evaluate the image correspondence visually, the FA intensity map of the golden standard image is given a red color, whereas the FA intensity map of the atlases are given a green color. Consequently, after overlaying these images, a yellow color appears in the corresponding voxels with similar FA values.*

the voxel based tensor correspondence results of Fig. 5.4 and the visual tract results of Fig. 5.6, demonstrating the highest tract accuracy for the PB tracts.
In Fig. 5.8, the inter-subject FA precision results of the SB and the PB atlas are superimposed on the axial, sagittal, and coronal FA slice of the PB atlas, as presented in (a) and (b), respectively. Fig. 5.8 (c) and (d) shows the corresponding histogram and boxplot. As can be seen in Fig. 5.8 (e), (f), (g), and (h), the OVL precision of the PB atlas is higher compared to the OVL precision of the SB atlas ($p < 10^{-10}$).
The tractography results of the corpus callosum are shown for 20 subjects in Fig. 5.9 (a). The callosal fiber tracts reconstructed from the SB and the PB atlas are visualized in Fig. 5.9 (b), (c), respectively.

5.4 Discussion

Recently, Jones et al. (2005, 2007) and Zhang et al. (2007) demonstrated the dependence of VBA results on the selection of the smoothing kernel, coregistration technique, and other choices in the in the pipeline of a VBA analysis. Furthermore, it has been shown in the research of cortical atrophy that the VBA results depend on the selection of the reference system [32, 33]. In order to enhance the reliability of a VBA analysis of DT images, a study specific DTI atlas should be constructed which can be regarded as a good representation of the subject group and which contains the relevant diffusion information in a reliable way. Although, the problem of atlas construction has been extensively studied and validated for scalar-valued images, similar studies for DT images are lacking [7, 11, 34–38].
In many VBA studies of DT images, an affine atlas is utilized as the reference image. However, since the data sets that are averaged to construct an affine atlas are only globally aligned, relevant, local diffusion information can be partially lost. In our work, the developed non-rigid atlases were also compared with an affine atlas (results not shown). As expected, the non-rigid atlases outperformed the affine atlas with respect to the accuracy and precision of the spatial and orientational diffusion information.
Many of the DTI atlases in VBA studies are based on the coregistration of T_2 weighted, non-diffusion weighted images, or FA maps. Consequently, the tensor information is not reliably present in the atlas, since it is not fully taken into account during the image alignment. As a result, this tensor information can not be used during the image alignment of different data sets to such an atlas in a VBA analysis.
In our work, the full DT was incorporated during the coregistration. However, similar atlases were also constructed using FA based image alignment (results not shown). We demonstrated using the simulated data sets that the accuracy and

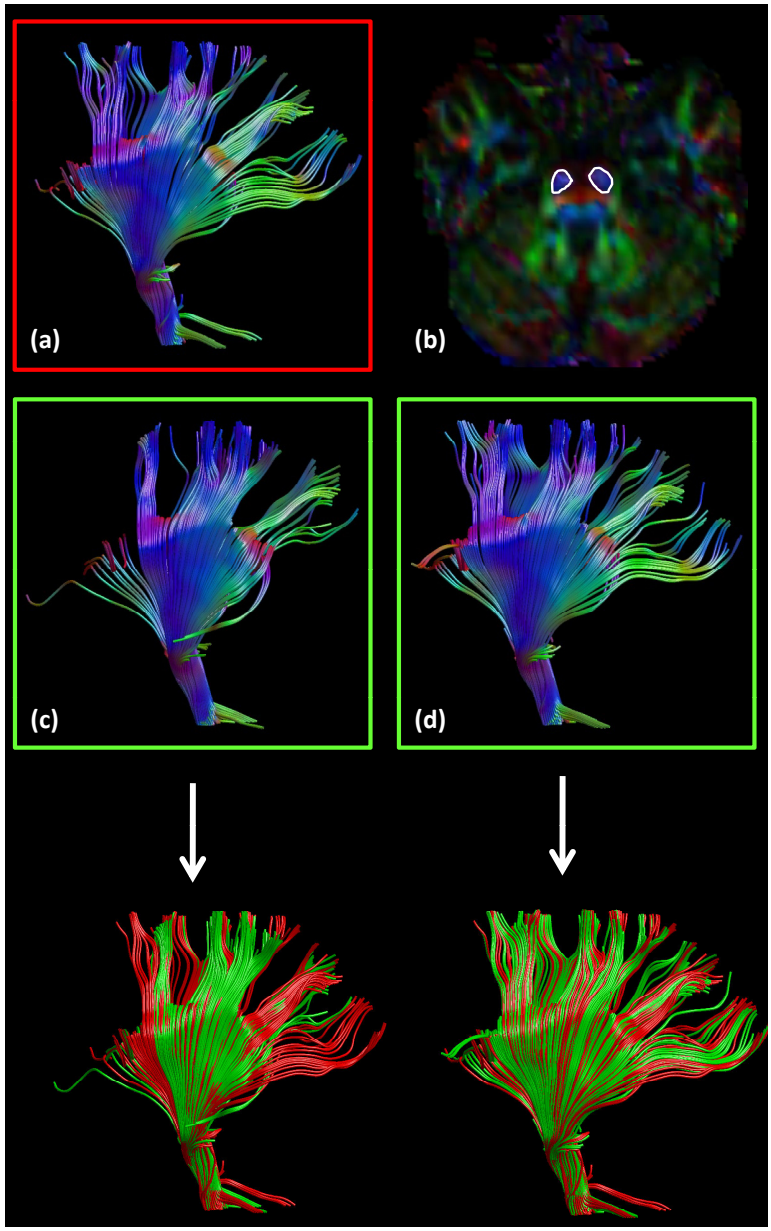

Figure 5.6. *The cortico-spinal tracts of the ground truth image are visualized in (a). An FA threshold of* 0.25 *and a maximal angle between consecutive points of* 30° *are used during the fiber tracking. The seed ROIs are defined on an axial slice, as depicted in (b). The same ROIs were used to define the seeding voxels for the tractography on the atlases. The cortico-spinal tracts of the SB and the PB atlas are shown in (c) and (d), respectively. For a better visual comparison of the tracts, the cortico-spinal tracts of the golden standard data set are given a red color, whereas the cortico-spinal tracts of the different atlases are given a green color.*

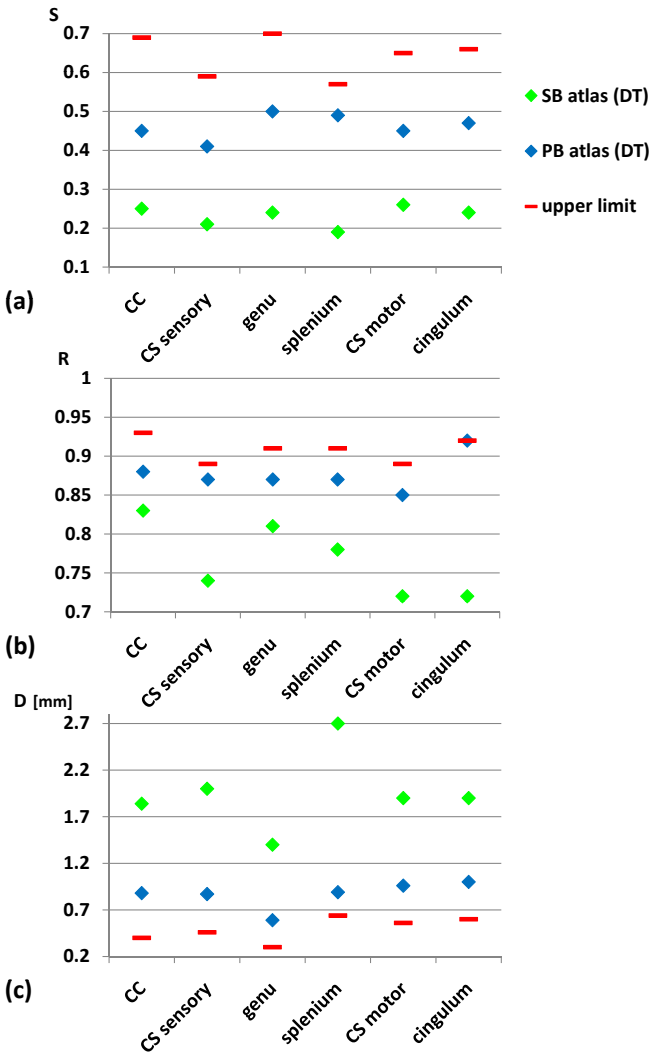

Figure 5.7. *The quantitative results of the tract correspondence are shown in (a), (b), and (c). In (a), a general tract similarity metric is shown for different WM pathways. A higher value of the tract similarity metric represents a better tract correspondence. The corresponding segment ratio R and the mean Euclidean distance between corresponding segments D are presented in (b) and (c), respectively. Note that an upper limit for the tract similarity measure is added. This upper limit is created by deforming the simulated images with a deformation field that is exactly opposite to the theoretical deformation field that was used to compose these images. The error bars were very small, cluttered the figure, and were therefore not added to the figure.*

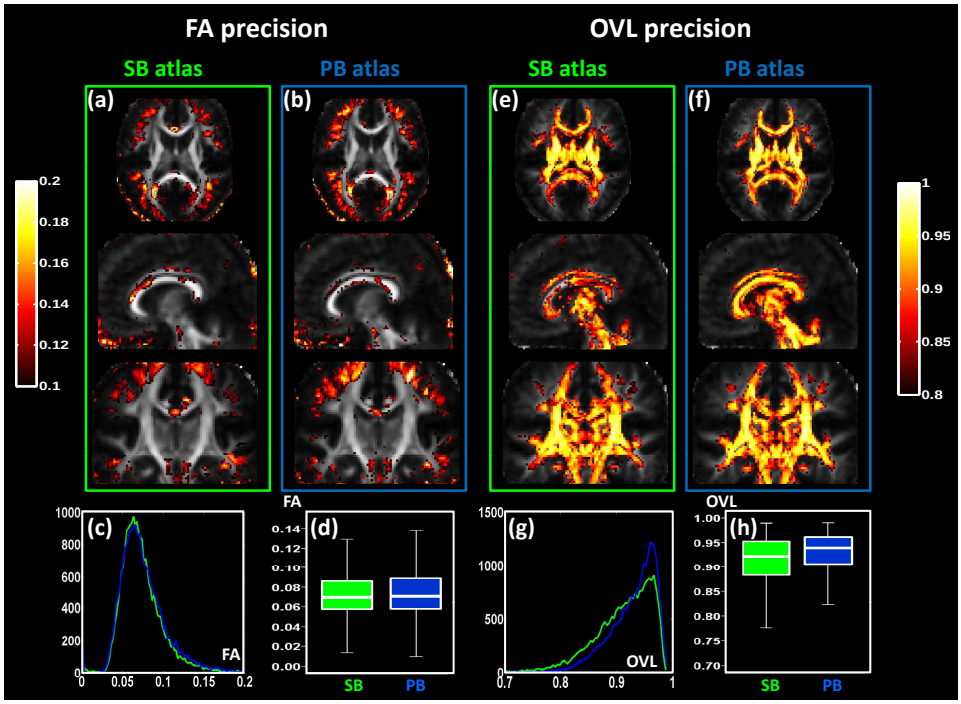

Figure 5.8. *The FA precision of the inter-subject SB and PB atlas are displayed in (a) and (b), respectively. The FA precision is superimposed on an axial, sagittal, and coronal slice of the PB atlas. In (c) and (d), the corresponding FA precision histograms and boxplots are depicted. The inter-subject OVL precision is visualized for the SB and the PB atlas in (e) and (f), respectively. In (f) and (g), the OVL precision histograms and boxplots are presented.*

precision of these atlases were significantly lower compared to the atlases that were constructed using the full DT during coregistration. As expected, the OVL accuracy and precision decreased when only FA information was used for coregistration. Many VBA studies of DT images incorporate structural T_2 weighted or non-diffusion weighted images to drive the image alignment during the atlas construction or the VBA analysis, thereby discarding valuable WM information, which is reflected by the diffusion tensor.

In almost all VBA studies of DT images, the standard MNI atlas is utilized as the reference system [39–41]. Since this is not a study-specific atlas, large deformation fields might be necessary to warp the data sets of the subject group to this atlas. Consequently, image alignment inaccuracies might be introduced, which can affect the accurateness of the VBA results. In other studies, the reference system is based on a detailed representation of a single subject's anatomy, as is the case in

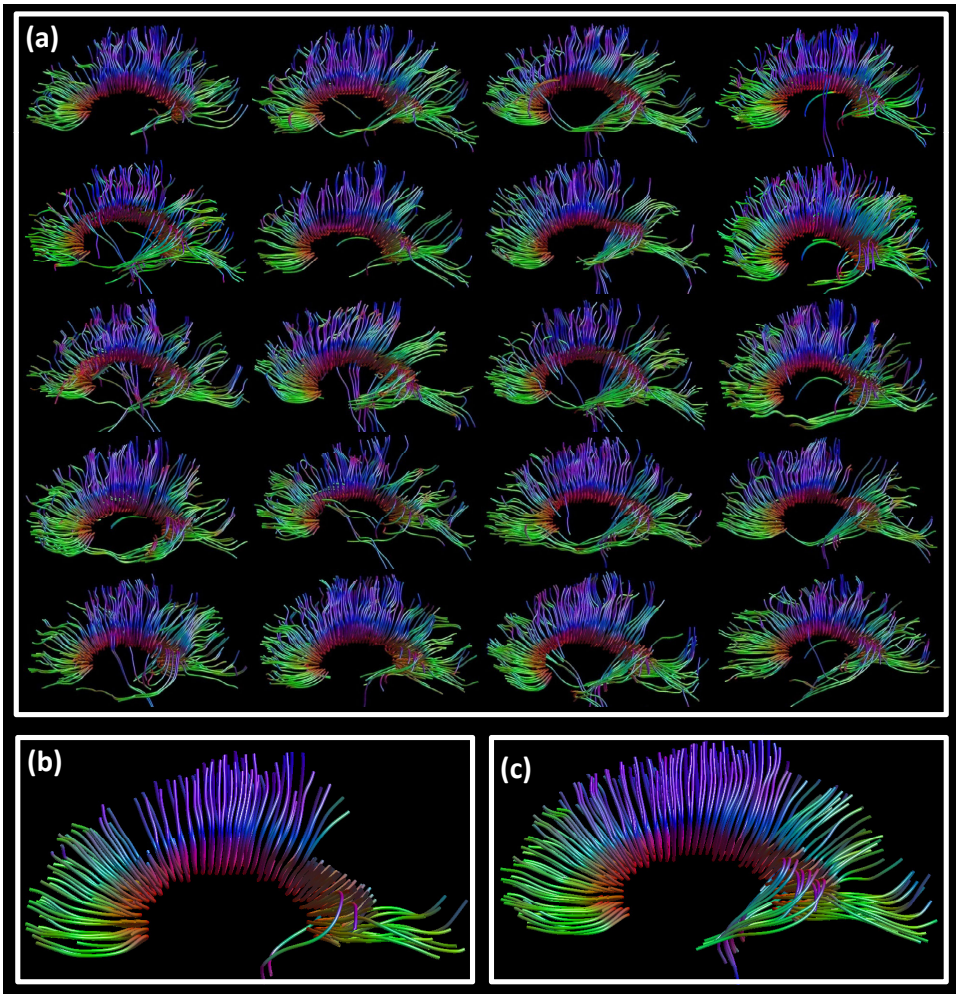

Figure 5.9. *In (a), the corpus callosum tracts of* 20 *different subjects are displayed. The corpus callosum tracts of the SB and the PB atlas, constructed from these* 20 *images, are shown in (b) and (c), respectively.*

the SB method [1, 5, 42]. The chosen data set then acts as a template to which the images of other subjects are coregistered. Subsequently, the transformed images of all subjects in the group are averaged, resulting in an new atlas. Thereafter, this atlas is transformed to a more representative atlas space, to minimize the magnitude of the deformation fields between the data sets of the subject group and the atlas. However, the choice of one image as a template unavoidably biases the atlas topology because of the substantial inter-subject variations in brain anatomy and WM morphology [7].

In this work, the optimal initial reference image for the SB approach was selected by evaluating the image correspondence – as calculated by the MI – between all data sets I_j of the image group and the golden standard data set. Obviously, this way of selecting the optimal initial reference image is not possible in an inter-subject setting, since no ground truth is available. One possible solution to this problem is to use an iterative approach for the SB atlas construction, whereby in the second iteration the atlas result of the first iteration is employed as the reference image, as suggested by Guimond et al. (2000) [6]. This strategy was also applied in this work, but did not lead to significant improvement of the final atlas. Another possibility to find the most typical subject for a given image group is to define the image that has a minimal mean distance to all other images – as calculated from the averaged deformation fields of each data set to all other data sets [4]. In this way, the amount of warping of all images of the subject group to the initial reference data set is minimized. In order to calculate this mean distance to all other image for every data set, all images have to be aligned to each other, making this approach as computational intensive as the PB atlas method. Since, in our study, all images were aligned to each other to construct the PB atlas, this strategy of finding the optimal initial reference image was applied in the SB atlas framework.

In contrast to the SB method, the PB framework is unbiased towards the brain topology of a single subject. However, the PB atlas construction method is computational intensive, since deformation fields are calculated between all subjects. On a Pentium(R) D CPU 3 GHz with 2 GB of RAM, and using a Matlab 7 platform (MathWorks, Natick, Mass), the computation time for the PB atlas for 20 data sets was approximately 12 hours. Computation time is approximately proportional with the square of the number of subjects.

Recently, group-based atlas frameworks, which consider all subjects in the population simultaneously, have been introduced to construct a population specific atlas. These methods might be advantageous in terms of finding the global optimum, since all data sets are iteratively optimized to minimize the discrepancies between these images. In the work by Studholme et al. (2004), a cost function is optimized with the aim of maximising the similarity between all images, while penalizing displacement of the reference space from the average shape [37]. Christensen et

al. (2006) present a method for synthesizing average $3D$ anatomical shapes using deformable templates based on averaging transformations [38]. Joshi et al. (2004) developed an algorithm for the simultaneous registration of subjects using large deformation diffeomorphisms [11]. Goodlett et al. (2006) applied this framework of Joshi et al. (2004) to scalar diffusion measures [12]. Lorenzen et al. (2006) also adapted the large deformation diffeomorphism framework for group based coregistration, but utilized a probabilistic segmentation of the images instead of the images intensities [36].

An important limitation in the evaluation of atlases and image coregistration is the lack of knowledge regarding the optimal representation of a given group of subjects. One approach of evaluating image correspondence is to define landmark points in different data sets. However, besides its labour-intensity, this method has a restricted reproducibility due to the intra- and inter-observer variability in the placement of the landmarks. In addition, it is hard to capture the complex $3D$ anatomical structures by the placement of landmarks on $2D$ slices. Moreover, this validation analysis is restricted to the anatomical structures that are delineated. Finally, this method can only provide information regarding the spatial accuracy of the image alignment, and not regarding the accuracy and validity of the orientational DT information in the atlas. Since recently developed coregistration techniques are incorporating multi-component DT information to obtain an optimal image alignment, it is important that this DT information is accurately represented in the atlas. In this context, the accuracy and precision of orientational DT information needs to be evaluated as well.

In order to tackle the limitations of the landmark based evaluation approach, a ground truth method was introduced, which allows one to evaluate the accuracy and precision of the spatial and orientational DT information in every brain voxel. Furthermore, since all data sets are constructed by deforming the same single subject image with different deformation fields, the unknown inter-subject variability of the diffusion properties can not introduce a bias in this evaluation method. A reduced accuracy and precision of the spatial and orientational diffusion properties in the atlases are therefore produced by spatial and orientational image alignment inaccuracies, interpolation artifacts, or the atlas construction framework, and not by variances in the topology and the diffusion measures across subjects. Consequently, the higher FA accuracy and precision that were observed in the PB atlas reflect the higher robustness of the PB atlas method against imperfect image alignment, compared to the SB approach (see Table 1). This better spatial image alignment in the PB method and the use of averaged deformation fields to transform the data sets in the PB atlas framework, result in a higher OVL accuracy and precision in the PB atlas compared to the SB atlas. These averaged deformation fields are less susceptible to tensor reorientation inaccuracies which are caused by small spatial image alignment imperfections [23]. In this context, the DTI coregistration

approaches of Cao et al. (2005,2006) and of Zhang et al. (2006), which incorporate the tensor reorientation as part of the image alignment optimization, might improve the orientational accuracy and precision of the DTI atlas.
In order to validate the different atlas frameworks for acquired brain DTI data sets, inter-subject atlases were constructed based on the data sets of 20 healthy subjects. Obviously, the presence of inter-subject variability of the WM topology and the diffusion properties complicate the evaluation of the inter-subject atlases. In Fig. 5.9, the callosal fiber tracts of the atlases were compared visually with the callosal pathways of the different subjects that compose the inter-subject image group. Qualitatively, the tract results of the PB atlas appear to provide the best expected averaged representation of the corpus callosum of these 20 subjects.

5.5 Conclusion

In summary, different strategies for constructing WM atlases from a set of DT images have been compared in this chapter. To the best of our knowledge, this work represents the first attempt at understanding the relative merits of two atlas construction strategies which were previously developed for scalar-valued images. The spatial and orientational diffusion information of these atlases were evaluated using both simulated and real DTI data sets. Our results indicate that the PB atlas provides the most robust representation for a group of subjects. We believe that the use of the proposed study specific, population based DT atlas with a reliable incorporation of all DT information, can reduce the image alignment inaccuracies and thus increase the reliability of the statistical tests in a VBA analysis.

Bibliography

[1] H.-J. Park, M. Kubicki, M. Shenton, A. Guimond, R. McCarley, S. Maier, R. Kikinis, F. Jolesz, C.-F. Westin, Spatial normalization of diffusion tensor MRI using multiple channels, NeuroImage 20 (4) (2003) 1995–2009.

[2] M. Kyriakopoulos, N. S. Vyas, G. J. Barker, X. A. Chitnis, S. Frangou, A diffusion tensor imaging study of white matter in early-onset schizophrenia., Biol Psychiatry 63 (5) (2007) 519–523.

[3] G. Douaud, S. Smith, M. Jenkinson, T. Behrens, H. Johansen-Berg, J. Vickers, S. James, N. Voets, K. Watkins, P. M. Matthews, A. James, Anatomically related grey and white matter abnormalities in adolescent-onset schizophrenia., Brain 130 (2007) 2375–2386.

[4] S. M. Smith, M. Jenkinson, H. Johansen-Berg, D. Rueckert, T. E. Nichols, C. E. Mackay, K. E. Watkins, O. Ciccarelli, M. Z. Cader, P. M. Matthews, T. E. Behrens, Tract-based spatial statistics: voxelwise analysis of multi-subject diffusion data., NeuroImage 4 (31) (2006) 1487–1505.

[5] D. Jones, S. Williams, D. Gasston, M. Horsfield, A. Simmons, R. Howard, Isotropic resolution diffusion tensor imaging with whole brain acquisition in a clinically acceptable time, Hum Brain Mapp 15 (2002) 216–230.

[6] A. Guimond, J. Meunier, J. P. Thirion, Average brain models: a convergence study, Comput Vision Imag Understand 77 (2000) 192–210.

[7] J.-J. Wang, R. Deichmann, I. Hsiao, H. Liu, Y. Wai, Y. Wan, R. Turner, R. Ordidge, Selective averaging for the diffusion tensor measurement, Magn Reson Imaging 23 (4) (2005) 585–590.

[8] S. Wakana, H. Jiang, L. Nagae-Poetscher, P. van Zijl, S. Mori, Fiber tract-based atlas of human white matter anatomy, Radiology 230 (1) (2004) 77–87.

[9] R. F. Dougherty, M. Ben-Shachar, G. Deutsch, P. Potanina, R. Bammer, B. A. Wandell, Occipital-Callosal Pathways in Children: Validation and Atlas Development, Ann N Y Acad Sci. 1064 (2005) 98–112.

[10] H. P. Muller, A. Unrath, A. C. Ludolph, J. Kassubek, Preservation of diffusion tensor properties during spatial normalization by use of tensor imaging and fibre tracking on a normal brain database., Phys Med Biol 52 (6) (2007) N99–N109.

[11] S. Joshi, B. Davis, M. Jomier, G. Gerig, Unbiased diffeomorphic atlas construction for computational anatomy., NeuroImage 23 (2004) S151–S160.

[12] C. Goodlett, B. Davis, R. Jean, J. Gilmore, G. Gerig, Improved Correspondence for DTI Population Studies via Unbiased Atlas Building, MICCAI (2006) 260–267.

[13] S. Ardekani, U. Sinha, Statistical representation of mean diffusivity and fractional anisotropy brain maps of normal subjects., J Magn Reson Imaging. 24 (6) (2006) 1243–1251.

[14] Y. Cao, M. I. Miller, R. L. Winslow, L. Younes, Large deformation diffeomorphic metric mapping of vector fields, IEEE Trans. Med. Imaging 24 (9) (2005) 1216–1230.

[15] Y. Cao, M. I. Miller, S. Mori, R. L. Winslow, L. Younes, Diffeomorphic matching of diffusion tensor images, Conference on Computer Vision and Pattern Recognition Workshop (2006) 67.

[16] H. Zhang, P. Yushkevich, D. Alexander, J. Gee, Deformable registration of diffusion tensor MR images with explicit orientation optimization, Medical Image Analysis 10 (5) (2006) 764–785.

[17] H. Zhang, B. B. Avants, P. A. Yushkevich, J. H. Woo, S. Wang, L. F. McCluskey, L. B. Elman, E. R. Melhem, J. C. Gee, High-dimensional spatial normalization of diffusion tensor images improves the detection of white matter differences: An example study using amyotrophic lateral sclerosis, IEEE Trans. Med. Imaging 26 (11) (2007) 1585–1597.

[18] D. Jones, The effect of gradient sampling schemes on measures derived from diffusion tensor

MRI: a Monte Carlo study, Magnetic Resonance in Medicine 51 (2004) 807–815.

[19] A. Leemans, J. Sijbers, P. Parizel, A graphical toolbox for exploratory diffusion tensor imaging and fiber tractography, in: 14th Annual Meeting - Section for Magnetic Resonance Technologists, Miami, USA, 2005.

[20] P. Basser, S. Pajevic, C. Pierpaoli, J. Duda, A. Aldroubi, In vivo fiber tractography using DT-MRI data, Magnetic Resonance in Medicine 44 (2000) 625–632.

[21] F. Maes, A. Collignon, D. Vandermeulen, G. Marchal, P. Suetens, Multimodality image registration by maximization of mutual information, IEEE Transactions on Medical Imaging 16 (2) (1997) 187–198.

[22] D. Alexander, C. Pierpaoli, P. Basser, J. Gee, Spatial Transformations of Diffusion Tensor Magnetic Resonance Images, IEEE Transactions on Medical Imaging 20 (11) (2001) 1131–1139.

[23] W. Van Hecke, A. Leemans, E. D'Agostino, S. De Backer, E. Vandervliet, P. M. Parizel, J. Sijbers, Nonrigid coregistration of diffusion tensor images using a viscous fluid model and mutual information, IEEE Trans Med Imaging. 26 (11) (2007) 1598–1612.

[24] E. DAgostino, F. Maes, D. Vandermeulen, P. Suetens, A viscous fluid model for multimodal non-rigid image registration using mutual information, Medical image analysis 7 (4) (2003) 565–575.

[25] V. Arsigny, P. Fillard, X. Pennec, N. Ayache, Log-Euclidean Metrics for Fast and Simple Calculus on Diffusion Tensors, Magnetic Resonance in Medicine 56 (2) (2006) 411–421.

[26] D. Seghers, E. D'Agostino, F. Maes, D. Vandermeulen, P. Suetens, Construction of a Brain Template from MR Images Using State-of-the-Art Registration and Segmentation Techniques, LNCS 3216 (2004) 696–703.

[27] A. Leemans, J. Sijbers, M. Verhoye, A. Van der Linden, D. Van Dyck, Mathematical framework for simulating diffusion tensor MR neural fiber bundles, Magn Reson Med 53 (4) (2005) 944–953.

[28] P. Basser, S. Pajevic, Statistical artifacts in diffusion tensor MRI (DT-MRI) caused by background noise, Magnetic Resonance in Medicine 44 (1) (2000) 41–50.

[29] Z. Ding, J. Gore, W. Anderson, Classification and quantification of neuronal fiber pathways using diffusion tensor mri, Magnetic Resonance in Medicine 49 (2003) 716–721.

[30] I. Corouge, S. Gouttard, G. Gerig, Towards a shape model of white matter fiber bundles using diffusion tensor MRI, in: ISBI, 2004, pp. 344–347.

[31] L. J. O'Donnell, C.-F. Westin, Automatic tractography segmentation using a high-dimensional white matter atlas., IEEE Trans Med Imaging 26 (11) (2007) 1562–75.

[32] S. Shen, A. J. Szameitat, A. Sterr, A template effect study on voxel-based morphometry in statistic parametric mapping, Conf Proc IEEE Eng Med Biol Soc 3 (2005) 3051–3054.

[33] S. Shen, A. J. Szameitat, A. Sterr, Vbm lesion detection depends on the normalization template: a study using simulated atrophy., Magn Reson Imaging 25 (10) (2007) 1385–1396.

[34] P. Kochunov, J. L. Lancaster, P. Thompson, R. Woods, J. Mazziotta, J. Hardies, P. Fox, Regional spatial normalization: toward an optimal target., J Comput Assist Tomogr 25 (5) (2001) 805–816.

[35] T. Rohlfing, R. Brandt, R. Menzel, C. R. Maurer, Evaluation of atlas selection strategies for atlas-based image segmentation with application to confocal microscopy images of bee brains., Neuroimage 21 (4) (2004) 1428–1442.

[36] P. Lorenzen, M. Prastawa, B. Davis, G. Gerig, E. Bullitt, S. Joshi, Multi-modal image set registration and atlas formation, Med Image Anal. 10 (3) (2006) 440–451.

[37] C. Studholme, V. Cardenas, A template free approach to volumetric spatial normalisation of brain anatomy, Pattern Recognition Letters 25 (10) (2004) 1191–1202.

[38] G. E. Christensen, H. J. Johnson, M. W. Vannier, Synthesizing average 3D anatomical

shapes, NeuroImage 32 (2006) 146–158.

[39] L. Snook, C. Plewes, C. Beaulieu, Voxel based versus region of interest analysis in diffusion tensor imaging of neurodevelopment., NeuroImage 34 (1) (2007) 243–252.

[40] J. H. Seok, H. J. Park, J. W. Chun, S. K. Lee, H. S. Cho, J. S. Kwon, J. J. Kim, White matter abnormalities associated with auditory hallucinations in schizophrenia: A combined study of voxel-based analyses of diffusion tensor imaging and structural magnetic resonance imaging., Psychiatry Res. 156 (2) (2007) 93–104.

[41] B. Borroni, S. M. Brambati, C. Agosti, S. Gipponi, G. Bellelli, R. Gasparotti, V. Garibotto, M. Di Luca, P. Scifo, D. Perani, A. Padovani, Evidence of white matter changes on diffusion tensor imaging in frontotemporal dementia., Arch Neurol. 64 (2) (2007) 246–251.

[42] H.-J. Park, C.-F. Westin, M. Kubicki, S. Maier, M. Niznikiewicz, A. Baer, M. Frumin, R. Kikinis, F. Jolesz, R. McCarley, M. Shenton, White matter hemisphere asymmetries in healthy subjects and in schizophrenia: a diffusion tensor MRI study, NeuroImage 23 (1) (2004) 213–223.

The origin and the causes of disease are far too recondite for the human mind to unravel them.

– Giorgio Baglivi (1669 – 1707)

The mind has great influence over the body, and maladies often have their origin there.

– Molière (1622 – 1673)

6

A voxel based analysis of diffusion tensor images

Contents

Overview

A voxel based analysis of DTI data sets is an automated method to perform DTI group studies. However, it has been recently demonstrated that the VBA approach is less standardized than it promised to be, due to the effect of different parameter settings in the algorithm on the final results. In the first section of this paragraph, simulated DTI data sets are developed, which allows for modeling of anomalies in the diffusion properties of a predefined location and in a predefined number of voxels. These simulated DTI data sets can be used to investigate the reliability, accuracy, and precision of different post-processing methods. In addition, the effect of the different parameters and post processing steps that are involved in the pipeline of a VBA analysis can be examined, which could lead to a more reliable, standardized, and consistent post-processing of DT images for studying different pathologies. In the second section of this chapter, these simulated data sets are used to evaluate the effect of image smoothing on the VBA results is examined. To this end, the data sets are filtered with various isotropic, Gaussian smoothing kernels with different widths. In addition, an advanced anisotropic smoothing kernel is introduced and compared to the isotropic kernel. In the final section of this chapter, a state-of-the-art VBA approach – including an optimized coregistration algorithm, population specific atlas, anisotropic smoothing – is used to examine the diffusion properties in patients with MS. In particular, the relation between cognitive dysfunction and white matter damage is investigated.

The work in this chapter has been published in:

6.1 On the construction of a ground truth framework for evaluating voxel-based diffusion tensor MRI analysis methods

There is a foolish corner in the brain of the wisest man.
– Aristotle (384 – 322 BC)

6.1.1 Introduction

In order to compare diffusion properties across subjects quantitatively, many studies perform a ROI analysis, in which these ROIs are marked on locations that have been associated with abnormalities for a given pathology [1–9]. Although this approach is straightforward and has gained its merits in earlier studies, several

drawbacks prevent it from being the analysis tool of choice for large scale, standardized DTI studies. These drawbacks include the labor intensity of the method, a restricted reproducibility due to the observer dependent ROI placement, difficulties to outline the complex 3D WM architecture by 2D ROIs, and the dependence of the results on the a priori hypothesis that is made regarding the spatial location and extent of the differences. Combined with the subject group and disease heterogeneity, including confounding factors such as age, sex, handedness, disease state, etc., these aforementioned limitations can explain the inconsistency of the published diffusion values that were derived by the ROI analysis, as for example in the study of patients with MS [10–17].

To mitigate the limitations of the ROI approach, an automated VBA is increasingly being used to study DT alterations for many diseases. In VBA, all data sets are spatially normalized to a certain template, whereafter a voxel-by-voxel statistical comparison between the control subjects and the patients is performed [18]. In this way, the whole brain is tested for control-patient differences without any a priori hypothesis of the expected spatial location of the abnormalities to be made. Furthermore, although the VBA approach is computationally more intensive, it is far less laborious compared to the ROI method. In addition, the user-dependency of the ROI approach is replaced by a parameter-dependency in VBA, making the subsequent quantitative analysis more reproducible and standardized. However, for example in the published DTI studies of patients with schizofrenia, there is no general correspondence between the findings [19–32]. Significant FA differences between healthy subjects and schizophrenia patients were reported in a large range of white matter structures, such as for example the cerebellar peduncle [29, 31], cortico-spinal tracts with schizofrenia [28], internal capsule with schizofrenia [24, 26], genu of the corpus callosum with schizofrenia [21, 28], splenium of the corpus callosum with schizofrenia [21, 28, 31], forceps major with schizofrenia [19, 31], body of the corpus callosum with schizofrenia [28], superior longitudinal fasciculus with schizofrenia [24, 26, 29, 31], and cingulum [24, 29]. The subject group and disease heterogeneity across the different studies, including confounding factors such as age, sex, handedness, disease state, etc., can partially explain these observed discrepancies. However, methodological differences in implementation of VBA are possibly even more decisive for explaining the variances in the VBA results of different studies.

Jones et al. (2005, 2007) and Zhang et al. (2007) demonstrated that different VBA results were obtained when different coregistration techniques, smoothing kernels, statistics, etc. were implemented during the VBA analysis of the same subject group. Since the location and extent of the underlying microstructural degradation was not known a priori in these studies, quantitative information regarding the accuracy, precision, or reliability of the obtained VBA results can not be provided. As such, these studies clearly demonstrate the need for a gold standard for

validating different post-processing methods and their relative merits.
To address the lack of ground truth knowledge regarding the underlying microstructural alterations, in this work, simulated DTI data sets are developed, which allows for modeling of anomalies in the diffusion properties of a predefined location and in a predefined number of voxels. In this context, an important requisite for the validity of the simulated DTI data sets is to model the induced pathology by simulating these diffusion properties accurately and realistically [33]. To the best of our knowledge, this is the first framework that allows for constructing simulated DTI data sets with ground truth information of pathology. These simulated DTI data sets can be used to investigate the reliability, accuracy, and precision of a VBA or ROI analysis. In addition, the effect of the different parameters and post processing steps that are involved in the pipeline of a VBA analysis can be examined, which could lead to a more reliable, standardized, and consistent post-processing of DT images for studying different pathologies.

6.1.2 Methods

6.1.2.1 Ground truth framework

In this work, simulated DTI data sets are constructed that contain a ground truth pathology with a predefined location, extent, and level of tissue degradation. In Fig. 7.1, a general overview of the construction of these simulated DTI data sets is presented and can be summarized as follows:

(a) H healthy subject and P pathology DTI data sets are acquired.

(b) The N (where $N = H + P$) DTI data sets are transformed to the MNI space with an affine transformation.

(c) Based on the N images in MNI space, a population specific atlas is constructed for the H healthy subjects.

(d) The atlas forms the fundamental data set of the ground truth method and is replicated N times.

(e) In P atlases, the diffusion properties are altered to introduce a pathology in certain voxels.

(f) The diffusion properties are modified to include inter-subject variability.

(g) All data sets are transformed to their native space.

(h) Noise is added to the data sets.

In the following sections, these steps are described in more detail.

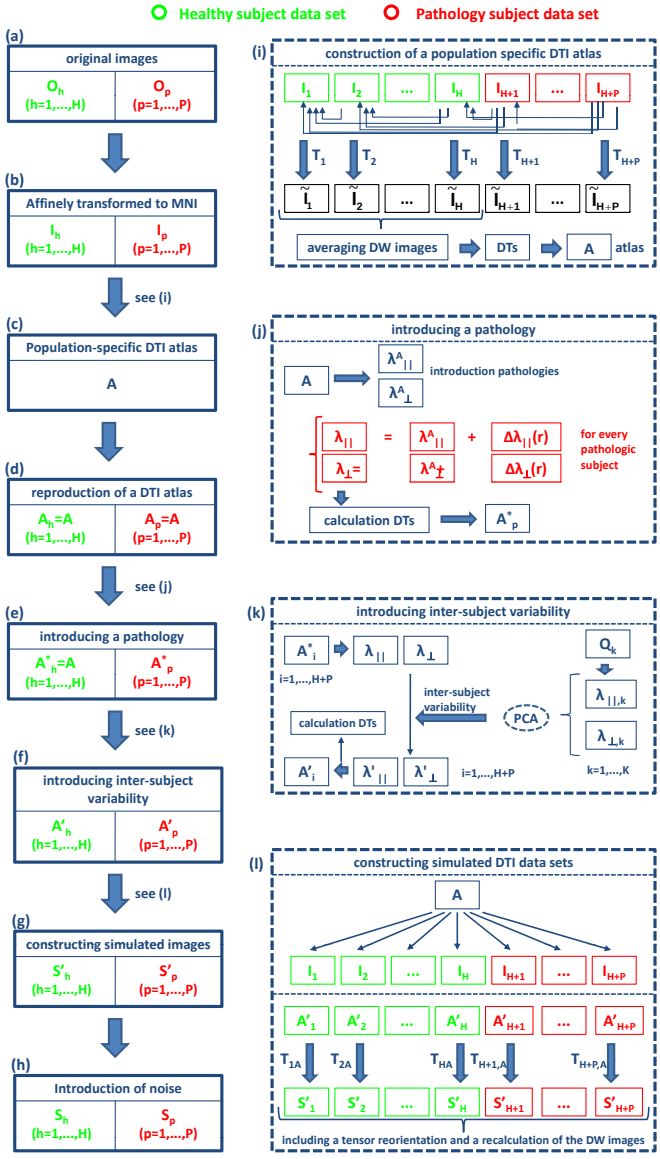

Figure 6.1. *A schematic overview of the ground truth method is presented. On the left, the main steps of this method are displayed in (a)-(h), including the construction of a population based atlas, the introduction of a pathology, inter-subject variability, and noise, and the deformation of the images to native space. More specific information about the different steps is provided in (i)-(p). All data sets O_i, I_i, A_i, $A*_i$, A'_i, S'_i, and S_i contain both the DW images and the diffusion tensor components. The healthy subject data sets are colored in green, whereas the pathology subject data sets are colored in red.*

6.1.2.1.1 Native images The ground truth method is based on the acquisition of H diffusion tensor data sets of healthy subjects and P diffusion tensor data sets of subjects with a certain pathology (Fig. 7.1 (a)). These native healthy subject and pathology data sets will be referred to as O_h (with $h = 1, ..., H$) and O_p (with $p = H + 1, ..., H + P$), respectively. In general, the subject data of the entire group will be denoted as O_i ($i = 1, ..., N$), with N the total number of subjects: $N = H + P$. When not explicitly specified that the DW images or the diffusion tensor components are used, the subject data O_i reflect both the DW images and the diffusion tensor components.

6.1.2.1.2 Atlas Construction A first step in the framework of the simulated data sets is the construction of a population specific DTI atlas based on the N native images (Fig. 7.1 (b) and (c)). This process involves different steps, as described in Van Hecke et al. (2008), and can be summarized as follows (see also Fig. 7.1 (i), (j), and (k)):

- All subjects data O_i (with $i = 1, ..., N$) are spatially normalized to a custom FA MNI template with an affine transformation using MIRIT, incorporating the preservation of principal direction (PPD) tensor reorientation strategy [34–36]. From the EPI MNI template, a custom FA based template was constructed as described in Jones et al. (2002). The transformed images will be referred to as I_h and I_p, or more generally as I_i (see Fig. 7.1 (b)).

- Non-affine deformation fields T_{ji} of data set I_i to data set I_j ($i, j = 1, ..., N$, $i \neq j$) are calculated for each image of the subject group (see Fig. 7.1 (i) and (j)). For the non-affine image alignment procedure, a coregistration algorithm based on a viscous fluid model and mutual information is used, which has been optimized to incorporate all DT information [37, 38].

- The deformation fields T_{ji} (with $j = 1, ..., N$ and $j \neq i$) are averaged for each image I_i ($T_i = \frac{1}{N-1} \sum_j T_{ji}$), as described in Fig. 7.1 (k). The deformation fields T_i characterize the anatomical variation between image I_i and all other data sets of the subject group.

- The deformation fields T_i are applied to all diffusion weighted (DW) images of data sets I_i. After estimating the diffusion tensor from the transformed DW images, the PPD reorientation strategy is applied to obtain the correct diffusion tensors (see Fig. 7.1 (k)) [34]. From these reoriented diffusion tensors, the DW images that correspond to this new space in which the DW images were transformed are recalculated by using the same equation to estimate the diffusion tensors. In doing so, the DW images of each subject have the same framework of diffusion weighted directions, and hence, can

be averaged appropriately. The resulting DTI data sets in atlas space are referred to as $\tilde{I}_i$ ($\tilde{I}_i$=$T_i(I_i)$) (see Fig. 7.1 (i) and (k)). More specifically, the healthy and pathology subject data sets in atlas space are referred to as $\tilde{I}_h$ and $\tilde{I}_p$, respectively.

- The atlas A is constructed by a voxel-wise averaging of the DW images of the H healthy data sets in atlas space $\tilde{I}_h$ followed by a recalculation of the diffusion tensors (see Fig. 7.1 (i)). Note that the application of an iterative estimation procedure to construct the population-based DTI atlas A did not significantly improve the accuracy of the diffusion tensor atlas [39].

Notice that a healthy subject atlas is constructed, since only the H data sets of the healthy subjects in atlas space $\tilde{I}_h$ are averaged to compute this atlas. As such, the diffusion properties of the pathology subjects are not included in the atlas. However, notice that the data sets of these P pathology subjects are still used during the atlas construction to calculate the deformation fields T_i ($i = 1, ..., N$). Hence, an atlas is constructed that represents a structural averaged image of the whole subject group, including the pathology subjects, but only containing diffusion properties of the healthy subjects. This population specific atlas is regarded as the fundamental image in our ground truth VBA methodology and will be referred to as A (see Fig. 7.1 (c)). All simulated data sets will be constructed from this atlas A. To this end, A is replicated N times, resulting in N times the same atlas data set $A_i = A$ (see Fig. 7.1 (d)).

6.1.2.1.3 Introducing pathology In DTI, a WM pathology can present itself generally in two different ways: as a more global morphological anomaly on the one hand and as local changes in diffusion properties on the other hand. In the former case, WM structures are altered due to the presence of brain atrophy, the growth of a tumor, or changes in ventricle size, etc. Commonly, these anomalies can also be detected on conventional MR images. The resulting WM deviations can be visualized with diffusion tensor tractography, a virtual reconstruction of the WM fiber pathways [40–42].
Since the changes in local diffusion properties can be related to changes in organization of the underlying microstructure, they provide very specific information regarding brain WM integrity, which is not always visible on a conventional MR examination. These diffusion parameters can indeed quantify the underlying mechanisms leading to neurological dysfunction in WM disorders, such as demyelination or axonal breakdown [43]. Because of this sensitive relationship between diffusion of water molecules and WM integrity, most DTI studies of pathologies are focused on the examination of these diffusion discrepancies using an ROI or VBA method. Therefore, in this framework, these diffusion alterations, which can be associated with a neurologic disorder, are introduced in different WM structures of

the ground truth data sets, which are subsequently regarded as belonging to the pathology group.
Although further studies are needed, recent work suggests that demyelination and axonal degeneration cause an increase of the average of the second and third eigenvalues (the transverse diffusivity, $\lambda_{\perp}^{A}$) and a decrease of the first eigenvalue (the longitudinal diffusivity, $\lambda_{\parallel}^{A}$), respectively [44–49]. In our work, these measures are therefore used to simulate axonal damage, myelin injury, or a combination of both in the DTI data sets. Notice that, in addition to the location and extent of the pathology, the level of tissue degradation, as reflected by the diffusion properties, can also be controlled in the simulated pathology data sets.
For each pathology data set, the eigenvalue alterations are introduced in the longitudinal $\lambda_{\parallel}^{A}$ and transverse $\lambda_{\perp}^{A}$ eigenvalue images of the atlas data sets A_p ($p = 1, ..., P$), which are subsequently regarded as the pathology group, resulting in the eigenvalue images $\lambda_{\parallel}$ and $\lambda_{\perp}$ (see Fig. 7.1 (e) and (l)):

$$\begin{aligned} \lambda_{\parallel}(\mathbf{r}) &= \lambda_{\parallel}^{A}(\mathbf{r}) + \Delta\lambda_{\parallel}(\mathbf{r}) \\ \lambda_{\perp}(\mathbf{r}) &= \lambda_{\perp}^{A}(\mathbf{r}) + \Delta\lambda_{\perp}(\mathbf{r}) \end{aligned} \quad . \tag{6.1}$$

The magnitude of the microstructural breakdown that is simulated in the longitudinal and transverse eigenvalue images is defined as $\Delta\lambda_{\parallel}(\mathbf{r})$ and $\Delta\lambda_{\perp}(\mathbf{r})$, respectively, where $\mathbf{r}$ describes the location and size of the different voxel clusters in which a pathology is introduced for the longitudinal and transverse eigenvalue images. Note that $\Delta\lambda_{\parallel}(\mathbf{r})$ and $\Delta\lambda_{\perp}(\mathbf{r})$ can be defined for each data set separately. The microstructural breakdown, represented by $\Delta\lambda_{\parallel}(\mathbf{r})$ and $\Delta\lambda_{\perp}(\mathbf{r})$, is introduced as a percentage change of the original values $\lambda_{\parallel}^{A}$ and $\lambda_{\perp}^{A}$. Note that $\Delta\lambda_{\parallel}(\mathbf{r})$ and $\Delta\lambda_{\perp}(\mathbf{r})$ can be modeled more specifically to constrain changes in FA and MD. For example, a FA decrease can be simulated while keeping the MD constant.
Since the purpose is to introduce eigenvalue alterations, and not to change the main direction of diffusion, care has to be taken that the transverse diffusivity does not become larger than the longitudinal diffusivity. The altered eigenvalue images $\lambda_{\parallel}$ and $\lambda_{\perp}$ are subsequently used to redefine the new diffusion tensors, whereby the diffusion eigenvectors are not modified. The resulting data sets A_p^* represent the atlas images with an additional simulated pathology in certain voxels (see Fig. 7.1 (e)). The data sets that are regarded as the simulated healthy subject images are not altered during this step of the processing pipeline: $A_h^* = A_h$.

6.1.2.1.4 Introducing inter-subject variability Even if data sets of different healthy subjects are acquired in the same scanner and with the same acquisition parameters, a significant inter-subject variance can be observed in these images. Many variables, such as age, sex, handedness, etc. of the subjects are known to contribute to this variability in the DT properties [50, 51]. Therefore, most VBA

and ROI studies circumvent these sources of variation by a careful selection of the subject groups. However, due to the inherent anatomical and physiological variability across subjects, the inter-subject variance is still present in the DTI data sets. In order to create more realistic DT images in our ground truth framework, this inter-subject variability should be integrated to both healthy A_h^* $(h = 1, ..., H)$ and pathology A_p^* $(p = 1, ..., P)$ data sets.
Analogously to the WM pathology, the inter-subject variability can present itself as a morphological WM variability or as variances of the diffusion properties. Examples of the former are the shape variance of the corpus callosum and the difference in the frontal WM architecture across healthy subjects. The latter source of inter-subject variability is more subtle, but will affect the statistics when different diffusion properties are compared between subject groups. Simulation of this type of inter-subject variance was obtained using a principal component analysis (PCA) on the longitudinal and the transverse eigenvalue images, since they contain all the information regarding the local diffusion properties. Variances in the local directional diffusion information, which can be considered as morphological WM variabilities, will be accounted for in a later step of the ground truth method. New longitudinal and transverse eigenvalue samples are produced from an estimated distribution, as explained as follows (see Fig. 7.1 (m)):

- First, the DT atlas A is masked by thresholding the FA map. An FA threshold of 0.2 was used to suppress areas consisting of CSF and deep GM in the analysis [52].

- K healthy subject DTI data sets are acquired to estimate the inter-subject variance of the diffusion properties. These K data sets are coregistered non-affinely to the DTI atlas A, resulting in the data sets Q_k $(k = 1, ..., K)$ (see Fig. 7.1 (n)).

- Subsequently, a vector is constructed as a concatenation of the masked longitudinal and transverse eigenvalue images of all data sets Q_k $(k = 1, ..., K)$. Hence, a $2V$-dimensional vector is obtained for each data set Q_k, with V the number of voxels included in the mask.

- Let M represent a $K \times 2V$ matrix, containing all the data. This data was made zero-mean by subtracting the mean $2V$-vector for every row. Since $K \ll 2V$, the K-dimensional subspace is used to generate new samples. For this, the eigenvalue decomposition $MM^T = E\Lambda E^T$ is calculated, with E an orthogonal matrix containing the eigenvectors, and Λ a diagonal matrix containing the eigenvalues of a $(K \times K)$ matrix.

- A new random sample R is generated as a $K \times 1$ vector which is defined as zero-mean, unit variance, Gaussian distributed random variables. This

sample is projected to the $2V$-dimensional space using $\frac{1}{\sqrt{K}} M^T ER$.

- Finally, the mean vector is added to these samples, which are then distributed according to the K original ones.

In this way, inter-subject variability is added to the longitudinal and transverse eigenvalues of both the healthy and pathology data sets, followed by a recalculation of the diffusion tensors. The resulting healthy and subject pathology data sets are referred to as A'_h and A'_p, respectively.

6.1.2.1.5 Constructing the simulated data sets As described in the paragraphs 3 and 4, the local diffusion properties were altered to include a pathology and inter-subject variability in the simulated DTI data sets. However, the resulting DT images are still situated in the atlas space of image A.
Realistic, simulated DTI data sets of different individuals are created by generating non-affine deformation fields that warp the data sets A'_h and A'_p to their respective subject spaces. These transformations are obtained by calculating the non-affine deformation fields between the atlas A and the native data sets I_i in the affine MNI space (see Fig. 7.1 (o)). Since realistic deformation fields, derived from the coregistration of A to different healthy subjects I_h, are used to transform the images A'_h, the inter-subject variability of the WM structures in native space is also taken into account appropriately. Structural WM pathologies and inter-subject variability of the WM structures are also included in the transformed images A'_p, since P deformation fields are obtained from the coregistration of A to the DTI data sets of the pathology subjects I_p.
In order to increase the accuracy of the inter-subject warps and to decrease the dependency of the spatial information of the simulated data sets on a single coregistration algorithm, three different image normalization methods are combined to compute a more general deformation field (see Fig. 7.1 (p)):

1. The aforementioned viscous fluid model, including all DT information during the image alignment, is used to obtain the deformation fields T^1_{iA} between the atlas A and the native data sets I_i.

2. The deformation fields T^2_{iA} are computed using a coregistration approach that is based on free-form deformations and B-splines, which is included in software packages as IRTK (Image Registration Toolkit) and FSL (FMRIB Software Library – *www.fmrib.ox.ac.uk/fsl*) [53].

3. The deformation fields T^3_{iA} are obtained by a linear combination of $(7 \times 8 \times 7)$ basis functions as is included in the SPM package [54].

Note that T^1_{iA} is obtained by incorporating all DT information during the coregistration, whereas FA maps are employed to obtain both T^2_{iA} and T^3_{iA}. The total non-affine transformation of the atlas A to each native images I_i is calculated as the average of the three deformation fields: $T_{iA}{=}\frac{1}{3}\sum_{j=1}^{3} T^j_{iA}$. These deformation fields are applied to the DW images of the data sets A'_h and A'_p. The accordingly obtained simulated DTI data sets will be referred to as $S'_h = T_{hA}(A'_h)$ $(h = 1, ..., H)$ and $S'_p = T_{pA}(A'_p)$ $(p = 1, ..., P)$, or as S'_i $(i = 1, ..., N)$ when referred to the simulated data sets in general.

6.1.2.1.6 Introducing noise In order to obtain realistic, simulated DTI data sets, a realistic amount of noise should be included in the images. To this end, the noise level in the native images is estimated with the method described in Sijbers et al., (2007). In their approach, a histogram of the Rayleigh distributed background intensities of the DW images is used to estimate the noise level, which will be referred to as σ_o. Hence, a similar noise level should be observed in the simulated images. In addition, since the noise is Rice distributed in MRI, realistic noise in the resulting simulated images also needs to be Rice distributed [55, 56]. The noise level is reduced in the simulated data sets due to the complete processing pipeline that is used to construct these images.
In order to calculate the noise level that has to be added to the simulated DTI data sets S'_i, the noise reduction during the processing pipeline should be estimated. To this end, extra Rician noise with variance σ_n^2 is added to the DW images of the native data sets O_i. These data sets are subsequently used to construct the simulated DTI data sets $S_i^{'n}$ as described in the previous paragraphs. Thereafter, the resulting noise variance is estimated from the difference between the original simulated data sets S'_i and the simulated data sets $S_i^{'n}$ that were constructed from original images O_i with extra noise:

$$\sigma_f^2 = \mathbb{E}\left[(S_i^{'n} - S'_i)^2\right], \tag{6.2}$$

in which the expectation $\mathbb{E}$ was replaced by a regional average. Finally, the noise reduction factor of this processing pipeline is computed as $r_o = \sigma_n/\sigma_f$.
To obtain simulated DW images with a similar noise standard deviation as in the original images O_i (i.e. σ_o), the amount of noise that has to be added (σ_a) to the simulated data sets, is given by:

$$\sigma_a = \sqrt{\sigma_o^2 - (\sigma_o/r_o)^2}. \tag{6.3}$$

However, it is important to note that the noise already present in S'_i can be explained by the diffusion tensors, i.e., it completely adds to the variance of the diffusion tensor estimates. Since in the further processing, the DTs and not the DW images are of interest, the final noise level of the simulated DTs should be

equal to the noise level of the DTs computed from the original images O_i. Since the dimensionality in parameter space is reduced by estimating the DTs from the DW images, a theoretical noise reduction r_t is expected:

$$r_t = \sqrt{u/l}, \tag{6.4}$$

with u the number of DW images and l the number of estimated DT parameters. Taking into account the reduction factor r_t, the noise standard deviation that has to be added to S_i' becomes:

$$\sigma_a = \sqrt{\sigma_o^2 - (\sigma_o.r_t/r_o)^2}. \tag{6.5}$$

The resulting simulated healthy subject and pathology data sets, which contain a realistic amount of noise, are referred to as S_h $(h = 1, ..., H)$ and S_p $(p = 1, ..., P)$, respectively, or as S_i $(i = 1, ..., H + P)$ in general.

6.1.2.2 Subjects and Data Acquisition

In this work, 100 DTI data sets were acquired on a 1.5T MR system. 80 of these images were obtained from a healthy subject group (age range: $18-65$ years, 32 M, 48 F). In addition, 20 data sets were obtained from patients with MS (age range: $20-42$ years, 6 M, 14 F).
Axial diffusion tensor images were obtained using an SE-EPI sequence with the following acquisition parameters: TR: 10.4 s; TE: 100 ms; diffusion gradient: 40 $mT.m^{-1}$; FOV = 256×256 mm^2; number of slices = 60; voxel size = $2 \times 2 \times 2$ mm^3; b = 700 $s.mm^{-2}$; acquisition time: 12 min 18 s. Diffusion measurements were performed along 60 directions with 10 b_0-images and a nonlinear diffusion tensor estimation procedure was used based on the Levenberg-Marquardt optimization method [57]. DTI post processing and visualization were performed with the diffusion toolbox 'ExploreDTI' [58].

6.1.2.3 Examining the effect of image alignment and tissue degradation on VBA results

40 simulated data sets were generated with a specific level of noise and inter-subject variability to investigate the effect of coregistration and level of pathology on the sensitivity of the VBA results. Several levels of pathology (predefined increase of the transverse eigenvalues $\lambda_\perp$) were simulated in the splenium of the corpus callosum (size: 54 voxels in 4 consecutive axial slices) for 20 data sets [21, 28, 31, 59–61].
Two VBA analyses were performed demonstrating the subtle changes in outcome of regions with a significant FA difference between healthy and diseased subjects due to imperfections in coregistration:

Analysis 1: The predefined deformation fields to transform the simulated data sets to native space were applied to invert the data back to atlas space. In doing so, perfect alignment is guaranteed taking into account the effects of data interpolation, allowing for the computation the effective levels of pathology (that is, prior to adding noise and inter-subject variability).

Analysis 2: The data sets in native space (as in Analysis 1, but with noise and inter-subject variability added) are coregistered to the atlas using the non-rigid coregistration approach [37].

For both analyses, the FA data were smoothed with a Gaussian kernel (3 mm FWHM) and a parametric t-test (the data were normally distributed according to the Lilliefors test) was used to compare the FA values between the healthy and the pathology data sets, followed by the Benjamini-Hochberg post-hoc correction for multiple comparisons [62]. To quantify the VBA results, the sensitivity - calculated as the ratio of the number of true positives with the sum of the number of true positives and false negatives - is computed for both analyses and repeated 10 times.

6.1.3 Experiments and Results

From the 100 (=H+P+K) acquired DTI data sets, 20 (=P) were obtained from pathology subjects with MS. The 20 (=H) healthy subject data sets were age- and sex-matched with the MS patient images. The remaining 60 (=K) healthy subject data sets were used to construct the inter-subject variability maps.

6.1.3.1 Native images

To illustrate the processing pipeline of the ground truth method, axial FA slices of six randomly selected native DTI data sets, color-encoded for the main diffusion direction, are displayed in Fig. 7.2 (a). Three of these (left) were acquired from healthy volunteers, whereas the other three (right) were obtained from MS patients.

6.1.3.2 Atlas Construction

A population specific atlas was constructed from the native DTI data sets, as explained in the Methods section. As illustrated in Fig. 7.2 (b), these data sets were warped affinely to MNI space, followed by the transformation to the atlas space by the use of averaged deformation fields. Thereafter, an atlas was computed with a minimal deformation to all images of the subject group, as shown in Fig. 7.2 (c) [39]. This DTI atlas, which is regarded as the fundamental data set of the ground truth method, was reproduced 40 (=H+P) times (see Fig. 7.2 (d)).

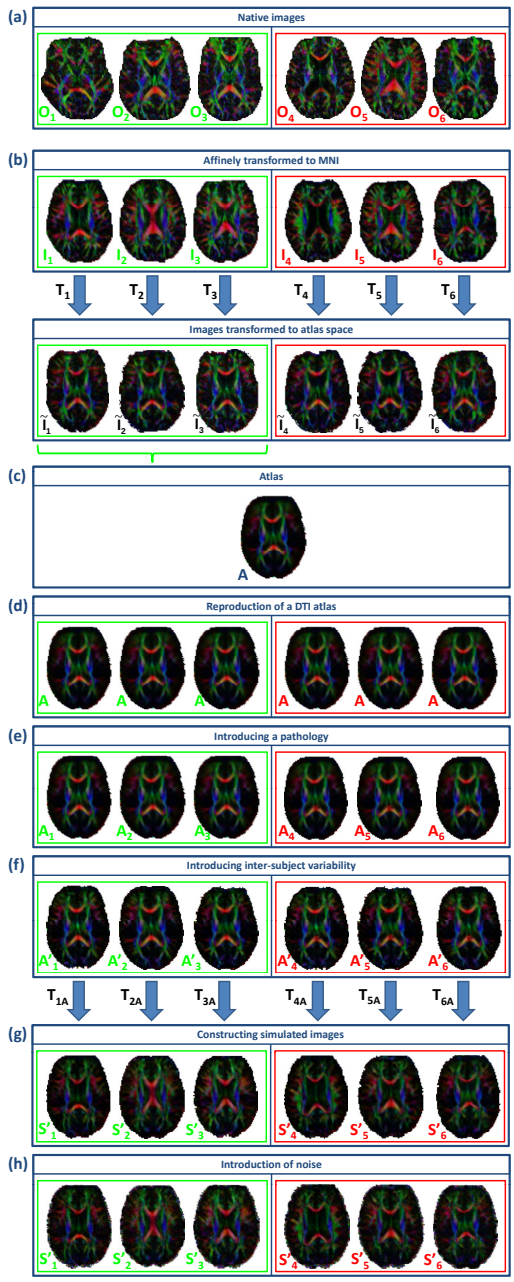

Figure 6.2. *In (a), axial FA slices of six randomly selected native DTI data sets are shown. Three of these images, O_1, O_2, and O_3, are healthy subject DTI data sets. On the other hand, images O_4, O_5, and O_6, are obtained from MS patients. In (b)-(i), the processing pipeline is illustrated using these data sets. Finally, in (i), the simulated images in affine space are visualized. Notice that these should resemble the native DTI data sets in affine space, as shown in (b).*

6.1.3.3 Introducing pathology

Based on the reported results in the DTI literature, a predefined microstructural breakdown was introduced in different voxel clusters of the simulated pathology data sets (see Fig. 7.2 (e)). As can be seen in Fig. 7.3, these selected WM structures and voxel clusters are coloured in white on different axial slices of the atlas data set. References to DTI studies in which the diffusion measures in these WM structures were observed to be significantly different between control subjects and patients are added to this Fig. [21, 24, 26, 28, 29, 31, 59–61, 63–71]. In addition, the number of voxels in which the diffusion properties are modified in this example are also presented in Fig. 7.3.
An example of different levels of tissue degradation in the splenium of the corpus callosum is given in Fig. 7.4 (a) and enlarged in Fig. 7.4 (b). The corresponding tensors are displayed in Fig. 7.4 (c). The degree of microstructural breakdown is here defined as a percentage of the original longitudinal and transverse eigenvalues in each voxel.

6.1.3.4 Introducing inter-subject variability

Inter-subject variability was estimated from 60 (=K) healthy subject DTI data sets. Examples of the images in atlas space that include inter-subject variability of the diffusion properties are shown in Fig. 7.2 (f). In Fig. 7.5, the inter-subject variance of the longitudinal and transverse eigenvalues is depicted, as reflected by the coefficient of variation, which is the standard deviation map of an eigenvalue image, normalized by the average of the different eigenvalue images. An axial, coronal, and sagital slice of the FA map is shown in Fig. 7.5 (a). In Fig. 7.5 (b), the inter-subject variance of the longitudinal eigenvalues is depicted for the same axial, coronal and sagital slices. Analogously, the inter-subject variance of the transverse eigenvalues is visualized in Fig. 7.5 (c). A high inter-subject variance is depicted in a bright colour, whereas a low inter-subject variance is depicted in a dark colour.

6.1.3.5 Constructing the simulated data sets

After generating the simulated DTI data sets in atlas space, a predefined set of deformation fields is applied to these data sets to transform them to native space. (see Fig. 7.2 (g)). A qualitative example of the image correspondence between the simulated and the native DTI data sets is shown in Fig. 7.6. In Fig. 7.6 (a), axial FA slices of five randomly selected native DTI data sets are displayed. Axial FA slices of the corresponding simulated data sets are visualized in Fig. 7.6 (b). After overlaying the blue coloured native FA image and the red coloured simulated FA map, corresponding voxels with similar FA values will be coloured purple, as

	WM structure	significant in these articles	number of voxels
(a)	Cerebellar peduncle	• Park et al. 2004 • Seok et al. 2007 • Kyriakopoulos et al. 2007	187
(b)	Cortico-spinal tract	• Sach et al. 2004 • Douaud et al. 2007 • Sage et al. 2007	90
(c)	Inferior longitudinal fasciculus	• Park et al. 2004 • Hubl et al. 2004 • Boronni et al. 2007	95
(d)	Cerebral peduncle	• Xie et al. 2005	54
(e)	Internal capsule	• Nagy et al. 2003 • Sage et al. 2007 • Sach et al. 2004 • Xie et al. 2005 • Kubicki et al. 2005 • Buchsbaum et al. 2006	76
(f)	Genu of the corpus callosum	• Ardekani et al. 2003 • Douaud et al. 2007 • Barnea-Goraly et al. 2003 • Anjari et al. 2007	50
(g)	Forceps minor	• Xie et al. 2005	115
(h)	External capsule	• Molko et al. 2004 • Barnea-Goraly et al. 2003	76
(i)	Splenium of the corpus callosum	• Simon et al. 2005 • Park et al. 2004 • Ardekani et al. 2003 • Douaud et al. 2007 • Barnea-Goraly et al. 2003 • Kyriakopoulos et al. 2007	70
(j)	Forceps major	• Agartz et al. 2001 • Kyriakopoulos et al. 2007	40
(k)	Corona Radiata	• Sach et al. 2004	136
(l)	Body of the corpus callosum	• Ardekani et al. 2003 • Douaud et al. 2007 • Barnea-Goraly et al. 2003 • Xie et al. 2005	44
(m)	Superior longitudinal fasciculus	• Seok et al. 2007 • Xie et al. 2005 • Kubicki et al. 2005 • Boronni et al. 2007 • Padovani et al. 2005 • Buchsbaum et al. 2006 • Kyriakopoulos et al. 2007	96
(n)	cingulum	• Park et al. 2004 • Kubicki et al. 2005 • Seok et al. 2007	42

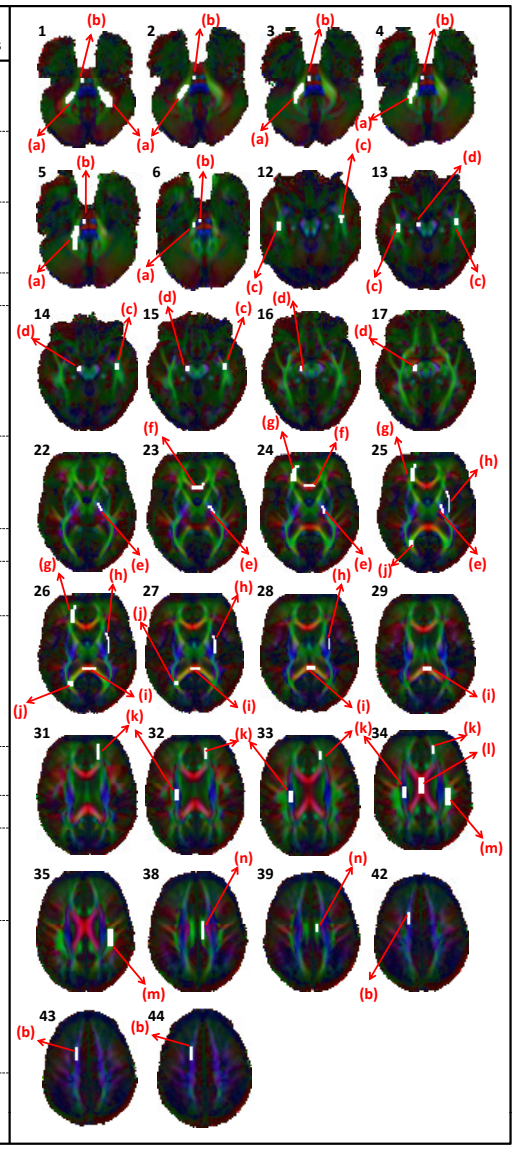

Figure 6.3. *On the left, different WM structures are displayed in which a simulated pathology is introduced. For each WM structure, the number of voxels in which a pathology is introduced is given for this example. In addition, references of studies are given that found a significant difference of the diffusion properties in this specific WM structure. The voxels in which the diffusion properties are altered are marked in white on the different axial slices of the DTI atlas.*

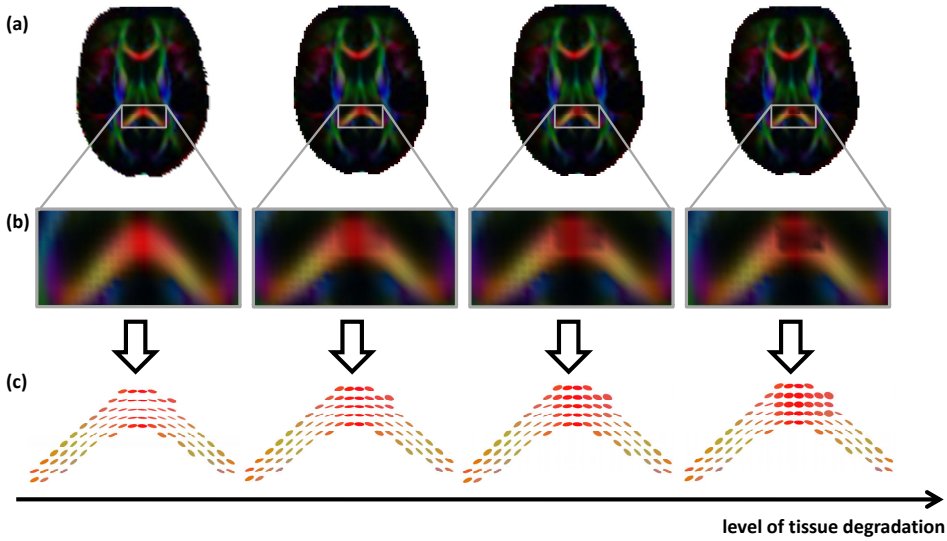

Figure 6.4. *An example is provided of the introduction of a pathology in the splenium of the corpus callosum. In (a), the axial slices are displayed for different levels of tissue degradation. The splenium is shown in more detail in (b). In (c), the diffusion ellipsoids of the splenium are visualized.*

visualized in Fig. 7.6 (c), (d), and (e).
In order to obtain a quantitative measure of the spatial image correspondence between the native and the simulated data sets, ROIs were manually drawn in different WM structures on the both the native and the simulated data sets (see Fig. 7.7). First, these ROIs, delineating the capsula externa, corpus callosum, cerebellar peduncle, and posterior limb of the internal capsule, are drawn twice on the native data sets to test the reproducibility. These ROIs are marked in red and blue, as indicated in Fig. 7.7. Thereafter, the same WM structures are delineated on the simulated data sets, and marked in green. Finally, the red and blue voxels as well as the red and green voxels are overlaid. In the case that a voxel is selected by the red and the blue ROI, it will be given a purple colour, describing the reproducibility of the manual ROI delineation. Analogously, voxels appear yellow when they are present in both red and green ROIs, describing the image correspondence between the native and the simulated data sets. A quantitative measure for the ROI correspondence is calculated as the percentage of voxels that are present in both ROIs related to the total number of selected voxels in both ROIs. This measure is computed for the aforementioned ROIs in all 40 corresponding native and simulated data sets resulting in the boxplots of Fig. 7.7. The difference between both overlap measures was not statistically significant, demonstrating the high spatial correspondence between the simulated and the native DTI data sets

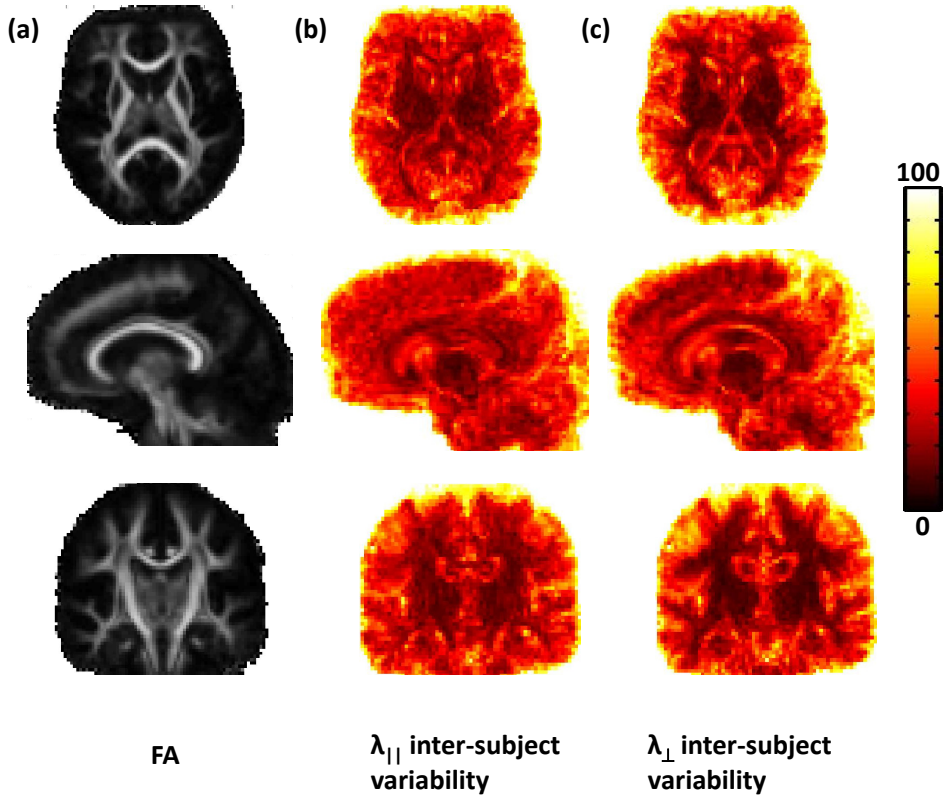

Figure 6.5. *In (a), an axial, sagital, and coronal slice of the FA map are displayed. A measure of the inter-subject variability of the longitudinal and the transverse eigenvalues is shown in (b) and (c), respectively. This measure is calculated as the standard deviation of the eigenvalue images that result from the PCA analysis, weighted by the average of these images. High and low inter-subject variances are represented by a bright and a dark colour, respectively.*

for these large well-defined WM structures.

In order to evaluate the tensor correspondence between the native and the simulated data sets, the OVL is computed [72]. This measure calculates the scalar product between corresponding eigenvectors, weighted by the magnitude of the corresponding eigenvalues. The minimum value 0 indicates no overlap and the maximum value 1 represents complete overlap of the diffusion tensors. In Fig. 7.9 (a), the OVL measure between an native data set and its corresponding simulated data set is calculated for four randomly selected data sets and overlaid on the FA map of the native images. As can be observed in Fig. 7.9 (a), a high OVL is found in the major WM structures. In Fig. 7.9 (b), a histogram of the OVL values

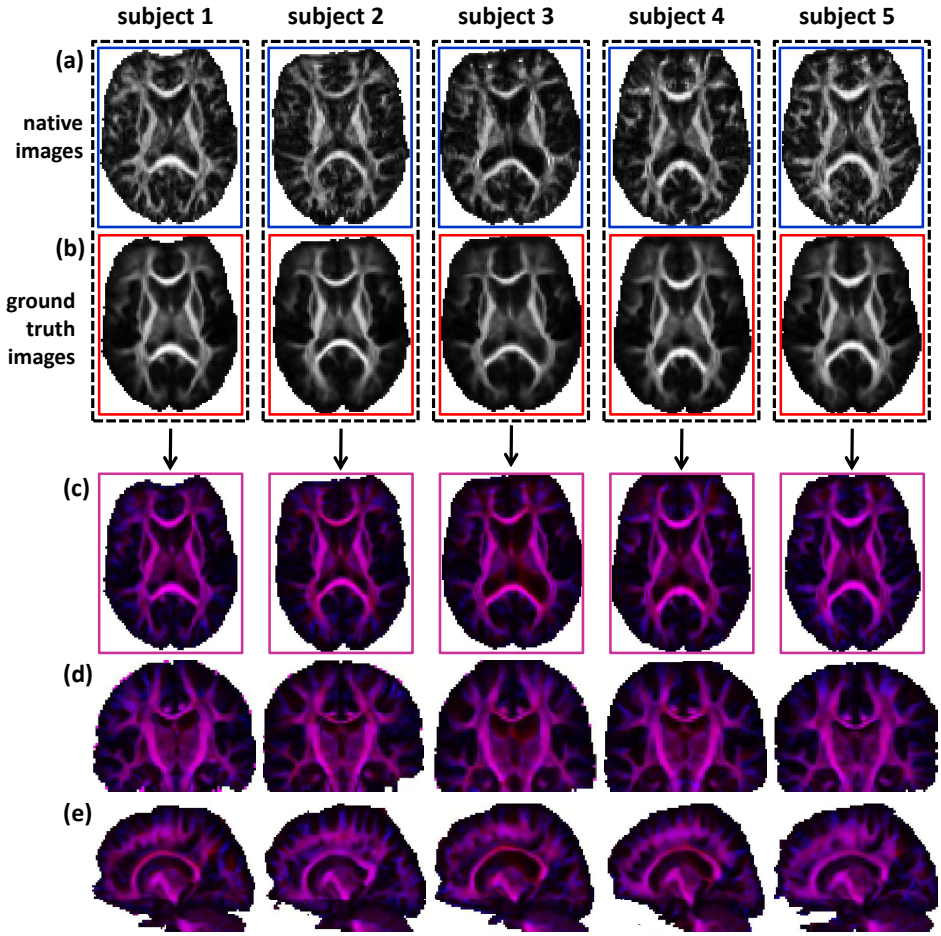

Figure 6.6. *The spatial image correspondence is represented visually for* 5 *randomly selected native data sets and their corresponding simulated data sets. The axial FA slices of these native and simulated data sets are visualized in (a) and (b), respectively. The FA maps of the native and the simulated data sets are colour encoded in blue and red, respectively. By overlaying these colour encoded images, the corresponding voxels with a similar FA value will be purple as can be seen on the axial, coronal, and sagittal slices, in (c), (d), and (e), respectively.*

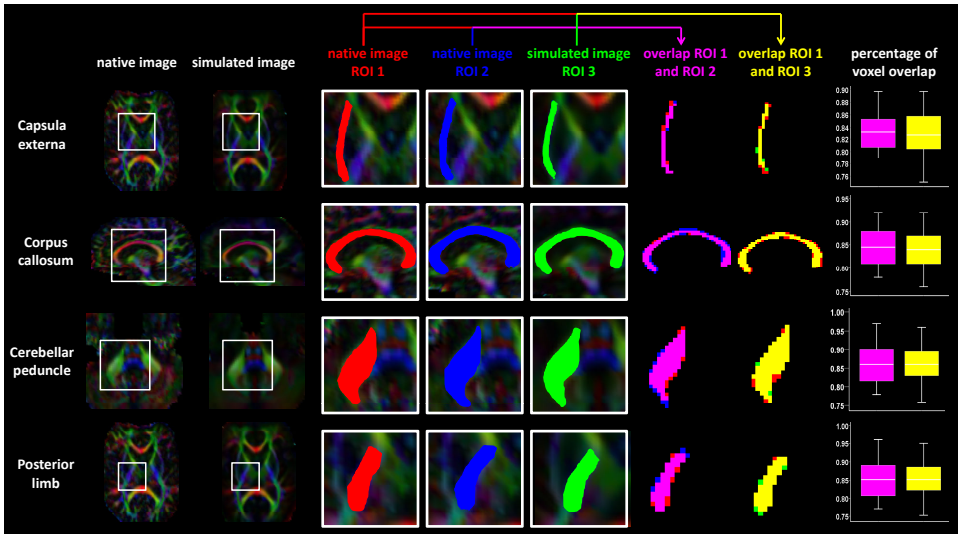

Figure 6.7. *ROIs are drawn twice in the capsula externa, the corpus callosum, the cerebellar peduncle, and the posterior limb of the native data sets, as displayed in red and blue. After overlaying these ROIs for each WM structure, voxels will appear purple, when they are included in both ROIs. The percentage of overlap is given on the right. Analogously, ROIs are delineated in the same WM structures of the simulated images, and displayed in green. The voxels that are included in the ROI of the native data set and of the simulated data set are then coloured yellow. Again, the percentage of overlap of these ROIs are shown on the right for the different WM structures.*

is displayed for these four data sets. All voxels with an FA value above 0.4 were included in this histogram. Finally, a scatter plot of the OVL and the FA values is displayed in Fig. 7.9 (c), demonstrating the high tensor correspondence in the major WM structures with a high FA.

6.1.3.6 Introducing noise

After applying the method of Sijbers et al. (2007) to the 40 native DTI data sets O_i, a noise level $\sigma_o = 18 \pm 1$ was found. Extra noise with a σ_i of 7 was added to the native images to estimate the observed noise reduction factor of the processing pipeline. After processing these images, the reduced noise level in the simulated data sets was observed to be $\sigma_f = 1.6$. Consequently, the noise reduction factor of the processing pipeline to construct the simulated data sets is $r_o = \sigma_i/\sigma_f = 4.3$.
In order to create simulated DT images that have the same noise level as the native images, extra noise has to be added to the DW images of data sets S_i. To obtain simulated DWI images with a similar noise level as in the original images (i.e. 18 ± 1), the noise that has to be added should have a $\sigma_a = \sqrt{\sigma_o^2 - (\sigma_o/r_o)^2} = 17.5$.

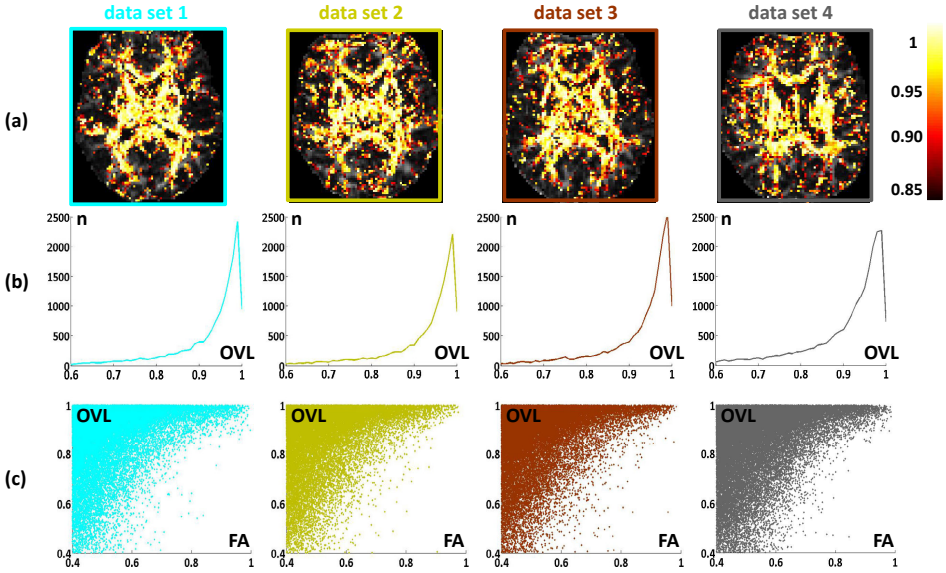

Figure 6.8. *The overlap of eigenvalue and eigenvector pairs (OVL) is calculated between 4 native images and their corresponding simulated data sets. In (a), this OVL measure is superimposed on the axial FA slices of the native data sets. A histogram of this OVL is calculated including all voxels with an FA>0.4, as shown in (b). In (c), a scatter plot of the OVL measure and the FA value is displayed, demonstrating the higher tensor correspondence in WM structures with a high FA.*

However, as explained in the previous section, only the noise on the estimated diffusion tensors is important for the further processing and interpretation of the data sets. The variance of the noise that should be added to the simulated images therefore becomes $\sigma_a = \sqrt{\sigma_o^2 - (\sigma_o.r_t/r_o)^2} = 12.2$. Examples of simulated DTI data sets that include a realistic level of noise are visualized in Fig. 7.2 (h).

6.1.3.7 Examining the effect of image alignment and tissue degradation on VBA results

In Figure 6.9, the VBA results of Analysis 1 and Analysis 2 are displayed for different levels of tissue degradation, expressed as a percentage of effective FA change. One of the axial slices, in which the pathology was simulated, is shown in Figure 6.9 (a). In Figure 6.9 (b), the VBA results of the splenium are shown qualitatively for analyses 1 and 2 for different levels of simulated pathology. The voxels, in which ground-truth pathology was introduced, are given a purple color. The subgroup of these voxels that were found as statistically significant in the VBA analysis are colored in blue. For an effective FA decrease of 7%, 10%, 13%, 16%,

19%, and 21%, different results were obtained between both analyses: in Figure 6.9 (c), these differences in sensitivity are displayed for the different levels of simulated pathology.

6.1.4 Discussion

In this work, a novel framework is presented for the construction of simulated DTI data sets, which include a predefined pathology. An increasing number of researchers apply VBA methods to analyse DTI data of control subjects and patients [21, 24–26, 28, 29, 31, 59–61, 63–71]. However, studies suggest that the VBA results are not always accurate and disease specific, since they depend on the parameter settings and implementations of the post processing method [27, 73–76]. In this context, our framework allows one to estimate the accuracy, precision, and reliability of different post processing approaches for detecting changes in diffusion properties with different predefined magnitudes and locations quantitatively.
The processing pipeline of the ground truth framework was based on the acquisition of 80 (=H+K) healthy subject and 20 (=P) MS patient DTI data sets. The MS patient data sets were included in the analysis in order to introduce morphological anomalies, such as enlarged ventricles or a thinned corpus callosum in our simulated data sets in order to increase the resemblance of the simulated study with realistic situations. For example, the inclusion of simulated DTI data sets with a morphological pathology in a VBA might hamper the coregistration accuracy, and thereby the reliability of the statistical analysis. However, it should be mentioned that the unknown alterations of the diffusion properties, which are present in the native DTI data sets of the MS patients, were not included in the simulated data sets. As such, the population specific atlas, which is considered as the fundamental image of our framework, only contains the diffusion information of the healthy subjects, although it is located in the atlas space of all subjects (i.e., both healthy subjects and MS patients).
As can be observed, for example, in Fig. 7.3, the population specific atlas particularly contains reliable information within the main WM structures. Since a large variability of the peripheral WM and the GM structures exists in the DTI data sets across different subjects, this information is less reliable in the atlas. This large inter-subject variability is also illustrated in Fig. 7.5 (b) and (c), showing the inter-subject variances, as calculated by a PCA analysis on 60 (=K) healthy subjects, of the longitudinal and transverse eigenvalue maps, respectively. Since these peripheral WM structures are not reliably present in the fundamental atlas data set, no pathology diffusion alterations are introduced in the peripheral WM structures of the simulated DTI data sets. In this context, it should be mentioned that in VBA studies of different pathologies, all results in the peripheral WM should be interpreted very cautiously.

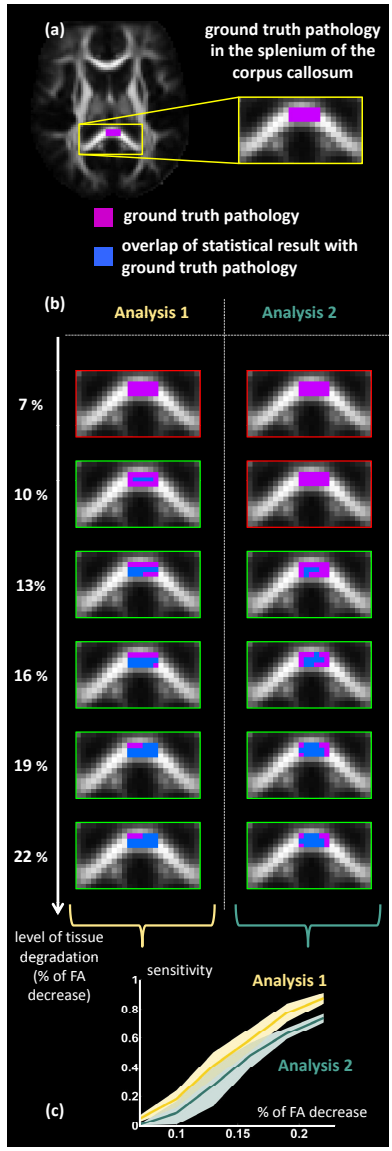

Figure 6.9. *VBA results for a ground truth pathology in the splenium of the corpus callosum. In (a), the ground truth pathology is shown on an axial slice of the atlas FA map. The VBA results after a simulated 'perfect' alignment (Analysis 1) and after non-rigid coregistration (Analysis 2) are visualized in (b). The voxels in which a ground truth pathology is introduced are colored in purple, whereas the significant voxels are colored in blue. In (c), the VBA sensitivity is displayed for different levels of tissue degradation, as presented by the corresponding effective FA decrease.*

Examples of voxel clusters, in which microstructural breakdown is simulated by changes in the diffusion characteristics, are visualized in Fig. 7.3. Obviously, the magnitude, the spatial location and size of the pathology can be chosen differently from this example and can be modified to address specific issues and validate specific hypotheses. In addition, the nature of the pathology (for example, constant MD and FA increase or MD and FA increase, etc.) can be modified to simulate specific pathologies. Furthermore, it should be mentioned that the exact location of the pathology can be varied across the pathology subjects to simulate more complex configurations.

After including a pathology and inter-subject variability, the simulated DTI data sets are still embedded in the population specific atlas space. In order to simulate a realistic situation, these DTI data sets should be located in a native space. To his end, deformation fields were used to transform the simulated data sets to their native space. Since, in this work, realistic deformation fields were adopted to transform the atlas image to the individual space, the spatial correspondence of the simulated data sets with realistic DT images will depend on the accuracy of these deformation fields. Therefore, inaccuracies in the image alignment to the native DT images are reduced by the use of a population specific DTI atlas as the fundamental DTI data set. The magnitude of the deformation fields from the atlas to the native images is then minimized, thereby reducing potential coregistration errors. To further minimize these image alignment inaccuracies, three different image normalization techniques were applied to estimate the deformation fields between the atlas and the native DTI data sets. These deformation fields were subsequently averaged and used to transform the simulated data sets to their native space. In addition, the use of averaged deformation fields prevents the generated transformations of being biased toward a family of deformations that can be generated by one particular warping algorithm. Finally, the use of averaged deformation fields to construct the simulated data sets enhances the tensor correspondence between the native data sets and the simulated images, since the effect of tensor reorientation inaccuracies is reduced [37, 39].

After the transformation of the DT images to an individual space and the subsequent addition of a realistic amount of noise, simulated DTI data sets are constructed. The images can then be used to quantitatively evaluate different DTI post processing approaches, since all the aspects of the pathology are known a priori. In this way, different implementation issues and parameter settings of the VBA methods can be examined separately. As shown by our example (Analysis 1 vs. Analysis 2), it is clear that the ground-truth framework can be applied to investigate the effect of coregistration on the sensitivity of VBA results. Key to comparing a specific aspect of the VBA pipeline using this simulation approach is to keep all other predefined parameters and methods identical. In this example, for instance, when investigating the adverse effects of coregistration, not only the levels

of noise and inter-subject variability, the size of smoothing kernel, and the applied statistical tests were the same, also the actual transformation steps were included to consider the partial volume averaging artifacts due to interpolation, which are also present during actual coregistration. With these simulated VBA analyses, coregistration methods can be compared or even optimized by fine-tuning user-defined parameters.

Conclusion

In this work, a framework for constructing simulated DTI data sets with a predefined pathology is presented. These data sets can be employed in studies to evaluate the accuracy, precision, and reproducibility of different VBA algorithms quantitatively. We are convinced that this will lead to an improved understanding of the reliability and shortcomings of these post processing methods to study different WM altering pathologies.

6.2 The effect of smoothing on the subsequent statistics in a voxel based analysis of diffusion tensor images: a study using simulated data sets

6.2.1 Introduction

Since patient-control differences are evaluated in every brain voxel, VBA is able to recover unexpected areas of neuro-anatomical alterations. However, despite this intuitively appealing approach, VBA results should be interpreted cautiously. For example, since statistical tests are performed in each voxel, the chance of statistical Type I errors is very high and a correction for multiple comparisons should be applied. In addition, VBA is based on the assumption that corresponding voxels of different subjects are perfectly overlaid after non-rigid coregistration of all data sets to the template [75, 77]. However, due to a significant variability of the WM topology across subjects, especially in the case of a pathology, residual image alignment inaccuracies can be present. In order to reduce the effect of these coregistration errors on the subsequent statistical analysis, the normalized data sets are often smoothed with an isotropic Gaussian kernel. An additional advantage of this smoothing is the increased SNR, since the matched filter theorem states that a signal is detected with an optimal sensitivity if a convolution kernel that matches the size and shape of the signal change is used [78]. Based on this matched filter theorem, a 'rule of thumb' is often used in the analysis of fMRI and PET data sets, stating that the full width at half maximum (FWHM) of the smoothing kernel should be at least $2-3$ times the voxel dimension when analyzing data of a single subject and even larger for a group analysis, since this FWHM corresponds to the hemodynamic response that should be detected [79–81].

According to the matched filter theorem, the sensitivity of the pathology detection in a DTI group study is enhanced when the data sets are smoothed with a kernel that exactly matches the size and the shape of the expected pathology [78]. Since the size of the pathology is rarely known a priori, it is very hard to determine the optimal Gaussian kernel width to smooth the DTI data sets. Consequently, in the VBA literature of DTI data sets, a large range of isotropic smoothing kernel widths from 0 mm to as much as 16 mm is used, making the VBA method less standardized than it promised to be (see Table 6.18 for an overview and references). This large variability in the smoothing kernel width across studies is particularly problematic since Jones et al. (2005) demonstrated that the reported VBA results depend on the applied smoothing kernel width.

Besides the size, the matched filter theorem states that the shape of the smoothing kernel should correspond to the expected signal differences. Although the shape of a pathology is rarely known in advance, it will probably follow the affected

Reference	Voxel Size	FWHM [mm³]	FWHM [voxels]
Albrecht, 2007	1.8 x 1.8 x 3 mm³	10 x 10 x 10 mm³	5.6 x 5.6 x 3.3
Ardekani, 2003	1.8 x 1.8 x 5 mm³	0 x 0 x 0 mm³	0 x 0 x 0
Barnea-Goraly, 2003	1.9 x 1.9 x 5 mm³	4 x 4 x 4 mm³	2.1 x 2.1 x 0.8
Barnea-Goraly, 2004	1.9 x 1.9 x 5 mm³	4 x 4 x 4 mm³	2.1 x 2.1 x 0.8
Barnea-Goraly, 2005	1.9 x 1.9 x 5 mm³	4 x 4 x 4 mm³	2.1 x 2.1 x 0.8
Borroni, 2007	1.7 x 1.7 x 5 mm³	10 x 10 x 10 mm³	5.9 x 5.9 x 2
Borroni, 2008	1.7 x 1.7 x 5 mm³	10 x 10 x 10 mm³	5.9 x 5.9 x 2
Bruno, 2008	2.5 x 2.5 x 5 mm³	15 x 15 x 15 mm³	6 x 6 x 3
Burns, 2008	1.9 x 1.9 x 5 mm³	12 x 12 x 12 mm³	6.4 x 6.4 x 2.4
Chappel, 2006	1.7 x 1.7 x 5 mm³	8 x 8 x 8 mm³	4.7 x 4.7 x 1.6
Eriksson, 2001	2.5 x 2.5 x 5 mm³	8 x 8 x 8 mm³	3.2 x 3.2 x 1.6
Eriksson, 2001	2.5 x 2.5 x 5 mm³	10 x 10 x 10 mm³	4 x 4 x 2
Focke, 2008	1.9 x 1.8 x 2.4 mm³	8 x 8 x 8 mm³	4.2 x 4.4 x 3.3
Foong, 2002	2.5 x 2.5 x 5 mm³	6 x 6 x 6 mm³	2.4 x 2.4 x 1.2
Foong, 2002	2.5 x 2.5 x 5 mm³	16 x 16 x 16 mm³	6.4 x 6.4 x 3.2
Gimenez, 2008	1.8 x 1.8 x 3.4 mm³	8 x 8 x 8 mm³	4.4 x 4.4 x 2.4
Golestani, 2006	0.94 x 0.94 x 2 mm³	5 x 5 x 5 mm³	5.3 x 5.3 x 2.5
Kumar, 2008	1.8 x 1.8 x 2 mm³	10 x 10 x 10 mm³	5.6 x 5.6 x 5
Holzapfel, 2006	1.9 x 1.9 x 5 mm³	4 x 4 x 4 mm³	2.1 x 2.1 x 0.8
Kyriakopoulos, 2007	1.9 x 1.9 x 2.5 mm³	4 x 4 x 4 mm³	2.1 x 2.1 x 1.6
Li, 2007	1.9 x 1.9 x 3 mm³	6 x 6 x 6 mm³	3.2 x 3.2 x 2
Man-Cheuk, 2008	2.2 x 2.2 x 5 mm³	5 x 5 x 5 mm³	2.3 x 2.3 x 1
Menzies, 2008	2.3 x 1.9 x 4 mm³	8 x 8 x 8 mm³	3.5 x 4.2 x 2
Molko, 2004	1.9 x 1.9 x 2.8 mm³	5 x 5 x 5 mm³	2.6 x 2.6 x 1.8
Nagy, 2003	1.7 x 1.7 x 5 mm³	5 x 5 x 5 mm³	2.9 x 2.9 x 1
Padovani, 2007	1.7 x 1.7 x 5 mm³	10 x 10 x 10 mm³	5.9 x 5.9 x 2
Pagani, 2008	1.9 x 1.9 x 4 mm³	8 x 8 x 8 mm³	4.2 x 4.2 x 2
Park, 2004	1.7 x 1.3 x 4 mm³	3 x 3 x 3 mm³	1.8 x 2.3 x 0.8
Park, 2004	1.7 x 1.3 x 4 mm³	6 x 6 x 6 mm³	3.6 x 4.6 x 1.6
Park, 2004	1.7 x 1.3 x 4 mm³	9 x 9 x 9 mm³	4.8 x 6.9 x 2.4
Porto, 2008	2 x 2 x 2 mm³	9 x 9 x 9 mm³	4.5 x 4.5 x 4.5
Rose, 2008	1.9 x 1.9 x 5 mm³	5 x 5 x 5 mm³	2.6 x 2.6 x 1
Sach, 2004	3 x 3 x 3 mm³	6 x 6 x 6 mm³	2 x 2 x 2
Sage, 2007	0.98 x 0.98 x 1.2 mm³	6 x 6 x 6 mm³	6.1 x 6.1 x 5
Seok, 2007	1.7 x 1.7 x 2 mm³	6 x 6 x 6 mm³	3.5 x 3.5 x 3
Shergill, 2007	2.5 x 2.5 x 2.5 mm³	4 x 4 x 4 mm³	1.6 x 1.6 x 1.6
Shin, 2006	1.7 x 1.7 x 4 mm³	10 x 10 x 10 mm³	5.9 x 5.9 x 2.5
Skelly, 2007	1.6 x 2 x 3 mm³	10 x 10 x 10 mm³	6.3 x 5 x 3.3
Snook, 2007	2.3 x 1.7 x 3 mm³	4 x 4 x 4 mm³	1.7 x 2.4 x 1.3
Thivard, 2007	1.3 x 1.3 x 5 mm³	10 x 10 x 10 mm³	7.7 x 7.7 x 2
Vangberg, 20086	1.8 x 1.8 x 5 mm³	4 x 4 x 4 mm³	2.2 x 2.2 x 0.8
White, 2007	2 x 2 x 2 mm³	5 x 5 x 5 mm³	2.5 x 2.5 x 2.5
MEAN	1.9 x 1.9 x 3.9 mm³	7.6 x 7.6 x 7.6 mm³	3.9 x 4 x 2.2
ST. DEV.	0.4 x 0.4 x 1.2 mm³	3.2 x 3.2 x 3.2 mm³	1.7 x 1.7 x 1

Figure 6.10. *In this table, an overview of the full width half maximum (FWHM) of the isotropic smoothing kernels that is used in published VBA studies of DTI data sets is provided. The voxel size of the acquired images and the FWHM of the applied smoothing kernel (in mm) are displayed in the second and third column, respectively. In the right column, the FWHM of the smoothing kernels as a function of the number of voxels is presented.*

WM fiber bundle, without harming other WM structures or nearby GM tissues or CSF. To the best of our knowledge, all published VBA studies of DT images use an isotropic Gaussian smoothing kernel, which significantly increases the partial volume averaging of the data. As a result, signal intensities from GM, WM, and CSF are averaged prior to the application of the voxel-wise statistical testing. Due to the anisotropic nature of most WM structures, isotropic smoothing of DT images might potentially reduce the sensitivity and specificity of the pathology detection. We hypothesize that the use of anisotropic filtering methods can increase the robustness of the pathology detection in a VBA setting, since these methods better preserve the WM boundaries.
In our work, the effect of different isotropic and anisotropic smoothing kernel widths are evaluated in a VBA setting of DT images. In contrast to the study of Jones et al. (2005), in which real DTI data sets of schizofrenia patients were used, we evaluated the effect of smoothing on the VBA result in simulated DTI data sets with a predefined pathology. Consequently, quantitative measures of VBA sensitivity and specificity can be calculated for different smoothing kernel widths and filtering approaches. This significantly improves the assessment of different parameter settings in the voxel based analysis of DTI data sets.

6.2.2 Methods

6.2.2.1 Constructing simulated DTI data sets

The framework of simulating DTI data sets that is used in this study is based on the acquisition of 20 healthy subject DTI data sets and 20 DT images of Multiple Sclerosis (MS) patients (Fig. 6.11 (a)). These data sets were obtained on a 1.5 T MR scanner using an SE-EPI sequence with the following acquisition parameters: TR: 10.4 s; TE: 100 ms; diffusion gradient: 40 $mT.m^{-1}$; FOV = 256×256 mm^2; number of slices = 60; voxel size = $2 \times 2 \times 2$ mm^3; b = 700 $s.mm^{-2}$; acquisition time: 12 min 18 s. Diffusion measurements were performed along 60 directions with 10 b_0-images for a robust estimation of the diffusion tensors [57].
Based on our previous work, 20 simulated DTI data sets are constructed, containing pathologies in different WM structures with a predefined level of tissue degradation and a known location [82]. In addition, 20 simulated healthy subject DTI data sets without a pathology are constructed. The framework of the DT image simulation can be summarized as follows [82]:

- All 40 DTI data sets are transformed to the MNI space with an affine transformation based on the FA maps (Fig. 6.11 (b)).
- A population specific DTI atlas was constructed from these affinely aligned 40 data sets by transforming the data sets non-rigidly to the population specific atlas space (Fig. 6.11 (c) and (d)) [39].

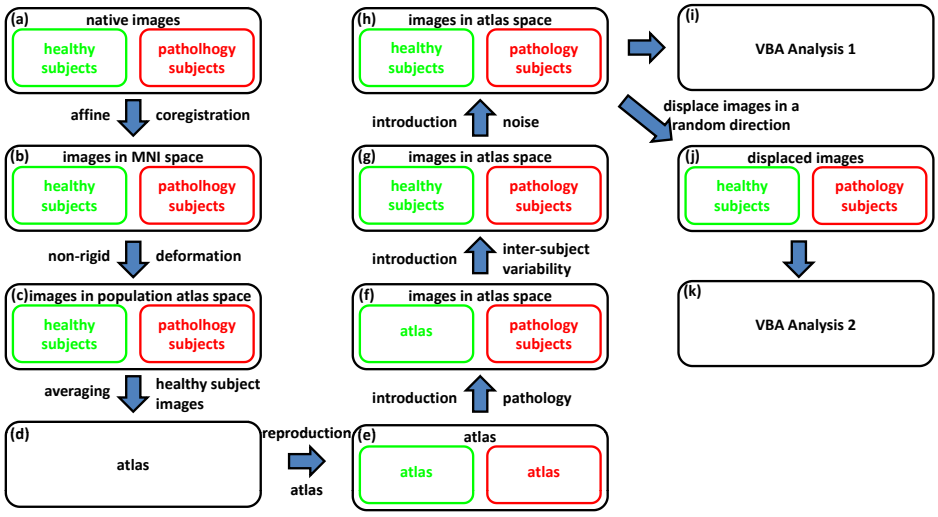

Figure 6.11. *In the construction framework of the simulated data sets, native images of healthy and pathology subjects (a) are transformed to the MNI template using an affine transformation (b). Thereafter a DTI atlas is constructed from these images (c,d). This atlas is reproduced 40 times (e) and a simulated pathology is added in half of these atlas data sets (f). Subsequently, inter-subject variability (g) and noise (h) are added to all images. The resulting data sets are used in the VBA Analysis 1 (i). In VBA Analysis 2, these data sets are displaced in a random direction by different distances (j,k).*

- The resulting atlas is regarded as the fundamental image and is copied 40 times (Fig. 6.11 (e)).

- In half of these 40 atlases, the diffusion properties are altered in a known WM location to simulate a pathology (Fig. 6.11 (f)). In this work, the transverse diffusivity, i.e. the average of the second and third eigenvalues, is increased by six different levels to simulate a microstructural breakdown of the WM. These six levels of pathology correspond with an FA decrease of 7%, 10%, 13%, 16%, 19%, and 22%. In Fig. 7.3, the location, size, and extent of the 19 simulated WM pathologies is displayed, whereby every pathology is given a different color. Diffusion alterations have been reported in these WM structures in various studies. As can be seen in Fig. 7.3, the pathologies differ in size, ranging from 24 to 187 voxels in which the diffusion properties are altered. In order to study the effect of the pathology size on the VBA results for different smoothing kernels, the group of pathologies is divided in three subgroups: small (i.e. number of voxels smaller than 50), medium (i.e. number of voxels between 50 and 65), and large (i.e. number of voxels larger than 65) pathologies.

- Inter-subject variability of the diffusion properties is introduced in all atlas images, i.e. in the 20 original atlases and in the 20 atlases with a pathology (Fig. 6.11 (g)). The inter-subject variability of the eigenvalues was estimated from 75 healthy subject DTI data sets based on a PCA analysis (see [82] for more information).
- A realistic amount of Rician noise is added to the resulting simulated data sets (Fig. 6.11 (h)).

6.2.2.2 Smoothing methods

In this work, isotropic and anisotropic smoothing approaches for filtering the FA maps before applying voxel based statistical tests are evaluated.

Isotropic smoothing: To the best of our knowledge, all VBA studies of DT images apply an isotropic, Gaussian smoothing kernel before performing the voxel-wise the statistical tests. To evaluate the effect of the isotropic smoothing kernel size on the sensitivity and the specificity of the VBA analysis, the data sets are smoothed with kernels of different full width at half maximum (FWHM): 3 mm, 6 mm, 9 mm, and 12 mm (σ of 1.27, 2.54, 3.81, and 5.08), corresponding with 1.5, 3, 4.5, and 6 voxels.

Anisotropic smoothing: Anisotropic smoothing has already been applied to denoise diffusion tensor images [83]. In this work, an edge and corner preserving filter for magnitude MR data was constructed using an anisotropic Gaussian smoothing kernel shaped by the eigenvalues and eigenvectors of a local gradient tensor and applied to the FA maps [84]. During smoothing, the Rice distribution of the magnitude MR data was taken into account as to minimize possible bias in the estimation of the noiseless, underlying signal. Analogously as in the isotropic smoothing approach, the effect of the smoothing kernel width on the VBA results is evaluated by smoothing the data sets with a similar range of FWHMs: 3 mm, 6 mm, 9 mm, and 12 mm.

6.2.2.3 Analyses of smoothing methods using simulated DTI data sets

The effect of smoothing on the VBA results is evaluated in two conditions.

Analysis 1: 20 simulated healthy and 20 pathology data sets are constructed according to the steps (a)-(h) of Fig. 6.11. The FA maps of these data sets are subsequently smoothed before the statistical tests are performed in each voxel. Since all images are located in the atlas space, no residual misalignment is present. The VBA results can thus be interpreted as the significant differences between the healthy and the pathologic subjects under perfect

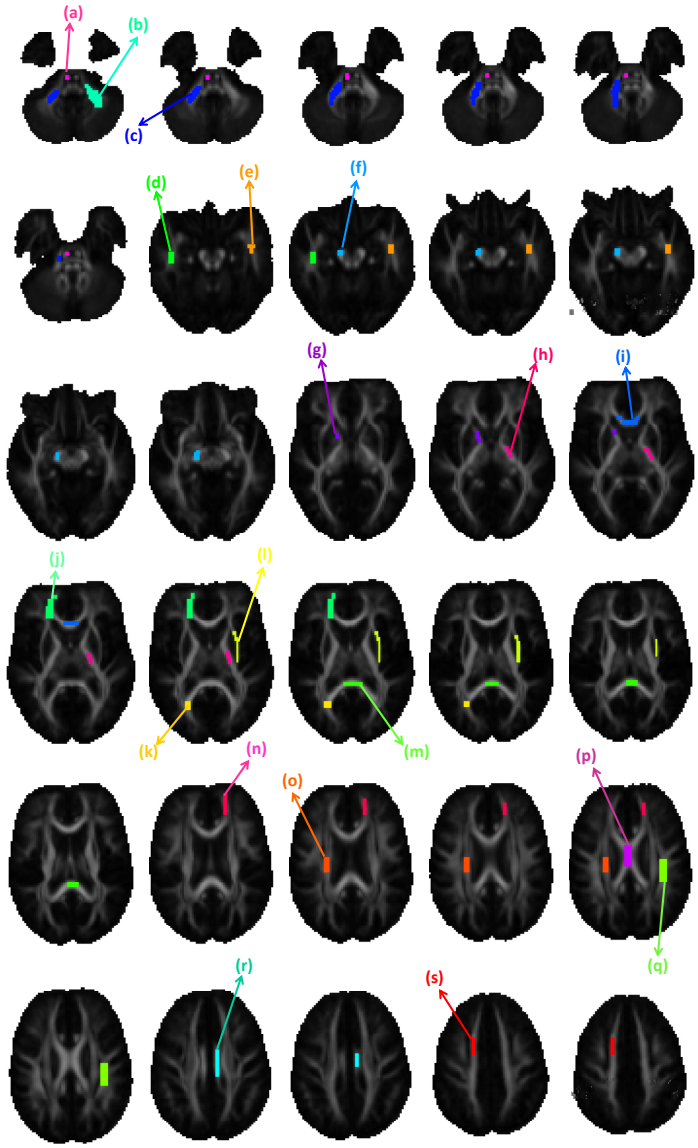

Figure 6.12. *The simulated pathology is visualized on 30 axial FA slices. The various pathology clusters are thereby given a different color: (a): cortico-spinal tract; (b) and (c): cerebellar peduncle; (d) and (e): inferior longitudinal fasciculus; (f): cerebral peduncle; (g): anterior limb of the internal capsule; (h): posterior limb of the internal capsule; (i): genu of the corpus callosum; (j): forceps minor; (k): forceps major; (l): capsula externa; (m): splenium of the corpus callosum; (n): anterior region of the corona radiata; (o): superior region of the corona radiata; (p): body of the corpus callosum; (q): superior longitudinal fasciculus; (r): cingulum; (s): superior region of the corona radiata.*

coregistration (see Fig. 6.11 (i)). In this setting, the validity of the matched filter theorem and the effect of different smoothing kernel widths and filtering approaches on the sensitivity and specificity of the pathology detection is examined.

Analysis 2: Since smoothing is also performed to correct for residual misalignment errors, coregistration inaccuracies are simulated. To this end, each of the 40 DTI data sets, which were derived in Analysis 1, are displaced by a certain distance in a random direction. This approach of simulating image misalignment was previously applied by Ashburner and Friston (2000). In their work, probability maps were translated in a fixed direction (left-right). To examine the effect of residual misalignment on the VBA results, the 40 DTI data sets are displaced by a distance d_i^k in a random direction θ_i ($i = 1, ..., 40$) (see Fig. 6.11 (j)). The distances d_i^k are thereby calculated as a Gaussian distribution around a given displacement k ($k = 2, 4, 6, 8$ mm, $\sigma = 0.65$ mm). The FA maps of the deformed data sets are subsequently smoothed and statistical tests are executed in each voxel(see Fig. 6.11 (k)).

After filtering all the data sets with the appropriate smoothing method and kernel width, a non-parametric Mann-Whitney U test is performed at every voxel to compare the FA values of the healthy and the pathologic subjects. In this work, only the FA is compared, since this is the diffusion measure that is most frequently reported in the literature. A correction for multiple comparisons needs to be incorporated subsequently to reduce the chance of Type I errors. In this work, the false discovery rate controlling method of Benjamini and Hochberg was used to correct the p-values for multiple comparisons [62]. A false discovery rate bound of 0.05 was thereby applied.

6.2.2.4 Measures of VBA accuracy

Since the location, size and extent of the WM pathology is predefined in the simulated data sets, the VBA results can be compared with this ground truth quantitatively. A very simple measure describing the accuracy of the VBA approach is to count the number of pathologies that is detected by the VBA study. This is the most important quantitative measure since it determines if this pathology would be reported in the results of the VBA study.
In addition, the sensitivity and specificity of the statistical VBA results are calculated. The sensitivity is defined as the ratio of the number of true positive voxels and the sum of the number of true positive and false negative voxels. The specificity is calculated as the ratio of the number of true negative voxels and the sum of the number of true negative and false positive voxels. A receiver-operating characteristic (ROC) plot, displaying the true positive rate (=sensitivity) as a function

of the false positive rate (=100−specificity), can then be drawn. The closer the points in the ROC plot are located to the upper left corner, the higher the overall accuracy of the analysis [85].

6.2.3 Results

The effect of isotropic and anisotropic smoothing on an FA image is visualized for a random axial slice in Fig. 6.13 for different smoothing kernels with a FWHM ranging from 0 mm to 12 mm. As can be observed, the different WM structures that can be discriminated on the original FA map are blurred after isotropic smoothing with larger FWHM. In addition, the overall FA intensity of the WM is decreased after isotropic smoothing due to the averaging of WM with GM and CSF, which contain much lower FA values. Since the image boundaries are preserved during anisotropic smoothing, a filtered signal is observed in the WM, without the inclusion of GM or CSF intensities. As can be seen in Fig. 6.13, the different WM structures can be discriminated even after anisotropic smoothing with a large FWHM.
The VBA results of Analysis 1 are displayed on 10 axial slices for both smoothing approaches and different smoothing kernel widths in Fig. 6.14. A level of pathology corresponding with an FA decrease of 19% was thereby introduced. The voxels that contain a ground truth pathology are colored in green, whereas the VBA results are colored in red. Consequently, the voxels in which the VBA results and the ground truth overlap, are colored in yellow. A green, red, and yellow color on the axial slices of Fig. 6.14 thus represent the presence of false negative, false positive, and true positive results, respectively. Voxels in which the background FA values are displayed correspond with true negative results. It can be seen in Fig. 6.14 that the number of false positive and false negative results increase and the number of true positive results decrease for increasing isotropic smoothing kernel width. On the other hand, a relatively high number of yellow true positive voxels are observed at larger anisotropic smoothing kernel widths.
Since the smoothing is performed principally to meet the matched filter theorem, the validity of this theorem is analyzed using the simulated data sets. To this end, the FWHM that produced the highest sensitivity to detect a certain pathology is mapped against the size of this pathology, as can be seen in Fig. 6.15. This is done for different levels of pathology, corresponding with an FA decrease of 10%, 13%, 16%, and 19%. In order to obtain more continuous results, smoothing kernel widths from 1 mm to 12 mm were used in this analysis. As can be observed in Fig. 6.15, a significant correlation is found between the optimal FWHM and the size of the pathologies when the data was smoothed with an anisotropic kernel. The correlation was measured statistically by the Spearman correlation coefficient ρ, which varied between 0.485 and 0.697 for the anisotropic smoothing results. It can also be observed in Fig. 6.15 that no correlation was found between the

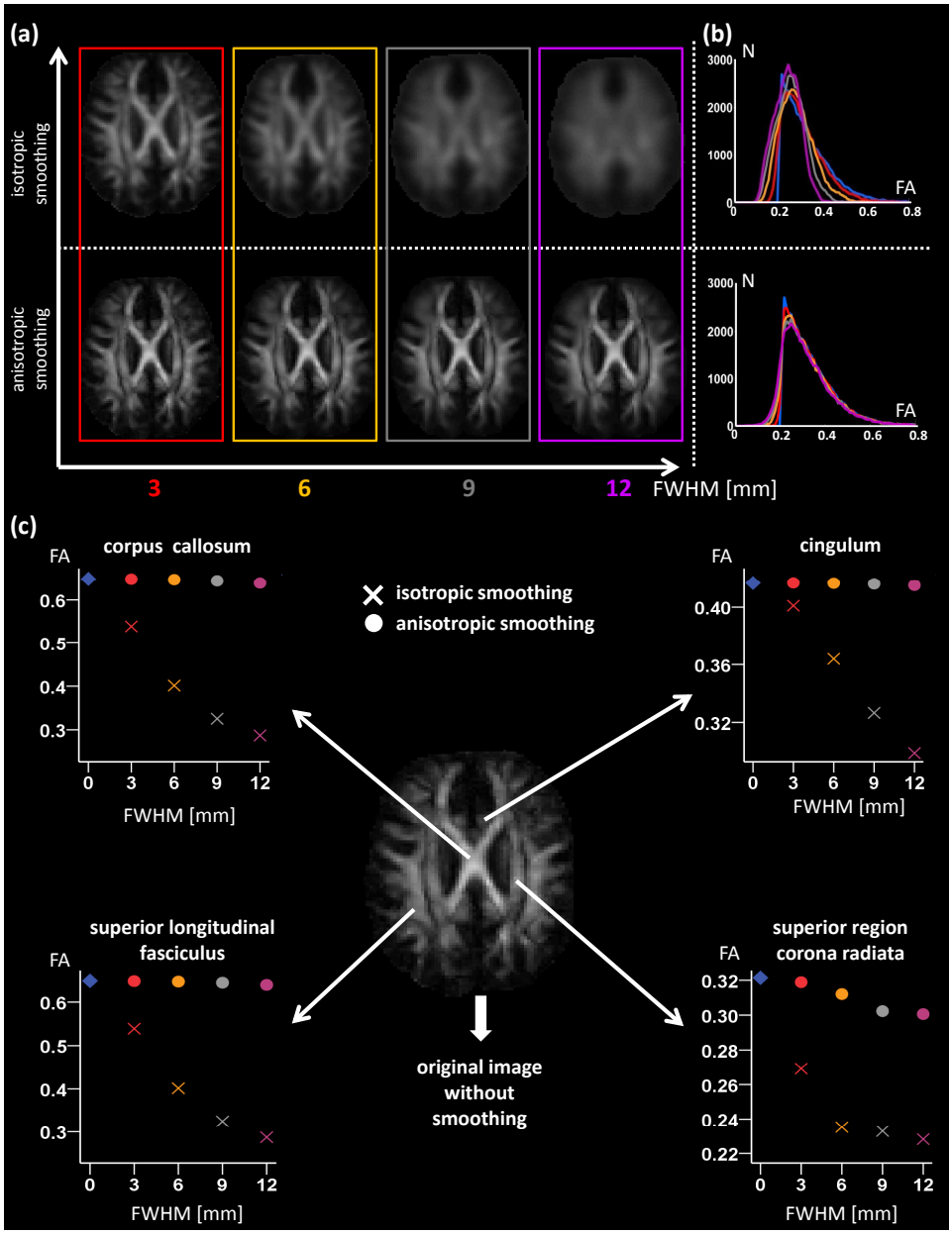

Figure 6.13. *In (a), an axial FA slice is shown after different levels of isotropic and anisotropic smoothing. The FA histograms after smoothing with different kernels are displayed in (b), using an FA threshold of 0.2 to only include the WM information. In (c), the effect of smoothing on the FA values of different WM structures is demonstrated.*

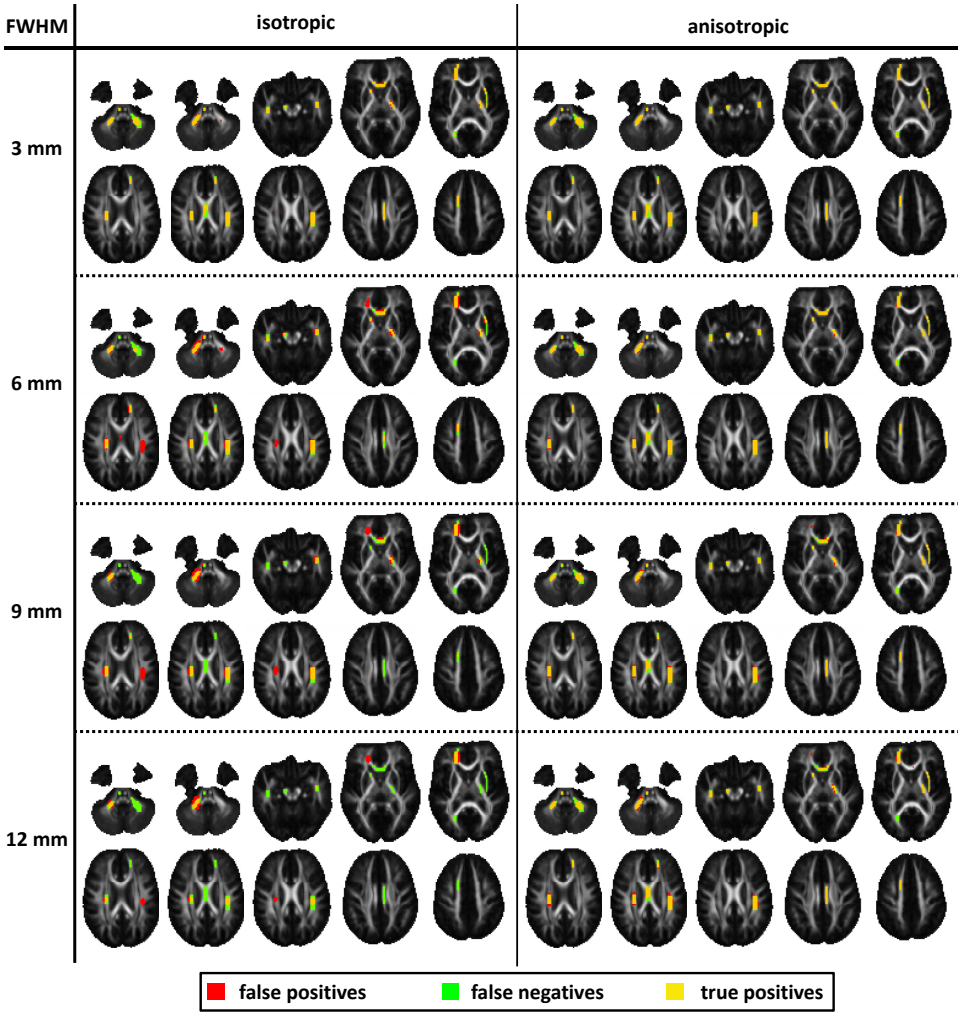

Figure 6.14. *VBA results are visualized using different smoothing methods and various smoothing kernel widths. The voxels that contain a ground truth pathology and the VBA results are displayed in green and red, respectively. When both overlap, a yellow color is assigned to that voxel. False positive, false negative, and true positive results are therefore colored in red, green, and yellow, respectively. The voxels in which the background FA map is shown can be regarded as containing true negative results.*

optimal FWHM and the size of the pathologies in the case of isotropic smoothing (i.e. Spearman correlation coefficient ρ between 0.122 and 0.18, and a p>> 0.5). An isotropic smoothing kernel with a FWHM of 3 mm almost always resulted in the highest sensitivity to detect the pathologies of various sizes.
In Fig. 6.16, the percentage of detected pathologies by the VBA analysis is displayed for different levels of simulated residual misalignment, for the two smoothing methods, and for different smoothing kernel widths. In addition, the analysis was performed for three groups of pathologies with different sizes. In the left column, the results are displayed for the pathologies that contain less than 50 voxels. In the middle and the right column, the results are shown for the pathologies with a number of voxels between 50 and 65 and with a number of voxels larger than 65, respectively. In the upper row, the results of the Analysis 1 are displayed, when no residual misalignment was added to the data sets. In the second, third, and fourth row of Fig. 6.16, results are shown after displacing the data sets with a mean distance of 2 mm, 4 mm, and 6 mm, respectively. All results were derived for a specific level of transverse diffusivity increase, which corresponded with a mean FA decrease of 22%. A pathology was assigned as detected when at least 1 voxel of this pathology was significant after the Benjamini-Hochberg correction for multiple comparisons. As can be observed in the upper row of Fig. 6.16, all pathologies were detected in the VBA analysis using anisotropic smoothing when no residual misalignment was present. The pathology detection rate obviously decreased for an increasing level of residual misalignment, especially for the smaller lesions, as can be seen in the left column. Additionally, a lower detection of pathologies was observed when the data sets were smoothed isotropically, with a FWHM > 3 mm. In particular, the smaller pathologies were detected less frequently. The pathology detection rate after isotropic and anisotropic are compared statistically using a non-parametric Mann-Whitney U-test. In Fig. 6.16, '*' denotes statistical significance at the 0.05 level, '**' at the 0.01 or lower level.
The sensitivity and the specificity of the VBA results are displayed in an ROC graph in Fig. 6.17 for the different smoothing approaches, various kernel widths, and different levels of pathology. In Fig. 6.17 (a), an ROC curve is visualized for perfectly aligned data sets. In Fig. 6.17 (b)-(d), the true positive and the false positive rate are displayed for the simulation of different levels of residual misalignment. The true positive and false positive rate were calculated for six levels of pathology, as reflected by an FA decrease of 7%, 10%, 13%, 16%, 19%, and 22%.

6.2.4 Discussion

The idea of performing a voxel-wise analysis of medical images originates from the study of fMRI and PET data sets [86–89]. In recent years, this method is increas-

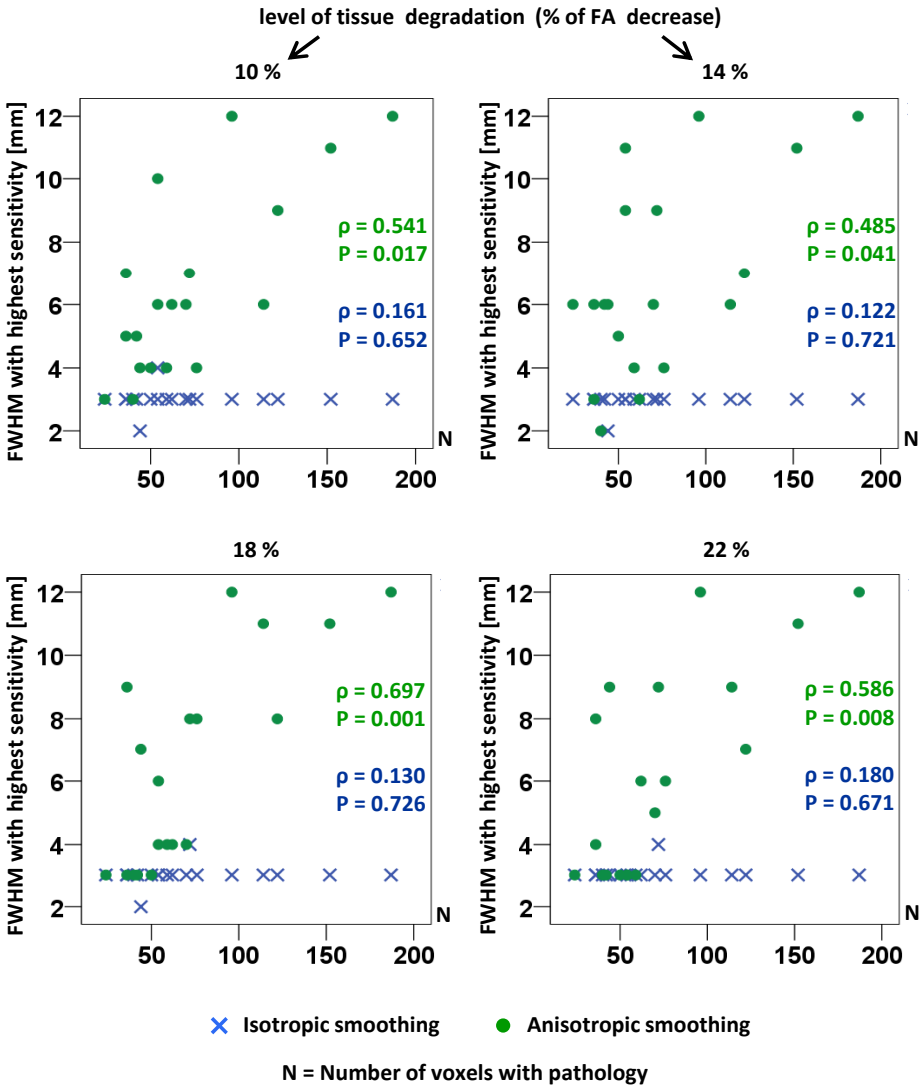

Figure 6.15. *The isotropic and anisotropic smoothing kernel widths that resulted in the highest sensitivity for pathology detection are visualized as a function of the size of the different pathologies. This analysis is performed using different levels of tissue degradation as reflected by the averaged FA decrease.*

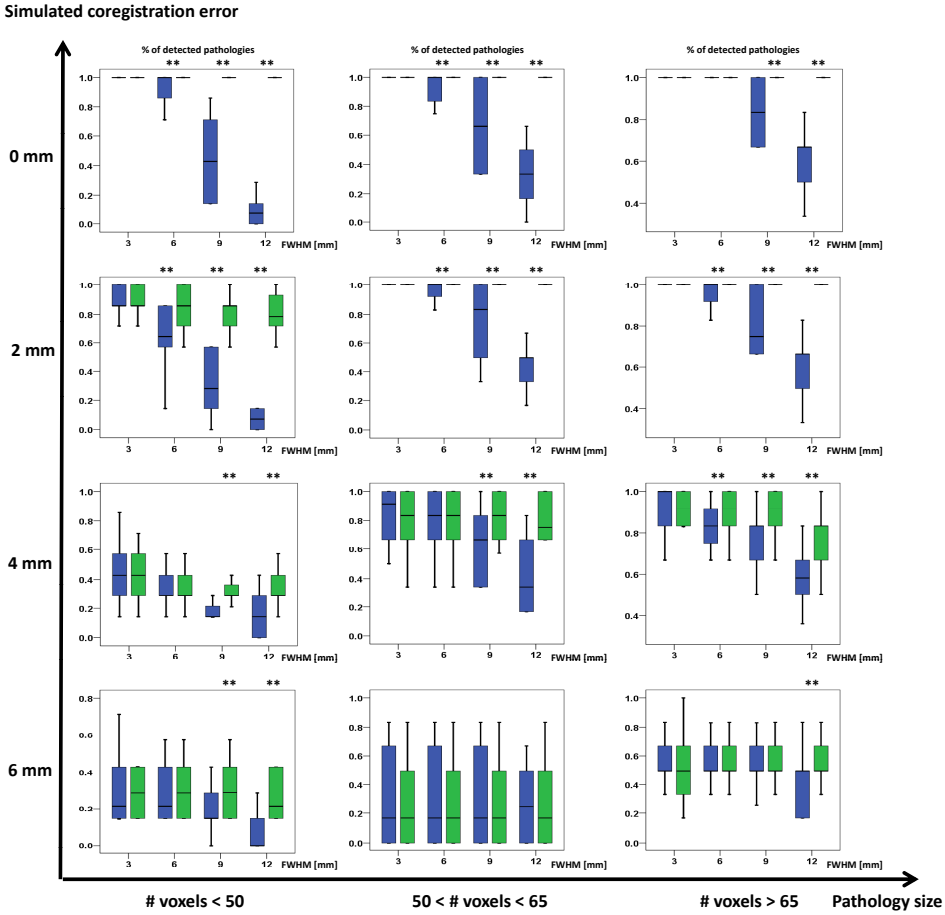

Figure 6.16. *The effect of isotropic and anisotropic smoothing kernel widths on the percentage of detected pathologies is examined. In the upper row, the results of VBA analysis 1 are displayed. In the other rows, the results are shown after an initial displacement of the data sets in a random direction by different distances (i.e. VBA analysis 2). All results are separately displayed for three pathology groups, depending on the size of the pathology.*

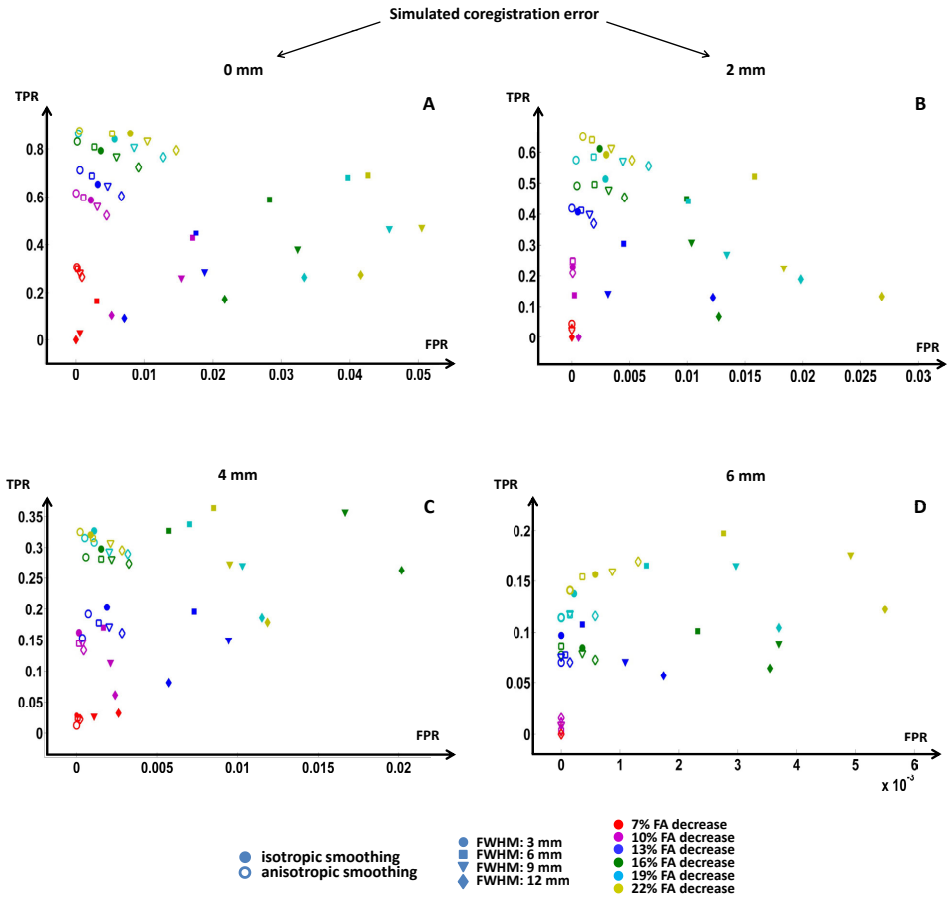

Figure 6.17. *The true positive and false positive rate is displayed for VBA Analysis 1 (left plot) and VBA Analysis 2 (all other plots). This is done for different isotropic and anisotropic smoothing kernel widths and for a pathology level corresponding with an FA decrease of 16%.*

ingly being applied to examine DTI data sets of subjects with various pathologies. In VBA, the whole brain is checked for patient-control differences. This is done in a standardized, automatic way, including a coregistration of the data sets to a template and a subsequent smoothing of the transformed images, followed by a voxel-wise statistical analysis and a post-hoc correction for multiple comparisons. Although this approach to analyze a group of data sets has many advantages compared to the ROI based method, recent studies suggest that its results are not always accurate and disease specific, because they depend on the parameter settings and implementations of the analysis [27, 73, 74]. Since fMRI, PET, and DT images are different in nature, there is no reason to assume that the optimal im-

plementation and parameter settings to analyze fMRI and PET images should also be applied to examine DTI data sets. For example, the image resolution of fMRI ($3-6$ mm) and PET ($5-7$ mm) data sets is significantly larger compared to DTI (2 mm in this study, see Table 6.18 for the image resolution in other studies). Since fMRI and PET aim to trace hemodynamic responses, which are representative for functional activation in the brain and are expressed on a scale of $5-8$ mm, a 'rule of thumb' was introduced, stating that the FWHM of the applied smoothing kernel should be at least be $2-3$ times the voxel dimension. Obviously, since DTI is totally unrelated to the hemodynamic response, there is no reason to apply this 'rule of thumb' in the analysis of DTI data sets. In order to fulfil the requirements of the matched filter theorem in DTI, a smoothing kernel should be used that matches the size and the shape of the underlying WM pathology. Since this depends on the specific pathology that is studied and on the size and shape of the specific WM structure in which the pathology is situated, it is very hard to postulate a 'rule of thumb' for the smoothing kernel width in the voxel based analysis of DT images. As aforementioned, this is reflected by the large range of isotropic smoothing kernel widths from 0 mm to as much as 16 mm that is reported in the DTI literature, making the VBA method less standardized than it promised to be (see Table 6.18). This large variability in the smoothing kernel width across studies is particularly problematic since Jones et al. (2005) demonstrated that the reported VBA results depend on the applied smoothing kernel width. In their work, Jones et al. (2005) compared the DTI data sets of healthy subjects and schizofrenia patients using a voxel based analysis with different smoothing kernels. No significant results were reported when the data sets were smoothed with a FWHM smaller than 7 mm. For a FWHM larger than 7 mm, a first cluster of significant voxels appeared and for a FWHM larger than 9 mm, a second cluster appeared. Although this study demonstrated the dependency of the VBA results on the smoothing kernel width, no conclusions could be drawn regarding the optimal smoothing kernel width for the analysis of these DTI data sets, since the underlying pathology was not known. The two clusters that appeared at larger smoothing kernels could indeed be assigned as true positive as well as false positive results. In addition, no conclusions could be drawn regarding the presence of true and false negative results.

After reviewing the VBA literature of DTI data sets, it can be concluded that all voxel based studies of DTI data sets use an isotropic Gaussian smoothing kernel, analogously as in the analysis of fMRI and PET data sets (see Table 6.18). An isotropic Gaussian smoothing method is applied in the VBA analysis of DTI data sets, since it is available in software packages, such as SPM. The use of this isotropic smoothing approach also helps to ensure the assumptions underlying the theory of Gaussian random fields, because smoothing renders the data more Gaussian distributed. The Bonferroni adjustment to control for false positive rate is generally considered to be excessively conservative since test statistics on neighboring vox-

els are correlated, and therefore the actual number of independent comparisons is less than the number used for correction. Since the assumptions of the Gaussian random field theory are not met when the data sets are smoothed anisotropically, a correction for multiple comparisons based on the false discovery rate method of Benjamini and Hochberg was used after the nonparametric statistics were applied in each voxel [62, 90]. In contrast to fMRI and PET, which investigate image intensity alterations in the GM, DTI examines the highly structured and anisotropic WM bundles. The application of an isotropic filter therefore averages information from different WM structures, from WM and GM or from WM and CSF, which can reduce the sensitivity and specificity of the VBA results. Due to the anisotropic nature of the WM, WM pathologies will also be rarely isotropic. Therefore, although the size of the pathologies is rarely known in advance, the shape of the pathology is likely to follow the shape of the corresponding WM structure.

In this study, simulated DTI data sets with a predefined pathology (i.e. a known size, shape, location, and level of diffusion alterations) were used to evaluate the sensitivity and specificity of the pathology detection in a VBA analysis involving isotropic as well as anisotropic smoothing with different FWHM. Our results of Fig. 6.15 indicate that the requirements of the matched filter theorem are satisfied when the data are filtered with an anisotropic smoothing kernel, since a significant correlation was found between the size of the pathology and the smoothing kernel size with the highest sensitivity. As can be observed in Fig. 6.15, the isotropically smoothed data are not in agreement with the matched filter theorem, due to the difference in shape between the isotropic smoothing kernel and the pathologies, and the reduced sensitivity of pathology detection at higher FWHM. The percentage of detected pathologies decreased for increasing FWHM of the isotropic smoothing kernel, since signal from other structures and tissues is included in the analysis of a WM voxel after isotropic smoothing (see Fig. 6.16). As observed in Fig. 6.16, especially the detection rate of the smaller pathologies decreased when larger smoothing kernels were used to filter the data. On the other hand, the percentage of pathology detection was not reduced for increasing FWHM of the anisotropic smoothing kernel. For a FWHM larger than 3 mm, the VBA results after anisotropic smoothing were significantly better in detecting the pathologies compared to the VBA results after isotropic smoothing. Besides a lower sensitivity, the specificity was also reduced for increasing FWHM of the isotropic smoothing kernel, as was observed in the ROC curves of Fig. 6.17. The difference in sensitivity and specificity between the smoothing approaches was lower for increasing levels of simulated residual misalignment, due to an overall decrease in the VBA sensitivity and specificity. In this context, note that a simulated coregistration error of 4 mm or 6 mm (or $2-3$ voxels) is much larger compared to the observed misalignment after non-rigid coregistration of real data sets. In addition, the simulation of residual misalignment is limited because a uniform displacement is applied to every voxel of

each data set. In practice, however, misalignment is spatially dependent and thus not uniform.
In conclusion, our results indicate that the sensitivity as well as the specificity of the pathology detection are significantly reduced when the data sets are smoothed isotropically with a FWHM larger than 3 mm in a VBA study. DTI researchers should therefore be careful in adopting parameter settings that are accepted for use in fMRI or PET studies to the group analysis of DTI data sets. In this work, we propose to apply an anisostropuic smoothing approach in the DTI group studies to increase the SNR and preserve the WM boundaries. Using simulated DTI data sets, we demonstrated that the use of anisotropic smoothing kernels can significantly increase the sensitivity and the specificity of detecting a pathology in a VBA study.

6.3 A voxel based diffusion tensor study of patients with multiple sclerosis

6.3.1 Introduction

Although it has been demonstrated that conventional MR images are sensitive for detecting M) lesions, the T_2 lesions reflect the clinical manifestations only to a limited extent [91, 92]. Recently, more advanced imaging techniques, such as DTI, have been employed to examine MS [93]. DTI provides in vivo information about the WM fiber architecture. It is therefore increasingly being applied to study neurological disorders, such as MS [94]. Diffusion measures that are often used to quantify WM damage include the FA, which is a normalized measure of the diffusion anisotropy, and the MD, which is the averaged diffusion in a voxel. Recent studies suggest that the longitudinal and the transverse diffusivities $\lambda_{\|}$ and $\lambda_{\perp}$ can provide additional information about demyelination and axonal loss in MS patients [44–49].

Different post-processing approaches can be used to compare the DTI data sets of MS patients and healthy control subjects. In a first method, ROIs are drawn to delineate different corresponding WM structures in the DTI data sets of all subjects separately. Subsequently, the diffusion measures of healthy and MS subjects that were derived from these ROIs are compared [10–12, 14–17, 95, 96]. Other studies use diffusion tensor tractography to select the WM bundles of interest and compare the diffusion measures of these specific fibers between different subjects [97–102]. A more automated approach to analyze groups of DTI data sets is provided by VBA. In this method, all DTI data sets are transformed to a template, followed by a smoothing of the images and a statistical analysis in every voxel. In this way, the whole brain is evaluated for group differences, without the need for an a priori hypothesis regarding the spatial location of the pathology. This VBA method was recently applied to examine DTI data sets of MS patients [103–105]. In a similar automated approach, called TBSS, diffusion data are projected onto a tract representation, or skeleton, whereafter the statistical analysis is restricted to the voxels on this skeleton [52]. Recently, this method was applied by Dineen et al. (2008) and Roosendaal et al. (2008) to evaluate differences between control subjects and MS patients [106, 107].

Cognitive deterioration is commonly reported in MS patients, and can present itself as an impairment of recent memory, sustained attention, verbal fluency, conceptual reasoning, and visual-spatial perception [108, 109]. The Paced Auditory Serial Addition Test (PASAT) and its visual analogue, the Paced Visual Serial Addition Test (PVSAT) are commonly used experimental paradigms to evaluate sustained attention, working memory and speed of information processing in MS [110]. It has been

suggested that cognitive disabilities in MS patients may be related to white matter lesions and normal appearing brain white matter (NAWM) in frontal, temporal, as well as parietal regions, although the exact correspondence of cognitive dysfunction with the underlying neuropathology remains unclear [108, 111–119]. Since DTI provides measures of WM integrity, it is therefore an interesting technique to investigate the correlation of WM damage with cognitive function in MS patients. Previous studies investigated the relation between WM injury and cognitive performance in patients with MS [106, 112, 113, 120]. Rovaris et al. examined the relationship between DTI and cognition in relapsing-remitting (RR) MS patients using a whole brain histogram analysis [114]. They found moderate correlations between the MD and neuro-psychological test scores that measured memory, speed of information processing and verbal fluency. Lin et al. found that the MD of the corpus callosum correlated with the PASAT score [121]. More recently, Dineen et al. examined the whole brain for correlations of FA and cognitive dysfunction [106]. They reported significant correlations of PASAT and FA in the body and splenium of the corpus callosum, the forceps major, the left cingulum, the right inferior longitudinal fasciculus, the left superior longitudinal fasciculus, the arcuate fasciculus. In their study, Mesaros et al. (2009) observed correlations of PASAT and FA in the corpus callosum [105].

The aim of this study was to examine differences in FA, $\lambda_{\parallel}$, $\lambda_{\perp}$, and MD between healthy subjects on the one hand and mildly and moderately affected MS patients on the other hand. In addition, the relationship between the PASAT and PVSAT tests of cognitive decline and microstructural WM breakdown, as assessed by the DTI measures, was studied in an automated whole brain analysis. To this end, an optimized VBA approach was used to compare the diffusion properties of all subjects in every brain voxel and to correlate them with PASAT and PVSAT scores.

6.3.2 Methods

6.3.2.1 Subjects

Twenty patients with definite multiple sclerosis according to the recently revised McDonald criteria were included [122, 123]. Enrolled subjects did not have a relapse for at least 30 days before entry into the study, did not use sedatives, and had a visual acuity above $20 - 40$, as measured on a Snellen chart. Ten patients with an expanded disability status scale (EDSS) between 0 and 3, referred to as MS group 1, and ten patients with an EDSS between 4 and 7, referred to as MS group 2, were selected [124]. MS patient group 1 contained 9 relapse-remitting MS patients and 1 secondary-progressive patient, whereas 4 relapse-remitting and 6 secondary-progressive MS patients were included in group 2. A control group of ten healthy volunteers was matched to both patient groups for age, gender and educational

	controls	MS1	MS2
number of subjects	10	10	10
gender (f/m)	5/5	5/5	4/6
MS type (RR/SP)	na	9/1	4/6
age (year, mean ± sd)	42 ± 10	43 ± 9	41 ± 7
education (year, mean ± sd)	14 ± 2	14 ± 2	13 ± 2
PASAT (mean ± sd)	53 ± 5	49 ± 9	46 ± 13
EDSS (mean ± sd)	na	2 ± 1	6 ± 1
disease duration (mean ± sd)	na	12 ± 7	11 ± 5

Figure 6.18. *Study information.*

level. Volunteers using medication, having a first or second degree relative with MS, or having visual impairment were excluded. The demographics, educational level, EDSS, and PASAT scores for the three subject groups are presented in Fig. 1. All subjects were right handed. The study was approved by the hospital ethics committee and all subjects gave written informed consent before entering the study.

6.3.2.2 Cognitive tests

During the PASAT, subjects were presented with 61 numbers between 1 and 9, at a rate of one per three seconds. After each stimulus, starting with the second, subjects had to calculate the sum of the two last stimuli, and vocalize their answer. During PVSAT the same task was performed. Numbers however, were presented on a computer screen [110]. Both procedures were explained and practiced. The PASAT and PVSAT tests were performed before as well as during scanning. Patients were asked not to vocalize their answers when tested in the scanner, in order to minimize motion and susceptibility artifacts. Instead, they were asked to activate a pneumatic switch with their right hand when the answer was ten or higher. This procedure was adapted from Mainero et al. (2004), and used for both PASAT and PVSAT responses.

6.3.2.3 Image acquisition

DTI data sets were obtained on a 1.5 T MR scanner using an SE-EPI sequence with the following acquisition parameters: TR: 10.4 s; TE: 100 ms; diffusion gradient: 40 $mT.m^{-1}$; FOV = 256×256 mm^2; number of slices = 60; voxel size = $2 \times 2 \times 2$ mm^3; b = 700 $s.mm^{-2}$; acquisition time: 12 min 18 s. Diffusion measurements

were performed along 60 directions with 10 b_0-images for a robust estimation of the diffusion tensors [57]. In the same scanning session a T_1-weighted magnetization prepared rapid acquisition gradient recalled echo image (MPRAGE, $1 \times 1 \times 1\ mm^3$, TE/TR 3.76/1700 ms) and a T_1-weighted spin echo image (SE, $1 \times 1 \times 1.5\ mm^3$, TE/TR 15/700) were also obtained.

6.3.2.4 Image processing

DTI data sets were processed as follows:

- From the EPI MNI template, a custom FA based template was constructed as described in Jones et al. (2002). All DTI data sets are transformed to this custom FA atlas with an affine transformation using MIRIT based on the FA maps [36]. The PPD tensor reorientation strategy was thereby incorporated [34, 35].
- A population specific DTI atlas was constructed from these affinely aligned data sets by transforming the data sets non-rigidly using a viscous fluid model and mutual information to the population specific atlas space [37, 39].
- All affinely coregistered data sets are transformed to this population specific atlas using high dimensional coregistration algorithm that was adopted to include all tensor information during the iterative alignment procedure [37]. Thereafter, the FA, $\lambda_\parallel$, $\lambda_\perp$, and MD images are calculated for all data sets in atlas space.
- The resulting images are smoothed with an adaptive, anisotropic smoothing kernel (FWHM = 3 mm). The spatially dependent, anisotropic kernel was estimated from the FA maps and subsequently applied to the FA, $\lambda_\parallel$, $\lambda_\perp$, and MD images. By using an adaptive, anisotropic smoothing kernel, the WM boundaries are preserved. As a result, the partial volume averaging of WM tissue with gray matter or cerebro spinal fluid is reduced, compared to a generally applied isotropic filter method.

After this pre-processing of the data sets, two analyses were performed:

Analysis 1: the diffusion properties of the different subject groups, i.e. the control group, MS patient group 1, and MS patient group 2, are compared using an analysis of variance (ANOVA) in each voxel. A correction for multiple comparisons based on the false discovery rate (FDR) (q-value threshold of 0.1) was thereby applied [62]. In order to verify the specific differences between the various groups, Mann-Whitney U-tests were subsequently applied between the control group and the MS patient group 1, the control group and the MS

patient group 2, and between both MS patient groups, including an FDR based correction for multiple comparisons.

Analysis 2: Spearman correlation tests are performed in each voxel to quantify the relation between the different diffusion properties and the various cognitive test results. Again, an FDR based correction for multiple comparisons was performed (q-value threshold of 0.1) [62].

6.3.3 Results

The three subject groups did not significantly differ in age, gender distribution, disease duration or educational level (Table 1). MS group 2 contained significantly more SP MS patients than RR MS patients, compared to MS group 1 (Chi square test, $p < 0.05$). No significant correlation between EDSS and pre-scan PASAT was found (Spearman's $\rho = -0.015$, $p = 0.949$). In addition, cognitive performance, assessed with the pre-scan PASAT, did not differ significantly between the experimental groups (Table 1). However, the PASAT and PVSAT scores that were acquired during scanning were significantly lower in the MS group 2 compared to the control group (see Fig. 2). In an ANOVA model, a significant difference between the subject groups was found ($p < 0.05$). A Tukey HSD post hoc comparison showed a significantly lower number of correct answers during the scan session for MS patient group 2, compared to controls ($p < 0.05$). There was no significant difference between the control group and the MS patient group 1 ($p = 0.484$), nor between both patient groups ($p = 0.239$) in this post hoc comparison. It was also observed that PASAT scores were significantly lower than PVSAT scores when obtained during scanning ($p < 0.001$). PASAT and PVSAT behavioral scores during the scan session were significantly correlated ($\rho = 0.585$, $p = 0.001$).
In Fig. 6.20, the significant voxels of the ANOVA test between the three subject groups are colored in white and superimposed on different axial slices of the atlas FA maps that were color-encoded for the diffusion direction. As can be seen in Fig. 6.20 (a), differences in FA between the subject groups are observed in the inferior longitudinal fasciculus, the capsula externa, and the forceps major. Differences in $\lambda_{\parallel}$ are found in the inferior longitudinal fasciculus, the capsula interna, the body of the corpus callosum, and the corona radiata (see Fig. 6.20 (b)). As can be seen in Fig. 6.20 (c) and (d), the $\lambda_{\perp}$ and MD are significantly different between the subject groups in the inferior longitudinal fasciculus, the capsula interna and externa, genu, body, and splenium of the corpus callosum, the forceps major, and the corona radiata. After applying Mann-Whithney U tests to examine the specific group differences, no significant voxels were found when comparing the control group and the MS patient group 1 or both MS patient groups. The differences that were observed in the ANOVA analysis thus originate from differences between the

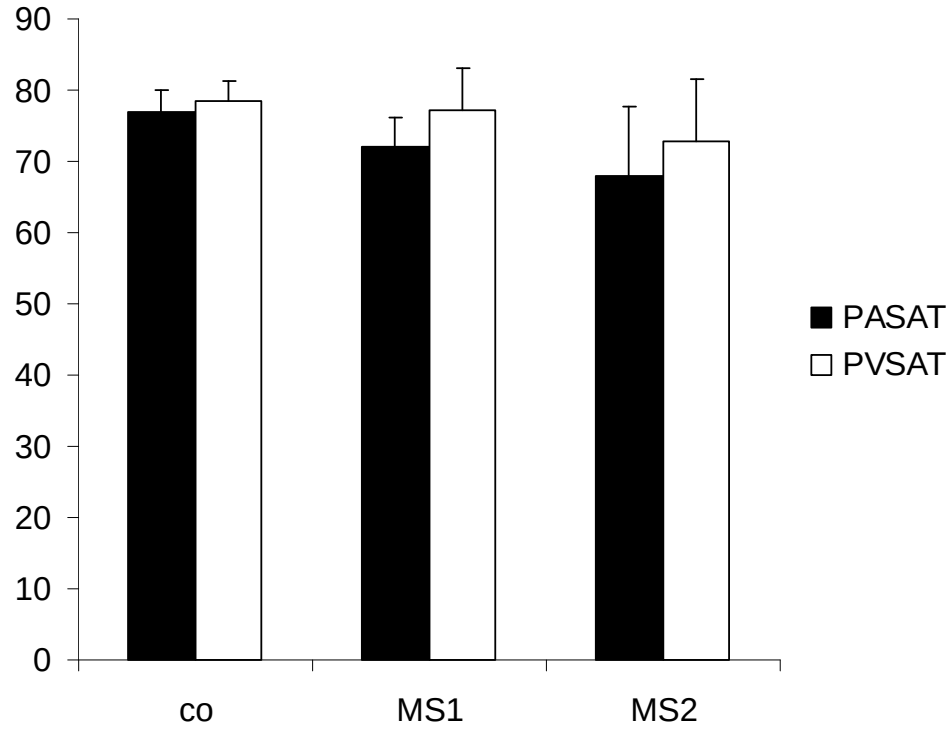

Figure 6.19. *Results of behavioral tests during scanning.*

control group and MS patient group 2, as can be observed in Fig. 6.21 (a), (b), (c), and (d).

The voxels in which the cognitive test scores are significantly correlated with the diffusion measures are depicted in white and superimposed on axial slices of the color encoded FA maps in Fig. 6.22. In Fig. 6.22 (a), (b), and (c), the correlation results of the PASAT score with the FA, $\lambda_\perp$, and MD are displayed, respectively. Significant correlations between PASAT and FA are found in the left inferior longitudinal fasciculus, the forceps minor, the capsula interna and externa, the genu of the corpus callosum, the left cingulum, the superior longitudinal fasciculus, and the corona radiata. As can be seen in Fig. 6.22 (b), similar regions contain significant correlations between the PASAT and the $\lambda_\perp$. Correlations between the PASAT score and the MD were observed in the capsula interna and externa, the superior longitudinal fasciculus, and the corona radiata (see Fig. 6.22 (c)). As can be observed in Fig. 6.22 (d), correlations between FA and PVSAT were found in similar WM locations as the correlations between PASAT and FA, except for the genu of the corpus callosum and the cingulum, where no correlations between PVSAT and

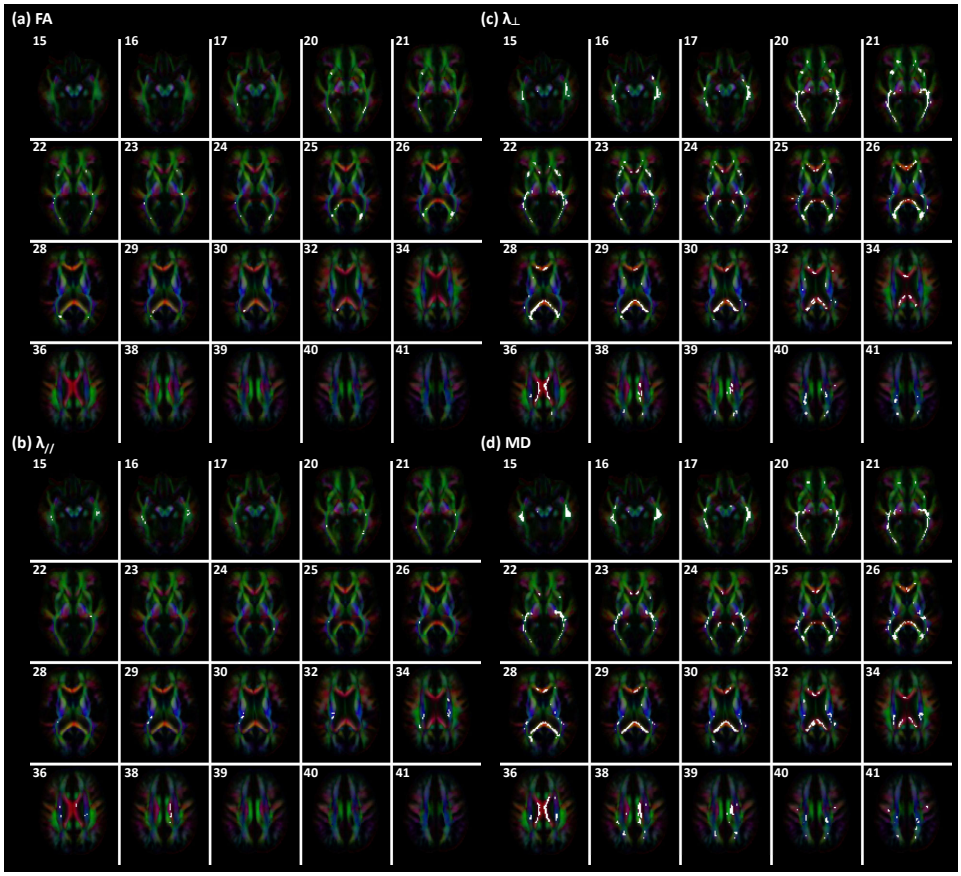

Figure 6.20. *VBA results of the ANOVA group analysis.*

FA were detected. Considerable less correlations were observed between PVSAT and the $\lambda_\perp$ and the MD, as demonstrated in Fig. 6.22 (e) and (f), respectively. In Fig. 6.23, the Spearman correlation coefficients ρ are depicted in the voxels that contain statistically significant correlations. The results are thereby superimposed on the atlas FA map. The correlation coefficients ρ of the PASAT scores with the diffusion measures are shown in Fig. 6.23 (a), (b), and (c). In Fig. 6.23 (d), (e), and (f), the correlation coefficients between PVSAT and FA, $\lambda_\perp$, and MD are displayed, respectively.

6.3.4 Discussion

In this work, diffusion properties were compared between healthy subjects, and patients with mild and moderate MS using an optimized VBA method. In addi-

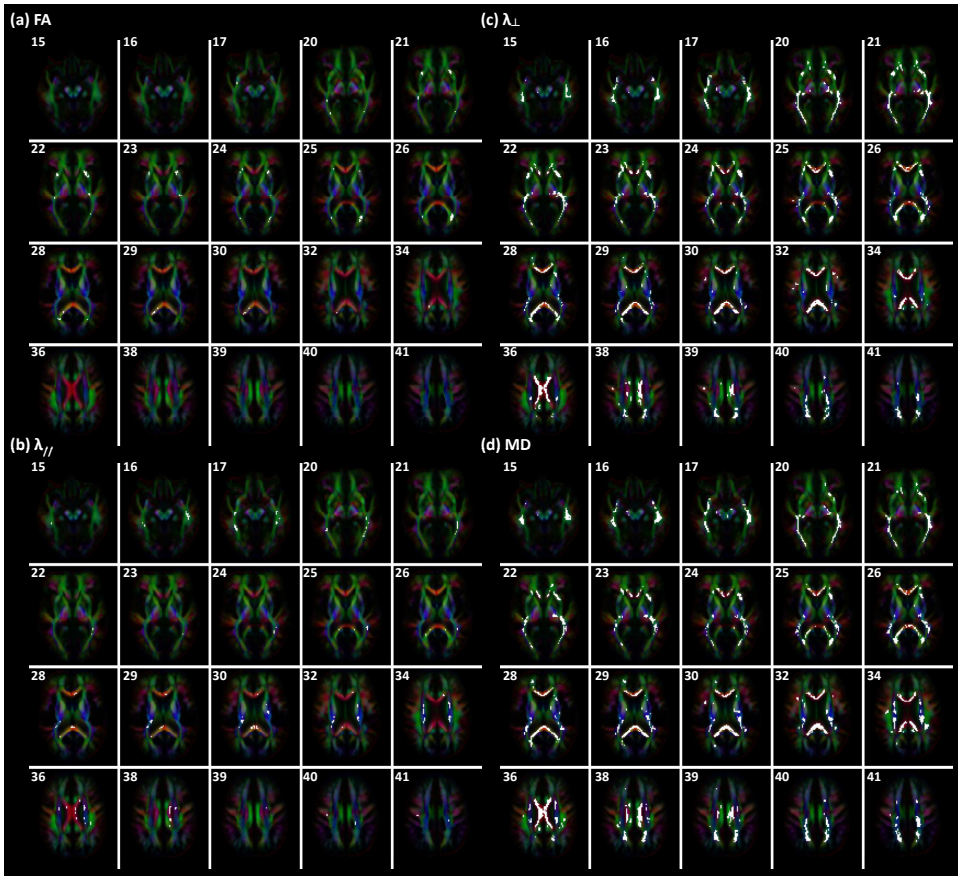

Figure 6.21. *VBA of healthy subjects vs moderately impaired MS patients.*

tion, correlations between the diffusion properties and cognitive test scores were examined in each brain voxel.

In recent years, VBA is increasingly being used to compare DTI data sets of healthy subjects and patients with a neurological and psychiatric disorders. Although VBA has many advantages compared to other post-processing methods, such as for example an ROI approach, it also has some important drawbacks. First, all the images need to be aligned perfectly to an atlas, which is not straightforward. In addition, the reported results depend on the selection of different parameter settings in the coregistration algorithm, the image smoothing, the statistical tests, and the post-hoc correction for multiple comparisons. As a result, the VBA technique is less standardized as it promised to be [73, 74]. An alternative whole brain analysis approach is provided by TBSS. In this method, however, only a relatively small proportion of the WM voxels is analyzed, i.e. only those voxels with the

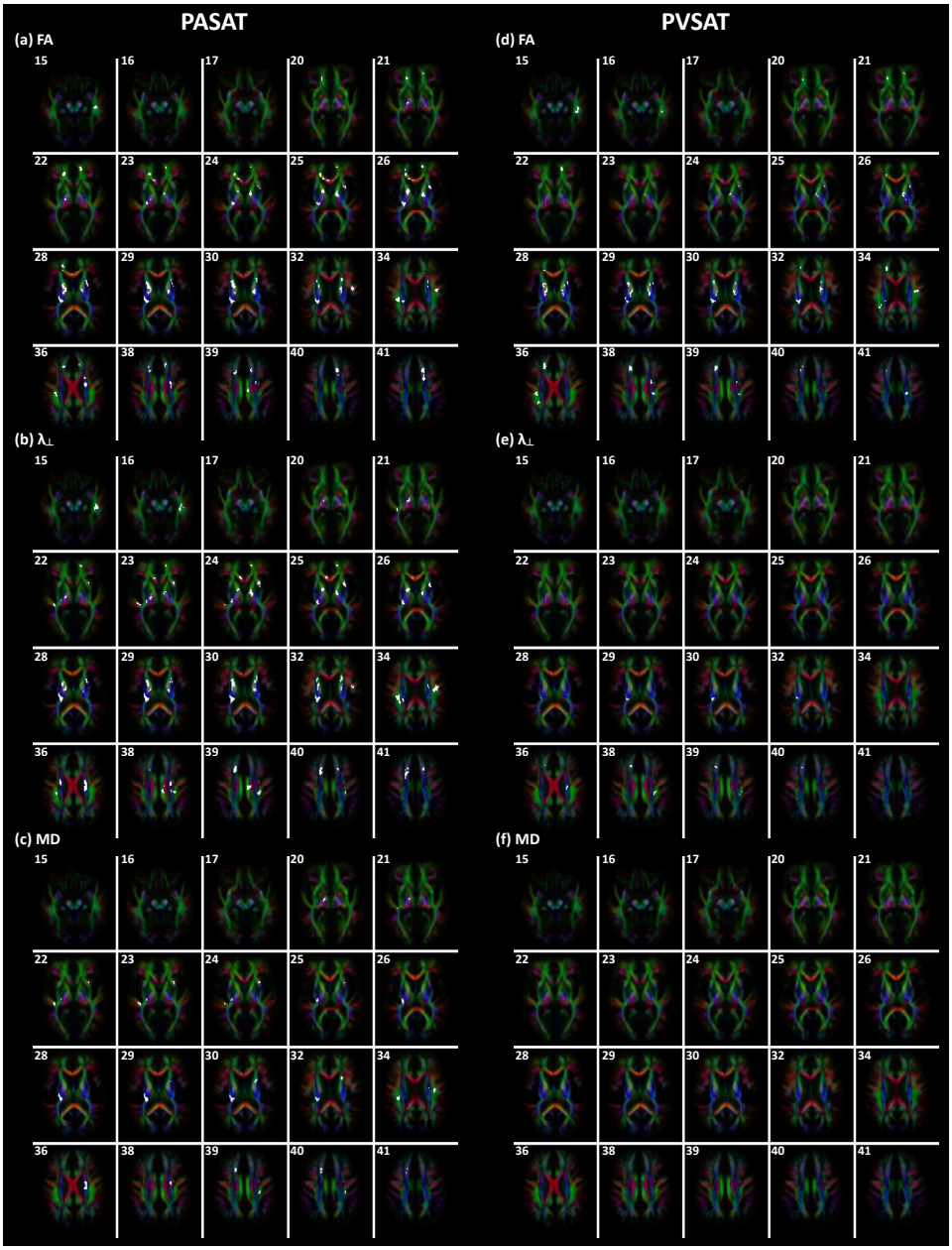

Figure 6.22. *VBA results of correlation between diffusion measures and cognitive tests.*

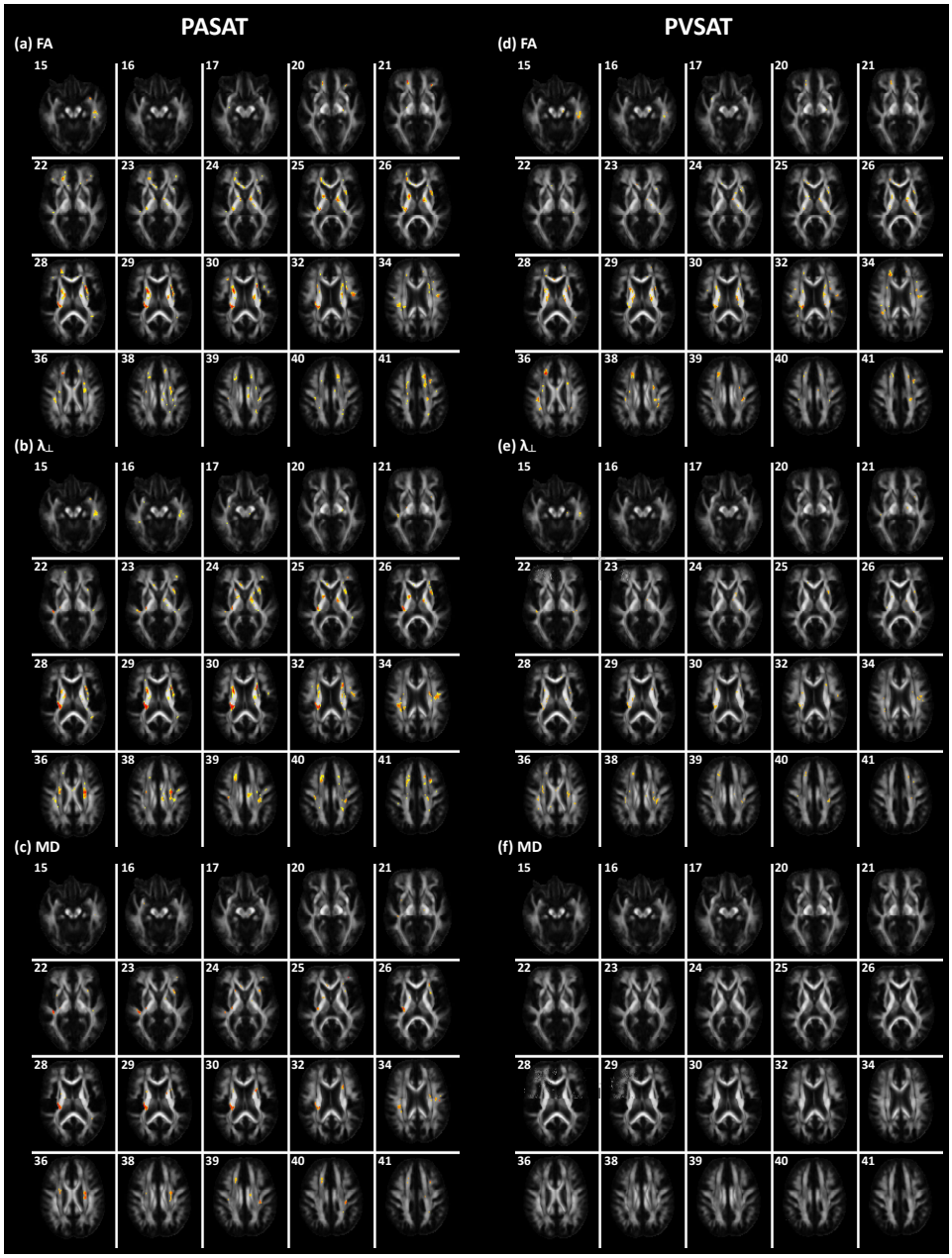

Figure 6.23. *Spearman coefficients of correlation between diffusion measures and cognitive tests.*

highest local FA. Valuable information from a large number of voxels is therefore lost. In this work, we opted for using an optimized VBA method to analyze the data. To this end, a high-dimensional viscous fluid model was used to align the DTs of different DTI data sets using mutual information as a similarity measure [37]. It is already been demonstrated that the residual misalignment is very small after applying this coregistration approach [37]. In addition, a population specific DTI atlas was constructed from our 30 data sets, in order to minimize the spatial deformations that are needed to align the different data sets to the template [39]. As a result, less residual misalignment is observed after the coregistration of the data sets to this atlas [39]. Finally, an anisotropic smoothing kernel was applied to filter the DTI data sets. It has been recently demonstrated that the use of anisotropic filtering methods, which better preserve the WM boundaries after smoothing, can increase the sensitivity and specificity of the pathology detection in a VBA study of DTI data [125].

Many of the published DTI studies that examined MS patients used ROIs or diffusion tensor tractography to delineate and evaluate the WM structures of interest [10–12, 14–17, 95–102, 126]. More recently, VBA and TBSS methods were applied to analyze DTI data sets of MS patients [103–107]. Similar as well as dissimilar results are reported in these DTI studies of MS patients. The subject group and disease heterogeneity across the different studies, including confounding factors such as age, sex, handedness, disease duration, MS type etc., can partially explain these observed discrepancies. MS is indeed a very heterogeneous condition, potentially involving different WM structures in the disease process, and microstructural breakdown can vary with the disease subtype, duration, etc. Additionally, different post processing methods (ROI vs. tractography vs. VBA vs. TBSS) and implementation choices (smoothing kernel, coregistration algorithm, placement of ROIs, statistics, etc.) can cause the observed discrepancies in the reported results. Differences of the diffusion between control subjects and MS patients were detected in various parts of the corpus callosum [10, 12, 16, 95, 105–107, 126], different parts of the cortico-spinal or pyramidal tracts [12, 98, 105–107, 126, 127], the frontal WM [127], the forceps major [12, 106, 107], the forceps minor [12], the inferior longitudinal fasciculus [106, 107], the fornix [107, 126], the cingulum [126], the superior longitudinal fasciculus [126], and the uncinate fasciculus [126]. Our findings overlap to a certain degree with these results, since differences in the corpus callosum, inferior longitudinal fasciculus, cortico spinal tracts, forceps major, superior longitudinal fasciculus, and cingulum were observed between the control subjects and the patients with MS in the ANOVA analysis. Our results indicate that these group differences were mainly caused by differences between the control subjects and the moderately impaired MS patients. In contrast to the studies of Ceccarelli et al. (2008) and Mesaros et al. (2009), no differences were found between the control subjects and the mildly affected MS patients. As can be

observed in Figs. 6.20 and 6.21, especially differences in $\lambda_\perp$ and MD were found between the subject groups, as was also observed in Oh et al. (2004) and Pagani et al. (2005). Although further studies are needed, recent work suggests that demyelination and axonal degeneration cause an increase of the transverse diffusivity $\lambda_\perp$ and a decrease of the longitudinal diffusivity $\lambda_\parallel$, respectively [44–49]. However, results from other studies indicate that an increase of $\lambda_\perp$ is not only associated to demyelination but also to axonal loss [128]. Since no ground truth about the underlying microstructural damage is known for our population, it is very hard to correlate the observed changes in the DTI measures with the exact pathology.

It has been reported in other studies that cognitive dysfunction in MS patients might involve changes in different areas, including white matter lesions, normal appearing brain tissue on conventional MRI, cortical and deep gray matter [111, 113, 116–119]. Rao et al. proposed that cognitive impairment is caused by a disruption of the cortico-subcortical circuits, connecting the frontal cortices to thalamus and basal ganglia. However, other studies reported that posterior brain regions and the corpus callosum are equally affected [105, 129]. In addition, it has been suggested that a slowing of processing speed might also be related to sensory-motor disturbances [130]. In a recent study, Turken et al. examined the correlation of FA and processing speed, as assessed by the DigitSymbol subtest from WAISIII in healthy subjects and patients with stroke [131]. They found significant correlations in parietal, frontal, and temporal regions, involving the corona radiata, the forceps minor, and the inferior longitudinal fasciculus. Another recent study investigated the correlations between the FA and cognitive test scores in patients with MS [106]. In this studies, significant correlations were observed in the genu, body and splenium of the corpus callosum, the forceps major, the cingulum, the inferior longitudinal fasciculus, the superior longitudinal fasciculus, the corona radiata, and the capsula externa.

In our study, the PASAT and PVSAT tests were used to evaluate the cognitive functioning of the MS patients. PASAT and PVSAT scores that were acquired before scanning did not significantly differ between experimental groups (Table 1). On the other hand, PASAT and PVSAT scores that were obtained during scanning were significantly lower in the MS group 2 than in the control group but not different between MS patient group 1 and controls or between both MS groups. One possible explanation for this is the noise during the MRI scanning, which may place higher demands on the subject's concentration. It has indeed been demonstrated that the difference in performance of a working memory task between MS patients and controls increased for increasing task difficulty [132, 133]. Significant correlations between PASAT scores and diffusion measures were found in the inferior longitudinal fasciculus, the inferior fronto-occipital fasciculus, the capsula interna and externa, the genu and body of the corpus callosum, the forceps minor, the superior longitudinal fasciculus, the corona radiata, and the cingulum.

Diffusion measures of similar WM structures were correlated with PVSAT scores, except for the body of the corpus callosum and the cingulum. We also found that especially FA and $\lambda_\perp$ were correlated with PASAT and PVSAT scores. Less correlations were found between the cognitive tests and the MD. Compared to PASAT, significantly less PVSAT correlations with $\lambda_\perp$ and MD were observed. Since stimuli are presented visually in the PVSAT, the effect of the noise in the MR scanner on the test performance is presumably lower compared to the PASAT test, making the PVSAT task more easy to perform. As aforementioned, task difficulty is an important factor in finding differences between control subjects and MS patients [132, 133]. In correspondence with previous studies, our results indicate an involvement of parietal, frontal, and temporal regions, as well as the corpus callosum in cognitive dysfunction. In addition, voxel based correlation tests between the diffusion measures and the EDSS scores was performed. Although group differences were found when subdividing the MS group based on the EDSS score, no significantly different correlations with the EDSS score was observed. Oh et al. (2004) also found no significant correlations with EDSS in MS patients with RR and SP type. On the other hand, Cader et al. (2007) found correlations with EDSS in the corpus callosum, which corresponds to the observations in our group study. The EDSS is limited, since it only measures motor performance. Spinal cord lesions, that are not detected in a brain group analysis, can therefore significantly affect the EDSS outcome. In addition, our subjects were recruited with low or moderate EDSS, which made the available EDSS scores discrete rather than continue. These factors can explain the fact that EDSS was not significantly correlated with the diffusion measures in this study.

In conclusion, state-of-the-art VBA techniques were used to track diffusion differences between control subjects and patients with MS. The MS patients were subdivided in a mild and moderate MS group, based on the EDSS score. We demonstrated that differences were found between control subjects and moderate MS patients, which are consistent with previously published studies. In addition, the diffusion properties were correlated in a whole brain analysis with tests that measure cognitive dysfunction. These results indicated the involvement of parietal, frontal, and temporal WM regions in the cognitive deterioration. We acknowledge that our findings are by no means conclusive and that our results should be interpreted cautiously, given that our study may have been limited by the relatively small number of subjects.

Bibliography

[1] N. Molko, S. Pappata, J. Mangin, C. Poupon, K. Vahedi, A. Jobert, D. LeBihan, M. Bousser, H. Chabriat, Diffusion tensor imaging study of subcortical gray matter in CADASIL, Stroke 32 (9) (2001) 2049–2054.

[2] O. Abea, S. Aokia, N. Hayashia, H. Yamadaa, A. Kunimatsua, H. Moria, T. Yoshikawaa, T. Okubob, K. Ohtomoa, Normal aging in the central nervous system: quantitative MR diffusion-tensor analysis, Neurobiol Aging 23 (3) (2002) 433–441.

[3] F. Wang, Z. Sun, X. Du, X. Wang, Z. Cong, H. Zhang, D. Zhang, N. Hong, A diffusion tensor imaging study of middle and superior cerebellar peduncle in male patients with schizophrenia, IEEE Trans Med Imaging 23 (8) (2004) 930–939.

[4] M. Kubicki, C.-F. Westin, S.-E. Maier, M. Frumin, P. Nestor, D. Salisbury, R. Kikinis, F. Jolesz, McCarley, M. Shenton, Uncinate fasciculus findings in schizophrenia: a magnetic resonance diffusion tensor imaging study, Am J Psychiatry 159 (5) (2002) 813–820.

[5] S. Kumra, M. Ashtari, M. McMeniman, J. Vogel, R. Augustin, D. Becker, E. Nakayama, K. Gyato, j. Kane, K. Lim, P. Szeszko, Reduced frontal white matter integrity in early-onset schizophrenia: a preliminary study, Biol Psychiatry 55 (12) (2004) 1138–1145.

[6] M. Kubicki, C.-F. Westin, P. Nestor, C. Wible, M. Frumin, S. Maier, R. Kikinis, F. Jolesz, R. McCarley, M. Shenton, Cingulate fasciculus integrity disruption in schizophrenia: a magnetic resonance diffusion tensor imaging study, Biol Psychiatry 54 (11) (2003) 1171–1180.

[7] R. Westerhausen, C. Walter, F. Kreuder, R. Wittling, E. Schweiger, W. Wittling, The influence of handedness and gender on the microstructure of the human corpus callosum: a diffusion-tensor magnetic resonance imaging study, Neurosci Lett 351 (2) (2003) 99–102.

[8] L. Snook, L.-A. Paulson, D. Roy, L. Phillips, C. Beaulieu, Diffusion tensor imaging of neurodevelopment in children and young adults, NeuroImage 26 (4) (2005) 1164–1173.

[9] L. Snook, C. Plewes, C. Beaulieu, Voxel based versus region of interest analysis in diffusion tensor imaging of neurodevelopment., NeuroImage 34 (1) (2007) 243–252.

[10] K. Hasan, R. Gupta, R. Santos, J. Wolinsky, P. Narayana, Fractional diffusion tensor anisotropy of the seven segments of the normal-appearing white matter of the corpus callosum in healthy adults and relapsing remitting multiple sclerosis, Journal of Magnetic Resonance Imaging 21 (2005) 735–743.

[11] O. Ciccarelli, D. J. Werring, G. J. Barker, C. M. Griffin, C. A. M. Wheeler-Kingshott, D. H. Miller, A. J. Thompson, A study of the mechanisms of normal-appearing white matter damage in multiple sclerosis using diffusion tensor imaging – Evidence of Wallerian degeneration., J Neurol 250 (3) (2003) 287–292.

[12] M. Cercignani, M. Bozalli, G. Iannucci, G. Comi, M. Filippi, Intra-voxel and inter-voxel coherence in patients with multiple sclerosis assessed using diffusion tensor MRI., J Neurol 249 (7) (2002) 875–883.

[13] A. Pfefferbaum, E. V. Sullivan, M. Hedehus, E. Adalsteinsson, K. O. Lim, M. Moseley, In vivo detection and functional correlates of white matter microstructural disruption in chronic alcoholism., Alcohol Clin Exp Res 24 (2000) 1214–1221.

[14] R. Bammer, M. Augustin, S. Strasser-Fuchs, T. Seifert, P. Kapeller, R. Stollberger, F. Ebner, H. P. Hartung, F. Fazekas, Magnetic resonance diffusion tensor imaging for characterizing diffuse and focal white matter abnormalities in multiple sclerosis., Magn Reson Med 44 (4) (2000) 583–91.

[15] C. M. Griffin, D. T. Chard, O. Ciccarelli, B. Kapoor, G. J. Barker, A. I. Thompson, D. H. Miller, Diffusion tensor imaging in early relapsing-remitting multiple sclerosis., Mult Scler 7 (5) (2001) 290–297.

[16] Y. Ge, M. Law, G. Johnson, J. Herbert, J. S. Babb, L. J. Mannon, R. I. Grossman, Preferential occult injury of corpus callosum in multiple sclerosis measured by diffusion tensor imaging., J Magn Reson Imaging 20 (1) (2004) 1–7.

[17] C. S. Yu, C. Z. Zhu, K. C. Li, Y. Xuan, W. Qin, H. Sun, P. Chan, Relapsing neuromyelitis optica and relapsing-remitting multiple sclerosis: differentiation at diffusion-tensor MR imaging of corpus callosum., Radiology 244 (1) (2007) 249–256.

[18] J. Ashburner, K. Friston, Voxel-based morphometry – the methods, NeuroImage 11 (2000) 805–821.

[19] I. Agartz, J. Andersson, S. Skare, Abnormal brain white matter in schizophrenia: a diffusion tensor imaging study, NeuroReport 12 (10) (2001) 2251–2254.

[20] J. Foong, M. R. Symms, G. J. Barker, M. Maier, D. H. Miller, M. A. Ron, Investigating regional white matter in schizophrenia using diffusion tensor imaging., NeuroReport 13 (3) (2002) 333–6.

[21] B. A. Ardekani, J. Nierenberg, M. J. Hotman, D. C. Javitt, K. O. Lim, MRI Study of White Matter Diffusion Anisotropy in Schizophrenia., NeuroReport 14 (16) (2003) 2025–2029.

[22] J. Burns, D. Job, M. Bastin, H. Whalley, T. Macgillivray, E. Johnstone, S. Lawrie, Structural disconnectivity in schizophrenia: a diffusion tensor magnetic resonance imaging study, British Journal of Psychiatry 182 (2003) 439–443.

[23] P. R. Szeszko, B. A. Ardekani, M. Ashtari, S. Kumra, D. G. Robinson, S. Sevy, H. Gunduz-Bruce, A. K. Malhotra, J. M. Kane, R. M. Bilder, K. O. Lim, White matter abnormalities in first-episode schizophrenia or schizoaffective disorder: a diffusion tensor imaging study., Am J Psychiatry 162 (3) (2005) 602–605.

[24] M. Kubicki, H. Park, C.-F. Westin, P. Nestor, R. Mulkern, S. Maier, M. Niznikiewicz, E. Connor, J. Levitt, M. Frumin, R. Kikinis, F. Jolesz, R. McCarley, M. Shentona, DTI and MTR abnormalities in schizophrenia: analysis of white matter integrity, NeuroImage 26 (4) (2005) 1109–1118.

[25] B. A. Ardekani, A. Bappal, D. D'Angelo, M. Ashtari, T. Lencz, P. R. Szeszko, P. D. Butler, D. C. Javitt, K. O. Lim, J. Hrabe, J. Nierenberg, C. A. Branch, M. J. Hoptman, Brain morphometry using diffusion weighted MRI: Application to schizophrenia., NeuroReport 16 (13) (2005) 1455–1459.

[26] M. S. Buchsbaum, J. Friedman, B. R. Buchsbaum, K. Chu, E. A. Hazlett, R. Newmark, J. S. Schneiderman, Y. Torosjan, C. Tang, P. R. Hof, D. Stewart, K. L. Davis, J. Gorman, Diffusion tensor imaging in schizophrenia., Biol Psych 60 (11) (2006) 1181–1187.

[27] D. K. Jones, X. A. Chitnis, D. Job, P. L. Khong, L. T. Leung, S. Marenco, S. M. Smith, M. R. Symms, What happens when nine different groups analyze the same DT-MRI data set using voxel-based methods?, Proc. ISMRM 15th Annual Meeting, Berlin (2007) 74.

[28] G. Douaud, S. Smith, M. Jenkinson, T. Behrens, H. Johansen-Berg, J. Vickers, S. James, N. Voets, K. Watkins, P. M. Matthews, A. James, Anatomically related grey and white matter abnormalities in adolescent-onset schizophrenia., Brain 130 (2007) 2375–2386.

[29] J. H. Seok, H. J. Park, J. W. Chun, S. K. Lee, H. S. Cho, J. S. Kwon, J. J. Kim, White matter abnormalities associated with auditory hallucinations in schizophrenia: A combined study of voxel-based analyses of diffusion tensor imaging and structural magnetic resonance imaging., Psychiatry Res. 156 (2) (2007) 93–104.

[30] K. H. Karlsgodt, T. G. M. van Erp, R. A. Poldrack, C. E. Bearden, K. H. Nuechterlein, T. D. Cannon, Diffusion tensor imaging of the superior longitudinal fasciculus and working memory in recent-onset schizophrenia., Biol Psych 63 (5) (2007) 512–518.

[31] M. Kyriakopoulos, N. S. Vyas, G. J. Barker, X. A. Chitnis, S. Frangou, A diffusion tensor imaging study of white matter in early-onset schizophrenia., Biol Psychiatry 63 (5) (2007) 519–523.

[32] T. White, A. T. K. Kendi, S. Lehricy, M. Kendi, C. Karatekin, A. Guimaraes, N. Davenport,

S. C. Schulz, K. O. Lim, Disruption of hippocampal connectivity in children and adolescents with schizophrenia - a voxel-based diffusion tensor imaging study., Schizophr Res 90 (1–3) (2007) 302–307.

[33] A. Leemans, J. Sijbers, M. Verhoye, A. Van der Linden, D. Van Dyck, Mathematical framework for simulating diffusion tensor MR neural fiber bundles, Magn Reson Med 53 (4) (2005) 944–953.

[34] D. Alexander, C. Pierpaoli, P. Basser, J. Gee, Spatial Transformations of Diffusion Tensor Magnetic Resonance Images, IEEE Transactions on Medical Imaging 20 (11) (2001) 1131–1139.

[35] A. Leemans, J. Sijbers, S. De Backer, E. Vandervliet, P. Parizel, Affine coregistration of diffusion tensor magnetic resonance images using mutual information, Lect Notes Comp Sci 3708 (2005) 523–530.

[36] F. Maes, A. Collignon, D. Vandermeulen, G. Marchal, P. Suetens, Multimodality image registration by maximization of mutual information, IEEE Transactions on Medical Imaging 16 (2) (1997) 187–198.

[37] W. Van Hecke, A. Leemans, E. D'Agostino, S. De Backer, E. Vandervliet, P. M. Parizel, J. Sijbers, Nonrigid coregistration of diffusion tensor images using a viscous fluid model and mutual information, IEEE Trans Med Imaging. 26 (11) (2007) 1598–1612.

[38] E. DAgostino, F. Maes, D. Vandermeulen, P. Suetens, A viscous fluid model for multimodal non-rigid image registration using mutual information, Medical image analysis 7 (4) (2003) 565–575.

[39] W. Van Hecke, A. Leemans, E. D'Agostino, F. Maes, S. De Backer, E. Vandervliet, J. Sijbers, P. M. Parizel, On the construction of an inter-subject diffusion tensor magnetic resonance atlas of the healthy human brain., NeuroImage 43 (1) (2008) 69–80.

[40] P. Basser, S. Pajevic, C. Pierpaoli, J. Duda, A. Aldroubi, In vivo fiber tractography using DT-MRI data, Magnetic Resonance in Medicine 44 (2000) 625–632.

[41] S.-K. Lee, D. I. Kim, J. Kim, D. J. Kim, H. D. Kim, D. S. Kim, S. Mori, Diffusion-Tensor MR Imaging and Fiber Tractography: A New Method of Describing Aberrant Fiber Connections in Developmental CNS Anomalies., RadioGraphics 25 (1) (2005) 53–68.

[42] M. Catani, Diffusion tensor Magn Reson Imaging tractography in cognitive disorders., Curr Opin Neurol 19 (6) (2006) 599–606.

[43] C. Beaulieu, The basis of anisotropic water diffusion in the nervous system - a technical review, NMR in Biomedicine 15 (7–8) (2002) 435–455.

[44] S. Song, S. Sun, M. Ramsbottom, C. Chang, J. Russell, A. Cross, Dysmyelination revealed through MRI as increased radial (but unchanged axial) diffusion of water, NeuroImage 17 (3) (2002) 1429–1436.

[45] S.-K. Song, S.-W. Sun, W.-K. Ju, S.-J. Lin, A. Cross, A. Neufeld, Diffusion tensor imaging detects and differentiates axon and myelin degeneration in mouse optic nerve after retinal ischemia, NeuroImage 20 (3) (2003) 1714–1722.

[46] S. Song, J. Yoshino, T. Le, S. Lin, S. Sun, A. Cross, R. Armstrong, Demyelination increases radial diffusivity in corpus callosum of mouse brain, Neuroimage 21 (2005) 132–140.

[47] M. D. Budde, J. H. Kim, H.-F. Liang, R. E. Schmidt, J. H. Russell, A. H. Cross, S. S-K., Toward accurate diagnosis of white matter pathology using diffusion tensor imaging., Magn Reson Med 57 (4) (2007) 688–695.

[48] E. D. Schwartz, E. T. Cooper, Y. Fan, A. F. Jawad, C. L. Chin, J. Nissanov, D. B. Hackney, MRI diffusion coefficients in spinal cord correlate with axon morphometry., NeuroReport 16 (1) (2005) 73–76.

[49] L. A. Harsan, P. Poulet, B. Guignard, J. Steibel, N. Parizel, P. L. de Sousa, N. Boehm, D. Grucker, M. S. Ghandour, Brain dysmyelination and recovery assessment by noninvasive in vivo diffusion tensor Magn Reson Imaging., J Neurosci Res 83 (3) (2006) 392–402.

[50] R. Huster, R. Westerhausen, F. Kreuder, E. Schweiger, W. Wittling, Hemispheric and gender related differences in the midcingulum bundle: A DTI study., Hum Brain Mapp (In Press).

[51] J.-L. Hsu, A. Leemans, C.-H. Bai, C.-H. Lee, Y.-F. Tsai, H.-C. Chiu, W.-H. Chen, Gender differences and age-related white matter changes of the human brain: A diffusion tensor imaging study., NeuroImage 39 (2) (2008) 566–577.

[52] S. M. Smith, M. Jenkinson, H. Johansen-Berg, D. Rueckert, T. E. Nichols, C. E. Mackay, K. E. Watkins, O. Ciccarelli, M. Z. Cader, P. M. Matthews, T. E. Behrens, Tract-based spatial statistics: voxelwise analysis of multi-subject diffusion data., NeuroImage 4 (31) (2006) 1487–1505.

[53] D. Rueckert, L. I. Sonoda, C. Hayes, D. L. Hill, M. O. Leach, D. J. Hawkes, Nonrigid registration using free-form deformations: application to breast MR images., IEEE Trans Med Imaging 18 (8) (1999) 712–721.

[54] J. Ashburner, K. J. Friston, Nonlinear spatial normalization using basis functions., Hum Brain Mapp 7 (4) (1999) 254–266.

[55] R. M. Henkelman, Measurement of signal intensities in the presence of noise in MR images., Med Phys 12 (2) (1985) 232–233.

[56] H. Gudbjartsson, S. Patz, The Rician distribution of noisy MRI data., Magn Reson Med 34 (1995) 910–914.

[57] D. Jones, The effect of gradient sampling schemes on measures derived from diffusion tensor MRI: a Monte Carlo study, Magnetic Resonance in Medicine 51 (2004) 807–815.

[58] A. Leemans, J. Sijbers, P. Parizel, A graphical toolbox for exploratory diffusion tensor imaging and fiber tractography, in: 14th Annual Meeting - Section for Magnetic Resonance Technologists, Miami, USA, 2005.

[59] N. Barnea-Goraly, S. Eliez, M. Hedeus, V. Menon, C. White, M. Moseley, A. Reiss, White matter tract alterations in fragile X syndrome: preliminary evidence from diffusion tensor imaging, Am J Med Genet 118 (1) (2003) 81–88.

[60] H.-J. Park, C.-F. Westin, M. Kubicki, S. Maier, M. Niznikiewicz, A. Baer, M. Frumin, R. Kikinis, F. Jolesz, R. McCarley, M. Shenton, White matter hemisphere asymmetries in healthy subjects and in schizophrenia: a diffusion tensor MRI study, NeuroImage 23 (1) (2004) 213–223.

[61] T. J. Simon, L. Ding, J. P. Bish, D. M. McDonald-McGinn, E. H. Zackai, J. Gee, Volumetric, connective, and morphologic changes in the brains of children with chromosome 22q11.2 deletion syndrome: an integrative study., NeuroImage 25 (1) (2005) 169–180.

[62] Y. Benjamini, Y. Hochberg, Controlling the false discovery rate: a practical and powerful approach to multiple testing., J. Roy. Statist. Soc. Ser. B (57) (1995) 289–300.

[63] M. Anjari, L. Srinivasan, J. M. Allsop, J. V. Hajnal, M. A. Rutherford, A. D. Edwards, S. J. Counsell, Diffusion tensor imaging with tract-based spatial statistics reveals local white matter abnormalities in preterm infants., NeuroImage 35 (3) (2007) 1021–1027.

[64] M. Sach, G. Winkler, V. Glauche, J. Liepert, B. Heimbach, M. A. Koch, C. Bchel, C. Weiller, Diffusion tensor MRI of early upper motor neuron involvement in amyotrophic lateral sclerosis., Brain 127 (Pt.2) (2004) 340–350.

[65] C. A. Sage, R. R. Peeters, A. Grner, W. Robberecht, S. Sunaert, Quantitative diffusion tensor imaging in amyotrophic lateral sclerosis., NeuroImage 34 (2) (2007) 486–499.

[66] D. Hubl, T. Koenig, W. Strik, A. Federspiel, R. Kreis, C. Boesch, S. E. Maier, G. Schroth, K. Lovblad, T. Dierks, Pathways that make voices: white matter changes in auditory hallucinations., Arch Gen Psychiatry. 61 (7) (2004) 658–668.

[67] B. Borroni, S. M. Brambati, C. Agosti, S. Gipponi, G. Bellelli, R. Gasparotti, V. Garibotto, M. Di Luca, P. Scifo, D. Perani, A. Padovani, Evidence of white matter changes on diffusion tensor imaging in frontotemporal dementia., Arch Neurol. 64 (2) (2007) 246–251.

[68] S. Xie, J. X. Xiao, G. L. Gong, Y. F. Zang, Y. H. Wang, H. K. Wu, X. X. Jiang, Voxel-based detection of white matter abnormalities in mild Alzheimer disease., Neurology 66 (12) (2006) 1845–1849.

[69] Z. Nagy, H. Westerberg, S. Skare, J. L. Andersson, A. Lilja, O. Flodmark, E. Fernell, K. Holmberg, B. Bohm, H. Forssberg, H. Lagercrantz, T. Klingberg, Preterm children have disturbances of white matter at 11 years of age as shown by diffusion tensor imaging., Pediatric Research 54 (8) (2003) 672–679.

[70] N. Molko, A. Cachia, D. Rivière, J.-F. Mangin, M. Bruandet, D. Le Bihan, L. Cohen, S. Dehaene, Brain anatomy in turner syndrome: Evidence for impaired social and spatial-numerical networks., Cereb Cort 14 (8) (2004) 840–850.

[71] A. Padovani, B. Borroni, S. Brambati, C. Agosti, M. Broli, R. Alonso, G. Scifo, P. Bellelli, A. Alberici, R. Gasparotti, D. Perani, Diffusion tensor imaging and voxel based morphometry study in early progressive supranuclear palsy., J Neurol Neurosurg Psychiatry 77 (4) (2006) 457–463.

[72] P. Basser, S. Pajevic, Statistical artifacts in diffusion tensor MRI (DT-MRI) caused by background noise, Magnetic Resonance in Medicine 44 (1) (2000) 41–50.

[73] H. Zhang, B. B. Avants, P. A. Yushkevich, J. H. Woo, S. Wang, L. F. McCluskey, L. B. Elman, E. R. Melhem, J. C. Gee, High-dimensional spatial normalization of diffusion tensor images improves the detection of white matter differences: An example study using amyotrophic lateral sclerosis, IEEE Trans. Med. Imaging 26 (11) (2007) 1585–1597.

[74] D. Jones, M. Symms, M. Cercignani, R. Howarde, The effect of filter size on VBM analyses of DT-MRI data, NeuroImage 26 (2) (2005) 546–554.

[75] F. L. Bookstein, Voxel-based morphometry should not be used with imperfectly registered images., Neuroimage 14 (6) (2001) 1454–1462.

[76] C. Davatzikos, Why voxel-based morphometric analysis should be used with great caution when characterizing group differences., NeuroImage 23 (1) (2004) 17–20.

[77] J. Ashburner, K. Friston, Why voxel-based morphometry should be used, NeuroImage 14 (6) (2001) 1238–1243.

[78] A. Rosenfeld, A. C. Kak, Digital Picture Processing 2, Academic Press, Orlando, FL, 1982.

[79] K. J. Worsley, A. C. Evans, S. Marrett, P. Neelin, A three-dimensional statistical analysis for CBF activation studies in human brain, Journal of Cerebral Blood Flow and Metabolism 12 (6) (1992) 900–918.

[80] K. J. Friston, J.-B. Holmes, A.and Poline, C. J. Price, C. D. Frith, Detecting activations in PET and fMRI: Levels of inference and power, NeuroImage 4 (3) (1996) 223–235.

[81] K. M. Petersson, T. E. Nichols, J. B. Poline, A. P. Holmes, Statistical limitations in functional neuroimaging II. Signal detection and statistical inference, Phil. Trans. R. Soc. London B 354 (1999) 1261–1281.

[82] W. Van Hecke, J. Sijbers, S. De Backer, D. Poot, P. M. Parizel, A. Leemans, On the construction of a ground truth framework for evaluating voxel-based diffusion tensor MRI analysis methods., NeuroImage, In Revision .

[83] Z. Ding, J. C. Gore, A. W. Anderson, Reduction of Noise in Diffusion Tensor Images Using Anisotropic Smoothing, Magnetic Resonance in Medicine (53) (2005) 485–490.

[84] J. Sijbers, A. den Dekker, M. Verhoye, A. Van der Linden, D. Van Dyck, Adaptive anisotropic noise filtering for magnitude MR data, Magn Reson Imaging 17 (10) (1999) 1533–1539.

[85] M. H. Zweig, G. Campbell, Receiver-operating characteristic (ROC) plots: a fundamental evaluation tool in clinical medicine, Clinical Chemistry (39) (1993) 561–577.

[86] P. T. Fox, M. A. Mintun, E. M. Reiman, M. E. Raichle, Enhanced detection of focal brain responses using intersubject averaging and change-distribution analysis of subtracted PET images, Journal of Cerebral Blood Flow and Metabolism 8 (1988) 642–653.

[87] P. T. Fox, M. A. Mintun, Noninvasive functional brain mapping by change-distribution analysis of averaged PET images of $H_2^{15}O$ tissue activity, J Nucl Med. 30 (2) (2006) 141–149.

[88] K. J. Friston, C. D. Frith, P. F. Liddle, R. J. Dolan, A. A. Lammertsmaa, R. S. J. Frackowiak, The relationship between global and local changes in PET scans, Journal of Cerebral Blood Flow and Metabolism 13 (6) (1990) 1038–1040.

[89] K. J. Friston, C. D. Frith, P. F. Liddle, R. S. J. Frackowiak, Comparing functional (PET) images: the assessment of significant change, Journal of Cerebral Blood Flow and Metabolism 11 (4) (1991) 690–699.

[90] C. R. Genovese, N. A. Lazar, T. Nichols, Thresholding of Statistical Maps in Functional Neuroimaging Using the False Discovery Rate, NeuroImage (15) (2002) 870–878.

[91] M. Filippi, M. A. Horsfield, H. J. Adr, F. Barkhof, P. Bruzzi, A. Evans, J. A. Frank, R. I. Grossman, H. F. McFarland, P. Molyneux, D. W. Paty, J. Simon, P. S. Tofts, J. S. Wolinsky, D. H. Miller, Guidelines for using quantitative measures of brain magnetic resonance imaging abnormalities in monitoring the treatment of multiple sclerosis., Annals of Neurology 43 (4) (1998) 499–506.

[92] D. H. Miller, R. I. Grossman, S. C. Reingold, H. F. Mcfarland, The role of magnetic resonance techniques in understanding and managing multiple sclerosis., Brain 121 (1) (1998) 3–24.

[93] M. Filippi, M. A. Rocca, G. Comi, The use of quantitative magnetic-resonance-based techniques to monitor the evolution of multiple sclerosis., Lancet Neurol 2 (6) (2003) 337–346.

[94] P. C. Sundgren, Q. Dong, D. Gomez-Hassan, S. K. Mukherji, P. Maly, R. Welsh, Diffusion tensor imaging of the brain: review of clinical applications., Neuroradiology 46 (5) (2004) 339–350.

[95] J. Oh, R. G. Henry, C. Genain, S. J. Nelson, D. Pelletier, Mechanisms of normal appearing corpus callosum injury related to pericallosal T1 lesions in multiple sclerosis using directional diffusion tensor and 1H MRS imaging., J Neurol Neurosurg Psychiatry 75 (9) (2004) 1281–1286.

[96] A. M. Saindane, M. Law, Y. Ge, G. Johnson, J. S. Babb, R. I. Grossman, Correlation of diffusion tensor and dynamic perfusion MR imaging metrics in normal-appearing corpus callosum: support for primary hypoperfusion in multiple sclerosis., AJNR Am J Neuroradiol. 28 (4) (2007) 767–772.

[97] M. Wilson, C. Tench, P. Morgan, L. Blumhardt, Pyramidal tract mapping by diffusion tensor magnetic resonance imaging in multiple sclerosis: improving correlations with disability, J Neurol Neurosurg Psychiatry 74 (2) (2003) 203–207.

[98] E. Pagani, M. Filippi, M. Rocca, M. Horsfield, A method for obtaining tract-specific diffusion tensor MRI measurements in the presence of disease: application to patients with clinically isolated syndromes suggestive of multiple sclerosis, NeuroImage 26 (1) (2005) 258–265.

[99] F. Lin, C. Yu, T. Jiang, K. Li, P. Chan, Diffusion tensor tractography-based group mapping of the pyramidal tract in relapsing-remitting multiple sclerosis patients., AJNR Am J Neuroradiol. 28 (2) (2007) 278–282.

[100] M. A. Rocca, E. Pagani, M. Absinta, P. Valsasina, A. Falini, G. Scotti, G. Comi, M. Filippi, Altered functional and structural connectivities in patients with MS: a 3-T study., Neurology 69 (23) (2007) 2136–2145.

[101] B. Audoin, M. Guye, F. Reuter, M. V. Au Duong, S. Confort-Gouny, I. Malikova, E. Soulier, P. Viout, A. A. Chrif, P. J. Cozzone, J. Pelletier, J. P. Ranjeva, Structure of WM bundles constituting the working memory system in early multiple sclerosis: a quantitative DTI tractography study., NeuroImage 36 (4) (2007) 1324–1330.

[102] X. Lin, C. R. Tench, P. S. Morgan, C. S. Constantinescu, Use of combined conventional

and quantitative MRI to quantify pathology related to cognitive impairment in multiple sclerosis., Journal of Neurology, Neurosurgery and Psychiatry 79 (4) (2008) 437–441.

[103] S. A. Patel, B. A. Hum, C. F. Gonzalez, R. J. Schwartzman, S. H. Faro, F. B. Mohamed, Application of voxelwise analysis in the detection of regions of reduced fractional anisotropy in multiple sclerosis patients., J Magn Reson Imaging 26 (3) (2007) 552–526.

[104] A. Ceccarelli, M. A. Rocca, E. Pagani, A. Ghezzi, R. Capra, A. Falini, G. Scotti, G. Comi, M. Filippi, The topographical distribution of tissue injury in benign MS: a 3T multiparametric MRI study., NeuroImage 39 (4) (2008) 1499–1509.

[105] S. Mesaros, M. A. Rocca, G. Riccitelli, E. Pagani, M. Rovaris, D. Caputo, A. Ghezzi, R. Capra, A. Bertolotto, G. Comi, M. Filippi, Corpus callosum damage and cognitive dysfunction in benign MS., Human Brain Mapping .

[106] R. A. Dineen, J. Vilisaar, J. Hlinka, C. M. Bradshaw, P. S. Morgan, C. S. Constantinescu, D. P. Auer, Disconnection as a mechanism for cognitive dysfunction in multiple sclerosis, Neurology 132 (Pt. 1) (2008) 239–249.

[107] S. D. Roosendaal, J. J. Geurts, H. Vrenken, H. E. Hulst, K. S. Cover, J. A. Castelijns, P. J. Pouwels, F. Barkhof, Regional DTI differences in multiple sclerosis patients., NeuroImage .

[108] S. M. Rao, G. J. Leo, L. Bernardin, F. Unverzagt, Cognitive dysfunction in multiple sclerosis. I. Frequency, patterns, and prediction., Neurology 41 (1991) 685–691.

[109] L. Leocani, G. . Comi, Neurophysiological investigations in multiple sclerosis., Curr Opin Neurol 13 (2000) 255–261.

[110] G. Nagels, L. Geentjens, D. Kos, L. Vleugels, D. M. B., P. Van Asch, K. Vuylsteke, P. P. De Deyn, Paced visual serial addition test in multiple sclerosis., Clin Neurol Neurosurg 107 (2005) 218–222.

[111] S. M. Rao, G. J. Leo, V. M. Haughton, P. St Aubin-Faubert, L. Bernardin, Correlation of magnetic resonance imaging with neuropsychological testing in multiple sclerosis., Neurology 39 (1989) 161–166.

[112] J. Foong, L. Rozewicz, G. Quaghebeur, C. A. Davie, L. D. Kartsounis, A. J. Thompson, D. H. Miller, M. A. Ron, Executive function in multiple sclerosis. the role of frontal lobe pathology, Brain 120 (1997) 15–26.

[113] M. Rovaris, M. Filippi, M. Falautano, L. Minicucci, M. A. Rocca, V. Martinelli, G. Comi, Relation between mr abnormalities and patterns of cognitive impairment in multiple sclerosis, Neurology 50 (1998) 1601–1608.

[114] M. Rovaris, G. Iannucci, M. Falautano, F. Possa, V. Martinelli, G. Comi, M. Filippi, Cognitive dysfunction in patients with mildly disabling relapsingremitting multiple sclerosis: an exploratory study with diffusion tensor MR imaging, J Neurol Sci 195 (2) (2002) 103–109.

[115] E. A. DeSousa, R. H. Albert, B. Kalman, Cognitive impairments in multiple sclerosis: a review., Am. J. Alzheimers Dis. Other Dement. 17 (2002) 23–29.

[116] M. R. Piras, I. Magnano, E. D. Canu, K. S. Paulus, W. M. Satta, A. Soddu, M. Conti, A. Achene, G. Solinas, I. Aiello, Longitudinal study of cognitive dysfunction in multiple sclerosis: neuropsychological, neuroradiological, and neurophysiological findings, Journal of Neurology, Neurosurgery and Psychiatry 74 (7) (2003) 878–885.

[117] G. Gainotti, Measures of cognitive and emotional changes in multiple sclerosis and underlying models of brain dysfunction, Journal of the Neurological Sciences 245 (2006) 15–20.

[118] M. Filippi, C. Tortorella, M. Rovaris, M. Bozzali, F. Possa, M. P. Sormani, G. Iannucci, G. Comi, Changes in the normal appearing brain tissue and cognitive impairment in multiple sclerosis, Journal of Neurology, Neurosurgery and Psychiatry 68 (2000) 157–161.

[119] S. G. Edwards, C. Liu, L. D. Blumhardt, Cognitive correlates of supratentorial atrophy on MRI in multiple sclerosis, Acta Neurol Scand 104 (2001) 214–223.

[120] P. A. Arnett, S. M. Rao, L. Bernardin, J. Grafman, F. Z. Yetkin, L. Lobeck, Relationship between frontal lobe lesions and wisconsin card sorting test performance in patients with

multiple sclerosis, Neurology 44 (1994) 420–425.

[121] X. Lin, C. R. Tench, P. S. Morgan, G. Niepel, C. S. Constantinescu, Importance sampling in MS: use of diffusion tensor tractography to quantify pathology related to specific impairment., J Neurol Sci 237 (1–2) (2005) 13–19.

[122] W. I. McDonald, A. Compston, G. Edan, D. Goodkin, H. P. Hartung, F. D. Lublin, H. F. McFarland, D. W. Paty, C. H. Polman, S. C. Reingold, M. Sandberg-Wollheim, W. Sibley, A. Thompson, S. van den Noort, B. Y. Weinshenker, J. S. Wolinsky, Recommended diagnostic criteria for multiple sclerosis: guidelines from the International Panel on the diagnosis of multiple sclerosis., Ann Neurol 50 (2001) 121–127.

[123] C. H. Polman, S. C. Reingold, G. Edan, M. Filippi, H. P. Hartung, L. Kappos, F. D. Lublin, L. M. Metz, M. H. F., P. W. O'Connor, M. Sandberg-Wollheim, A. J. Thompson, B. G. Weinshenker, J. S. Wolinsky, Diagnostic criteria for multiple sclerosis: 2005 revisions to the "McDonald Criteria"., Ann Neurol 58 (2005) 840–846.

[124] J. F. Kurtzke, Rating neurologic impairment in multiple sclerosis: an expanded disability status scale (EDSS)., Neurology 33 (1983) 1444–1452.

[125] W. Van Hecke, A. Leemans, S. De Backer, B. Jeurissen, P. M. Parizel, J. Sijbers, Comparing isotropic and anisotropic filtering for voxel based DTI analyses: a simulation study., Human Brain Mapping, In Revision .

[126] M. A. Rocca, P. Valsasina, A. Ceccarelli, M. Absinta, A. Ghezzi, G. Riccitelli, E. Pagani, A. Falini, G. Comi, G. Scotti, M. Filippi, Structural and functional MRI correlates of Stroop control in benign MS., Human Brain Mapping 30 (1) (2009) 276–290.

[127] R. Bammer, F. Fazekas, M. Augustin, J. Simbrunner, S. Strasser-Fuchs, T. Seifert, R. Stollberger, H. Hartung, Diffusion-weighted MR imaging of the spinal cord, Am J Neuroradiol. 21 (2000) 587–591.

[128] S. Cader, H. Johansen-Berg, M. Wylezinska, J. Palace, T. E. Behrens, S. Smith, P. M. Matthews, Discordant white matter n-acetylasparate and diffusion mri measures suggest that chronic metabolic dysfunction contributes to axonal pathology in multiple sclerosis, NeuroImage 36 (2007) 19–27.

[129] J. T. Brassington, N. V. Marsh, Neuropsychological aspects of multiple sclerosis, Neuropsychol Rev 8 (1998) 43–77.

[130] J. M. Peyser, C. M. Poser, Neuropsychological correlates of multiple sclerosis. Handbook of clinical neuropsychology, vol. 2, Willey, New York, 1986, pp. 364–397.

[131] A. Turken, S. Whitfield-Gabrieli, R. Bammer, J. V. Baldo, N. F. Dronkers, J. D. Gabrieli, Cognitive processing speed and the structure of white matter pathways: convergent evidence from normal variation and lesion studies., NeuroImage 42 (2) (2008) 1032–1044.

[132] H. A. Wishart, A. J. Saykin, B. C. McDonald, A. C. Mamourian, L. A. Flashman, K. R. Schuschu, Brain activation patterns associated with working memory in relapsing-remitting multiple sclerosis, Neurology 62 (2004) 234–238.

[133] S. Cader, A. Cifelli, Y. Abu-Omar, J. Palace, P. M. Matthews, Reduced brain functional reserve and altered functional connectivity in patients with multiple sclerosis, Brain 129 (2006) 527–537.

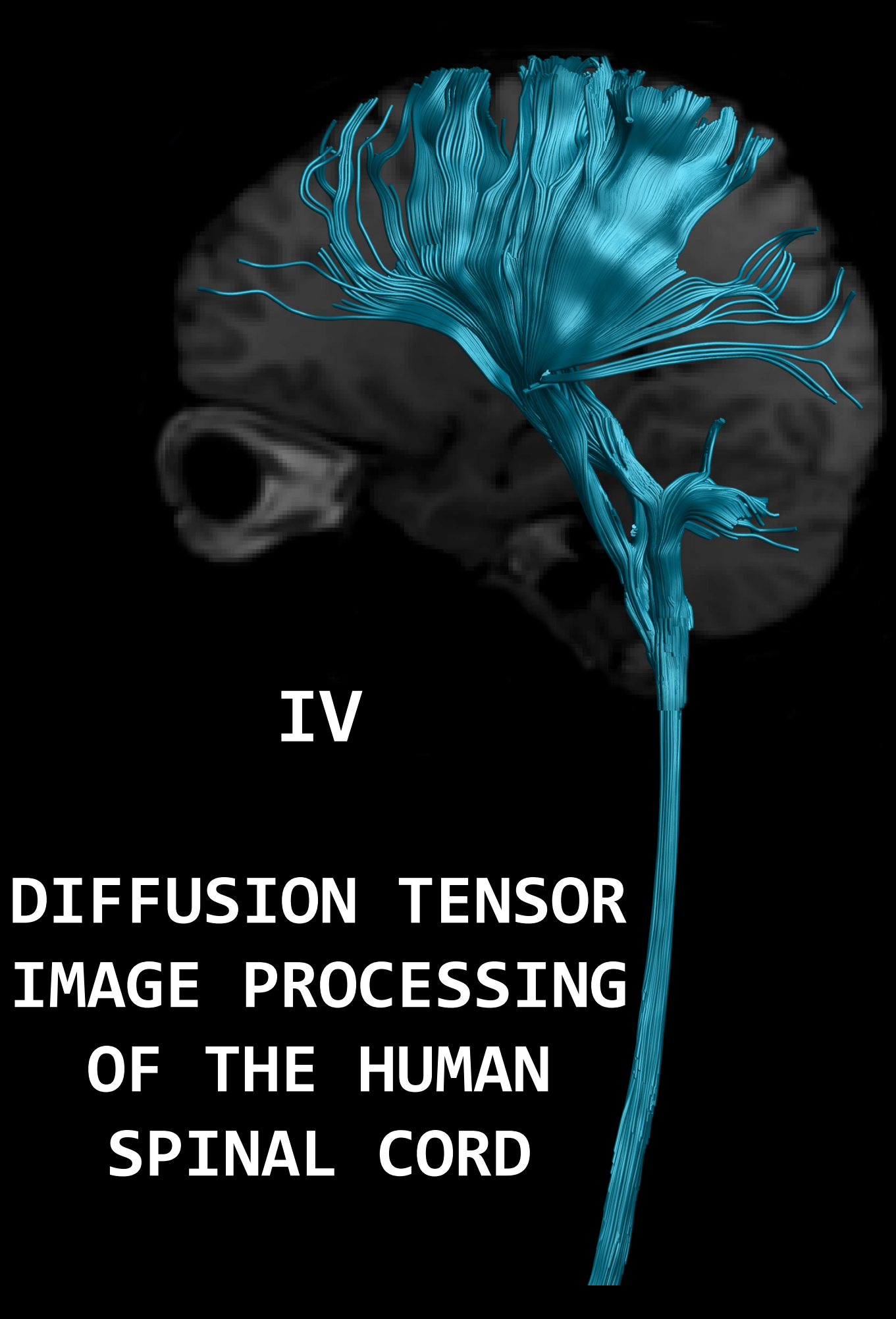

IV

DIFFUSION TENSOR IMAGE PROCESSING OF THE HUMAN SPINAL CORD

The spine is a series of bones running down your back. You sit on one end of it and your head sits on the other.

– Anonymous

7

A tracking based DTI segmentation method for the detection of diffusion-related changes of the cervical spinal cord with aging

Contents

Overview

The work in this chapter has been published in:

7.1 Introduction

It is generally known that during aging nerve cells die, and that the amount of nerve tissue gradually reduces [1]. Other age-related changes in the central nervous system are the swelling of the axons, the subsequent diminishing of myelin, and a decreasing quantity of the cytoskeleton [2]. Although conventional MRI can detect morphological WM changes, it can not reflect the tissue quality with respect to the WM microstructure coherence [3, 4]. These microstructural alterations will especially affect the local diffusion and are therefore measurable with DTI. This relatively new MRI technique measures the diffusion of water molecules and provides insight into the WM structure of the central nervous system [5]. Local quantitative measures can be derived from the diffusion tensor, such as the FA, which is a normalized measure for the degree of anisotropy, and the mean diffusivity (MD), i.e. the averaged diffusion. Recent DTI studies of different pathologies are starting to use these quantitative measurements, demonstrating the potential of this in vivo and non-invasive imaging technique for detecting microstructural pathological alterations [6, 7].
The spinal cord, a clinically important part of the central nervous system containing motor-and sensory pathways, is an interesting anatomical WM structure, because degeneration of its microstructure has been reported in many diseases [8, 9]. Due to its specific nature of measuring microstructural WM alterations, DTI can be seen as an exquisite diagnostic technique for a spinal cord examination. The spinal cord is surrounded by CSF where, in contrast to the brain, the GM is situated on the inside of the WM. Although there exists a great potential for studying spinal cord with DTI, only a limited number of papers has been published regarding this topic [10–17].
It is known that several factors hamper a robust DTI study, such as physiologic and respiratory movement of the subject and the relative motion of the spinal cord itself due to the pulsation of the surrounding CSF. Furthermore, small susceptibility variations are present in the proximity of the cervical vertebrae. In addition, the relatively small diameter of the spinal cord (12 mm on average) and the restricted resolution of the diffusion tensor images (in this study $2\times2\times2mm^3$) further impede a quantitative study. Indeed, it is known that a large number of voxels suffer from a partial volume effect (PVE), i.e. a combined signal originating from both the spinal cord and the CSF [18].

Previously reported DTI spinal cord studies generally employ a ROI based approach to segment the spinal cord tissue [10–12, 17, 19, 20]. In 1999, the first in vivo report of the diffusion properties of the human spinal cord was published in which only apparent diffusion coefficients and not the full diffusion tensor were calculated [19]. In a subsequent DTI study of the spinal cord, diffusion information was extracted from only two diffusion weighted images [10]. In the work of Ries et al. (2000), a DTI study of the spinal cord was performed with a large in-plane resolution, resulting in highly anisotropic voxels [20]. In their approach, the full diffusion tensor was calculated. Apparent diffusion coefficients were obtained from ROIs that were delineated in the middle of the sagittal spinal cord plane, in order to avoid contamination by the surrounding CSF. The first axial DTI study of the spinal cord was published by Wheeler-Kingshott et al. (2002), in which they segmented the whole spinal cord cross-section with ROIs to obtain FA, MD, and eigenvalues along the spinal cord [12]. In the work of Valsasina et al. (2005), a DTI acquisition with highly anisotropic voxels was implemented [21]. Only voxels originating from the central slice of the sagittal slab were incorporated in the further analysis and no ROIs were used. Mamata et al. (2005) investigated age-related spinal cord changes using DTI and reported both an FA decrease and an MD increase as a function of age [17].

To the best of our knowledge, almost all previously reported DTI studies of the spinal cord utilize a ROI based approach to delineate the tissue of interest. Because a ROI delineation method is based on the manual selection of voxels, it is highly labor-intensive and user-dependent. Moreover, to avoid PVE contaminated voxels in the analysis, other researchers proposed drawing very small ROIs to evaluate only the central sagittal slice of the spinal cord, thereby strongly reducing the number of data [21]. The aim of this chapter is to introduce a more standardized and robust segmentation technique for the analysis and interpretation of DTI spinal cord data based on diffusion tensor tractography (DTT) [22]. We demonstrate that the proposed segmentation approach outperforms the ROI based method in terms of reproducibility and sensitivity. In order to verify the proposed methods, alterations of diffusion properties - that can occur due to morphological changes with normal aging - were studied in the human spinal cord. We believe that a profound understanding of the aging process on the one hand, and of the quantitative spinal cord DTI results on the other hand, are of major importance for future studies that aim to detect diffusion related spinal cord changes in the case of different pathologies.

7.2 Methods

7.2.1 Data Acquisition

Diffusion tensor measurements of the cervical spinal cord (C1–C5) were performed with a 1.5T MR scanner (Siemens, Erlangen, Germany) on 45 healthy subjects (23 male and 22 female persons), with a mean subject age of 45 with a SD of 16 years (19–87 years). An informed consent was signed by all participants. All subjects had a normal appearing spinal cord on conventional T2-weighted MR images and none had pathological spinal cord symptoms as reviewed by a radiologist A severe signal dropout due to ghosting or susceptibility artifacts, caused by the movement of the subject or the use of an echo-planar sequence was observed in data sets of 3 subjects. These data sets were excluded from the analysis. All diffusion-weighted images were analyzed visually to check the presence of distortions in the data. Data sets were included in the analysis without the use of a specific distortion correction algorithm, when the geometric distortions were smaller than approximately 1 voxel. For the analysis of the diffusion properties along the spinal cord length the subject are split up into three groups: age $<$ 35 years (number of subjects: 12), 35 $<$ age $<$ 50 years (number of subjects: 15), age $>$ 50 years (number of subjects: 15).
Axial diffusion tensor images were obtained using a SE-EPI sequence with the following acquisition parameters: TR: 10.4s; TE: 100ms; diffusion gradient: 40mT/m; FOV = $256 \times 256mm^2$; matrix size: 128×128; number of slices = 30; image resolution = $2 \times 2 \times 2mm^3$; b = $700s/mm^2$; acquisition time: 12 min 18 s. Diffusion measurements were performed along 60 directions (+ 10 non-diffusion weighted (b0) images) for a robust estimation of FA, tensor orientation, and MD [23]. A combination of 2 elements of the CP (circular polarization) spine coil and 1 element of the neck coil was used. Diffusion tensor estimation, tractography, visualization, and quantitative analysis, was performed with the graphical toolbox 'ExploreDTI' (http://www.dti.ua.ac.be) [24]. No specific distortion correction was applied.

7.2.2 Quantitative Diffusion Parameters of Interest

Several quantitative diffusion parameters were analyzed for all subjects, using different segmentation methods (which are described in the following paragraphs). The FA and MD were calculated and averaged over all selected voxels for all subjects and segmentation methods. In addition, the three eigenvalues (λ_1, λ_2 and λ_3), the ratio of the first and the second eigenvalue (λ_1/λ_2), and the ratio of the first and the third eigenvalue (λ_1/λ_3) were also computed, since there has been suggested in [25] that these ratios can better differentiate between healthy and diseased subjects.

7.2.3 Spinal Cord Segmentation

Three segmentation techniques were investigated and their results were compared. First, the generally used ROI analysis was implemented. Second, a fiber tracking based segmentation technique was developed, in which the results were derived from the tracts [26]. Third, a hybrid segmentation approach was developed, incorporating information from both the tracts and the underlying voxels.

ROI Based Segmentation: Due to the PVE of spinal cord tissue and CSF, it is very hard to identify the edge voxels of the spinal cord. Three different ROI based segmentation approaches referred to as 'b0-ROI', 'L-ROI', and 'S-ROI' are introduced that aim for an optimal selection of the spinal cord voxels. In Fig. 1(a), a mid-sagittal slice of the spinal cord is depicted. An axial slice is selected to illustrate the three ROI based segmentation approaches, which are visualized in Fig. 1(b), (c), and (d). The border voxels are included in the analysis, when their center is situated inside the polygonal.

b0-ROI: In a first approach, ROIs are manually drawn around the spinal cord on the axial slices of the b0 image (see Fig. 1(b)). The b0 image provides a contrast that is independent of the quantitative diffusion properties that are evaluated in the subsequent analysis.

L-ROI: Since FA maps provide a better contrast between the spinal cord tissue (high FA) and the surrounding CSF (low FA), large ROIs are manually defined on axial FA slices, in this second ROI approach (see Fig. 1(c)).

S-ROI: When large ROIs are used to select the spinal cord, PVE contaminated voxels are included in the analysis. In an attempt to select voxels that contain only spinal cord information and no PVE with CSF, small ROIs are manually placed on the axial FA maps in this third ROI based segmentation method (see Fig. 1(d)).

All ROIs are drawn manually on each slice by the use of a polygonal. This was done by two observers, in order to evaluate the inter-observer reproducibility.

Tracking Based Segmentation (TS): In order to diminish the user-dependent factor of the ROI based method, diffusion tensor tractography (DTT) was performed on the spinal cord that was preparatory delineated by large ROIs, including WM, GM, and the voxels that suffer from a PVE with CSF. A standard deterministic streamline-based fiber tracking approach was applied with only one seed point per voxel in which the step size was $1mm$ [27]. Subsequently, all quantitative diffusion parameters of interest are selected on the tracts [28]. Note that the results of this DTT based analysis are dependent

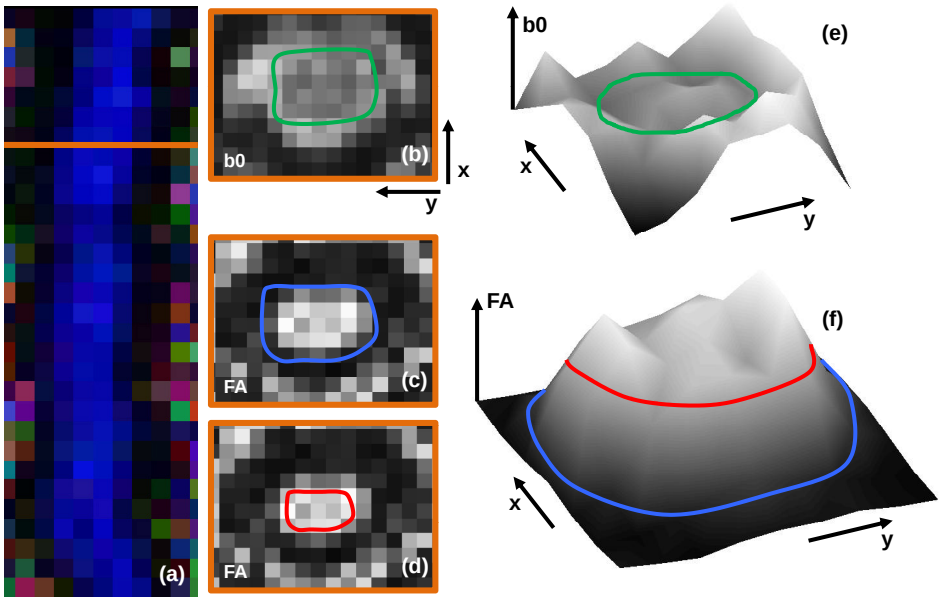

Figure 7.1.

on the interpolation technique to build the tracts, the step size, and a possible seed point interpolation factor. In the remainder of this paper, we will refer to this technique as 'Tract based Segmentation' (TS). Compared with the ROI delineation methods, the user-dependent factor is replaced by a DTT parameter-dependency in the TS approach. It is therefore very important to choose the appropriate DTT parameters. The maximal angle between two consecutive tract points was set to 20°. Since the spinal cord is cylindrically shaped, the maximal angle between two consecutive points on the tract of 20° will not create any bias, and prevents tracts to leave the spinal cord and propagate through surrounding tissue. This was confirmed visually. On the other hand, by enforcing the tracts to have a minimal length of $5mm$, the very small tracts only covering one or two voxels are filtered out. In the case of a low FA threshold during tracking, tracts will appear in voxels containing CSF or a PVE of spinal cord tissue with CSF. Since all tract data is included in the further analysis, this PVE contaminated information will bias the results. Moreover, the reproducibility of the method will be worse, since less restriction is imposed by the DTT algorithm, increasing the effect of the ROI delineation on the results. On the other hand, when high FA values are chosen for the tracking procedure, only the very high anisotropic part of the spinal cord is selected. In this way, again a bias can be introduced,

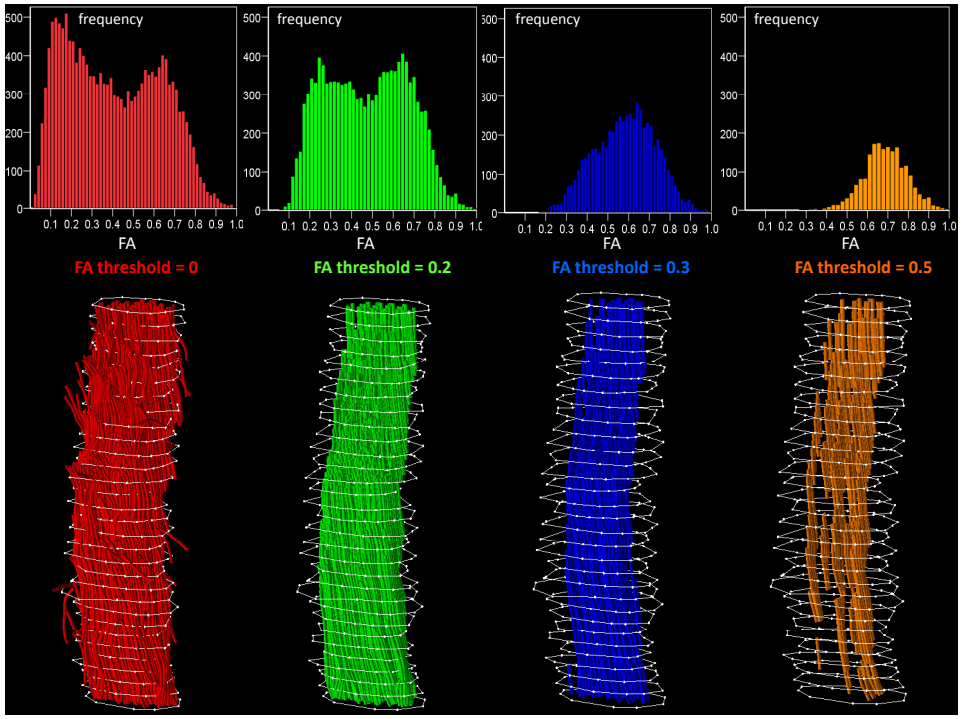

Figure 7.2.

because a degenerative or an older spinal cord, containing lower FA values, will not be fully taking into account and the FA will be overestimated. This bias is always present when FA thresholds are used, independent of their value, but their effect is much larger in the case of high FA thresholds. In Fig. 2, the tracts and their FA histograms of a randomly chosen 46 year old subject are presented for different DTT FA thresholds. In our study, a value of 0.3 was observed to be optimal as a minimal FA for seed point selection and a minimal FA to stop tracking in the TS approach. When using FA thresholds lower than 0.3, the results are biased by an important presence of CSF contaminated voxels. This FA threshold analysis was also performed on all other subjects, demonstrating analogous results as in Fig. 2. Note that this optimal FA threshold of 0.3 can depend on the data and the study protocol.

Hybrid Segmentation Approach (HS): This segmentation approach also employs DTT to select the spinal cord. Hereby, lower FA thresholds can be used in the DTT algorithm as compared with the TS method, since only voxels containing 8 tracts - referred to as the tract threshold - are subsequently

included in the analysis. In the remainder of this paper, this method is referred to as 'Hybrid Segmentation' (HS). The term 'Hybrid' originates from the fact that this method combines properties of the previous two methods. Indeed, DTT is performed as in the TS approach, but the diffusion parameters are evaluated on the selected voxels as in the ROI approach and not on the tracts. The HS approach is based on the idea that when many fiber tracts run through a voxel, this voxel is more reliable for the analysis. The method basically consists of two steps:

1. The spinal cord is preparatory delineated by large ROIs, including the spinal cord and the PVE with CSF. Thereafter, DTT is performed on all selected voxels, using only one seed point per voxel. Tracts with a length of $5mm$ and smaller are excluded from the analysis. The maximal angle between two consecutive tracking segments is set to $20°$. An FA threshold of 0.2 is used in the DTT algorithm.
2. In a second step, only voxels containing a predefined number of tracts - referred to as the tract threshold - are analyzed, instead of examining all quantitative fiber tracking results, like in the TS approach (see Fig. 3).

When a high FA for seed point selection and a high FA to stop tracking are used, a bias can be introduced, like stated similarly in the TS approach. Since only voxels containing a significant amount of tracts are considered in the subsequent analysis, the effect of PVE contaminated voxels on the results will be reduced. Therefore, a lower FA threshold could be implemented in the DTT algorithm of the HS approach, compared to TS. The optimal tract threshold obviously depends on the FA threshold that was used in the DTT algorithm. No FA threshold or an FA threshold of 0.1 resulted in a similar number of fiber tracts in the CSF voxels, the PVE contaminated voxels, and the spinal cord tissue voxels. In this case, applying a low tract threshold will result in the incorporation of many voxels containing CSF or a PVE with CSF. On the other hand, a high tract threshold will create a bias in the results by excluding spinal cord voxels from the analysis. An optimal FA threshold of 0.2 was found. This value was high enough to prevent too much tracking in PVE contaminated voxels and low enough to restrict the potential bias of a high FA threshold, especially in data sets of older subjects. A study was performed, concerning the optimal tract threshold when an FA threshold of 0.2 was used. When the tract threshold was high (> 16), spinal cord voxels with a high FA were excluded and the number of selected voxels was reduced, thus increasing the standard error of the FA histogram of the selected voxels and creating a bias (see Fig. 4). In the case of a small tract threshold,

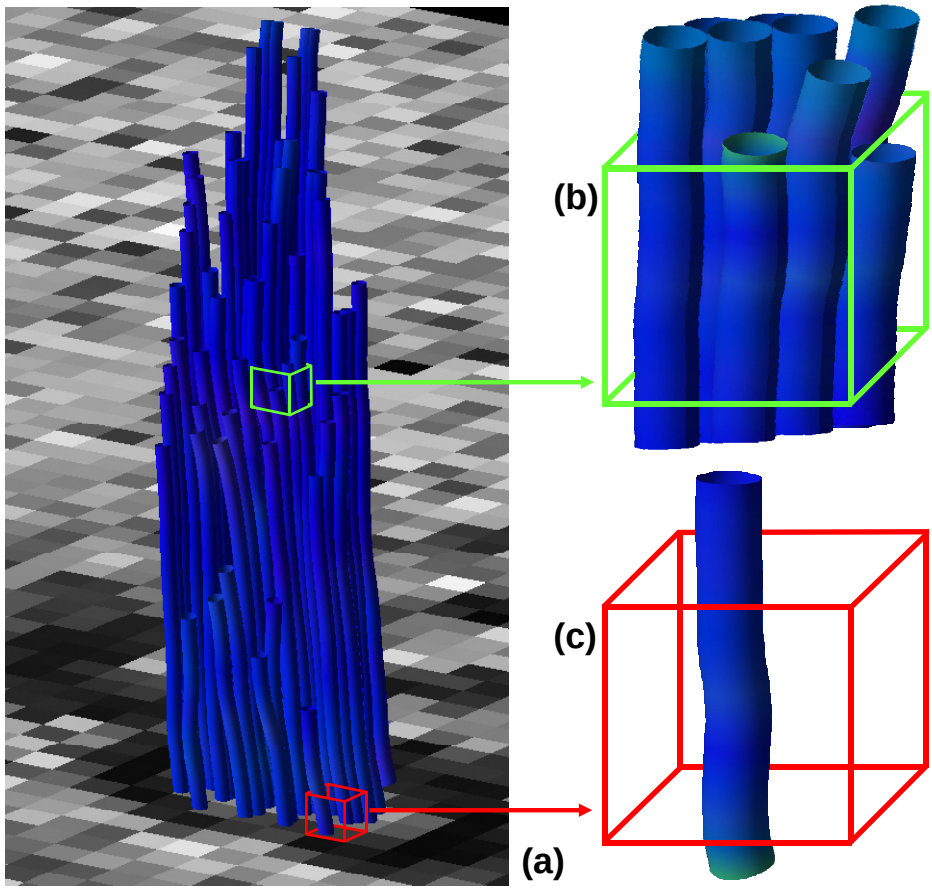

Figure 7.3.

more voxels containing PVE with CSF are retained, again increasing the standard error of the FA histogram. An optimal tract threshold of 8 was found in the analysis. This value excludes many PVE contaminated voxels and retains as many spinal cord tissue voxels as possible. Furthermore, these thresholds resulted in the lowest standard error in the FA histogram of the selected voxels. In the case of higher FA thresholds during tracking or higher tract thresholds, this standard error rises because less voxels are selected. On the other hand, this standard error will increase with lower FA-and tract thresholds, since more PVE contaminated voxels are included in the analysis. In Fig. 4, FA histograms and scatter plots of the number of tracts in the selected voxels (denoted as t) and the FA value of these voxels are displayed for different FA-and tract thresholds. To summarize, the tract threshold is

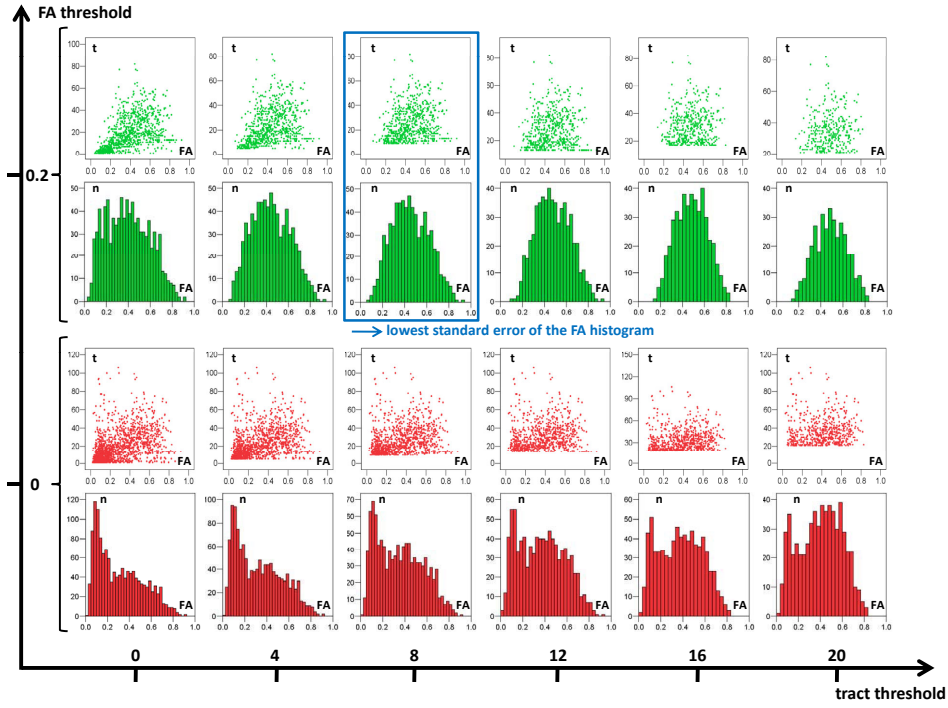

Figure 7.4.

obtained by a qualitative analysis (a visual inspection of the tractography results), as well as a quantitative analysis (evaluation of the standard error of the FA). Again, it is important to note that the optimal parameters for a HS analysis can depend on the data and the study protocol.

7.2.4 Statistical Analysis Procedures

Statistical tests were performed with the SPSS analysis package (http://www.spss.com). The intra-and inter-subject reproducibility of the different segmentation methods was tested using the intra-class correlation coefficient (ICC). This coefficient is used to measure the inter-rater reliability for two or more raters and can be conceptualized as the ratio of the between-groups variance to the total variance. A measurement is deemed highly reproducible for ICC > 0.9. In the case of $0.7 <$ ICC < 0.9 the reproducibility is considered acceptable. Finally, ICC < 0.7 was interpreted as poorly reproducible. In order to investigate correlations between the diffusion measurements and age, Pearson (r) and Spearman (ρ) correlation tests were performed - depending on the data distribution as investigated by the Kolmogorov-Smirnov test. Kolmogorov-Smirnov tests, checking normality, were

applied in the case of the diffusion parameters for the different subjects and resulted in p>> 0.05, suggesting a parametric approach for the correlation analysis. However, the parametric Pearson correlation test is dependent on the presence of outliers. In this study, outliers occurred and because they could be assumed as genuine values, a Spearman correlation test was also applied. The DTI results of male and female subjects were combined since a Mann-Whitney U-test showed no differences of all the diffusion parameters between the sexes (p>> 0.05). Moreover, the age distribution was not significantly different for both sexes (p>> 0.05, with 21 males vs 19 females). In the figures, '*' denotes statistical significance at the 0.05 level, '**' at the 0.01 level.

7.3 Results

7.3.1 Reproducibility

The ICC values are shown in Table 1 for the different DTI parameters, demonstrating that the tracking based methods are highly reproducible with ICC values above 0.9. ROI based delineation of the spinal cord on the FA maps was observed to have a lower reliability. When ROIs were defined on the non-diffusion weighted images, the reproducibility was even lower. Note that an intra-rater as well as an inter-rater reproducibility is measured.
figure

	b0-ROI		L-ROI		S-ROI		TS		HS	
	intra	inter	intra	inter	intra	inter	intra	inter	intra	inter
FA	0.36	0.28	0.67	0.62	0.69	0.66	0.96	0.91	0.97	0.96
MD	0.40	0.31	0.72	0.70	0.73	0.71	0.97	0.92	0.98	0.93
λ_1	0.54	0.40	0.75	0.72	0.70	0.68	0.97	0.93	0.98	096
λ_2	0.36	0.30	0.70	0.65	0.74	0.68	0.98	0.94	0.99	0.95
λ_3	0.30	0.28	0.70	0.65	0.70	0.66	0.98	0.92	0.99	0.96

figure

7.3.2 Correlation Analysis

In this section, the correlation results, depicted in Figs. 5, 6, 7, and 8, are described. Only in the case of a statistically significant correlation, a trendline is drawn.

ROI Based Segmentation: It is clear that MD, λ_1, λ_2, and especially λ_3 are higher, for the 'L-ROI' compared to the 'S-ROI' approach. On the other hand, the FA is lower in the case of 'L-ROI'. These results mark the presence

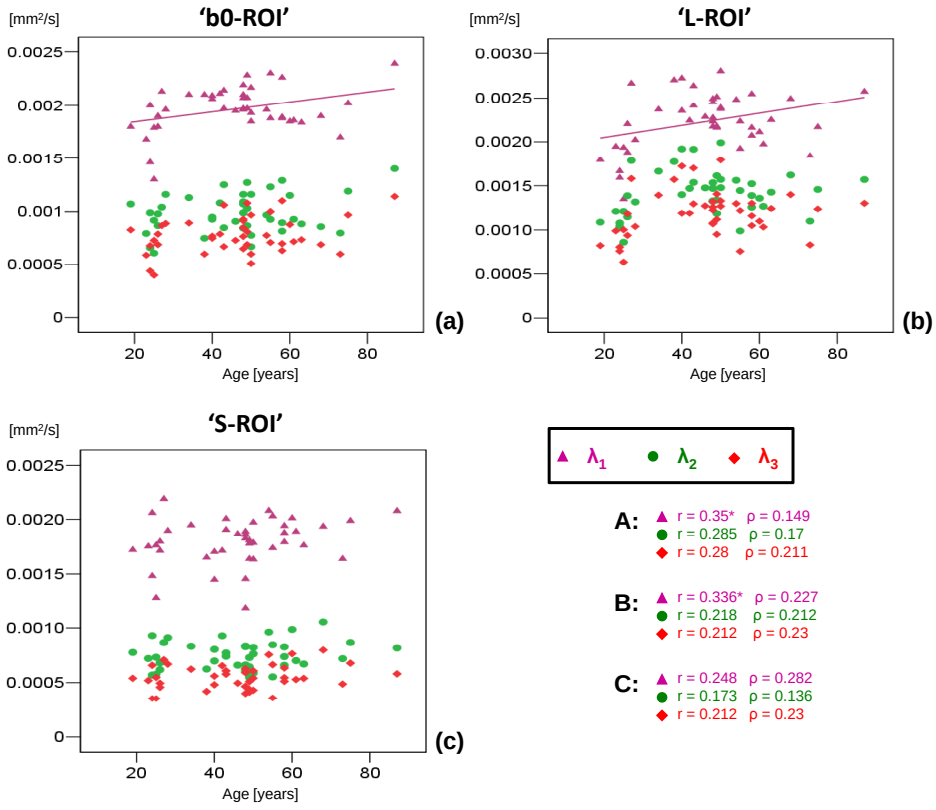

Figure 7.5.

of CSF or voxels contaminated with a PVE of CSF in the 'L-ROI' results. Pearson and Spearman correlation tests revealed that the results derived with a large and a small ROI are positively correlated ($p < 0.001$ and ρ and r values of approximately 0.5), indicating similar relative results. The DTI properties that are derived with the 'b0-ROI' approach are positively correlated ($p < 0.001$) with both the 'L-ROI' and the 'S-ROI' results. Although the diffusion tensor eigenvalues indicate some tendencies as a function of age, only λ_1 is significantly correlated in the case of 'b0-ROI' and 'L-ROI', as shown in Fig. 5. In Fig. 5 (a), the eigenvalues from the 'b0-ROI' delineation are displayed. Figs. 5 (b) and (c) show the results of the 'L-ROI' and 'S-ROI' segmentation methods, respectively. In Fig. 6, the correlation of FA, MD, λ_1/λ_2, and λ_1/λ_3 as a function of age is shown. No statistically significant correlations were found.

The results obtained by the 'S-ROI' analysis contain less PVE contaminated

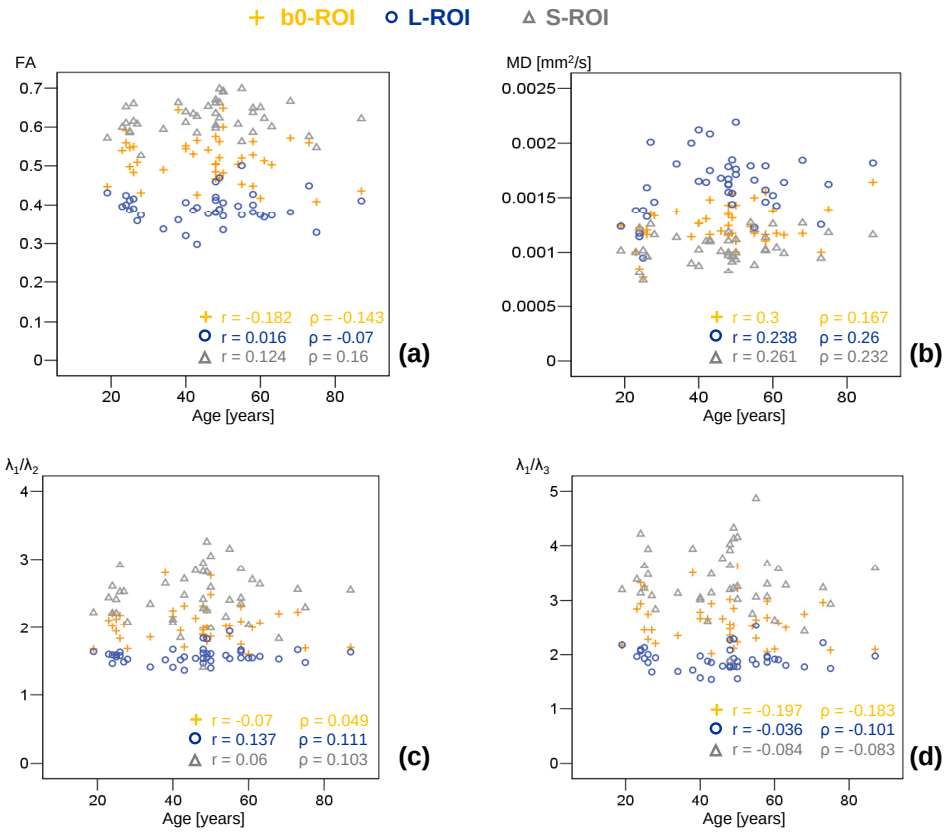

Figure 7.6.

voxels with CSF compared with the 'L-ROI' analysis. To further reduce the PVE in the results, Valsasina et al. (2005) selected only voxels coming from the central slice of the sagittal images [21]. However, this strongly reduces the number of data. Furthermore, the diffusion properties of the central spinal cord voxel can differ. On the one hand, a decreased FA was observed in the central spinal cord voxels of different subjects, indicating a possible PVE of WM and GM. In some data sets, on the other hand, central voxels with a relatively high FA in the middle were noted (Fig. 7).

Tracking Based Segmentation: The DTI parameters FA, MD, λ_1, λ_2, λ_3, and λ_1/λ_3 were found to be significantly correlated with age, when using the TS approach. λ_1/λ_3 tends to decrease with age, but not on a statistically significant basis. These results are shown in Fig. 8.

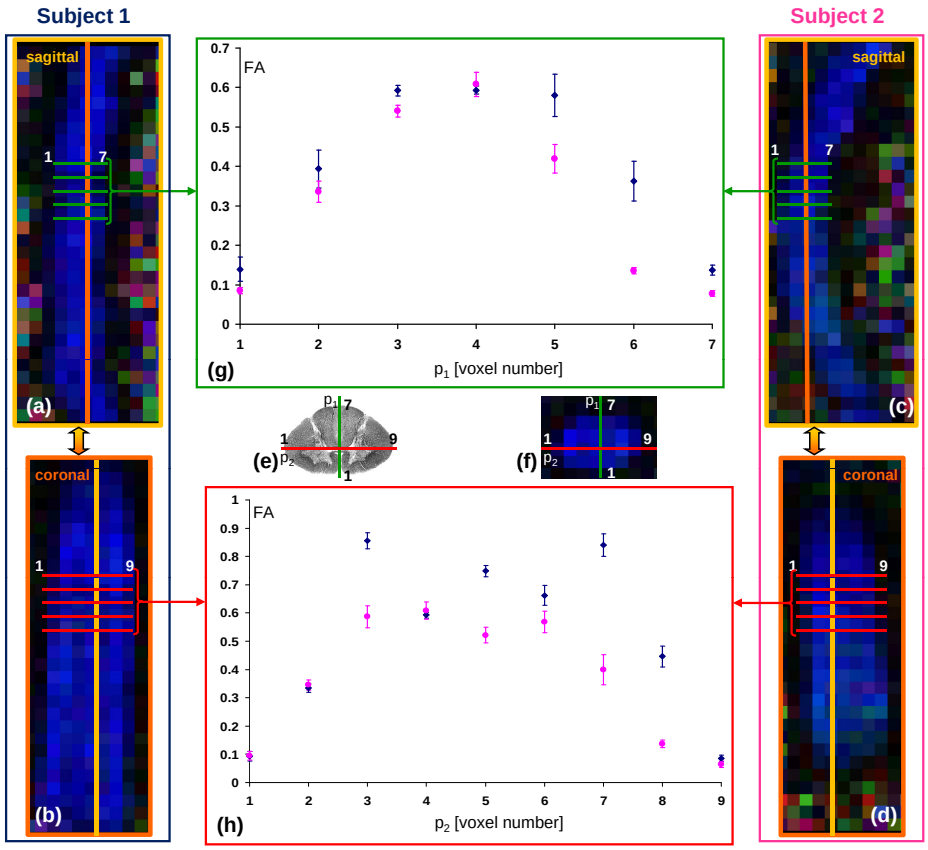

Figure 7.7.

Hybrid Segmentation Approach: The correlation of all DTI parameters is statistically significant with age, and often at a $p < 0.01$ level with $0.3 < r,\rho < 0.5$. Results are displayed in Fig. 8. The HS approach is the only segmentation method that detects statistically significant correlations for all parameters. In Fig. 8 (e) and (f) it is shown that, although all three eigenvalues increase during aging, λ_2 and especially λ_3 will have a stronger effect than λ_1.

7.3.3 Diffusion Parameters along the Cervical Spinal Cord Length

In Fig. 9, the diffusion properties are evaluated along the length of the spinal cord. Hereby, the HS method with the above mentioned parameters is used to select

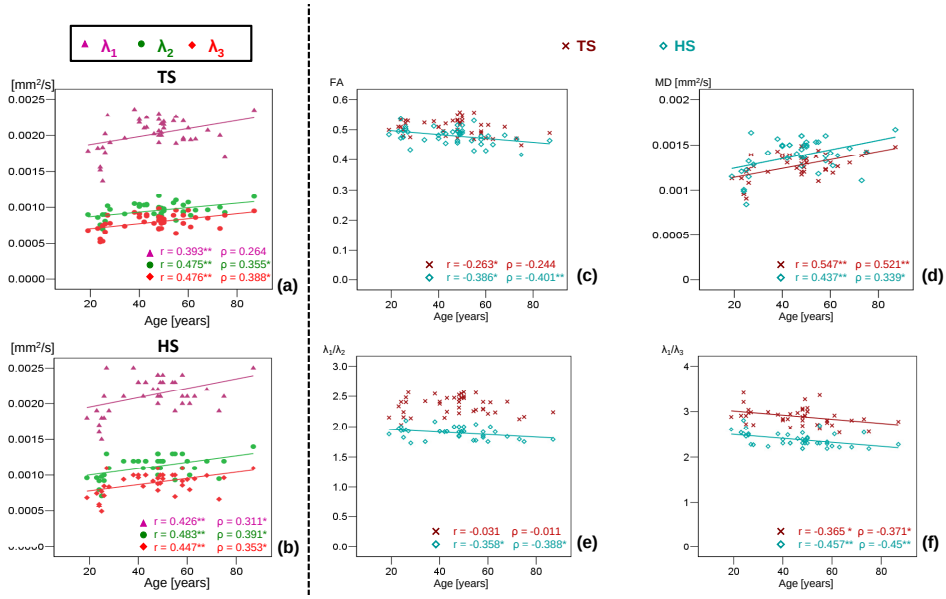

Figure 7.8.

the spinal cord voxels of the different slices. The subject group was subdivided in three groups: under 35 years, between 35 and 50 years, and above 50 years. In Fig. 9 (a)-(e), the averaged diffusion parameters of the selected voxels with the HS method are calculated for each slice. Since the HS method is based on the number of tracts that run through a voxel, a small bias can be created at the edges of the image. This is due to the fact that tracts can penetrate a voxel in the middle of the image from both sides of that voxel, whereas a voxel that is situated at the edge of the image can only be penetrated along on side. A small decrease of selected voxels with the HS method was observed at the edges along 3 to 4 slices. The results of these slices are therefore deleted from the Figs. 9 (a)-(e). The trends observed in Figs. 9 (a)-(e) are confirmed by a ROI analysis, as shown in Figs. 9 (f)-(j). An FA increase was found at higher cervical levels, for all age groups (see Figs. 9 (a) and (f)). A decrease of MD, λ_1, λ_2, and λ_3, was found for the youngest group at higher cervical levels (see Fig.s 9 (b)-(e)). In contrast to this, these diffusion values were increasing at the higher spinal cord slices for the middle-aged and the older group (see Figs. 9 (b)-(e)). These results are confirmed by the ROI analysis (see Figs. 9 (f)-(j)).

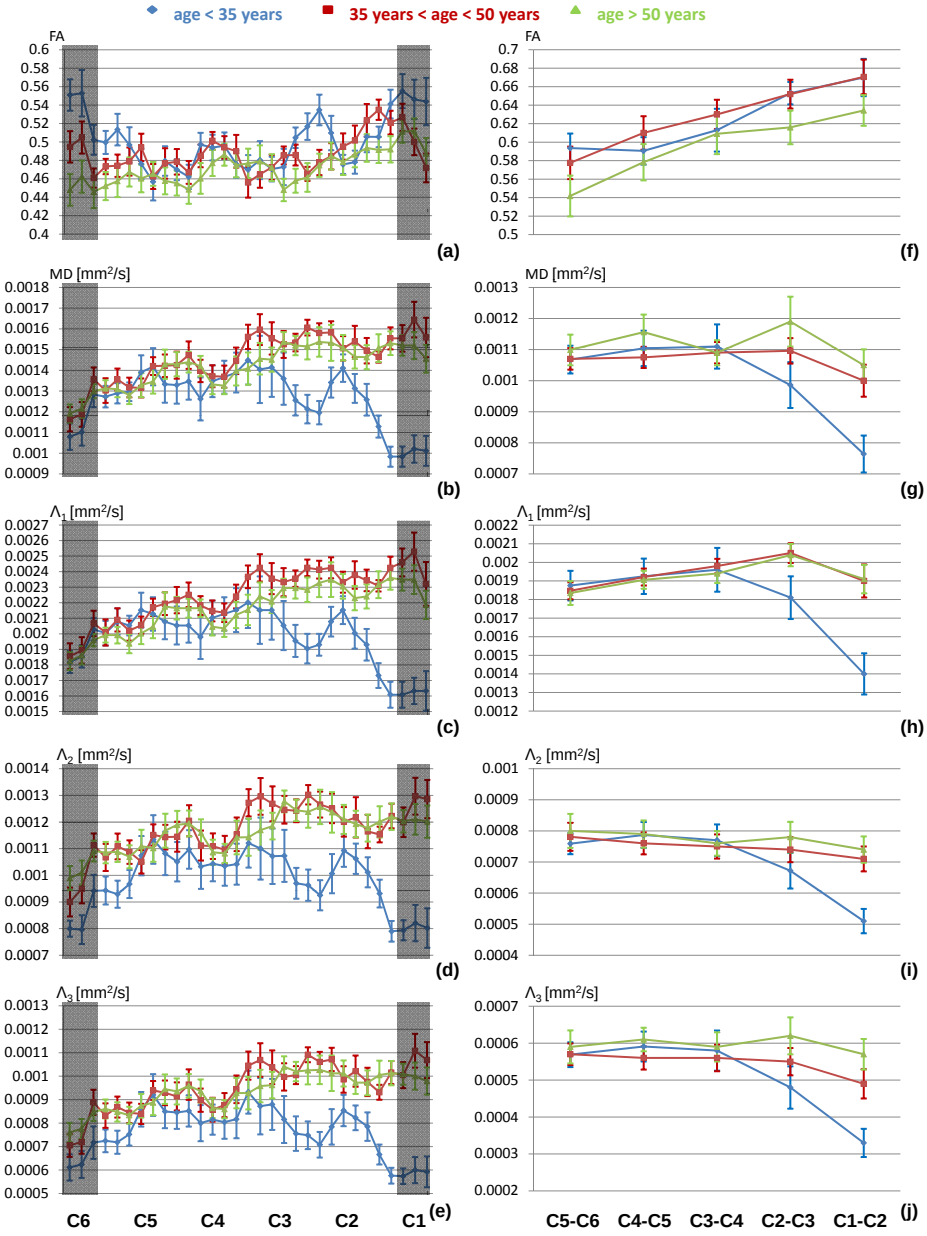
age < 35 years
35 years < age < 50 years
age > 50 years
FA
(a)
FA
(f)
MD [mm²/s]
(b)
MD [mm²/s]
(g)
Λ1 [mm²/s]
(c)
Λ1 [mm²/s]
(h)
Λ2 [mm²/s]
(d)
Λ2 [mm²/s]
(i)
Λ3 [mm²/s]
(e)
Λ3 [mm²/s]
(j)
C6 C5 C4 C3 C2 C1
C5-C6 C4-C5 C3-C4 C2-C3 C1-C2

Figure 7.9.

7.4 Discussion

In this work, all subjects had a normal cervical spinal cord and no pathological spinal cord symptoms. The FA, MD, λ_1, λ_2, λ_3, λ_1/λ_2, and λ_1/λ_3 were studied as a function of age, indicating that the ROI based segmentation method is less sensitive to age related effects compared to the proposed tract or hybrid based approaches. In the tracking based segmentation methods (TS and HS), the user-dependent factor is negligible, but replaced by a DTT parameter-dependence. Only the proposed methodology using DTT results and the underlying voxel data (HS) demonstrated a statistically significant correlation of all diffusion parameters with age. The drawback of the semi-automated approaches is that the absolute, quantitative results depend on certain parameters. The validity of the proposed methods still has to be confirmed in studies of different pathologies, which is the subject of future work. A lot of valuable research is performed regarding the optimization of the DTI acquisition with respect to bulk motion and pulsatile flow artifacts from the surrounding CSF [16, 29–32]. Other studies use cardiac gating to reduce motion artifacts, or interleaved echo-planar diffusion imaging to reduce the scan time [33, 34]. Line scan imaging is a fast technique that relies on the acquisition of columns [30, 35]. However, in this work, a standard acquisition scheme was used with isotropic voxel sizes, to reduce the PVE in the slice direction. Optimized and adapted DTI acquisition schemes might improve the image quality and therefore the reliability of the subsequent analysis.
Fig. 3 demonstrates that the 'S-ROI','L-ROI', and the 'b0-ROI' segmentation techniques strongly suffer from a low intra-and inter-subject reproducibility. The two experts that performed the segmentation were equally instructed on the ROI delineation and had no prior knowledge about the age or sex of the subjects. The lack of inter-and intra-subject reproducibility is therefore originating from a different interpretation of the data and can be seen as an indicator for the sensitive operator-dependency of the ROI definition. It is clear that, when examining the spinal cord with DTI, this problem will be manifested, due to the combination of the small spinal cord size, the limited resolution, and the PVE. TS and HS result have shown to be highly reproducible (high ICC values, see Fig. 3). The ROI definition is less stringent for TS and HS, compared to the ROI based method, since ROIs are only used to mark out the spinal cord, including the PVE with CSF, from the surrounding vertebrae and other tissues. Furthermore, only the voxels with significant a priori information, i.e. containing a predefined number of tracts with certain anisotropy values, are evaluated in the analysis of the HS approach.
The 'b0-ROI', 'L-ROI', and 'S-ROI' methods demonstrate correlation trends between the different DTI parameters and age (Figs. 4 and 5), but this is never considerably statistically significant. The user-dependency, the small spinal cord diameter, and the PVE result in a low reliability of the ROI segmentation method,

especially when ROIs are drawn on the non-diffusion weighted images. As seen in Fig. 4 (a) and (b), the 'b0-ROI' and 'L-ROI' approaches found a statistically significant Pearson correlation coefficient. However, this result is not confirmed by a statistically significant Spearman correlation coefficient. Therefore, the Pearson correlation significance is probably affected by the presence of outliers. Since the ROIs are defined on the FA maps as in the 'L-ROI' and 'S-ROI' approaches, a potential bias can exist when studying the FA. This bias originates from the fact that FA maps are used for a ROI based segmentation of the spinal cord on the one hand, and that the FA is compared between subjects on the other hand. Spinal cord voxels with a lower FA value, for example in the case of a pathology, can therefore potentially be excluded from the analysis since they are interpreted as non-spinal cord voxels or PVE contaminated voxels during the ROI delineation on the spinal cord FA map. More succinctly, the dependent variable is used to define the independent variable in the analysis, which is statistically not correct. However, when an unrelated image contrast such as the non-diffusion weighted image (b0) is used for the ROI delineation, results are biased by a lack of reproducibility (see Fig. 3). We therefore believe the FA map presents a more adequate image contrast for an accurate ROI definition, when DT images are acquired with the acquisition parameters of this study. Furthermore, the possible bias caused by the ROI delineation on the FA maps will not affect the quantitative results in the 'L-ROI' method, since all spinal cord tissue and the PVE with CSF is included in the analysis. The results obtained by the 'S-ROI' analysis contain less PVE contaminated voxels with CSF compared with the 'L-ROI' analysis. Valsasina et al. (2005) selected only voxels coming from the central slice of the sagittal images in order to reduce this PVE with CSF [21]. As shown in Fig. 7, the DT properties of the central spinal cord voxel can vary. A possible explanation is the variation in spinal cord diameter between different subjects. Indeed, a smaller spinal cord diameter might result in a more important PVE of WM and GM, thus reducing the anisotropy values in certain voxels. Since it is reported that the spinal cord narrows and the spinal cord diameter decreases with age, only interpreting these central voxels, might affect the age-related results [36]. In addition to the aging effects on the spinal cord diameter, cervical cord atrophy is a frequent finding in different pathologies [37].

The tractography results were observed to be more reproducible, since the manual ROI segmentation is only required to differentiate the spinal cord tissue and CSF roughly from the surrounding vertebrae and other tissues (see Fig. 3). Although results can be biased by the DTT parameter selection, when using tractography to select the spinal cord voxels, no such bias was observed in our study. A visual inspection confirmed that tracts were observed along the spinal cord region of interest (C1–C5). Diffusion measures were compared in the case of three different DTT parameter sets for all subjects. A correlation analysis and an ICC measurement

was performed comparing the results of the TS segmentation approach under different DTT parameters. Pearson and Spearman correlation coefficients were larger than 0.85 and an ICC > 0.9 was found, demonstrating the high reliability of the TS approach and the rather high insensitivity of the diffusion results to the DTT parameter selection. In the case of all DTT parameter sets, a statistically significant correlation with age was observed for the diffusion parameters λ_1, λ_2, λ_3, and MD. However, when subject groups, suffering from certain degenerative spinal cord pathologies, are studied, the DTT parameter selection has to be approached very cautiously. Nevertheless, we believe that, because of the much higher standardization of the tractography based method - each data set is treated in exactly the same way - its results are more reliable compared to the results of the manual ROI based segmentation.

In the hybrid segmentation approach, only voxels containing 8 tracts - referred to as the tract threshold - were analyzed. The results of the HS segmentation method are, similar to those of the TS approach, parameter-dependent instead of user-dependent. Analogous as in the TS segmentation, the quantitative diffusion results were compared in the case of three different FA and tract thresholds for all subjects. Again, a correlation analysis and an ICC measurement was performed comparing the results of the HS method under different threshold values. Pearson and Spearman correlation coefficients were larger than 0.82 ($p< 0.001$) and an ICC > 0.9 was found. These results indicate a high reliability of the HS approach and the rather insensitivity of the diffusion results to the threshold selection. In the case of all DTT parameter sets, a statistically significant correlation with age was observed for all the diffusion parameters λ_1, λ_2, λ_3, MD, FA, λ_1/λ_2, and λ_1/λ_3. We postulate that the HS approach is a segmentation method that retrieves the available spinal cord information in the most reproducible and robust way.

A drawback of all implemented approaches to select the spinal cord voxels of interest, is the fact that the diffusion properties are averaged along the cervical spinal cord (C1–C6). Wheeler-Kingshott et al. (2002) demonstrated that these diffusion values (FA, MD, eigenvalues) could vary along the spinal cord [12]. They used a ROI analysis on four subjects. In Fig. 7, the FA, MD, and the eigenvalues are evaluated along the spinal cord (C1–C6). The HS method was used to select the spinal cord voxels of the different slices. The healthy subject group was subdivided in three groups according to the age. In contrast to the results of Wheeler-Kingshott et al. (2002), high FA values were observed at C1. Many factors can attribute to these contradictory results. First of all, Wheeler-Kingshot et al. (2002) used anisotropic voxels and a different acquisition scheme compared to our study. Also, the analysis of Wheeler-Kingshot et al. (2002) was based on 4 subjects, which can affect the results. Furthermore, in their study the most superior slices were at the level of the pons where different conditions arise, i.e. less mono-directional oriented fibers in comparison with the spinal cord. The HS method is based on the number

of tracts that run through a voxel. Therefore, a small bias can be created at the edges of the image, due to the fact that tracts can penetrate a voxel in the middle of the image from both sides of that voxel, in contrast to voxels at the edges of the image. Therefore, the results of the three outermost slices at both edges, are withdrawn from this analysis. In contrast to the work of Wheeler-Kingshott et al. (2002), we subdivided our healthy population into three age groups. As Figs. 7 (b)-(e) demonstrate, the MD, λ_1, λ_2, and λ_3 decreased at higher cervical levels in the youngest age group, whereas these values increased in the other two age groups. These results are confirmed by a ROI analysis along the spinal cord (see Fig.s 7 (f)-(j)). A higher penetration of CSF through the spinal cord in older subjects can explain these findings, although other factors, such as a broadening of the spinal cord diameter at the upper levels in the younger subject group compared to the older groups, might also explain the decrease of the MD and the eigenvalues at the upper spinal cord levels in the youngest group. However, no statistically significant correlation was observed between the number of selected voxels in the different segmentation approaches and the age ($p > 0.6$ for all segmentation approaches).

The DTI results of the different segmentation methods should be interpreted with care, since no histological and thus no ground-truth data of the examined persons is available. This stresses the importance of animal studies, where the measurement of diffusion properties can be correlated with histological findings [38]. It is therefore im-possible to consider one of the segmentation techniques as a perfect match with the real, underlying situation. Consequently, the objective in this study was not to determine the absolute, quantitative spinal cord DTI parameters, but to find the most reliable and robust segmentation method that can extract the relevant information, given the mentioned problematic nature of spinal cord DTI. When the tendencies of the different DTI parameters are compared for the different segmentation methods, a certain similarity can be observed (see Figs. 4, 5, and 6). This suggests that, independent of the segmentation approach that was used, the diffusion parameters indeed evolve as a function of age. The fact that these underlying trends of the diffusion characteristics are only detected on a statistically significant basis by the proposed HS approach, reflect the high reproducibility, sensitivity and robustness of this segmentation method. In addition, our DTI results are confirmed by the histological findings in literature of spinal cord degeneration with aging [39]. Furthermore, these tendencies are validated by the available DTI literature of both brain and spinal cord [17, 40–43]. Ota et al. (2006) detected a statistically significant increase of MD, λ_2, and λ_3 values and a decrease of the FA in function of age in most parts of the corpus callosum [40]. They did not observe a significant increase of λ_1. Another age-related DTI study of the brain demonstrated a decreased FA, and an increased MD as a function of age in frontal fiber systems, whereas only small differences were detected in the posterior regions of the brain [41]. Salat and colleagues presented analogous results [42]. Yoshiura

et al. (2005) discovered an FA increase in younger adults, whereas no age-related changes were observed in indices derived from mean diffusivity maps [43]. In their study, Mamata et al. (2005) detected an FA decrease (r = 0.244) and an apparent diffusion coefficient increase (r = 0.242) as a function of age in cervical spondylosis patients with a normal spinal cord at the C2–C3 level [17]. The data were derived after a ROI based delineation, whereby only the strictly central part of the spinal cord was delineated in an attempt to exclude any CSF. In conclusion, different spinal cord DTI segmentation methods are compared in this study. We can conclude that the tendencies that were observed match with the expected evolution of the diffusion characteristics during normal aging. We demonstrate an increase of λ_1, λ_2, λ_3, MD, and a decrease of FA, λ_1/λ_2, and λ_1/λ_3 as a function of age. HS is the only segmentation method that traces the tendencies of all considered diffusion properties on a statistically significant basis. We postulate that the HS approach retrieves the available spinal cord information in the most reproducible and robust way, given the specific problematic nature of the spinal cord DTI data.

Bibliography

[1] J. Morrison, P. Hof, Life and death of neurons in the aging brain, Science. 278 (1997) 412–419.

[2] A. Peters, The effects of normal aging on myelin and nerve fibers: a review, J Neurocytol. 8–9 (2002) 581–593.

[3] M. Albert, Neuropsychological and neurophysiological changes in healthy adult humans across the age range, Neurobiol Aging. 14 (1993) 623–625.

[4] C. Guttman, F. Jolesz, R. Kikinis, R. Killiany, M. Moss, T. Sandor, M. Albert, White matter changes with normal aging, Neurology 50 (1998) 972–978.

[5] P. Basser, D. Jones, Diffusion-tensor MRI: theory, experimentel design and data analysis - a technical review, NMR biomed 15 (2002) 456–467.

[6] W. Taylor, E. Hsu, K. Krishnan, J. MacFall, Diffusion tensor imaging: Background, potential, and utility in psychiatric research, Biol Psychiatry 55 (2004) 201–207.

[7] M. Schocke, K. Seppi, R. Esterhammer, C. Kremser, K. Mair, B. Czermak, W. Jaschke, W. Poewe, G. Wenning, Trace of diffusion tensor differentiates the Parkinson variant of multiple system atrophy and Parkinsons disease, NeuroImage 21 (2004) 1443–1451.

[8] M. Rocca, S. Hickman, L. Bo, F. Agosta, D. Miller, G. Comi, M. Filippi, Imaging spinal cord damage in multiple sclerosis., J Neuroimaging. 15 (4) (2005) 297–304.

[9] M. Valencia, M. Castillo, MRI findings in posttraumatic spinal cord Wallerian degeneration., Clin Imaging. 30 (6) (2006) 431–433.

[10] C. Clark, D. Werring, D. Miller, Diffusion imaging of the spinal cord in vivo: estimation of the principal diffusivities and application to multiple sclerosis, Magn Reson Med. 43 (2000) 133–138.

[11] C. Clark, D. Werring, Diffusion tensor imaging in spinal cord: methods and applications - a review, NMR Biomed. 15 (2002) 578–586.

[12] C. Wheeler-Kingshott, S. Hickman, G. Parker, O. Ciccarelli, M. Symms, D. Miller, G. Barker, Investigating cervical spinal cord structure using axial diffusion tensor imaging, NeuroImage 16 (2002) 93–102.

[13] G. Barker, Diffusion-weighted imaging of the spinal cord and optic nerve, J Neurol Sci. 186 (2001) 1:S45–9.

[14] A. Toosy, D. Werring, R. Orrell, R. Howard, M. King, G. Barker, D. Miller, A. Thompson, Diffusion tensor imaging detects corticospinal tract involvement at multiple levels in amyotrophic lateral sclerosis, J Neurol Neurosurg Psychiatry. 74 (2003) 1250–1257.

[15] F. Agosta, B. Benedetti, M. Rocca, P. Valsasina, M. Rovaris, G. Comi, M. Filippi, Quantification of cervical cord pathology in primary progressive MS using diffusion tensor MRI, Neurology 64 (2005) 631–635.

[16] S. Maier, H. Mamata, Diffusion tensor imaging of the spinal cord, Ann N Y Acad Sci. 1064 (2005) 50–60.

[17] H. Mamata, F. Jolesz, S. Maier, Apparent diffusion coefficient and fractional anisotropy in spinal cord: age and cervical spondylosis-related changes, J Magn Reson Imaging 22 (2005) 38–43.

[18] A. Pfefferbaum, E. Sullivan, Increased brain white matter diffusivity in normal adult aging: relationship to anisotropy and partial voluming, Magn Reson Med 49 (5) (2003) 953–961.

[19] C. Clark, G. Barker, P. Tofts, Magnetic resonance diffusion imaging of the human cervical spinal cord in vivo, Magn Reson Med. 41 (1999) 1269–1273.

[20] M. Ries, R. Jones, V. Dousset, C. Moonen, Diffusion tensor MRI of the spinal cord, Magn Reson Med. 44 (2000) 884–892.

[21] P. Valsasina, M. Rocca, F. Agosta, B. Benedetti, M. Horsfield, A. Gallo, M. Rovaris, G. Comi, M. Filippi, Mean diffusivity and fractional anisotropy histogram analysis of the cervical cord

in MS patients, NeuroImage 26 (2005) 822–828.

[22] S. Mori, P. van Zijl, Fiber tracking: principles and strategies - a technical review, NMR Biomed 15 (7–8) (2002) 468–480.

[23] D. Jones, The effect of gradient sampling schemes on measures derived from diffusion tensor MRI: a Monte Carlo study, Magnetic Resonance in Medicine 51 (2004) 807–815.

[24] A. Leemans, J. Sijbers, P. Parizel, A graphical toolbox for exploratory diffusion tensor imaging and fiber tractography, in: 14th Annual Meeting - Section for Magnetic Resonance Technologists, Miami, USA, 2005.

[25] S. Song, J. Yoshino, T. Le, S. Lin, S. Sun, A. Cross, R. Armstrong, Demyelination increases radial diffusivity in corpus callosum of mouse brain, Neuroimage 21 (2005) 132–140.

[26] D. Jones, A. Travis, G. Eden, C. Pierpaoli, P. Basser, PASTA: pointwise assessment of streamline tractography attributes, Magn Reson Med 53 (6) (2005) 1462–1467.

[27] P. Basser, S. Pajevic, C. Pierpaoli, J. Duda, A. Aldroubi, In vivo fiber tractography using DT-MRI data, Magnetic Resonance in Medicine 44 (2000) 625–632.

[28] D. Jones, M. Catani, C. Pierpaoli, S. Reeves, S. Shergill, M. O'Sullivan, P. Maguire, M. Horsfield, A. Simmons, S. Williams, R. Howard, A diffusion tensor magnetic resonance imaging study of frontal cortex connections in very-late-onset schizophrenia-like psychosis, Am J Geriatr Psychiatry 13 (12) (2005) 1092–1099.

[29] R. Bammer, F. Fazekas, M. Augustin, J. Simbrunner, S. Strasser-Fuchs, T. Seifert, R. Stollberger, H. Hartung, Diffusion-weighted MR imaging of the spinal cord, Am J Neuroradiol. 21 (2000) 587–591.

[30] R. Robertson, S. Maier, R. Mulkern, S. Vajapayam, C. Robson, P. Barnes, MR line-scan diffusion imaging of the spinal cord in children, Am J Neuroradiol. 21 (7) (2000) 1344–1348.

[31] M. C. Chou, Y. R. Lin, T. Y. Huang, C. Y. Wang, H. W. Chung, C. J. Juan, C. Y. Chen, FLAIR diffusiontensor MR tractography comparison of fiber tracking with conventional imaging., AJNR Am J Neuroradiol 26 (2005) 591–597.

[32] J. Carballido-Gamio, D. Xu, D. Newitt, E. T. Han, D. B. Vigneron, S. Majumdar, Single-shot fast spinecho diffusion tensor imaging of the lumbar spine at 1.5 and 3 T., Magn Reson Imaging 25 (2005) 665–670.

[33] P. Summers, P. Staempfli, T. Jaermann, S. Kwiecinski, S. Kollias, A preliminary study of the effects of trigger timing on diffusion tensor imaging of the human spinal cord., AJNR Am J Neuroradiol 27 (2006) 1952–1961.

[34] S. Zhang, D. Laidlaw, DTI fiber clustering and cross-subject cluster analysis, in: ISMRM, 2005, p. 2727.

[35] S. E. Maier, Examination of spinal cord tissue architecture with magnetic resonance diffusion tensor imaging., Neurotherapeutics 4 (2007) 453–459.

[36] M. Ishikawa, M. Matsumoto, Y. Fujimura, K. Chiba, Y. Toyama, Changes of cervical spinal cord and cervical spinal canal with age in asymptomatic subjects, Spinal Cord 41 (2003) 159–163.

[37] V. Stevenson, S. Leary, N. Losseff, G. Parker, G. Barker, Y. Husmani, D. Miller, A. Thompson, Spinal cord atrophy and disability in MS: a longitudinal study, Neurology 51 (1998) 234–238.

[38] C. A. De Boy, J. Zhang, S. Dike, I. Shats, M. Jones, D. S. Reich, S. Mori, T. Nguyen, B. Rothstein, R. H. Miller, J. T. Griffin, D. A. Kerr, P. A. Calabresi, High resolution diffusion tensor imaging of axonal damage in focal inflammatory and demyelinating lesions in rat spinal cord., Brain 130 (2007) 2199–2210.

[39] L. R. Morrison, The effect of advancing age upon the human spinal cord, Harvard University Press, Cambridge, MA, 1959.

[40] M. Ota, T. Obata, Y. Akine, H. Ito, H. Ikehira, T. Asada, T. Suhara, Age-related degen-

eration of corpus callosum measured with diffusion tensor imaging, Neuroimage 31 (2006) 1445–1452.

[41] A. Pfefferbaum, E. Adalsteinsson, E. V. Sullivan, Frontal circuitry degradation marks healthy adult aging: evidence from diffusion tensor imaging., Neuroimage 26 (2005) 891–899.

[42] D. Salat, D. Tuch, D. Greve, A. van der Kouwe, N. Hevelone, A. Zaleta, B. Rosen, B. Fischl, S. Corkin, H. Rosas, A. Dale, Age-related alterations in white matter microstructure measured by diffusion tensor imaging, Neurobiol Aging 26 (2005) 1215–1227.

[43] T. Yoshiura, F. Mihara, A. Tanaka, O. Togao, T. Taniwaki, A. Nakagawa, T. Nakao, T. Noguchi, Y. Kuwabara, H. Honda, Age-related structural changes in the young adult brain shown by magnetic resonance diffusion tensor imaging, Academic Radiology 12 (3) (2005) 268–275.

Hungry Joe collected lists of fatal diseases and arranged them in alphabetical order so that he could put his finger without delay on any one he wanted to worry about.

– Joseph Heller

8

Spinal cord alterations in MS patients without T2 spinal cord lesions: detection with Diffusion Tensor Imaging

Contents

8.1 Introduction

MS is a chronic demyelinating disease of the central nervous system, which is characterized by both inflammatory and neurodegenerative processes. Nowadays, MR imaging is increasingly used in the diagnosis of MS patients with spinal cord involvement [1]. In addition, MR can also be useful in patients who do not have clinical spinal cord involvement, because asymptomatic spinal cord lesions are common in MS and uncommon in other WM disorders [2]. However, the spinal cord lesion information as obtained by a conventional MR examination does not always correlate well with the clinical disability of the patient and/or with histological information [3–5]. It has been demonstrated that the WM regions that appear normal on conventional MR images, referred to as NAWM, are also involved in the MS disease process [6, 7]. In this context, DTI can provide complementary diagnostic information regarding the microstructural WM organization in MS lesions and NAWM [8]. This technique is based on the fact that water molecules have a larger probability to diffuse along the axonal structures than perpendicular to them [8]. Recent studies demonstrate the potential of quantitative DTI parameters, such as the FA, which is a normalized measure of the degree of anisotropy, and the MD, i.e. the averaged diffusion, for detecting WM alterations in patients with MS [9–13].
Since the spinal cord is frequently involved in MS, DTI can be regarded as a valuable technique to examine WM alterations in the spinal cord of patients with MS. However, in contrast to the potential of such a DTI study of the spinal cord, only a limited number of papers are published regarding this topic [1, 14–20]. In this context, it is known that several factors hamper a robust DTI study of the spinal cord, such as restricted DT image resolution, the small size of the spinal cord, and artifacts related to cardiac and respiratory motion, and magnetic field inhomogeneities [21, 22]. As a result, a relatively large number of voxels contain a combined signal originating from both the spinal cord and the CSF, which is also known as a PVE [23].
In a preliminary study of three MS patients, Clark et al. (2000) demonstrated a significant FA decrease and MD increase in MS cord lesions using a ROI based approach [14]. In order to increase the robustness and the reproducibility of the image processing, Valsasina et al. (2005) and Agosta et al. (2005) performed a histogram analysis on the central slice of the sagittal images [15, 16]. In these studies, a significant FA decrease was observed in the cervical spinal cord of MS patients, compared to healthy subjects. This histogram analysis approach was also adopted by Benedetti et al. (2006) in a DTI study of MS patients and patients with neuromyelitis optica [17]. Hesseltine et al. (2006) reported a significant FA decrease in the NAWM of patients with MS in the lateral, central, and posterior regions of the spinal cord at the C2-C3 level compared to healthy subjects [18]. Their image processing method was based on the manual placement of circular ROIs on a single

axial slice. Ohgiya et al. (2007) demonstrated a reduced FA in lesions and NAWM regions of MS patients compared to healthy subjects by manually placing small, ovoid ROIs at the C2-C3, C3-C4, and C4-C5 level [19]. Recently, Ciccarelli et al. (2007) demonstrated that the FA is reduced in MS patients compared to normal controls, using diffusion tensor tractography [20].
Previous DTI studies of the spinal cord in MS patients focused on the examination of diffusion measures in spinal cord lesions or in NAWM near these lesions using ROIs. We hypothesize that the spinal cord can also be involved in the disease when no lesions are reported on the conventional MR scans. In addition, we hypothesize that a tractography based spinal cord segmentation method is more reliable and sensitive to detect diffusion alterations in the normal appearing spinal cord of MS patients compared to the generally applied ROI approach [24]. The aim of this work was therefore to examine the spinal cord diffusion properties of MS patients without T2 spinal cord lesions using diffusion tensor tractography. To the best of our knowledge, this is the first quantitative DTI study of the cervical spinal cord that appears entirely normal on a conventional MR examination in patients with MS.

8.2 Methods

8.2.1 Subjects

Diffusion tensor measurements of the cervical spinal cord (C1–C5) were acquired with a 1.5T MR scanner (Siemens, Erlangen, Germany) from 21 MS patients (age: 38 ± 9 years; 8 males, 13 females). 21 sex- and age-matched healthy subjects were additionally scanned (age: 40 ± 10 years; 8 males, 13 females). All healthy subjects had a normal appearing spinal cord on conventional T_2-weighted MR images. An informed consent was signed by all participants. In 11 of the MS patients, which we will refer to as MS patient group 1, one or more lesions were detected in the spinal cord on conventional MR images. In the other 10 MS patients, which will be referred to as MS patient group 2, no spinal cord lesions were detected on the conventional MR scan. Twelve patients had relapse-remitting MS (6 in MS patient group 1 and 6 in MS patient group 2), 9 patients had secondary progressive MS (5 in MS patient group 1 and 4 in MS patient group 2). There was no clinical suspicion of an acute MS attack in any of the patients at the time of imaging.

8.2.2 MRI Acquisition

The acquisition parameters can be summarized as follows: TR: 10.4 s; TE: 100 ms; diffusion gradient: 40 mT/m; FOV = $256 \times 256 mm^2$ matrix size: 128×128; number of slices = 60; image resolution = $2 \times 2 \times 2 mm^3$; b = $700 s/mm^2$; acquisition

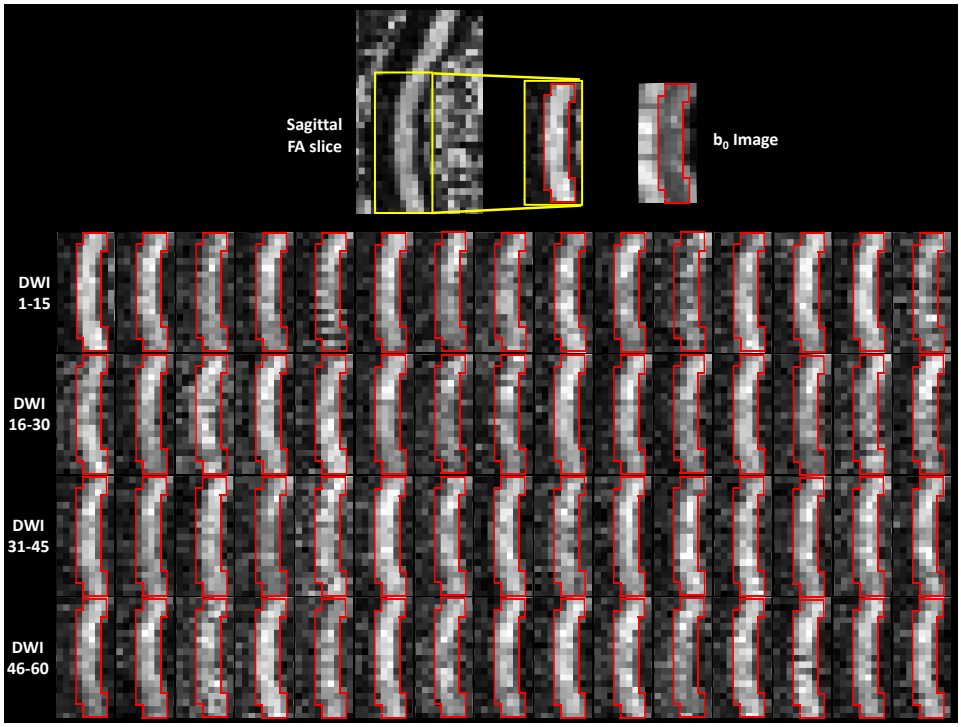

Figure 8.1. *A contour that delineates the spinal cord is drawn in red on a sagittal slice of all diffusion weighted images and the FA map*

time: 12 min 18 s. Diffusion measurements were performed along 60 directions (+ 10 non-diffusion weighted (b0) images) for a robust estimation of FA, tensor orientation, and MD [25]. A combination of 2 elements of the CP (circular polarization) spine coil and 1 element of the neck coil was used to obtain the data. A severe signal dropout due to ghosting, susceptibility, or respiratory artifacts, was observed in data sets of 2 subjects. These data sets were excluded from the analysis. All diffusion-weighted images were analyzed visually to check for the absence of distortions in the data. Data sets were included in the analysis without the use of a specific distortion correction algorithm, when the geometric distortions were smaller than approximately 1 voxel. An example of the diffusion weighted images is provided in Fig. 1. A contour that delineates the spinal cord is drawn on a sagittal slice of the FA map. Exactly the same contour is also placed on the same sagittal slice of all DW images to demonstrate the acceptable spatial correspondence between the different DW images. Diffusion tensor estimation, tractography, visualization, and quantitative analysis, was performed with the diffusion toolbox 'ExploreDTI' (http://www.ExploreDTI.com) [26].

8.2.3 Diffusion Parameters of Interest

Multiple quantitative diffusion parameters were analyzed in all subjects. FA and MD were calculated and averaged over all selected voxels for all subjects. In addition, the longitudinal ($\lambda_{\parallel}$) and transverse ($\lambda_{\perp}$) diffusivities, and the ratio of the longitudinal versus transverse diffusivities ($\lambda_{\parallel}/\lambda_{\perp}$) were also computed, since it has been suggested that this ratio can better differentiate between healthy and diseased subjects [27–30].

8.2.4 Image Analysis

It is generally known that it is difficult to determine spinal cord diffusion measures, because many voxels at the edge of the spinal cord contain a signal of both the spinal cord tissue and CSF. In a first image analysis approach, ROIs were manually placed on each axial slice, thereby carefully delineating the spinal cord to avoid the inclusion of PVE contaminated voxels in the analysis. All ROIs were defined on the axial slices of the FA maps, color encoded for the diffusion direction, since they provided the best contrast between the spinal cord tissue and the surrounding CSF (see Fig. 2 a,b).

In a second image analysis method, also referred to as the tract based segmentation approach, diffusion tensor tractography was performed on the spinal cord that was first manually delineated by ROIs (see Fig. 2 c) [24]. A standard deterministic streamline-based fiber tracking approach was applied with only one seed point per voxel in which the step size was 1 mm [31]. The maximal angle between two consecutive tract points was set to 20° and an FA threshold of 0.3 was used during tractography, as in [24, 32, 33]. Subsequently, all quantitative diffusion parameters of interest are selected on the tracts. The tractography parameters were defined as in Chapter 7, and a careful visual inspection was performed to make sure that the whole spinal cord was covered by fiber tracts without any interruptions in all subjects c. Diffusion tensor tractography is thus used to further segment the spinal cord tissue, using the orientational diffusion information that is present in each voxel. The spinal cord was thereby initially separated from the background noise by drawing an ROI on every axial slice. Multiple ROIs were used to make sure the whole cervical spinal cord was included in the analysis.

The diffusion properties of the MS lesions and the NAWM in the patients with MS lesions were also evaluated. The MS lesions were identified on the anatomical MR images that were acquired at exactly the same cord levels as the diffusion tensor data sets. The ROIs that were used to delineate the lesions on the anatomical MR images were transferred to the DTI data set to obtain the diffusion properties. Analogously, ROIs were drawn on the conventional MR images to delineate the NAWM tissue and subsequently transferred to the DTI data set. As in the work of

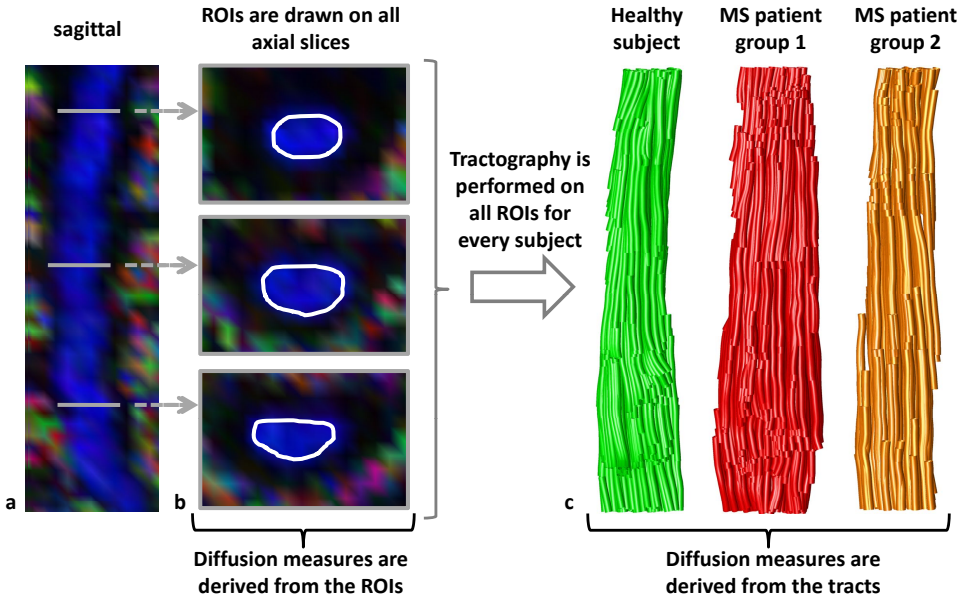

Figure 8.2. *In (a), a sagittal slice of the spinal cord is shown. The color is encoded for the diffusion direction, and the intensity is proportional with the diffusion anisotropy. In the ROI based segmentation method, ROIs are drawn on all axial slices, as demonstrated for three axial slices in (b). In the tractography based segmentation method, diffusion measures are derived from the tracts. In (c), the tactography result of a healthy subject an MS patient with T2 spinal cord lesions and an MS patient without T2 spinal cord lesions are visualized.*

Filippi et al. (2000), spinal cord tissue was assigned to be normal appearing when no lesion was found in the adjacent slices [34].

8.2.5 Statistical Analysis Procedures

Statistical tests were performed with the SPSS analysis package (http://www.spss.com). Male and female data sets were combined since a t-test showed no difference in any of the diffusion parameters between both sexes (p¿¿0.05, with 16 males vs 26 females). Moreover, the age distribution in the three subject groups was not significantly different for both sexes (p>> 0.05, with 16 males vs 26 females). An analysis of covariance (ANCOVA) was employed to compare the cervical cord diffusion properties from the control subject group with both MS patient groups. Kolmogorov-Smirnov tests demonstrated that a parametric approach could be applied (p>> 0.05). Potentially confounding factors, such as the subject's age and the cross-sectional area of their cervical spinal cord - measured as the number of

Table 1: Average A, FA, MS, $\lambda_{||}$, $\lambda_{\perp}$, and $\lambda_{||}/\lambda_{\perp}$ are displayed using three different spinal cord segmentation approaches in control subjects, MS patients with plaques in the spinal cord, and MS patients without plaques in the spinal cord.

Average (Standard Deviation)	control subjects		MS patients with plaques in the spinal cord		MS patients without plaques in the spinal cord	
	ROI	TS	ROI	TS	ROI	TS
A	80.3	89.2	70.7	79.9	75.4	82.0
FA	0.58	0.53	0.54	0.48	0.55	0.48
MD $x10^{-3}$ mm^2/s	1.09	1.21	1.23	1.31	1.18	1.24
$\lambda_{||}$ $x10^{-3}$ mm^2/s	1.89	2.02	2.04	2.18	1.97	2.10
$\lambda_{\perp}$ $x10^{-3}$ mm^2/s	0.69	0.86	0.83	0.96	0.79	0.92
$\lambda_{||}/\lambda_{\perp}$	2.76	2.38	2.47	2.21	2.51	2.23

Abbreviations:
A: cross-sectional spinal cord area; FA: fractional anisotropy; MD: mean diffusivity; $\lambda_{||}$: longitudinal diffusivity; $\lambda_{\perp}$: transverse diffusivity; ROI: region of interest; TS: tract based segmentation method

selected voxels - were included in the ANCOVA model. Although the age and the cross-sectional area were not differently distributed in the different subject groups, both factors were included in the analysis of covariance. Differences in diffusion measures between groups could therefore be attributed to an intrinsic difference between the diffusion properties of the subjects groups. In this context, the cervical spinal cord cross sectional area A was calculated separately for both image analysis approaches as the number of selected voxels for analysis. In addition, the statistical results were adjusted in order to correct for multiple comparisons using Fisher's least significant difference approach. The intra-observer reproducibility of the different image analysis methods was tested using the ICC. To this end, the ROIs were drawn a second time by the same observer. A measurement is deemed highly reproducible if ICC > 0.9. In the case of $0.7 <$ ICC < 0.9, the reproducibility is considered acceptable. Finally, results with an ICC < 0.7 are interpreted as poorly reproducible.

8.3 Results

Using the ROI approach, a mean cross sectional surface A of $80.3mm^2$, $70.7mm^2$, and $75.4mm^2$ was observed for the control group, the MS patient group with le-

sions, and the MS patient group without spinal cord lesions, respectively (see Table 1 and Fig. 3). Although larger cross sectional areas of $89.2mm^2$, $79.9mm^2$, and $82.0mm^2$ were found for the different subject groups using the tractography based image analysis method (see Table 1 and Fig. 3), Pearson correlation tests demonstrated a significant correlation between the cross sectional areas of the ROI and the tractography based approach ($p << 0.001$, $r > 0.9$, results not shown). These results suggest that a smaller cross sectional area of the spinal cord can be observed in the MS patient groups compared to the control group. However, this difference was not found to be statistically significant, as can be observed in Table 2.

The cervical spinal cord diffusion metrics of the different subject groups are presented for the ROI and the tractography based image analysis approaches in Table 1. The distribution of these diffusion measures is visualized using boxplots in Fig. 3, whereby the boxplots of the control group, the MS group with spinal cord lesions, and the MS group without known spinal cord lesions are colored in green, red, and orange, respectively. The results of ANCOVA tests, which compare the diffusion measures across the different subject groups, thereby taking into account the subject age and the cross-sectional spinal cord area, are displayed in Table 2. It can be observed that the FA, the transverse diffusivity $\lambda_\perp$, and the ratio of the longitudinal and transverse diffusivities ($\lambda_\parallel/\lambda_\perp$) are significantly lower for the MS patients with spinal cord lesions compared to the control subjects using the ROI method ($p = 0.014$, $p = 0.028$, and $p = 0.039$, respectively) and the tractography based approach ($p = 0.006$, $p = 0.037$, and $p = 0.012$, respectively). Although the visual results of Fig. 3 suggest an increased MD in the MS patient group with spinal cord lesions, no statistically significant difference in MD was found (Table 2).

The FA and the $\lambda_\parallel/\lambda_\perp$ values were significantly different between the control group and the MS patient group without spinal cord lesions. These FA differences are statistically significant with a p-value of 0.013 for both image analysis methods (Table 2). For $\lambda_\parallel/\lambda_\perp$, a p-value of 0.018 and 0.020 was found for the ROI and the tractography based method, respectively. The diffusion values of the MS patients without spinal cord lesions were not observed to be different from the diffusion measures of the MS patients with spinal cord lesions (see Fig. 1, statistical results not shown). In addition to the study of the NAWM of MS patients without spinal cord lesions, the NAWM diffusion measures of MS patients with spinal cord lesions are examined. To this end, the lesions and the NAWM were separated manually by ROIs. As can be observed in Table 4, all diffusion measures are significantly different in the spinal cord plaques compared to the measures of the control subjects.

Finally, the reproducibility of image processing methods is examined using the intra-class correlation coefficient. As can be observed in Table 3, the ICC is very high for the tractography based method. Since the ROI approach is more user dependent due to the manual delineation of the ROIs, lower ICC values were observed

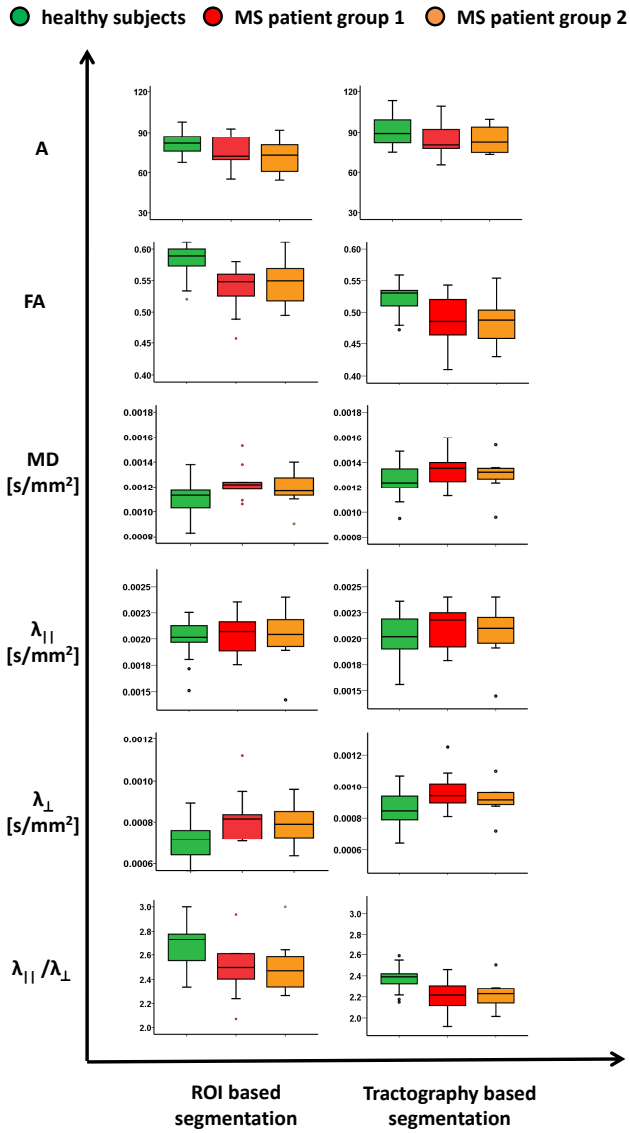

Figure 8.3. *Boxplots are shown for the cross-sectional spinal cord area A, the fractional anisotropy, the mean diffusivity, the longitudinal and the transverse diffusivities, and for the ratio of the longitudinal and transverse eigenvalues. Results of both segmentation methods are displayed for the control subjects, the MS patients with T_2 spinal cord lesions (MS patient group 1), and the MS patients without T_2 spinal cord lesions (MS patient group 2).*

Table 2: Statistical results (p-values) of the comparision of the diffusion measures between the control group and both the MS patient groups. The statistically significant values are marked in red.

	control subjects vs MS patients with plaques in the spinal cord			control subjects vs MS patients without plaques in the spinal cord		
	ROI[c]	ROI[d]	TS	ROI[c]	ROI[d]	TS
A[a]	0.283	0.114	0.174	0.090	0.078	0.168
FA[b]	0.014	0.119	0.006	0.013	0.058	0.013
MD[b]	0.063	0.235	0.138	0.353	0.461	0.584
$\lambda_{\|\|}$[b]	0.192	0.385	0.350	0.607	0.681	0.930
$\lambda_{\perp}$[b]	0.028	0.209	0.037	0.258	0.371	0.155
$\lambda_{\|\|}/\lambda_{\perp}$[b]	0.039	0.139	0.012	0.018	0.111	0.020

[a] ANOVA analysis, corrected for multiple comparisons using Fisher's least significant difference method
[b] ANCOVA analysis, corrected for the cross sectional area of the spinal cord and for age, including a multiple comparisons correction based on Fisher's least significant difference method
[c] Results of the first ROI delineation analysis
[d] Results of the second ROI delineation analysis by the same observer as the first ROI analysis
Abbreviations:
A: cross-sectional spinal cord area; FA: fractional anisotropy; MD: mean diffusivity; $\lambda_{||}$: longitudinal diffusivity; $\lambda_{\perp}$: transverse diffusivity; ROI: region of interest; TS: tract based segmentation method

(see Table 3). Although these ICC values ($0.66 - -0.85$) represent an acceptable reproducibility, the observer-dependency affects the statistical results of the ROI analysis (see Table 2).

8.4 Discussion

Conventional MR is used in daily clinical routine to detect spinal cord lesions in patients with MS. However, it has been demonstrated that findings on conventional MR scans do not always correlate well with the clinical status of the MS patients [35, 36]. In addition, previous studies did not find a correlation between the clinical disability of MS patients and the number and extent of the spinal cord lesions that were detected on MR [3, 37–39]. Since DTI provides information about the microstructural WM organization, the resulting diffusion metrics are potentially more sensitive to detect spinal cord involvement in MS patients than conventional MR is.

Table 4: On the one hand, diffusion measures in the plaques of the MS patients are compared with diffusion measures of the control subjects. On the other hand, the diffusion metrics of the control subjects are compared with these of the NAWM in the MS patients with spinal cord plaques. ROIs were used for this analysis.

	control vs plaques	control vs NAWM
FA	0.001	0.012
MD $x10^{-3}$ mm^2/s	0.017	0.175
$\lambda_{\|\|}$ $x10^{-3}$ mm^2/s	0.035	0.761
$\lambda_{\perp}$ $x10^{-3}$ mm^2/s	0.005	0.071
$\lambda_{\|\|}/\lambda_{\perp}$	0.011	0.035

Abbreviations:
FA: fractional anisotropy; MD: mean diffusivity; $\lambda_{\|\|}$: longitudinal diffusivity; $\lambda_{\perp}$: transverse diffusivity; NAWM: normal appearing white matter

In this work, the spinal cord of MS patients without any lesions on the conventional MR scans is studied with DTI. To the best of our knowledge, all DTI studies of the spinal cord in MS patients evaluated the diffusion metrics in spinal cord lesions or in NAWM in the proximity of lesions. Our results suggest that the FA and the ratio of the longitudinal and transverse eigenvalues are significantly reduced in the spinal cord of MS patients without lesions (see Fig. 3 and Tables 1-2). These results were confirmed by the analysis of the NAWM in the spinal cord with lesions (see Table 4). In concordance with the literature, the FA was found to be significantly reduced in the MS patients with spinal cord lesions compared to the FA of the age- and sex-matched control subjects [1, 14–20]. In addition, a significant increase of the transverse eigenvalues and decrease of the ratio of the longitudinal and transverse eigenvalues was observed in the spinal cord of these MS patients compared to the control subjects. Within the spinal cord lesions, the FA and the ratio of the longitudinal and transverse eigenvalues were decreased and the MD, the longitudinal, and transverse eigenvalues were increased, compared to the diffusion measures of the healthy spinal cord tissue of the control subjects.

Table 3: Intra-class correlation coefficients (ICC) measure the intra-rater reproducibility of the different diffusion measures

ICC	ROI	TS
FA	0.79	0.96
MD $x10^{-3}$ mm^2/s	0.79	0.97
$\lambda_{\|\|}$ $x10^{-3}$ mm^2/s	0.85	0.97
$\lambda_{\perp}$ $x10^{-3}$ mm^2/s	0.83	0.98
$\lambda_{\|\|}/\lambda_{\perp}$	0.66	0.96

Abbreviations:
FA: fractional anisotropy; MD: mean diffusivity; $\lambda_{||}$: longitudinal diffusivity; $\lambda_{\perp}$: transverse diffusivity; ROI: region of interest; TS: tract based segmentation method

In agreement with the literature, our results suggest that the FA and the ratio of the longitudinal and transverse diffusivities are the most sensitive diffusion measures to detect microstructural alterations that are induced by the MS disease process. These differences were observed in the NAWM and the lesions of MS patients with T2 spinal cord lesions and in the NAWM of MS patients without T_2 spinal cord lesions (see Table 2 and 4). Additionally, an increased MD, longitudinal diffusivity, and transverse diffusivity was observed within the spinal cord lesions. A recent post-mortem study, which correlated diffusion measures with the myelin content and the axonal count, suggested that an FA decrease and a MD increase is primary correlated with loss of myelin [40]. Recent studies using animal models further demonstrated that a loss of axons is represented by a decreased longitudinal diffusivity and a normal transverse diffusivity, whereas myelin breakdown is represented by an increased transverse diffusivity and a normal longitudinal diffusivity [27–30]. Another post-mortem study demonstrated a strong correlation of the axonal density and loss of myelin with the diffusion anisotropy and a weaker correlation with the MD [41]. As also proposed by Agosta et al. (2005), astrocytic proliferation, cell debris, fibrillary gliosis, and inflammatory infiltrates can result in a normalization of the MD values and can therefore prevent the MD differences to be statistically sig-

nificant, as observed in our study [1, 16, 42]. Some studies report differences in the diffusion measures between relapse-remitting, primary-progressive and secondary-progressive MS patients [1, 15]. In our study, the diffusion properties were not found to be statistically different between the subjects with relapse-remitting MS and secondary-progressive MS, which might be explained by the low statistical power due to the limited number of patients in our study.

The magnitude of the quantitative diffusion measures that were found in this study (see Table 1), are within the range of the previously reported values (see Table 5). Notice that a large variability exists in the FA and MD measures across different studies [14–20]. This is probably due to disease heterogeneity in the different groups (different age range, disease state,), the use of different image acquisition and analysis methods, and the relatively low reproducibility of some of these methods. All previous DTI studies of the spinal cord of MS patients reported a statistically significant FA difference between the control group and the MS patient group, whereas MD was only found to be different in some studies. In addition to the group and disease heterogeneity and the use of various image analysis methods, the application of different statistical methods and post-hoc tests, and the incorporation of various co-factors in the statistics can explain the differences in the reported p-values. Different co-factors, such as the age of the subjects and the cross-sectional area of the spinal cord were incorporated in the statistics since it is known that these factors can affect diffusion values of the spinal cord [24].

Since many spinal cord voxels are affected by different degrees of partial volume averaging with CSF it is not straightforward to reliably select the relevant spinal cord voxels of interest in the different subjects. Some studies evaluate histogram information originating from the central part of the spinal cord [15–17]. In this approach, a lot of valuable information is discarded. In addition, the sensitivity to find differences between control subjects and MS patients can be reduced, since Hesseltine et al. (2006) demonstrated that only minor differences were found in the central part of the spinal cord, which mainly consist of grey matter [18]. Most of the studies utilize an ROI based approach to obtain diffusion data. However, it has been demonstrated that the reproducibility of this method can be very low [24]. Although the ICC values that were found in this study were acceptable (see Table 3), the statistical results and conclusions differed significantly when the ROIs were drawn a second time by the same observer (see Table 2). In this context, there is a need for a standardized approach for analyzing spinal cord DTI data, which, in our opinion, is provided by diffusion tensor tractography based segmentation. In contrast to studies that incorporated diffusion tensor tractography results of the spinal cord to provide qualitative information regarding the fiber architecture, tractography was applied in this study to provide quantitative diffusion information regarding the WM damage induced in the spinal cord of patients with MS [33, 43–47]. Compared to the ROI method, an observer dependency is replaced by

Table 5: Comparison of FA and MD values across different DTI studies of the spinal cord in MS patients

reference	control subjects		MS patients	
	FA	MD $x10^{-3}$ mm²/s	FA	MD $x10^{-3}$ mm²/s
Van Hecke et al.	0.58	1.09	0.55	1.21
Van Hecke et al.	0.53	1.21	0.48	1.28
Valsasina et al. (15)	0.43	1.22	0.36	1.28
Agosta et al. (16)	0.42	1.20	0.38	1.28
Benedetti et al. (17)	0.42	1.22	0.37	1.32
Hesseltine et al. (18)	0.60	0.82	0.52	0.88
Ohgiya et al. (19)	0.74	0.64	0.56	0.72
Cicarelli et al. (20)	0.47	0.71	0.42	0.73

Abbreviations:
FA: fractional anisotropy; MD: mean diffusivity

a parameter dependency of the tractography algorithm, resulting in a more reproducible and standardized measurement of the diffusion characteristics (see Table 3).

A standard acquisition scheme was used, which is available on most scanners in a clinical setting, without the need of specific hardware. In addition, isotropic voxels were acquired to reduce the PVE of spinal cord tissue with the surrounding CSF in the slice direction. However, due to the limited in-plane resolution, it was hard to separate WM and GM. In addition, other reported modifications of the DTI acquisition scheme might improve image quality and therefore the reliability of the subsequent analysis. For example, studies have focused on the optimization of the DTI acquisition with respect to bulk motion and pulsatile low artifacts from the surrounding CSF [48–52]. Other studies employed cardiac gating and interleaved echo-planar diffusion imaging to reduce motion artifacts and scan time, respectively [53, 54]. Line scan imaging is a fast technique that relies on the acquisition of columns [50, 55]. The advantage of our work is that it uses a standard, widely available acquisition scheme with isotropic voxels. 60 diffusion directions were used to increase the SNR and the reliability of our estimated diffusion measures in order to perform tractography reliably [25]. Another limitation of our study is that no correlation was made of the diffusion metrics with clinical symptoms, as measured for example by the EDSS [56]. However, the primary aim of our

study was to demonstrate the feasibility and potential of the tractography based segmentation approach to evaluate the spinal cord damage of MS patients and to investigate the diffusion measures of MS patients without T2 spinal cord lesions. The correlation of the diffusion metrics with the clinical status of the patients is already thoroughly reported in earlier studies [15–17, 20]. We believe that our results demonstrate that diffusion tensor tractography has the potential to be used a standardized segmentation tool of spinal cord DT images for the interpretation of NAWM results in MS patients. We also acknowledge that our findings are by no means conclusive and that our results should be interpreted cautiously, given that our study may have been limited by the relatively small number of subjects.
In conclusion, diffusion measures of the normal appearing white matter were evaluated in MS patients without spinal cord lesions. A reduced FA and ratio of the longitudinal and the transverse eigenvalues was observed in the spinal cord of MS patients without any detected spinal cord lesion on a conventional MR scan. These results therefore suggest that the spinal cord is not preserved in MS when lesions are only detected in the brain. Furthermore, this confirms previous findings, which demonstrated that DTI is more sensitive compared to conventional MR imaging in assessing the tissue damage in MS patients. In addition, we demonstrated that diffusion tensor tractography is a robust tool to analyze the spinal cord of MS patients and that the use of tractography is more reproducible and reliable compared to an ROI analysis to evaluate the diffusion measures of the spinal cord.

Bibliography

[1] F. Agosta, M. Absinta, M. P. Sormani, A. Ghezzi, A. Bertolotto, E. Montanari, G. Comi, M. Filippi, In vivo assessment of cervical cord damage in MS patients: a longitudinal diffusion tensor MRI study., Brain 130 (2007) 2211–2219.

[2] J. C. Bot, F. Barkhof, C. H. Polman, G. . Lycklama Nijeholt, V. de Groot, E. Bergers, H. J. Ader, J. A. Castelijns, Spinal cord abnormalities in recently diagnosed MS patients: added value of spinal MRI examination, Neurology 62 (2004) 26–33.

[3] D. Kidd, J. Thorpe, T. A., B. E. Kendall, I. F. Moseley, D. G. MacManus, McDonald., D. H. W. I, Miller, Spinal cord MRI using multi-array coils and fast spin echo. II. Findings in multiple sclerosis., Neurology 43 (1993) 2632–2637.

[4] C. Bjartmar, R. P. Kinkel, G. Kidd, R. A. Rudick, B. D. Trapp, Axonal loss in normal-appearing white matter in a patient with acute MS., Neurology 57 (2001) 1248–1252.

[5] L. Tartaglino, D. Friedman, A. Flanders, F. Lublin, R. Knobler, M. Liem, Multiple sclerosis in the spinal cord: MR appearance and correlation with clinical parameters., Radiology 195 (1995) 725–732.

[6] D. H. Miller, R. I. Grossman, S. C. Reingold, H. F. Mcfarland, The role of magnetic resonance techniques in understanding and managing multiple sclerosis., Brain 121 (1) (1998) 3–24.

[7] D. Werring, C. Clark, G. Parker, D. Miller, A. Thompson, G. Barker, A direct demonstration of both structure and function in the visual system: combining diffusion tensor imaging with functional magnetic resonance imaging, NeuroImage 9 (3) (1999) 352–361.

[8] E. Cassol, J. P. Ranjeva, D. Ibarrola, C. Mkies, C. Manelfe, M. Clanet, I. Berry, Diffusion

tensor imaging in multiple sclerosis: a tool for monitoring changes in normal-appearing white matter., Mult Scler 10 (2004) 188–196.

[9] C. Beaulieu, The basis of anisotropic water diffusion in the nervous system - a technical review, NMR in Biomedicine 15 (7–8) (2002) 435–455.

[10] P. Basser, D. Jones, Diffusion-tensor MRI: theory, experimentel design and data analysis - a technical review, NMR biomed 15 (2002) 456–467.

[11] Y. Ge, M. Law, R. Grossman, Applications of diffusion tensor MR imaging in multiple sclerosis., Ann N Y Acad Sci 1064 (2005) 202–219.

[12] A. C. Guo, T. J. Cummings, R. C. Dash, J. M. Provenzale, Lymphomas and high-grade astrocytomas: comparison of water diffusibility and histologic characteristics, Radiology 224 (2002) 177–183.

[13] M. A. Horsfield, H. B. Larsson, D. K. Jones, A. Gass, Diffusion magnetic resonance imaging in multiple sclerosis, Journal of Neurology, Neurosurgery and Psychiatry 64 (S1) (1998) S80–S84.

[14] C. Clark, D. Werring, D. Miller, Diffusion imaging of the spinal cord in vivo: estimation of the principal diffusivities and application to multiple sclerosis, Magn Reson Med. 43 (2000) 133–138.

[15] P. Valsasina, M. Rocca, F. Agosta, B. Benedetti, M. Horsfield, A. Gallo, M. Rovaris, G. Comi, M. Filippi, Mean diffusivity and fractional anisotropy histogram analysis of the cervical cord in MS patients, NeuroImage 26 (2005) 822–828.

[16] F. Agosta, B. Benedetti, M. Rocca, P. Valsasina, M. Rovaris, G. Comi, M. Filippi, Quantification of cervical cord pathology in primary progressive MS using diffusion tensor MRI, Neurology 64 (2005) 631–635.

[17] B. Benedetti, P. Valsasina, E. Judica, V. Martinelli, A. Ghezzi, R. Capra, R. Bergamaschi, G. Comi, M. Filippi, Grading cervical cord damage in neuromyelitis optica and MS by diffusion tensor MRI., Neurology 67 (2006) 161–163.

[18] S. M. Hesseltine, M. Law, J. Babba, M. Rad, S. Lopez, Y. Ge, G. Johnson, R. I. Grossman, Diffusion Tensor Imaging in Multiple Sclerosis: Assessment of Regional Differences in the Axial Plane within Normal-Appearing Cervical Spinal Cord., AJNR 27 (2006) 1189–1193.

[19] Y. Ohgiya, M. Oka, A. Hiwatashi, X. Liu, N. Kakimoto, P. L. Westesson, S. E. Ekholm, Diffusion tensor MR imaging of the cervical spinal cord in patients with multiple sclerosis., Eur Radiol 17 (10) (2007) 2499–2504.

[20] O. Ciccarelli, C. A. Wheeler-Kingshott, M. A. McLean, M. Cercignani, K. Wimpey, D. H. Miller, A. J. Thompson, Spinal cord spectroscopy and diffusion-based tractography to assess acute disability in multiple sclerosis., Brain 130 (2007) 2220–2231.

[21] C. Clark, D. Werring, Diffusion tensor imaging in spinal cord: methods and applications - a review, NMR Biomed. 15 (2002) 578–586.

[22] C. Wheeler-Kingshott, S. Hickman, G. Parker, O. Ciccarelli, M. Symms, D. Miller, G. Barker, Investigating cervical spinal cord structure using axial diffusion tensor imaging, NeuroImage 16 (2002) 93–102.

[23] A. Pfefferbaum, E. Sullivan, Increased brain white matter diffusivity in normal adult aging: relationship to anisotropy and partial voluming, Magn Reson Med 49 (5) (2003) 953–961.

[24] W. Van Hecke, A. Leemans, J. Sijbers, E. Vandervliet, J. Van Goethem, P. M. Parizel, A tracking based DTI segmentation method for the detection of diffusion-related changes of the cervical spinal cord with aging., Journal of Magnetic Resonance Imaging 27 (2008) 978–991.

[25] D. Jones, The effect of gradient sampling schemes on measures derived from diffusion tensor MRI: a Monte Carlo study, Magn Reson Med 51 (4) (2004) 4607–4621.

[26] A. Leemans, J. Sijbers, P. Parizel, A graphical toolbox for exploratory diffusion tensor imaging and fiber tractography, in: 14th Annual Meeting - Section for Magnetic Resonance Technologists, Miami, USA, 2005.

[27] S. Song, S. Sun, M. Ramsbottom, C. Chang, J. Russell, A. Cross, Dysmyelination revealed through MRI as increased radial (but unchanged axial) diffusion of water, NeuroImage 17 (3) (2002) 1429–1436.

[28] S. K. Song, S. W. Sun, W. K. Ju, S. J. Lin, A. H. Cross, A. H. Neufeld, Diffusion tensor imaging detects and differentiates axon and myelin degeneration in mouse optic nerve after retinal ischemia., NeuroImage 20 (2003) 1714–1722.

[29] S. Song, J. Yoshino, T. Le, S. Lin, S. Sun, A. Cross, R. Armstrong, Demyelination increases radial diffusivity in corpus callosum of mouse brain, Neuroimage 21 (2005) 132–140.

[30] C. Pierpaoli, A. Barnett, S. Pajevic, R. Chen, L. Penix, A. Virta, P. Basser, Water diffusion changes in Wallerian degeneration and their dependence on white matter architecture, NeuroImage 13 (6) (2001) 1174–1185.

[31] P. Basser, S. Pajevic, C. Pierpaoli, J. Duda, A. Aldroubi, In vivo fiber tractography using DT-MRI data, Magnetic Resonance in Medicine 44 (2000) 625–632.

[32] E. Melhem, S. Mori, G. Mukundan, M. Kraut, M. Pomper, P. van Zijl, Diffusion tensor MR imaging of the brain and white matter tractography, Am J Roentgenol 178 (1) (2002) 3–16.

[33] K. Tsuchiya, A. Fujikawa, K. Honya, T. Nitatori, S. Y., Diffusion tensor tractography of the lower spinal cord., Neuroradiology 50 (2008) 221–225.

[34] M. Filippi, C. Tortorella, M. Rovaris, M. Bozzali, F. Possa, M. P. Sormani, G. Iannucci, G. Comi, Changes in the normal appearing brain tissue and cognitive impairment in multiple sclerosis, Journal of Neurology, Neurosurgery and Psychiatry 68 (2000) 157–161.

[35] G. Lovas, N. Szilagyi, K. Majtenyi, M. Palkovits, S. Komoly, Axonal changes in chronic demyelinated cervical spinal cord plaques., Brain 123 (2000) 308–317.

[36] E. Bergers, J. C. Bot, P. van der Valk, J. A. Castelijns, G. J. Lycklama a Nijeholt, W. Kamphorst, C. H. Polman, E. L. Blezer, K. Nicolay, R. Ravid, F. Barkhof, Diffuse signal abnormalities in the spinal cord in multiple sclerosis: direct postmortem in situ magnetic resonance imaging correlated with in vitro high-resolution magnetic resonance imaging and histopathology., Ann Neurol 51 (2002) 652–656.

[37] G. J. Lycklama Nijeholt, M. A. A. van Walderveen, J. A. Castelijns, J. H. van Waesberghe, C. Polman, P. Scheltens, P. F. Rosier, P. J. Jongen, F. Barkhof, Brain and spinal cord abnormalities in multiple sclerosis. Correlation between MRI parameters, clinical subtypes and symptoms., Brain 121 (1998) 687–697.

[38] V. Stevenson, S. Leary, N. Losseff, G. Parker, G. Barker, Y. Husmani, D. Miller, A. Thompson, Spinal cord atrophy and disability in MS: a longitudinal study, Neurology 51 (1998) 234–238.

[39] V. L. Stevenson, I. F. Moseley, C. C. Phatouros, D. MacManus, A. J. Thompson, D. H. Miller, Improved imaging of the spinal cord in multiple sclerosis using three-dimensional fast spin echo., Neuroradiology 40 (1998) 416–419.

[40] K. Schmierer, C. A. Wheeler-Kingshott, P. A. Boulby, F. Scaravilli, D. R. Altmann, G. J. Barker, P. S. Tofts, D. H. Miller, Diffusion tensor imaging of post mortem multiple sclerosis brain., NeuroImage 35 (2007) 467–477.

[41] J. P. Mottershead, K. Schmierer, M. Clemence, J. S. Thornton, F. Scaravilli, G. J. Barker, P. S. Tofts, J. Newcombe, M. L. Cuzner, R. J. Ordidge, W. I. McDonald, D. H. Miller, High field MRI correlates of myelin content and axonal density in multiple sclerosis. A post-mortem study of the spinal cord., J Neurol 250 (2003) 1293–1301.

[42] G. J. Lycklama Nijeholt, E. Bergers, W. Kamphorst, J. Bot, K. Nicolay, J. A. Castelijns, J. H. van Waesberghe, R. Ravid, C. H. Polman, F. Barkhof, Post-mortem high-resolution MRI of the spinal cord in multiple sclerosis: a correlative study with conventional MRI, histopathology and clinical phenotype., Brain 124 (2001) 154–166.

[43] D. Facon, A. Ozanne, P. Fillard, J. F. Lepeintre, C. Tournoux-Facon, D. Ducreux, MR diffusion tensor imaging and fiber tracking in spinal cord compression., AJNR 26 (2005)

1587–1594.

[44] D. Ducreux, J. F. Lepeintre, P. Fillard, C. Loureiro, M. Tadi, P. Lasjaunias, MR diffusion tensor imaging and fiber tracking in 5 spinal cord astrocytomas., AJNR 27 (2006) 214–216.

[45] H. Voss, R. Watts, A. Uluğ, D. Ballon, Fiber tracking in the cervical spine and inferior brain regions with reversed gradient diffusion tensor imaging, Magn Reson Imaging .

[46] J. Renoux, D. Facon, P. Fillard, I. Huynh, P. Lasjaunias, D. Ducreux, MR Diffusion Tensor Imaging and Fiber Tracking in Inflammatory Diseases of the Spinal Cord., AJNR 27 (2006) 1947–1951.

[47] M. Vargas, J. Delavelle, H. Jlassi, B. Rilliet, M. Viallon, C. D. Becker, K. O. Lvblad, Clinical applications of diffusion tensor tractography of the spinal cord., Neuroradiology 50 (2008) 25–29.

[48] S. Maier, H. Mamata, Diffusion tensor imaging of the spinal cord, Ann N Y Acad Sci. 1064 (2005) 50–60.

[49] R. Bammer, F. Fazekas, M. Augustin, J. Simbrunner, S. Strasser-Fuchs, T. Seifert, R. Stollberger, H. Hartung, Diffusion-weighted MR imaging of the spinal cord, Am J Neuroradiol. 21 (2000) 587–591.

[50] R. Robertson, S. Maier, R. Mulkern, S. Vajapayam, C. Robson, P. Barnes, MR line-scan diffusion imaging of the spinal cord in children, Am J Neuroradiol. 21 (7) (2000) 1344–1348.

[51] M. C. Chou, Y. R. Lin, T. Y. Huang, C. Y. Wang, H. W. Chung, C. J. Juan, C. Y. Chen, FLAIR diffusiontensor MR tractography comparison of fiber tracking with conventional imaging., AJNR Am J Neuroradiol 26 (2005) 591–597.

[52] J. Carballido-Gamio, D. Xu, D. Newitt, E. T. Han, D. B. Vigneron, S. Majumdar, Single-shot fast spinecho diffusion tensor imaging of the lumbar spine at 1.5 and 3 T., Magn Reson Imaging 25 (2005) 665–670.

[53] P. Summers, P. Staempfli, T. Jaermann, S. Kwiecinski, S. Kollias, A preliminary study of the effects of trigger timing on diffusion tensor imaging of the human spinal cord., AJNR Am J Neuroradiol 27 (2006) 1952–1961.

[54] S. Zhang, D. Laidlaw, DTI fiber clustering and cross-subject cluster analysis, in: ISMRM, 2005, p. 2727.

[55] S. E. Maier, Examination of spinal cord tissue architecture with magnetic resonance diffusion tensor imaging., Neurotherapeutics 4 (2007) 453–459.

[56] J. F. Kurtzke, Rating neurologic impairment in multiple sclerosis: an expanded disability status scale (EDSS)., Neurology 33 (1983) 1444–1452.

List of abbreviations

2D	two-dimensional
3D	three-dimensional
ADC	Apparent Diffusion Coefficient
ANOVA	Analysis of Variance
ANCOVA	Analysis of Covariance
CC	Corpus Callosum
CNS	Central Nervous System
CSF	Cerebrospinal Fluid
CT	Computed Tomography
DOF	Degrees Of Freedom
DT	Diffusion Tensor
DSI	Diffusion Spectrum Imaging
DTI	Diffusion Tensor Imaging
DTT	Diffusion Tensor Tractography
DT-MRI	Diffusion Tensor Magnetic Resonance Imaging
DW	Diffusion-Weighted
DWI	Diffusion-Weighted Imaging
EDSS	Expanded Disability Status Scale
EPI	Echo-Planar Imaging
FA	Fractional Anisotropy
FDR	False Discovery Rate
FS	Finite Strain
fMRI	functional Magnetic Resonance Imaging
FOV	Field of View
FWHM	Full Width at Half Maximum
GM	Gray Matter
HARD	High-Angular-Resolution Diffusion
HARDI	High-Angular-Resolution Diffusion-weighted Imaging
HS	Hybrid Segmentation
ICC	Intra-Class Correlation
MD	Mean Diffusivity
MI	Mutual Information
MIRIT	Multimodality Image Registration using Information Theory
MNI	Montreal Neurological Institute
MPRAGE	Magnetization Prepared Rapid Acquisition Gradient Recalled Echo
MR	Magnetic Resonance

MRI	Magnetic Resonance Imaging
MS	Multiple Sclerosis
NAWM	Normal Appearing White Matter
OVL	Overlap of eigenvalue-eigenvector pairs
PASAT	Paced Auditory Serial Addition Test
PB	Population Based
PBA	Population Based Atlas
PCA	Principal Component Analysis
PD	Principal Diffusivity
PDF	Probability Density Function
PET	Positron Emission Tomography
PPD	Preservation of Principal Direction
PVE	Partial Volume Effect
PVSAT	Paced Visual Serial Addition Test
RF	Radio Frequency
ROI	Region Of Interest
ROC	Receiver Operating Characteristic
RR	Relapse Remitting
SB	Subject Based
SBA	Subject Based Atlas
SE	Spin Echo
SNR	Signal-to-Noise Ratio
SSD	Sum of Squared Distances
TBSS	Tract Based Spatial Statistics
TR	Tensor Reorientation
TS	Tract Based Segmentation
QBI	Q-Ball Imaging
US	Ultrasound
VBA	Voxel Based Analysis
WM	White Matter

List of publications

Journal articles

1. W. Van Hecke, A. Leemans, E. D'Agostino, S. De Backer, E. Vandervliet, P. M. Parizel and J. Sijbers, *Nonrigid Coregistration of Diffusion Tensor Images Using a Viscous Fluid Model and Mutual Information*, IEEE Transactions on Medical Imaging, Vol. 26, Nr. 11, p. 1598-1612, (**2007**)

2. P.M. Parizel, V. Van Rompaey, R. Van Loock, W. Van Hecke, J. W. Van Goethem, A. Leemans and J. Sijbers, *Influence of User-Defined Parameters on Diffusion Tensor Tractography of the Corticospinal Tract*, The Neuroradiology Journal, Nr. 20, p. 139-147, (**2007**)

3. W. Van Hecke, A. Leemans, J. Sijbers, E. Vandervliet, J. Van Goethem and P.M. Parizel, *A tracking based DTI segmentation method for the detection of diffusion-related changes of the cervical spinal cord with aging*, Journal of Magnetic Resonance Imaging, Vol. 27, Nr. 5, p. 978-991, March (**2008**)

4. W. Van Hecke, J. Sijbers, E. Dagostino, F. Maes, S. De Backer, E. Vandervliet, P.M. Parizel and A. Leemans, *On the construction of an inter-subject diffusion tensor magnetic resonance atlas of the healthy human brain*, NeuroImage, (**2008**)

Conference proceedings (full paper)

First-author contributions: 12 international (8 oral presentations and 4 posters) and 2 national (2 oral presentations) conference proceedings.

1. W. Van Hecke, A. Leemans, E. D Agostino, S. De Backer, E. Vandervliet, P.M. Parizel and J. Sijbers, *The evaluation of a population based diffusion tensor image atlas using a ground truth method*, Proceedings of SPIE Medical Imaging, Ed: Reinhardt, Joseph M.; Pluim, Josien P. W., Vol. 6914, San Diego, USA, February, (**2008**)

2. W. Van Hecke, A. Leemans, S. De Backer, E. Vandervliet, P.M. Parizel, E. D Agostino and J. Sijbers, *Multi-channel coregistration of diffusion tensor images based on a viscous fluid model*, Belgian Day on Biomedical Engineering - IEEE/EMBS Benelux Symposium, p. 139-142, Brussels, Belgium, (**2006**)

Conference proceedings (abstract)

1. W. Van Hecke, A. Leemans, S. De Backer, E. Vandervliet, P.M. Parizel, J. Sijbers and E. d'Agostino, *A ground truth analysis of the preservation of diffusion tensor information in a population specific atlas*, 16nd meeting of the International Society for Magnetic Resonance in Medicine (ISMRM), Toronto, Canada, **2008**

2. W. Van Hecke, A. Leemans, J. Sijbers, P.M. Parizel and J. Van Goethem, *Diffusion tensor tractography reveals white matter alterations in the normal appearing spinal cord of Multiple Sclerosis patients*, 24rd Annual Scientific Meeting of the European Society for Magnetic Resonance in Medicine and Biology, Valencia, Spain, **2008**

3. W. Van Hecke, A. Leemans, S. De Backer, P.M. Parizel, and J. Sijbers, *On the construction of a ground truth methodology to evaluate VBM analysis results of diffusion tensor images*, 24rd Annual Scientific Meeting of the European Society for Magnetic Resonance in Medicine and Biology, Valencia, Spain, **2008**

4. A. Leemans, W. Van Hecke, C. Lebel, L. Walker, J. Sijbers and C. Beaulieu, *A model based approach for voxelwise analysis of multi-subject diffusion tensor data*, Joint Annual Meeting ISMRM-ESMRMB, Berlin, (**2007**)

5. P.M. Parizel and W. Van Hecke, *Diffusion Tensor Imaging: Is it really useful?*, 32nd Congress of the Europea Society of NeuroRadiolog, (**2007**)

6. W. Van Hecke, A. Leemans, E. Vandervliet, P.M. Parizel and J. Sijbers, *An optimized tensor orientation strategy for non-rigid alignment of DT-MRI data*, Joint Annual Meeting ISMRM-ESMRMB, Berlin, (**2007**)

7. W. Van Hecke, E. Dagostino, A. Leemans, P.M. Parizel, F. Maes and J. Sijbers, *On the construction of a healthy brain inter-subject diffusion tensor image and tractography atlas*, 32nd Congress of the Europea Society of NeuroRadiolog, p. 146, (**2007**)

8. W. Van Hecke, A. Leemans, N. De Brabander, A. Laridon, K. Claeys, B. Ceulemans, J. Van Goethem, P.M. Parizel and J. Sijbers, *Diffusion Tensor Fiber Tracking Reveals Probst Bundles in Patients with Agenesis of the Corpus Callosum*, 32nd Congress of the Europea Society of NeuroRadiolog, p. 135, (**2007**)

9. W. Van Hecke, A. Leemans, J. Sijbers, P.M. Parizel and J. Van Goethem, *Diffusion Tensor Tractoghraphy Reaveals Spinal Cord Alterations in Patients with Multiple Sclerosis*, 32nd Congress of the Europea Society of NeuroRadiolog, p. 129, (**2007**)

10. G. Nagels, E. Vandervliet, W. Van Hecke, S. Engelborghs, M.B. D hooghe, P. Cras, P.M. Parizel and P.P. De Deyn, *fMRI during PASAT and PVSAT in mild MS, moderate MS and normal volunteers*, 22nd Congress of the European Committee for, Madrid, Spain, (**2006**)

11. W. Van Hecke, A. Leemans, J. Sijbers, P.M. Parizel and J. Van Goethem, *A comparison of diffusion tensor analysis methods for detecting age-related changes of the normal appearing spinal cord*, 23rd Annual Scientific Meeting of the European Society for Magnetic Resonance in Medicine and Biology, p. 293-294, Warsaw, Poland, (**2006**)

12. W. Van Hecke, A. Leemans, S. De Backer, E. Vandervliet, P.M. Parizel, J. Sijbers and E. d Agostino, *Non-rigid coregistration of diffusion tensor images using a viscous fluid model*, 23rd Annual Scientific Meeting of the European Society for Magnetic Resonance in Medicine and Biology, p. 191-192, Warsaw, Poland, (**2006**)

13. W. Van Hecke, A. Leemans, N. De Brabander, A. Laridon, B. Ceulemans, J and P.M. Parizel, *Diffusion tensor fiber tracking in patients with agenesis of the corpus callosum*, 23rd Annual Scientific Meeting of the European Society for Magnetic Resonance in Medicine and Biology, p. 34-35, Warsaw, Poland, (**2006**)

14. E. Vandervliet, G. Nagels, A. Heinecke, W. Van Hecke, A. Leemans, J. Sijbers and P.M. Parizel, *On the cause and mechanisms of the negative BOLD*

response in fMRI, 23rd Annual Scientific Meeting of the European Society for Magnetic Resonance in Medicine and Biology, p. 308, Warsaw, Poland, (**2006**)

15. W. Van Hecke, A. Leemans, P.M. Parizel, J.W.M. Van Goethem, J. Sijbers, *DTI of normal appearing spinal cord in elderly*, 21th Annual Symposium – Belgian Hospital Physicists Association, p. 61, Ghent, Belgium, **2006** (oral presentation)

16. W. Van Hecke, A. Leemans, P.M. Parizel, J.W.M. Van Goethem, J. Sijbers, *DTI of normal appearing spinal cord in elderly*, 44th Annual Meeting of the American Society of Neuroradiology, San Diego, USA, **2006** (poster)

Awards

1. *Educational Stipend Award* for the submitted work, entitled: "Multiscale white matter fiber tract coregistration: a new feature–based approach to align diffusion tensor data" at the 14th Annual ISMRM Meeting – Seattle, USA, **2006**

Nederlandse samenvatting

Context

De menselijke hersenen bevatten een complex netwerk van vezelbundels die verschillende delen van de hersenen met elkaar verbinden, zodat communicatie ertussen mogelijk is. Iets meer dan 10 jaar geleden waren dissecties en histologie studies op post-mortem hersenen of invasieve onderzoeken op primaten de enige manier om informatie over de hersenvezelstructuur te verkrijgen. Recente ontwikkelingen in de magnetische resonantie beeldvormings (MRI) techniek laten echter toe om de witte materie (WM) bundels van de hersenen virtueel te reconstrueren in levende mensen. De informatie over de WM bundels wordt verkregen door de diffusie van water moleculen te bestuderen met de diffusie tensor beelvormings (DTI) techniek. Een virtuele 3D reconstructie van de hersenvezelbanen kan dan worden verkregen door gebruik te maken van tractografie.

DTI maakt het mogelijk om de vezelarchitectuur van de WM microstructuur te beschrijven door een persoon voor enkele minuten in een MRI scanner te plaatsen. Daardoor bezit DTI een groot potentieel om de menselijke hersenconnectiviteit te onderzoeken in gezonde personen en in patiënten met verschillende neurologische of psychiatrische aandoeningen. Tegenwoordig wordt dan ook veel onderzoek gedaan naar het uitklaren van het verband tussen de gemeten diffusie waarden en de veranderingen in de onderliggende microstructuur door de aanwezigheid van een pathologie. DTI wordt reeds gebruikt in de dagelijkse klinische routine van vele ziekenhuizen voor de pre-operatieve planning van patiënten met een hersentumor. DTI heeft echter ook veel potentieel om te worden gebruikt in ziekenhuizen als een diagnostische techniek voor patiënten met neurologische symptomen. Daaryoe zijn grootschalige groepstudies noodzakelijk die de DTI resultaten van gezonde mensen en patiënten met een bepaalde pathologie vergelijken.

Het doel van dit doctoraat is het optimaliseren van de DTI dataverwerking van de menselijke hersenen om aldus tot een meer betrouwbare detectie van WM aantastende pathologieën te komen. Verder werd eveneens de DTI dataverwerking van het ruggenmerg onderzocht voor de detectie van neurologische ruggenmerg aandoeningen.

Overzicht van het manuscript

Deze doctoraatsthesis is onderverdeeld in drie delen:

Achtergrond: In het eerste deel worden een het centrale zenuwstelsel (Hoodstuk 2) en de diffusie tensor beeldvormingstechniek (Hoodstuk 3) geïntroduceerd. De anatomie van het centrale zenuwstelsel wordt kort beschreven op een cellulair en een functioneel niveau. Daarna wordt een overzicht van hersen beeldvormingstechnieken gegeven. In Hoodstuk 3 worden de basisprincipes van de DTI techniek uitgelegd, van de Brownse beweging van water moleculen tot de virtuele reconstructie van de drie dimensionele hersenverbindingen en klinische toepassingen. Daarna worden de verschillende DTI beeldverwerkingsmethodes geïntroduceerd.

Diffusie Tensor Beeldverwerking van de Menselijke Hersenen: In het tweede deel van deze thesis worden nieuwe technieken voor de DTI beeldverwerking voorgesteld.

In Hoodstuk 4 wordt een niet-affiene coregistratie methode gebaseerd op een viskeus vloeistofmodel en mutuele informatie gepresenteerd. Dit algoritme werd specifiek ontworpen voor de coregistratie van de meerwaarduge DTI beelden. Het doel van coregistratie is het transformeren van een beeld naar een ander, zodat de corresponderende anatomische structuren met elkaar gealigneerd zijn. Indien dit het geval is kan de beeldinformatie objectief vergeleken worden in het zelfde ruimtelijke kader. Hoewel de verschillende anatomische structuren meestal in verschillende personen aanwezig zijn, kunnen ze sterk verschillen in vorm en grootte. Om medische beelden van verschillende personen naar elkaar te transformeren, zijn daardoor niet-affiene vervormingen, die lokaal kunnen worden aangepast, noodzakelijk. In tegenstelling tot andere medische beelden, zoals anatomische magnetische resonantie, ultra-sound of tomografie data sets, die een scalaire waarde in elke voxel bevatten, bezitten DTI data sets meerwaardige informatie in elke voxel. Coregistratie algoritmes moeten daarom aangepast worden zodat deze meerwaardige diffusie informatie in rekening kan worden gebracht.

Het maken van een atlas laat toe om beelden van verschillende personen naar een gemeenschappelijk referentiekader te transformeren. Daarna kunnen de beeldeigenschappen vergeleken worden tussen data sets van gezonde en zieke personen op een voxel-niveau. In Hoofdstuk 5 wordt een populatiespecifieke atlas gemaakt en vergeleken met een 'subject'-gebaseerde atlas, gebruik makend van simulaties en reë beelden.

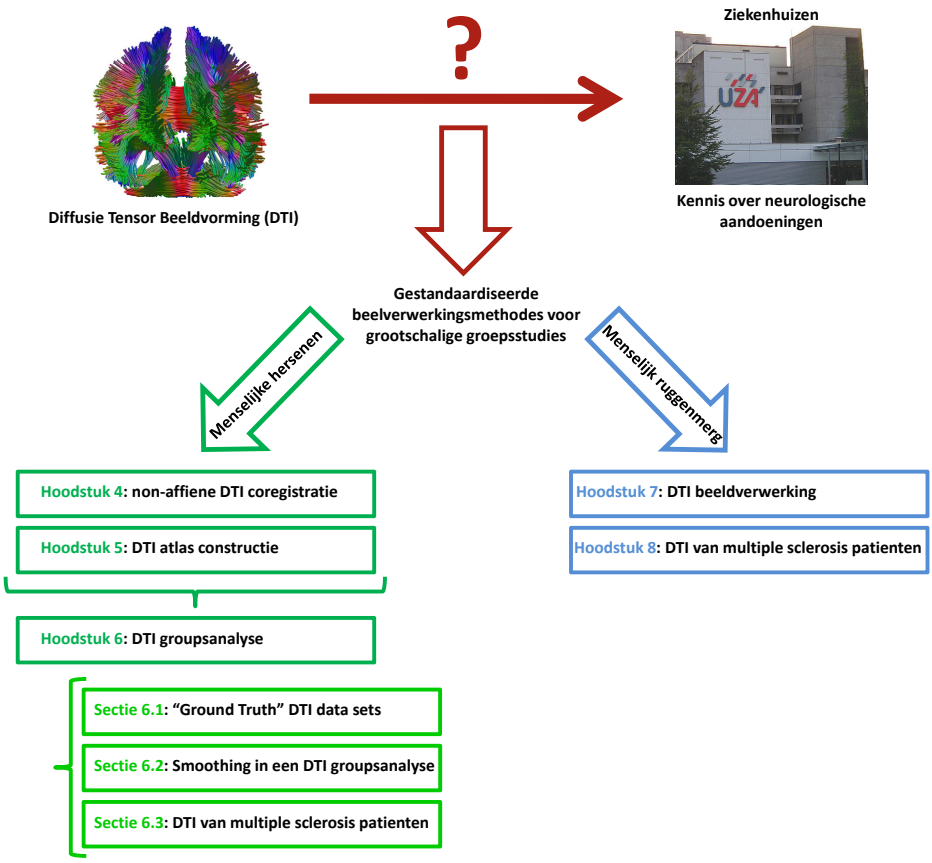

Figuur 8.4. *Een schematisch overzicht van dit doctoraat.*

Nadat alle DTI data sets van een groep getransformeerd werden naar de atlas ruimte kunnen de diffusie-eigenschappen van deze beelden vergeleken en geanalyseerd worden op een voxel-niveau. Daartoe worden statistische testen toegepast in elke voxel om de verschillen tussen de gezonde personen en de patiënten te detecteren. Deze beeldverwerkingstechniek wordt een voxel gebaseerde analyse (VBA) genoemd. In VBA worden de hele hersenen getest voor controle-patiënt verschillen zonder de noodzaak aan een a priori hypothese over de ruimtelijke locatie in de hersenen van de verwachte verschillen. Deze VBA methode bezit vele voordelen vergeleken met andere beeldverwerkingstechnieken, zoals de regio van interesse (ROI) gebaseerde methode. Overeenkomsten tussen resultaten van verschillende studies worden echter niet altijd waargenomen, zoals bijvoorbeeld het geval

is in de studies van patiënten met schizofrenie [1–14]. De heterogeniteit van de patiëntgroepen en van de ziekte zelf kunnen deze tegenstrijdigheden deels verklaren. Methodologische verschillen in de VBA beeldverwerkingsmethode tussen de verschillende studies, zijn mogelijk echter nog meer bepalend om de variabiliteit in de resultaten te verklaren [9, 15, 16].

In Hoodstuk 6 worden gesimuleerde DTI data sets gemaakt. Deze laten toe om een bepaalde pathologie te modeleren in een gekende WM lokatie. De gesimuleerde DTI data sets kunnen dan ook gebruikt worden om de sensitiviteit en specificiteit om een pathologie te vinden met een VBA of ROI analyse te onderzoeken. Ook het effect van verschillende parametersettings en beelverwerkingsstappen die gekozen dienen te worden in een VBA analyse, kunnen onderzocht worden. Dit zal uiteindelijk leiden tot een meer betrouwbare, gestandaardiseerde en consistente DTI beeldverwerking voor het onderzoek naar verschillende pathologieën. Als een eerste toepassing van de gesimuleerde DTI data sets, werd het effect van beeldsmoothing op de sensitiviteit en specificitiet van de VBA analyse onderzocht (Hoodstuk 6).

In het laatste deel van Hoofdstuk 6 worden de nieuwe beeldverwerkingsmethodes voor de analyse van DTI beelden van de menselijke hersenen toegepast in een studie naar het cognitieve achteruitgang bij patiënten met multiple sclerose.

Diffusie Tensor Beeldverwerking van het Menselijke Ruggenmerg: Het derde deel van dit doctoraat handelt over de DTI beelverwerking van ruggenmerg data. Verschillende factoren, zoals fysiologische en ademhalingsbeweging van de persoon in de scanner en relatieve beweging van het ruggenmerg zelf door de nabije aanwezigheid van pulserend cerebor spinaal vocht, belemmeren een robuuste DTI studie van het ruggenmerg. Bovendien heeft een ruggenmerg een beperkte diameter (gemiddeld 12 mm) en is ook de DTI beeldresolutie beperkt, waardoor een betrouwbare kwantitatieve DTI analyse van het ruggenmerg moeilijk wordt. In Hoofdstuk 7 wordt een gestandardiseerde en robuuste segmentatie techniek, gebaseerd op tractografie, voor de analyse en interpretatie van ruggenmerg data voorgesteld. Deze nieuwe beeldverwerkingsmethode wordt daarna toegepast voor de analyse van DTI data sets van patiënten met multiple sclerose (Hoofdstuk 8.)

Bibliografie

[1] I. Agartz, J. Andersson, S. Skare, Abnormal brain white matter in schizophrenia: a diffusion tensor imaging study, NeuroReport 12 (10) (2001) 2251–2254.

[2] J. Foong, M. R. Symms, G. J. Barker, M. Maier, D. H. Miller, M. A. Ron, Investigating regional white matter in schizophrenia using diffusion tensor imaging., NeuroReport 13 (3) (2002) 333–6.

[3] B. A. Ardekani, J. Nierenberg, M. J. Hotman, D. C. Javitt, K. O. Lim, MRI Study of White Matter Diffusion Anisotropy in Schizophrenia., NeuroReport 14 (16) (2003) 2025–2029.

[4] J. Burns, D. Job, M. Bastin, H. Whalley, T. Macgillivray, E. Johnstone, S. Lawrie, Structural disconnectivity in schizophrenia: a diffusion tensor magnetic resonance imaging study, British Journal of Psychiatry 182 (2003) 439–443.

[5] P. R. Szeszko, B. A. Ardekani, M. Ashtari, S. Kumra, D. G. Robinson, S. Sevy, H. Gunduz-Bruce, A. K. Malhotra, J. M. Kane, R. M. Bilder, K. O. Lim, White matter abnormalities in first-episode schizophrenia or schizoaffective disorder: a diffusion tensor imaging study., Am J Psychiatry 162 (3) (2005) 602–605.

[6] M. Kubicki, H. Park, C.-F. Westin, P. Nestor, R. Mulkern, S. Maier, M. Niznikiewicz, E. Connor, J. Levitt, M. Frumin, R. Kikinis, F. Jolesz, R. McCarley, M. Shentona, DTI and MTR abnormalities in schizophrenia: analysis of white matter integrity, NeuroImage 26 (4) (2005) 1109–1118.

[7] B. A. Ardekani, A. Bappal, D. D'Angelo, M. Ashtari, T. Lencz, P. R. Szeszko, P. D. Butler, D. C. Javitt, K. O. Lim, J. Hrabe, J. Nierenberg, C. A. Branch, M. J. Hoptman, Brain morphometry using diffusion weighted MRI: Application to schizophrenia., NeuroReport 16 (13) (2005) 1455–1459.

[8] M. S. Buchsbaum, J. Friedman, B. R. Buchsbaum, K. Chu, E. A. Hazlett, R. Newmark, J. S. Schneiderman, Y. Torosjan, C. Tang, P. R. Hof, D. Stewart, K. L. Davis, J. Gorman, Diffusion tensor imaging in schizophrenia., Biol Psych 60 (11) (2006) 1181–1187.

[9] D. K. Jones, X. A. Chitnis, D. Job, P. L. Khong, L. T. Leung, S. Marenco, S. M. Smith, M. R. Symms, What happens when nine different groups analyze the same DT-MRI data set using voxel-based methods?, Proc. ISMRM 15th Annual Meeting, Berlin (2007) 74.

[10] G. Douaud, S. Smith, M. Jenkinson, T. Behrens, H. Johansen-Berg, J. Vickers, S. James, N. Voets, K. Watkins, P. M. Matthews, A. James, Anatomically related grey and white matter abnormalities in adolescent-onset schizophrenia., Brain 130 (2007) 2375–2386.

[11] J. H. Seok, H. J. Park, J. W. Chun, S. K. Lee, H. S. Cho, J. S. Kwon, J. J. Kim, White matter abnormalities associated with auditory hallucinations in schizophrenia: A combined study of voxel-based analyses of diffusion tensor imaging and structural magnetic resonance imaging., Psychiatry Res. 156 (2) (2007) 93–104.

[12] K. H. Karlsgodt, T. G. M. van Erp, R. A. Poldrack, C. E. Bearden, K. H. Nuechterlein, T. D. Cannon, Diffusion tensor imaging of the superior longitudinal fasciculus and working memory in recent-onset schizophrenia., Biol Psych 63 (5) (2007) 512–518.

[13] M. Kyriakopoulos, N. S. Vyas, G. J. Barker, X. A. Chitnis, S. Frangou, A diffusion tensor imaging study of white matter in early-onset schizophrenia., Biol Psychiatry 63 (5) (2007) 519–523.

[14] T. White, A. T. K. Kendi, S. Lehricy, M. Kendi, C. Karatekin, A. Guimaraes, N. Davenport, S. C. Schulz, K. O. Lim, Disruption of hippocampal connectivity in children and adolescents with schizophrenia - a voxel-based diffusion tensor imaging study., Schizophr Res 90 (1–3) (2007) 302–307.

[15] D. Jones, M. Symms, M. Cercignani, R. Howarde, The effect of filter size on VBM analyses of DT-MRI data, NeuroImage 26 (2) (2005) 546–554.

[16] H. Zhang, B. B. Avants, P. A. Yushkevich, J. H. Woo, S. Wang, L. F. McCluskey, L. B. Elman, E. R. Melhem, J. C. Gee, High-dimensional spatial normalization of diffusion tensor images improves the detection of white matter differences: An example study using amyotrophic lateral sclerosis, IEEE Trans. Med. Imaging 26 (11) (2007) 1585–1597.

List of Figures

The human brain contains a very complex network of fiber bundles that connect different brain regions, allowing them to communicate. A little more than a decade ago, dissection and histology studies on postmortem human brains or invasive studies on primates were the only way to acquire information on the neural architecture.
However, recent advancements in magnetic resonance imaging (MRI) allow virtual in-vivo dissection of major white matter bundles in the brain. Information about the white matter fibers is obtained by measuring the diffusion of water molecules, using a technique called diffusion tensor magnetic resonance imaging (DT-MRI) or diffusion tensor imaging (DTI). A virtual reconstruction of the fiber network in three dimensions can then be derived from this diffusion information using diffusion tensor tractography.

Since DTI is capable of accurately describing the underlying architecture of the WM microstructure in a non-invasive way, i.e. by placing a subject for a few minutes in an MRI scanner, it has a lot of potential for unraveling the human brain connectivity in healthy subjects and in patients with neurological and psychiatric disorders. Nowadays, a lot of research is done to reveal the relationship between DTI measures and the underlying microstuctural alterations that are induced by a pathology. DTI is already used in the daily clinical routine of many hospitals for the presurgical planning of patients with a brain tumor. In addition, DTI has the potential of being applied in the hospitals as a diagnostic tool for patients with neurological symptoms. To this end, large scale group studies that compare patient and healthy subject DTI data sets need to be performed.

The goal of the work in this book is to optimize the post-processing of DTI data sets of the human brain for a reliable detection of WM altering pathologies. In addition, the post-processing of spinal cord DTI data sets is examined for the detection of neurological spinal cord affecting disorders.